A REATTACHING TURBULENT SHEAR LAYER IN INCOMPRESSIBLE FLOW

by

C. CHANDRSUDA, B.Sc., A.C.G.I., M.R.Ae.S.

Department of Aeronautics

Imperial College of Science and Technology

A Thesis submitted for the Doctor of Philosophy Degree of the University of London, December 1975.

SUMMARY

To develop calculation methods for more complex flows, apart from well-understood boundary layers and other thin shear layers, an understanding of the main physical features of the flow field and the relevant experimental data for testing the calculation results are both essential. The present thesis describes the investigation of a flow involving separation and reattachment, which is one of the most interesting and important of the types of flow that are common in engineering practice. The investigation is confined to a low speed flow over a simple backward-facing step, where special attention is focused on the reattachment region which is expected to have a great influence on the downstream relaxation process.

The results demonstrate further complications of flow of this nature, in particular the complex relationship between various parameters. Although the mean-flow measurements agree reasonably well with the data of previous workers, the fluctuating-quantity measurements show clearly that a more reliable and accurate means of measurement than hot-wire anemometry is needed for more effective investigation in the separated-flow and reattachment regions. However the present turbulence measurements provide an adequate description of the part of the free shear layer that is deflected downstream after reattachment and determines the properties of the relaxing boundary layer. It is found that close to the point of separation the free shear layer approximates to a plane mixing layer, possessing extremely high turbulent intensities, large turbulent shear stress, and large transport terms. The reattachment region involves a rapid decrease of most turbulence quantities, and the decrease continues to about 4 step heights downstream of reattachment. At the end of this region of rapid decrease the values of most terms are still much higher than those in the equilibrium boundary layer, indicating that a great distance is required for the

shear layer to relax to such a state, but the results definitely show the trend of monotonic return to that state. The shear layer appears to be a hybrid between a mixing layer and an ordinary boundary layer many step heights downstream of reattachment.

ACKNOWLEDGEMENTS

I wish to express my sincere thanks to all those in the Department of Aeronautics of the Imperial College of Science and Technology who contributed to the success of the research undertaken, and especially to Mr. P. Bradshaw who supervised the work and gave painstaking guidance throughout, and to Professor P. R. Owen for many helpful discussions.

Considerable help was given by the technical staff in the Workshop and Electronics Laboratory. My thanks are also due to Mr. J. O'Leary, Photographer, and Miss A. Pindelska, Librarian.

I am greatly indebted to the Royal Thai Air Force for financial support during my stay in this country: to Air Vice Marshal B. Riddhagni, Dean of the Royal Thai Air Force Academy, for being instrumental in making this venture possible, and to Group Captain S. Panyasook, Head of the Technical Department, RTAF Academy, for advice and encouragement.

Finally, I would like to thank my wife and children for waiting so patiently during my long absence from home.

CONTENTS

	Page No.
SUMMARY	i, ii
ACKNOWLEDGEMENT	iii
LIST OF CONTENTS	iv - viii
LIST OF FIGURES	ix, x, xi
LIST OF SYMBOLS	xii - xiv
CHAPTER 1 INTRODUCTION	1
1.1 GENERAL REMARKS	1
1.2. BRIEF REVIEW OF PREVIOUS WORK	4
1.3 PURPOSES AND SCOPE OF PRESENT INVESTIGATION	6
CHAPTER 2 THE EXPERIMENTAL ARRANGEMENTS AND INSTRUMENTATION	9
2.1. THE WIND TUNNEL AND THE TEST RIG	9
2.1.1 The Wind Tunnel	9
2.1.2 The Automatic Speed Control Unit	9
2.1.3 Description of the Test Rig	10
2.1.4 The Working Section for Plane Mixing Layer Experiments	11
2.2. FLOW VISUALIZATION EQUIPMENT	12
2.2.1 The Smoke Tunnel, The Smoke Generator and the Light Source	
2.2.2 Oil-flow Mixture and Tufts	14
2.3 TRAVERSE GEAR	14
2.4. PRESSURE MEASUREMENT INSTRUMENTATION	15
2.4.1 Surface Pressure Tappings	15
2.4.2. Pressure Probes	16
(a) Pitot Tubes	16
(b) Disc-Static Probe	17

	Page No
2.4.3. Preston and Stanton Tubes	17
2.4.4. Manometers	18
2.5. THE DATA LOGGING SYSTEM	19
2.6. HOT WIRE ANEMOMETRY	20
2.6.1 Hot Wire Probes	20
2.6.2 Anemometers and Associated Units	21
2.7 THE HOT WIRE DYNAMIC CALIBRATOR AND INSTRUMENTATION	21
2.7.1 The Dynamic Calibrator	21
2.7.2 Instrumentation	22
2.8. ANALOGUE AND DIGITAL RECORDING INSTRUMENTATION	22
2.8.1 Analogue Measuring Equipment	22
2.8.2 Analogue Recording Equipment	22
2.8.3 Digital Recording Equipment	23
2.9 REFERENCE-MEAN-STREAMLINE TRACING SET-UP	24
CHAPTER 3. THE EXPERIMENTS AND ASSOCIATED TECHNIQUES	31
3.1. FLOW VISUALIZATION	31
3.1.1 Flow Study in the Smoke Tunnel	31
3.1.2 Determination of the Reattachment Line	32
3.1.3 Plane Mixing Layer Experiments	33
3.2. SURFACE PRESSURE AND SKIN FRICTION MEASUREMENTS	34
3.2.1. Streamwise Surface Pressure Distribution Measurements	34
3.2.2 Local Skin Friction Measurements	34
3.3 CALIBRATION PROCEDURES AND TECHNIQUES	35
3.3.1 Pitot Tube Calibration in Reverse Flow	35
3.3.2 Disc-Static Probe Calibration	35

Page No

3.3.3 Stanton Tube Calibration 36

3.3.4 Hot Wire Calibration 37

3.4. MEAN FLOW MEASUREMENTS 38

3.4.1. Mean Velocity Profile Measurements Using Pressure Probes 38

3.4.2. Mean Velocity Profile Measurements by U-Probe Hot Wire 39

3.4.3. Reference-Mean-Streamline Tracing 39

3.5. MEASUREMENTS OF FLUCTUATING QUANTITIES 40

3.5.1 Longitudinal Turbulence Intensity Using a Single-Wire Probe 40

3.5.2 X-Probe Hot Wire Traverse 40

3.5.3 Sampling Techniques 41

CHAPTER 4. EXPERIMENTAL RESULTS 55

4.1. GENERAL FLOW BEHAVIOUR 55

4.2. MEAN FLOW MEASUREMENTS 56

4.3 MEASUREMENTS OF FLUCTUATING QUANTITIES 65

4.4 THE TURBULENT ENERGY BALANCE 67

4.5. THE SHEAR STRESS BALANCE 70

CHAPTER 5. DISCUSSION OF RESULTS 135

5.1. ZONES OF TRUSTWORTHY MEASUREMENTS 135

5.2 MEAN FLOW RESULTS 139

5.2.1. General Features of a Flow Field Involving Separation and Reattachment 139

5.2.2 Surface-Pressure Distribution 144

5.2.3 Total Pressure Profiles 148

5.2.4 Static Pressure Profiles 148

5.2.5 Mean Velocity Profiles 150

5.2.6 Semi-Logarithmic Profiles and Skin Friction 151

Page No

5.3 FLUCTUATING QUANTITY RESULTS 152

5.3.1 Turbulent Intensities 152

5.3.2 Turbulent Shear Stress 156

5.3.3 Triple Products of Fluctuating Velocity 158

5.3.4 Statistical Description of Turbulence 160

5.3.5 The Intermittency 164

5.4. THE TURBULENT ENERGY BALANCE 167

5.4.1 Upstream of the Reattachment Region 168

- Production 168

- Dissipation 170

- Diffusion and Advection 171

5.4.2 The Reattachment Region 173

5.4.3 Downstream of the Reattachment Region 174

- Production 175

- Dissipation 176

- Diffusion and Advection 177

5.4.4 Overall Features of Turbulent Energy Balance 178

5.5. SHEAR STRESS BALANCE 178

5.5.1 Upstream of the Reattachment Region 179

5.5.2 The Reattachment Region 180

5.5.3 Downstream of the Reattachment Region 180

5.5.4 Overall Features of Shear Stress Balance 181

CHAPTER 6. GENERAL DISCUSSION AND CONCLUSIONS 223

6.1 THE SEPARATED-FLOW REGION 224

6.2 REATTACHMENT AND RELAXATION REGIONS 227

6.3 CONCLUSIONS 231

REFERENCES - Page 235.

APPENDIX I AN ASSESSMENT OF THE EVIDENCE FOR ORDERLY STRUCTURE IN TURBULENT MIXING LAYER

APPENDIX II IMPROVED METHOD OF HOT-WIRE CALIBRATION CURVE FITTING

APPENDIX III A NOTE ON RMS VELOCITY OF DYNAMIC CALIBRATOR

LIST OF FIGURES

		Page No.
2.1	Side View of Tunnel with Test Rig	25
2.2	Wind Tunnel Automatic Speed Control	26
2.3	Light Box and Lens Arrangements	27
2.4	Pressure Probes	28
2.5	Cross-Section of Test Rig Showing Heated Wire Arrangement and Filling at Roof	29
2.6	Passive RC Low-Pass Filter Circuit	29
2.7	Dynamic Calibrator	30
3.1	Pitot-Tube Calibration	43
3.2	Disc-Static Probe Calibration	44
3.3	Stanton Tube Calibration	45
3.4(a)	Typical U-Wire Static Calibration	46
3.4(b)	Typical Linearized U-Wire Calibration	47
3.5(a)	Typical X-Wire Static Calibration	48
3.5(b)	Typical Linearized X-Wire Calibration - Wire 1	49
3.5(c)	Typical Linearized X-Wire Calibration - Wire 2	50
3.5(d)	Typical Linearized X-Wire Yaw Calibration	51
3.6	Typical Hot-Wire Dynamic Calibration	52
3.7	Apparatus for Pressure Measurements	53
3.8	Apparatus for U-Probe Traverse	53
3.9	Apparatus for X-Wire Traverse	54
4.1	Sketch of Typical Reattaching Shear Layer	71
4.2	Oil-Flow Photographs of Reattachment Line	72
4.3	Surface-Pressure Distribution	73
4.4	Streamwise Variation of Surface-Pressure in Roshko & Lau's Reduced Co-Ordinates	74
4.5	Effect of Reynolds number on C_p	75
4.6	Skin Friction Coefficient	76

		Page No
4.7 (a)-(b)	Transverse Variation of Static Pressure	77-78
4.8 (a)-(c)	Total Pressure Profiles	79-81
4.9	Contour Plot of Total Pressure Coefficient	82
4.10(a)-(c)	Mean Velocity Profiles	83-85
4.11	Contour Plot of U/U_{ref} from Pitot Results	86
4.12	Contour Plot of U/U_{ref} from U-Wire results	87
4.13(a)-(b)	Clauser Charts	88-89
4.14(a)-(b)	Semi-Logarithmic Plot of Mean Velocity Profiles	90-91
4.14(c)	Comparison of Pitot and U-Wire Results	92
4.15	Collective Plot of Semi-Logarithmic Velocity Profiles	93
4.16(a)-(c)	Temperature Profiles Downstream of Heated Wire	94-96
4.17	Reference Mean Streamline	97
4.18	Streamwise Variation of External Stream Velocity at y/h = 1.8	98
4.19(a)-(l)	Fluctuating Quantities	99-110
4.20	Contour Plot of $\overline{u^2}/U^2_{ref}$ - U-Wire Results	111
4.21	Contour Plot of $\overline{u^2}/U^2_{ref}$ - X- Wire Results	112
4.22	Contour Plot of $\overline{v^2}/U^2_{ref}$	113
4.23	Contour Plot of $-\overline{uv}/U^2_{ref}$	114
4.24(a)-(j)	Energy Balance	115-124
4.25(a)-(j)	Shear Stress Balance	125-134
5.1	Demarcation of Reliable Region of Results	183
5.2	Method of Approximate Reattachment Location Determination from Surface-Pressure Distribution	184
5.3	Streamwise Variation of Maximum $\overline{u^2}/U^2_{ref}$, $\overline{v^2}/U^2_{ref}$ and $-\overline{uv}/U^2_{ref}$	185
5.4	Comparison of Maximum Turbulent Intensities with Other Workers' Data	186
5.5	Maximum Shear Stresses	187
5.6(a)-(b)	$\overline{u^3}/U^3_{ref}$ vs. y/h	188-189
5.7	$\overline{v^3}/U^3_{ref}$ vs. y/h	190

		Page No
5.8(a)-(b)	$\overline{u^2 v}/U^3_{ref}$ vs. y/h	191-192
5.9(a)-(b)	$\overline{uv^2}/U^3_{ref}$ vs. y/h	193-194
5.10(a)-(d)	Flatness Factors	195-198
5.11	Minimum Values of Flatness Factor	199
5.12	Loci of Minimum Flatnesses	200
5.13(a)-(f)	Skewness Factors	201-206
5.14	Location of Zero Skewness Factor	207
5.15(a)-(f)	Intermittency Factors	208-213
5.16	Approximate Location of Maximum Intermittency Factor	214
5.17	5% Intermittency Interface	215
5.18	Comparison of Intermittency Factor with Results of Other Workers	216
5.19	Approximate Streamwise Variation of Peak Values of Energy Balance Terms	217
5.20	Approximate Location of Peaks of Energy Balance Terms	218
5.21	Streamwise Variation of Shear-Stress Production	219
5.22	Streamwise Variation of Dissipation	219
5.23	Streamwise Variation of Transverse Diffusion	220
5.24	Streamwise Variation of Advection	220
5.25	Streamwise Variation of Energy Integrals	221
5.26	Comparison between Streamwise Variation of $(\partial U/\partial y + \partial V/\partial x)_{max}$ and $(-\overline{uv})_{max}$	222
6.1	Approximate Variation of Reversed Volume Flow	233
6.2	Approximate Variation of Forward Volume Flow	233
6.3	Location of Maxima, Minima and Zeros	234

LIST OF SYMBOLS

A, B, C	constants in hot-wire response equations, $E^2 = A+BU^n$ and $E^2 = A+BU^n+CU^{2n}$; C is also a constant of proportionality in linearized hot-wire calibration, E=CU.
c	constant in approximate correction expression for disc-static pressure measurements.
C_f	skin friction coefficient } all based on U_{ref}
Cp	static pressure coefficient } all based on U_{ref}
Cp_b	base pressure coefficient } all based on U_{ref}
Cp_T	total pressure coefficient } all based on U_{ref}
E	anemometer mean output voltage
E_{lin}	linearized anemometer mean output voltage
e	anemometer fluctuating output voltage
H	boundary layer shape factor = δ^*/θ
h	step height
k	ratio $\sqrt{\overline{v^2}} / \sqrt{\overline{u^2}}$
M	Mach number
n	constant index in hot-wire response equations
P	total pressure
P_{ref}	reference total pressure
p	true static pressure
p_D	static pressured measured by disc-static probe
p_{ref}	reference static pressure
Q_R	reversed volume flow per unit span
Q_F	forward volume flow in shear layer per unit span
$\frac{1}{2}\overline{q^2} = \frac{1}{2}(\overline{u^2}+\overline{v^2}+\overline{w^2})$	turbulent energy
R_e	Reynolds number; additional suffices indicate 'length' on which it bases, e.g. $R_{e\,\delta_o}$ is Reynolds number based on initial boundary layer thickness.

List of Symbols (Cont)

t	time in transport equations
U	mean velocity in x - direction
U_e	free (external) stream velocity at given x
U_{ref}	reference velocity $\sqrt{[2(P_{ref} - p_{ref})/\rho]}$
U_1	external stream velocity at chosen y
U meas.	measured mean velocity
u	fluctuating velocity in x-direction
u_r	friction velocity
v	fluctuating velocity in y-direction
w	fluctuating velocity in z-direction (spanwise)
x, y, z	Cartesian co-ordinates as defined in figure 4.1; z is in spanwise direction (not shown); referred to as longitudinal (or streamwise), transverse and lateral (or spanwise) directions respectively reattachment distance from step (see figure 4.1)
$\tilde{x}$	non-dimensional streamwise co-ordinates = x/x_r
y_s	ordinate of reference mean streamline
y^+	$=yu_\tau/\nu$
β	angle the velocity vector makes with the x-axis
γ	intermittency factor or disc-static probe calibration constant
δ, δ_{995}	boundary layer thickness
δ_o	initial boundary layer thickness
δ^*	displacement thickness of boundary layer
Δp_s	Stanton tube pressure difference
ϵ	dissipation
η	=y/x in Castro's (1973) results

List of Symbols (cont)

θ	momentum thickness of boundary layer or temperature
ν	kinematic viscosity
ρ	density
σ	$= \rho v^2 / \rho_o v_o^2$; 'o' indicates the standard atmosphere values, or standard deviation
ψ_s	angle the reference mean streamline makes with the x-axis
τ_w	wall shearing stress

CHAPTER 1

INTRODUCTION

1.1. GENERAL REMARKS

The importance of understanding turbulence has been emphasized in many technical reports and text-books. The emphasis is almost always on practical applications of the knowledge in engineering design, such as ways to overcome or decrease drag for economy in power, the usefulness of turbulent mixing in combustion processes, and so on. Turbulent flows range from fairly simple cases - which we now understand quite well - to very complex flows. The rapid development of electronic measuring equipment in the recent years has made possible the investigations of turbulent boundary layers and other thin shear layers, so that calculation methods for these flows are now reliable and well documented. We are therefore in a position to attempt extending the state of the art towards the calculation of the more complicated flows that occur in engineering practice. As suggested by Bradshaw & Wong (1972), an important class of flows, and an obvious target for extension of thin-shear-layer studies, is the class of strongly perturbed shear layers; both the immediate response to the perturbation and the relaxation back to the thin-shear-layer state are of interest. The most common perturbations which are strong enough to invalidate the boundary-layer approximation are those involving separation and reattachment, of which the classical example is flow over a backward-facing step. In order to develop calculation methods for such flows, firstly an understanding of the main physical features of the flow field is necessary, and secondly experimental date are needed to test the calculated results. Although a large number of investigations of separated flow has been reported in the literature, the phenomena of turbulent separation, reattachment and relaxation are still far from well understood; and there is definitely a great need for data to formulate and test calculation methods. The present work is an attempt to fulfil

both requirements, but only the reattachment and relaxation regions are the main interest here; we will return to this point in section 1. 3.

The complication of the flow of this nature has long been realized; it changes from boundary layer to mixing layer after separation, and back to boundary layer again after reattachment. A closely related flow is that behind a bluff body where the mixing layers merge to form a wake which relaxes to a self-preserving form. At low speeds the flow is oscillatory but at supersonic speeds it is steady. Work on reattaching flows or base flows is more advanced at high speeds, partly because the absence of a vortex street makes experiments and calculations easier and partly because of the importance of shock-induced separation bubbles and the great need for data on drag of bodies like bullets and shells, or even space re-entry vehicles at these speeds. At high speeds the results of investigation on flow over a simple backward-facing step can apply quite well to the blunt-base problems, owing to the relatively steady nature of flows involving shock-wave interaction. A brief review of work at high speeds will be included in the next section. Despite the fact that all high-speed flight must, at one time or another, go through a low-speed range, comparatively less work at low speed has been so far carried out in the past. One obvious reason is that the low-speed base flow is of unsteady nature; while the base flow with a splitter plate or the flow over a backward-facing step is nominally steady, the results are not directly applicable to the base flow. Thus the low-speed separated flow work in the past leaned heavily on the investigations of base pressure and wake characteristics of mostly cylindrical or blunt-trailing-edged bodies, so that the body drag could be estimated or the effects of vortex shedding - e. g. singing-wire problems - could be understood. Earlier investigations involving separation-reattachment were mainly on separation bubbles on aerofoils, cavity flows and flows over different types of roughness elements, which have more direct engineering applications (see brief

review in the next section). More recently, investigations of separated-reattached flows - such as flow in a sudden expansion of channel or pipe, flow over two-dimensional or axisymmetrical backward-facing step, and a plane jet issuing from a wall - have markedly increased in number (although still far from adequate to understand this type of flow), because of a great need of such data for more efficient designs in many branches of modern engineering.

It is impossible to describe all flows of this type that occur in practice. At best, we can give a few examples of more important ones which are readily seen in various applications. In flow around an aircraft, there are a number of places that separation - reattachment can occur - for example, leading-edge separation bubbles on aerofoils at high incidence, separation bubble behind a shock wave at any part of the aircraft, cut-out, badly designed canopy, certain types of fuselage, engine cowlings - and an aircraft designer must have sufficient data to keep lift and drag penalties to a minimum. The problems in mechanical engineering range from separation bubbles on turbine blades, sudden expansion of pipe-lines, flame stabilizers, heat transfer characteristics at reattachment, down to noise generation by flow separation (and possibly reattachment) on cars and other vehicles. A civil engineer concerns himself with flow in pipes or water-ways; such as flow over weirs, water-gates, and so on. Fluidics control engineers live with jet reattachment at smaller scales. Environmental engineers should realize the importance of the atmospheric boundary layer flow over hills or mountain ranges. 'Banner' cloud forms in the separated regions in the lee of mountains because of the reduction in pressure. The importance of architectural aerodynamics has been urged for quite some time (see for example Owen 1971 a, b) because modern buildings are much taller and are built to lower factors of safety than in the past. It is obvious that flow round a block of modern buildings will undergo numerous separations and reattachments. As a last example

unsteady (transitional) separation and reattachment play an important part in the dynamics of the aortic valve (Bellhouse & Talbot 1969).

From the few examples given above, it should not be difficult to see the importance of research work on this particular type of flow. The brief review of previous work in the next section will show clearly the sparseness of data in this area, which are desperately needed by many branches of engineering if more economical or effective engineering or architectural designs are to be achieved.

1.2. BRIEF REVIEW OF PREVIOUS WORK

Most previous work which is relevant to the present investigation is discussed in later chapters. This section is designed merely to give a general background to the present state of art in this area by reviewing a selected number of previous works and showing the great need of data.

As mentioned in the previous section, a great number of past investigations of separation-reattachment flow, particularly flow over a backward-facing step, were at high speeds. Work in the supersonic field was related mostly to ballistics research until the mixing theory of Crocco & Lees (1952) and the simplified model of Chapman et al (1958) emerged, after which much work at high speeds followed - for example, Charwat & Yakura (1958), Badrinarayanan (1961), Hastings (1963), Roshko & Thomke (1964), Scherberg & Smith (1967), Statham (1970). A review paper by Nash (1962) emphasized the need of data about base flow at low speeds. Nash et al (1966) carried out an investigation on two-dimensional base flow at subsonic and transonic speeds, using both blunt-trailing-edge sections and backward-facing steps. Some experimenters, e.g. Roshko (1955) and Bearman (1965), investigated base flow at low-speeds and found that if splitter plates were used and the lengths were sufficiently long, the flow-reattached and the oscillating vortex shedding was suppressed. Base flow with a

splitter plate is in fact a flow over a backward-facing step. The early investigations on flow involving separation-reattachment, as already mentioned above, were mostly on flow over roughness elements, some of which involved two separation bubbles, e.g. Tillmann(1945), Mueller & Robertson (1963), Plate & Lin (1964), Petryk & Brundrett (1967); and on cavity flow, e.g. Maull/East (1963), Kistler & Tan (1967). A number of experiments on the reattachment of plane jet to a nearby wall were carried out in parallel, such as Bourque & Newman (1960), Sawyer (1963) Bourgue (1967), McKee & Edwards (1971), Mathews & Whitelaw (1973). Some other experimenters - e.g. Simpson (1975), Perry & Fairlie (1975) - induced their separation bubbles by imposing adverse pressure gradient, in which case the separation lines are not known prior to the experiment. Quite a few investigators studied heat transfer characteristics in separated-flow downstream of a backward-facing step, e.g. Seban (1964), Aung & Goldstein (1971)(All reviewed by Fletcher et al 1974).

The very limited number of previous works on low-speed flow over a backward-facing step relevant to the present investigation includes Hsu (1950), Moore (1960), Tani et al (1961), Abbott & Kline (1962), Bradshaw & Wong (1972) and Gesso (1975). Hsu (1950) investigated both mean-flow and turbulent properties of the flow behind a suddent expansion at a very low speed and a large step height. Moore (1960), on the other hand, in an attempt to correlate the flow over backward-facing step with a short leading edge bubble, used step heights ranging from very small to the same order as the initial boundary-layer thickness (laminar); only pressure distribution, a few mean-velocity profiles and reattachment distance were measured in his experiments. Tani et al (1961) also used several sizes of step with fixed initial boundary-layer thicknesses (both laminar and turbulent) and pressure distribution, mean velocity profiles, turbulent intensities and turbulent shear stress. Abbott & Kline (1962) measured mean velocity profiles for both single and double steps with variable geometry in order to study

the stall pattern (recirculation)behind the steps. Bradshaw & Wong (1972) whose work is the 'groundwork' for the present investigation used more or less the same equipment as that used here, but with smaller step height. They measured pressure distribution and mean velocity profiles, and also measured turbulent properties at one station only. Their working section was extended as far as about 50 step heights in an attempt to investigate the relaxation behaviour of the shear layer after reattachment. They found that even at 50 step heights from the step the shear layer is still very different from the equilibrium boundary layer and suggested that the bifurcation of the shear layer at reattachment is the main influence on the relaxation process. Gesso (1975), in trying to improve the method of hot-wire signal analyses when measured in high turbulence rather than investigating the features of flow over backward-facing step, measured mean velocity profiles, turbulent intensities, turbulent shear stress and autocorrelation. Bradshaw & Wong's conclusion shows the need for better understanding of the reattachment region, and the scarcity of the existing data cited above shows clearly that a great deal of work in this direction is warranted.

1. 3. PURPOSES AND SCOPE OF PRESENT INVESTIGATION

The present work is a continuation of Wong's (1970) work (see also Bradshaw & Wong 1972), and it has been mentioned in the previous section that the immediate need would be the investigation of reattachment region. The simple backward-facing step seems to be the best configuration for inducing separation-reattachment flow, since the separation line is fixed on the step edge. Brederode (1975) discusses the complications of flows with unconstrained separation lines, with special reference to three-dimensional effects. He shows that for the aspect ratio (span/step height) greater than 10, the flow over a backward-facing step is effectively two-dimensional except in the regions close to the side walls. Therefore we used an aspect ratio of 15, while Bradshaw & Wong used 30. With the same order of the initial boundary-layer thickness but with about twice the step height compared with that of Bradshaw & Wong, we thus have much stronger perturbation flow than

that of Bradshaw & Wong; the larger step height in our case also has an advantage of more convenience in traversing.

The main purpose of the experiments reported in the present thesis is to extract as much information as possible on the characteristics of the flow over a backward-facing step, with special attention focused to the reattachment region, using hot-wire anemometers. It is rather unfortunate that laser anemometers, which should be more suitable than hot-wire anemometers for measurements in very high turbulent intensity, have not been available. Nevertheless, hot-wire measurements are expected to be adequately accurate in most of the region outside the separation streamline - i.e. the downstream-going fluid which later relaxes into the equilibrium boundary-layer state. As mentioned in section 1.1, the direction of research in this area should be towards the development of calculation methods, for which better understanding of the turbulent shear stress transport equation is essential. We therefore measured all terms except the pressure redistribution terms because there is no reliable method of fluctuating-pressure measurement known at present. The lateral fluctuating velocity, w, was not measured and we have to rely entirely on Castro's (1973) results for the ratio of w terms to u terms. Since Castro used the same tunnel and tunnel speed and similar equipment as compared to the present experiments, the differences in mixing layer at a given streamwise distance are ascribable to the step effect more-or-less irrespective of experimental error. The recorded signals were digitized and used as input data of the computer program. Due to the time limitation, so far only conventional and intermittency-conditioned averages have been obtained. Since the present experiments also aim at providing useful data for future work, the analogue tapes are available for further analysis.

The experimental arrangements and instrumentation are described in Chapter 2, while the experiments and associated techniques are discussed in Chapter 3. All experimental results are presented in Chapter 4 with some immediate discussion. Detailed discussions of the results, with further deduced results, appear in Chapter 5, and in the last Chapter a more connected account of the main findings is given, together with conclusions and recommendations for future work. In this thesis the numbering of sections and figures is based on Chapter numbers, e.g. section 3.4 is the fourth section in Chapter 3; section 2.2.3. is the third sub-section of second section in Chapter 2; figure 4.5 indicates the fifth figure at the end of Chapter 4. A list of figures is given on page ix.

CHAPTER 2

THE EXPERIMENTAL ARRANGEMENTS AND INSTRUMENTATION

2.1 THE WIND TUNNEL AND THE TEST RIG

2.1.1 The Wind Tunnel

The experimental programme was carried out in the 30" x 5" No. 1 open circuit boundary layer blower tunnel of the Department of Aeronautics, Imperial College of Science and Technology (figure 2.1). A full description of this tunnel is given elsewhere (Wong 1970, Bradshaw 1972) and will not be repeated here. It is driven by a $12\frac{1}{2}$ kW aerofoil-type centrifugal blower which is in turn driven by a DC motor supplied from a variable-output thyristor rectifier giving a speed range of 0 to about 45 m/s. The speed is kept constant by the Automatic Speed Control Unit described in section 2.1.2.

The tunnel has a two-dimensional contraction of area 9:1, with a rectangular exit section 76.2 cm x 12.7 cm (30" x 5"). The spatial variation of total pressure at the exit is quoted by Bradshaw (1972) to be nearly within the experimental scatter of about 0.002 x dynamic pressure with a turbulence level of about 0.07% at about 30m/s. The boundary layer 0.8 mm forward of the lower lip of the exit in the presence of the test rig, was found to be laminar and approximately 2mm thick, as opposed to 2.5 mm quoted by Bradshaw (1972) with a conventional parallel-sided working section.

In the present investigation the static port on the centre line of the lower surface at 6.3 cm forward of the exit lip was chosen as reference for measuring the tunnel speed.

2.1.2 The Automatic Speed Control Unit

The unit has been designed and developed in this Department, mainly by Dr. I.P. Castro with later work by the present author, and is shown diagrammatically in figure 2.2. The "sensing box" contains

a light source and photocells in a bridge circuit facing one another at each side of the inclined glass tube. This tube is connected at one end to the reference static port and the other end to the lower part of the unit's manometer reservoir. The top opening of the reservoir is connected to a reference total pressure probe. The bridge is balanced when the meniscus in the inclined tube is at a certain position between the light source and the photocell. A displacement of the meniscus away from this position will cause an out-of-balance voltage (with different sign for different direction) which is fed to an operational amplifier in the auto-control unit, driving a Vactric servo motor. The motor rotates a potentiometer connected in place of the manual speed control potentiometer of the thyristor power supply. Thus the tunnel speed is raised or lowered until the meniscus in the inclined tube is brought to the balance position. When properly adjusted the unit keeps the tunnel speed constant to within $\pm$ 0.1 mm water of reference dynamic pressure.

2.1.3 Description of the Test Rig

The test rig or "working section" (also shown in figure 2.1) employed throughout the present investigation was specially designed to form a 5.08-cm (2") backward-facing step at the contraction exit when attached to the above-mentioned tunnel. It was constructed in the Departmental Workshop and has a streamwise length of 83.8 cm (33"). It is made of 1.9 cm ($\frac{3}{4}$") Weydec board with a removable roof which can be held on to the top edge of side walls by sets of embedded studs and butterfly nuts. Two interchangeable roofs were used: a Weydec one which has a 2.54 cm (1") guiding slot cut along the centre line for traversing purposes, and a Perspex one for flow visualization. Long flanged T-shaped wooden pieces of various lengths are used in filling the guiding slot for any desired traversing distance from the step, and be held firmly in place by two aluminium clamping plates (figure 2.3). These clamping plates are slightly bent into small angles at the inner edges to provide a flexible contact when tightened onto the roof by sets of studs and butterfly nuts. They also have stud sliding guide-holes for easy removal of the covering pieces.

Unlike Wong's (1970) adjustable roof which was arranged to give a zero pressure gradient from soon after reattachment, the fixed roof inclination of 1.7^{o} was designed to simulate a streamline in an infinitely high tunnel. The chosen inclination was based on the boundary layer displacement thickness of Wong's results and it was felt that, due to the very small streamline curvature in question, a sophisticated determination of the roof shape was unnecessary. The floor of the rig is fitted with five 8.9cm ($3\frac{1}{2}$") inside diameter standard brass rings at a spacing of 15.2cm (6") along the centre line (starting 15.2cm (6") from the floor leading edge), so that standard brass discs with pressure tappings, Preston tubes, Stanton tubes or traverse gear can be fitted as desired.

A black-sprayed 1.6mm ($\frac{1}{16}$") aluminium sheet was used to cover the floor completely when performing tuft or oil-flow visualization.

The test rig stands on a scaffolding frame. Four 5.1cm - 9.5mm (2-$\frac{3}{8}$") L-section aluminium beams screwed on to the leading and trailing edges of the rig floor and roof prevent warping of the Weydec and reinforce the Perspex, and the one at the front edge of the rig floor is also used for clamping the test rig to the tunnel's main supporting legs by means of two G-clamps.

2.1.4 The Working Section for Plane Mixing Layer Experiments

Two existing working sections of streamwise length 1.45m (4.75ft) were used in the plane mixing layer experiments. They are fully described by Wong (1970) and Bradshaw (1972). When the adjustable roof is removed and the two sections are attached in a streamwise direction they form a channel 2.9m long with Perspex side walls 38cm high, suitable for flow visualization work. The smoke injector frame from the smoke tunnel described later in section 2.2.1 can be sandwiched between the tunnel exit and the working section,

so that the inside edge of the smoke injector frame is aligned with the upper internal surface of the contraction exit to form a continuous surface up to the injector slot.

The floor and one of the side walls were covered with photographic matt black paper to eliminate all possible reflections when viewing the illuminated smoke-filled mixing layer and also when smoke photographs were taken.

2.2 FLOW VISUALIZATION EQUIPMENT

2.2.1 The Smoke Tunnel, The Smoke Generator and The Light Source

In the early stage of investigation the 4' x 2' smoke tunnel of the Department of Aeronautics was used for studying the overall flow behaviour of the flow behind a backward-facing step. This is a suction tunnel of constant rectangular cross-section 1.22 x 0.61m (4' x 2') and 11m (6 sections of 6') long with its exit connected to the intake of 30" x 5" wind tunnel No. 2; thus both the smoke tunnel and the latter blower tunnel use the same centrifugal blower and driving motor. The smoke tunnel has a bell-mouth, one honeycomb and four screens at entry but has no contraction. A removable frame with a narrow slot, stiffened with corrugated aluminium, at one of the inside edges is situated immediately behind the last screen for injecting a full-span sheet of smoke filament horizontally close to the tunnel floor in a streamwise direction. The lowest tunnel speed is about 1m/s which is desirable for most smoke-flow visualization work. The free stream turbulence level measured by the present author with an unlinearized hot wire was found to be approximately 0.2% at a free stream speed of about 2m/s.

The backward-facing step used in the smoke tunnel flow visualization work was made up of a thin aluminium sheet spanning the tunnel floor and bent into an approximately half sine-wave form in the streamwise direction. The crest edge of the sheet was screwed on to

a 3.8cm (3") high wooden beam of rectangular cross-section which served as a backward-facing step on the tunnel floor while the other edge lay flat and held down to the floor by sticky tape close to the smoke injector frame. The combination therefore formed a mildly contraction section at the tunnel floor up to the step height of 3.8cm.

A portable Taylor smoke generator type 3020 was used for both the boundary layer flow visualization in the smoke tunnel and the plane mixing layer flow visualization in the blower tunnel No. 1. This smoke generator has an automatic switch to cut off the mains supply when the correct temperature is reached and to switch on again when the temperature is lowered. It can produce white smoke by electrically heating high grade kerosene fed from the internal supply reservoir and forced out at a chosen rate by compressed CO_2 supply. The CO_2 used for this purpose may be either from a small cylinder mounted within the generator or an external cylinder. The smoke output pipe on the generator can be connected directly, using rubber or plastic tube, to the inlet pipe of the smoke injector frame of the smoke tunnel.

Since our flow visualization work involved observation of the illuminated smoke, it was obvious then that an adequate light source was essential if photographic records were to be made. A light source was designed to replace the temporary one used in earlier work. A three-lens arrangement similar to that used by Fiedler & Head (1966) (figure 2.3) was adopted using existing lens available in the Department. The design requirement was to obtain as thin as possible a sheet of light with maximum possible intensity from a 1000W Halogen mercury bulb. Two identical aluminium light boxes as shown in figure 2.3, were made and tried. It was found that the intensity of the light output was poor and inadequate for most photographic purposes. The excessively thick lenses used were responsible for the unsatisfactory results. The idea of using a single lens system suggested by Dr. Falco of Cambridge University (figure 2.3) was considered; the reasoning was that a certain amount of light intensity is always lost when passing through a lens and therefore

the smaller number of lenses used the better results would be obtained. The lenses in each light box was then replaced by a single bi-convex Perspex lens, manufactured in the Departmental Workshop, with a focal length of approximately 1m. This was found to be quite satisfactory as it provides a sheet of reasonably intense light of about 2cm thick, 60cm wide at a distance of 60cm from the end of the box, i. e. when the light boxes standing on the Perspex roof of the smoke tunnel the focussed part of the beam will be close to the tunnel floor. These two light boxes have been used most successfully for smoke-flow visualization in the Department during the past three years.

2. 2. 2 Oil-flow Mixture And Tufts

The oil-flow method and tufts were used to observe and determine the reattachment distance, fluctuating band of reattachment, two-dimensionality and reseparation lines behind the backward-facing step. The oil mixture used in all experiments was similar to that used by de Brederode (1975) with a slight change to account for the difference in surface conditions. The approximate oil mixture proportion used was as follows:

4 parts of 'Plus-Gas', formula 'A' penetrating oil,

2 parts of 'Speedivac' grade 16 vacuum pump oil,

1 part of titanium dioxide,

& small drop of oleic acid.

Tufts of thin cotton about 2. 5cm long were used mainly to observe the width of the fluctuating band of reattachment, which oil-flow method would not reveal, and to get a rough idea of the flow patterns on the side walls. A tuft fixed to the end of a thin rod, and the stethoscope technique, using simply a plastic tube connected to a hypodermic tube, were also found useful in checking the flow condition at any doubtful point, or in detecting the edges of the boundary layer.

2. 3 TRAVERSE GEAR

Exclusive use was made of a "slide rule" type traverse gear with a 15cm (6") stroke driven by a Portescap P26 12V DC electric

motor (see figure 2.4 (a) of Dean (1974) or figure 7.3 of de Brederode (1975)). It is fitted with a Sakae linear potentiometer type 20LP100 with 10cm travel and 0.04mm resolution. The potentiometer mounting is adjustable and can be set at any desired vertical position within the traverse gear stroke, which is required when a traverse height greater than 10cm is needed. Both the motor and the potentiometer are fed from a remote control box, with a built-in voltage stabilizer and zero adjustment for the potentiometer. The potentiometer output voltage, which is the measure of the traverse distance, can be monitored on a digital voltmeter for visual display and/or connected to the Data Transfer Unit described in section 2.5.

Since in the present investigation all traverses were made from the roof of the test rig which is slightly inclined, a special T-shaped wooden base of 10 cm long, similar to those used in filling the guiding slot on the test rig roof, was made so that the traverse gear stood vertically with respect to the plane of the rig floor.

The traverse gear can be fitted with various probes such as Pitot tube, disc-static tube, hot wire or thermocouple.

2.4 PRESSURE MEASUREMENT INSTRUMENTATION

2.4.1 Surface Pressure Tappings

Some of the standard brass discs mentioned in section 2.1.3 have three 1-mm static ports drilled along a diameter at 3.8 cm ($1\frac{1}{2}$") spacing with the middle one at the centre of the disc. In the early stage of the work these 3-tapping discs were used to replace all five plain discs and carefully aligned to give fifteen static tappings along the centre line of the test rig floor. This number of static tappings was however found to be inadequate, particularly in the recirculation region where the pressure gradient was extremely high. Six more tappings were then drilled on the test rig floor space, along the floor centre line, between the rig leading edge and the third ring. Hypodermic tubes of 1mm outside diameter were inserted flush with the floor surface and held in

place by Araldite. In addition, the third disc was later replaced by a special disc with 7 tappings equally spaced at 1.25 cm to investigate the reattachment region, where the pressure gradient was changing signs, in more detail. Consequently, in the final stage of the surface pressure measurements 25 static tappings in all were used and their distances from the step were as tabulated below:

Tapping No.	1	2	3	4	5	6	7	8	
x (cm)	3.4	7.15	11.2	15.0	18.8	21.65	23.55	25.9	
Tapping No.	9	10	11	12	13	14	15	16	
x (cm)	27.1	28.35	29.6	30.9	32.1	33.4	36.9	38.8	
Tapping No.	17	18	19	20	21	22	23	24	25
x (cm)	41.6	45.45	49.3	56.9	60.75	64.6	71.15	76.0	29.85

2.4.2 Pressure Probes

a) Pitot Tubes

In the mean-flow measurements, the velocity profiles were first measured with a Pitot tube. A plane-ended circular Pitot tube of 1-mm outside diameter was chosen because it was believed that this size should give sufficient accuracy in measuring total pressure in the present flow configuration and it was easy to manufacture. Originally the tube bent into an L-shape with an overhanging length of 6.7 cm was used but found to be unsuitable. In the reverse flow region the measurements with Pitot tube facing downstream was more appropriate because of the unreliability of the downstream-facing calibration of the tube; and with the L-shape configuration it was difficult to maintain the tip exactly at the same position when turned to face the opposite direction. The Pitot tube bent into C-shape with tip exactly at the stem axis was

therefore adopted. The C-shape tube also had plane-ended tip of 1-mm diameter and it had a C-width of 3.8cm. With this Pitot tube the same measuring point at the tip of the tube could be maintained whichever direction it was pointed without the necessity of removing the traverse gear.

Both Pitot tubes were made of hypodermic tubes stepped down from a 4-mm stem, to suit traverse gear mounting, to 1mm at the tip as shown in figure 2.4.

b) Disc-Static Probe

The preliminary results of the velocity profiles obtained from the Pitot traverse, assuming zero pressure gradient across the boundary layer, revealed some peculiarities especially in the recirculation region. The effects of static pressure gradient across the layer was suspected to be the main cause, thus the static pressure distribution at the same stations as those in Pitot traverse was investigated. A disc-static pressure probe, similar to those described in Bryer & Pankhurst (1971), was chosen. It had a brass disc of 6.4mm ($\frac{1}{4}$") diameter, 0.9mm thick, attached to the tip of C-shape tube with a 0.38-mm bore hole on both sides of the disc, as shown in figure 2.4. The centre of the disc, where static ports were located, was in alignment with the stem axis for convenience in rotating to opposite direction in reverse flow. This type of static probe is believed to be nearly insensitive to yaw within $\pm$ 3° (Bryer & Pankhurst, 1971).

2.4.3 Preston and Stanton Tubes

Although the values of local skin friction can be derived from the mean velocity profiles using the logarithmic law, direct measurement is advisable as a check on accuracy of the velocity measurements and of the logarithmic law itself. A Stanton tube mounted on a standard brass disc was used for this purpose. However it was not a conventional Stanton tube with a razor blade fence, but, similar to that developed and used by Sivasgaram (1971), consisted of two narrow rectangular slots on the same diameter each side of the disc centre. One longer

edge of each slot was scraped down a few thousandths of an inch to provide a small forward-facing step in one slot and a backward-facing step in the other when placed so that the common axis of both slots was perpendicular to the flow direction. When the pressure difference between the two openings is properly calibrated, this type of Stanton tube is believed to represent the most accurate method of friction measurement because no part projects out in the flow so that the pressure difference should be determined solely by conditions in the sublayer.

In the present work a set of Preston tubes was used merely as a means of Stanton tube calibration. The objection to using these Preston tubes to measure directly the skin friction in this case was the uncertainty of whether the tubes were totally immersed in laminar sublayer. Preston tubes of outside diameters of 0. 9 mm (0. 036"), 1. 5 mm (0. 058"), 1. 7 mm (0. 065"), 2 mm (0. 080") and 2. 9 mm (0. 115"), each mounted on a standard brass disc with two static tappings on both sides, were used for the calibration purpose.

2. 4. 4 Manometers

The reference speed of the blower tunnel No. 1 was monitored throughout the investigation by an AVA Betz manometer with accuracy better than 0. 02% in the speed range of the experiment.

All flow visualization work in the smoke tunnel was done at very low speeds, therefore monitoring the much faster speed of the blower tunnel No. 2 by inclined Airflow Mk 5 manometer was found to be more convenient. The actual smoke tunnel speeds could then be easily calculated. A VARIAC transformer controls the motor speed so that the voltage setting could be used as a rough guide when an accurate measure of the tunnel speed was not essential.

In the early stage of the surface-pressure measurements, all static tappings were connected to a TEM multi-tube manometer in order to visualize the entire pressure distribution. Although a number of pressure readings were taken in a preliminary study, the severe fluctuation of pressure in the recirculation and reattachment regions made this type of manometer unsuitable for more rigorous measurements, even with the use of the clamp on the manometer to obtain instantaneous pressure readings. The final surface pressure distribution (regularly checked throughout the investigation) was measured by a Furness Control type MDC multi-range capacitor micromanometer as well as in all the Pitot and static pressure traverses. The linearity of this manometer was found to be better than 0.2% in the present test range. However, in the high turbulence region the peak-to-peak fluctuations at the manometer reached as high as 15% of the local dynamic pressure, even with long lengths of small bore tubing and a large micromanometer time constant. The passive RC low-pass filter circuit, as shown in figure 2.6, was connected between the micromanometer output and the DTU (described in section 2.5) in order to reduce the total amplitude of fluctuation to less than 3% (about 0.5% rms). TEM multi-tube manometer was also used in the calibration of Preston tubes.

As the pressure difference indicated by the Stanton tube was very small, a Combist null-displacement manometer was employed. The accuracy claimed by its makers is of the order of 0.01 mm of water.

2.5 THE DATA LOGGING SYSTEM

Traverses were made at 13 stations at the distance as stated in section 3.4.1 and for each traverse about 50 points were taken with several readings at each point to yield good averages. Taking these numerous readings by hand would be error-prone as well as time consuming, thus the Departmental Data Logging System was employed for all traverse work.

The system consists of a Solartron Data Transfer Unit (DTU), a Solartron LM 1420.2 Digital Voltmeter (DVM) and a Teletype ASR 33 Teleprinter. The DTU can receive up to five steady input signals simultaneously and the output can be printed or printed and punched on paper tape in ISO/ASC II code by the teletype. The scan can be set as a single scan or to repeat until it is manually stopped, which is convenient when a number of samples at one position are required.

A so-called "coder box", which is a discrete potentiometer, is nearly always a part of the system if the punched tapes are to be processed later by a computer. This "coder box" provides ten discrete voltage outputs which can be logged on to one of the DTU channels for data control purposes.

2.6 HOT WIRE ANEMOMETRY

2.6.1 Hot Wire Probes

DISA probes were used exclusively for all hot wire measurements with either DISA original tungsten wires or, when no probes with original wires were available, home-made 5 μm and 7.5 μm Wollaston wires. However, the results reported herein were all measured with DISA original tungsten wires. The DISA U-probe type 55 P01 used for measuring mean velocity and longitudinal turbulence intensity has a platinum-plated tungsten wire of 5 μm diameter, 3 mm overall length, 1.25 mm sensitive wire length and the ends were copper-and-gold plated to a diameter of approximately 30 μm. For other measurements, i.e. $\overline{v^2}$, $\overline{uv}$, and higher products, a DISA 55 P51 X-probe was used. The physical size of the X-probe is the same as those of the U-probe except that the cross-array is arranged so that the overall length of the wires are the diagonal length of a 2.1 mm square.

2.6.2 Anemometers and Associated Units

All hot wire measurements were made by DISA 55-D01 constant temperature anemometers in conjunction with DISA 55 D25 auxilliary units which provided a square-wave for the frequency-response check. Hot wire signals were linearized by DISA 55 D10 linearizers and when necessary the mean square of the fluctuating quantities were measured with DISA 55 D35 RMSmeters monitored by Solartron DVM's. A Solartron RMS sub-unit in the 1420 DVM was also used for some calibration purposes. A two-beam Tektronix type 502 oscilloscope was used to monitor the hot wire signals throughout the hot wire work. A Farnell sine-square oscillator type LFM 2 was also used in gain calibration and other purposes, such as to supply the calibration signals for analogue recording.

2.7 THE HOT WIRE DYNAMIC CALIBRATOR AND INSTRUMENTATION

2.7.1 The Dynamic Calibrator

The original version of the dynamic calibrator constructed in the Departmental Workshop was almost identical to that used by Perry & Morrison (1971) but with a different driving motor which gave a fixed shaking frequency of about 12 Hz. Calibration work done with this calibrator showed inconsistent results and vibration due to rapid wear of some parts seemed to be the main cause. A few modification were tried without success in improving the results and this particular calibrator was abandoned.

Consequently, the present calibrator employing a crank mechanism was designed by P. Bradshaw and the present author, as shown in figure 2.7. It is driven by a 900 rpm AC commutator motor to give shaking frequency of approximately 15 Hz. Two alternate crank lengths can be used, with the crank ratio of 5.2 in the case of smaller crank length. The deviation from a pure sine wave due to finite crank ratio has a negligible effect on the rms measurements (Bruun 1975) as shown in Appendix III.

2.7.2 Instrumentation

In both versions, a linear displacement transducer (Electro Mechanism Ltd., Slough) is connected to the sliding shaft of the calibrator for measuring the frequency of oscillation. A DC supply of 20V is fed to the transducer and with the motor running the shaking frequency is measured by a RACAL SA 532 1.2 Mc/s Universal Counter-Timer, from which the imposed rms velocity can be calculated.

The hot wire instrumentation is the same as that described in section 2.6.2, namely DISA 55D01 anemometer, DISA 55D25 auxiliary unit, DISA 55 D35 RMSmeter and Solartron digital voltmeter.

2.8 ANALOGUE AND DIGITAL RECORDING INSTRUMENTATION

2.8.1 Analogue Measuring Equipment

During the analogue recording of the signals from a cross-wire probe, a few analogue measurements were taken at an early stage in order to check the digital results. The analogue measuring system consisted of two data amplifiers, a multiplier, an integrator and a DISA test unit, all plugged in to a PHI console (Servicon Ltd.) with common $\pm$ 15V power supply. The integrating time was set and controlled by a WATESTA timer. The DISA test unit was designed to resolve the two input signals from the cross-wires into u and v velocity components so that the output could be fed into the multiplier and integrator to give $\overline{u^2}$, $\overline{v^2}$ and $\overline{uv}$ directly with some scaling factors. Details of system operation and measuring technique are described in chapter 3.

2.8.2 Analogue Recording Equipment

An Ampex FR 1300 Analogue Tape Recorder was used to record the linearized signals from the crossed-wires which were scaled with two data amplifiers. The recorder has 14 channels, with speeds of 0.0476 m/s ($1\frac{7}{8}$ in/sec), 0.0953 m/s ($3\frac{3}{4}$" in/sec), 0.1905 m/s ($7\frac{1}{4}$ in/sec), 0.381 m/s (15 in/sec), 0.762 m/s (30 in/sec), 1.524 m/s (60 in/sec) and records on to 2.54 cm (1") analogue magnetic tape.

The peak-to-peak amplitude of input signals is limited to 2 volts (i.e. $\pm$1V max). By using record and reproduce connections simultaneously the signals can be played back through an oscilloscope while recording. A Farnell Sine-wave generator was used to provide the calibration signals throughout the recording work.

2.8.3 Digital Recording Equipment

The cross-wire signals recorded on analogue tapes were digitized by the Imperial College Aeronautics Department Digital Data-logging System, described fully by Weir & Bradshaw (1974), to obtain computer-compatible digital magnetic tapes for data processing. The system consists of an Ampex FR 1300 Portable Analogue Tape Recorder, a Data Laboratories Ltd. Simultaneous Sample and Hold type 800, a multiplexer, a Data Laboratories Ltd. A/D Converter 710, a Digital Equipment Co. Ltd. PDP-8/L minicomputer, an interface unit built by DEC and an Ampex TM 16 Digital Recorder. The maximum analogue frequency is limited by KEMO 1Hz - 100KHz Dual Variable Filter Type VBF/1 to avoid aliasing and the rate of transfer from the A/D converter to the core store of the minicomputer is set by a crystal clock.

The system can accept up to 12 parallel channels carrying analogue voltages ($\pm$ 1V max) and converts them into 10-bit binary numbers, then records them in pure binary form on 7-track, 1.27 cm ($\frac{1}{2}$") digital magnetic tape in "block IBM" format compatible with the Imperial College and London University CDC computers. The conversion rate is adjustable up to approximately 25,000 samples/sec; a rate of 20,000 samples/sec (10,000 per channel) was used in the present work.

2.9 REFERENCE-MEAN-STREAMLINE TRACING SET-UP

To determine V from the existing data by integrating with respect to y, a reference mean streamline in the free stream is needed because measurements in the recirculation region are uncertain so it is not possible to integrate from the floor surface. A Nichrome wire, stretched across the span of the test rig at 2.4 cm behind the step and 11.5 cm above the rig floor, was electrically heated by a voltage supplied by a VARIAC transformer. A system of weights hanging over a pulley, as shown in figure 2.5, was used to keep the wire taut when heated. A thermocouple probe was traversed at a number of distances downstream of the heated wire, and a reference thermocouple was placed in the free stream at the end of the rig. The temperature difference between the two thermocouples at each point was measured by a Comark Differential Thermometer.

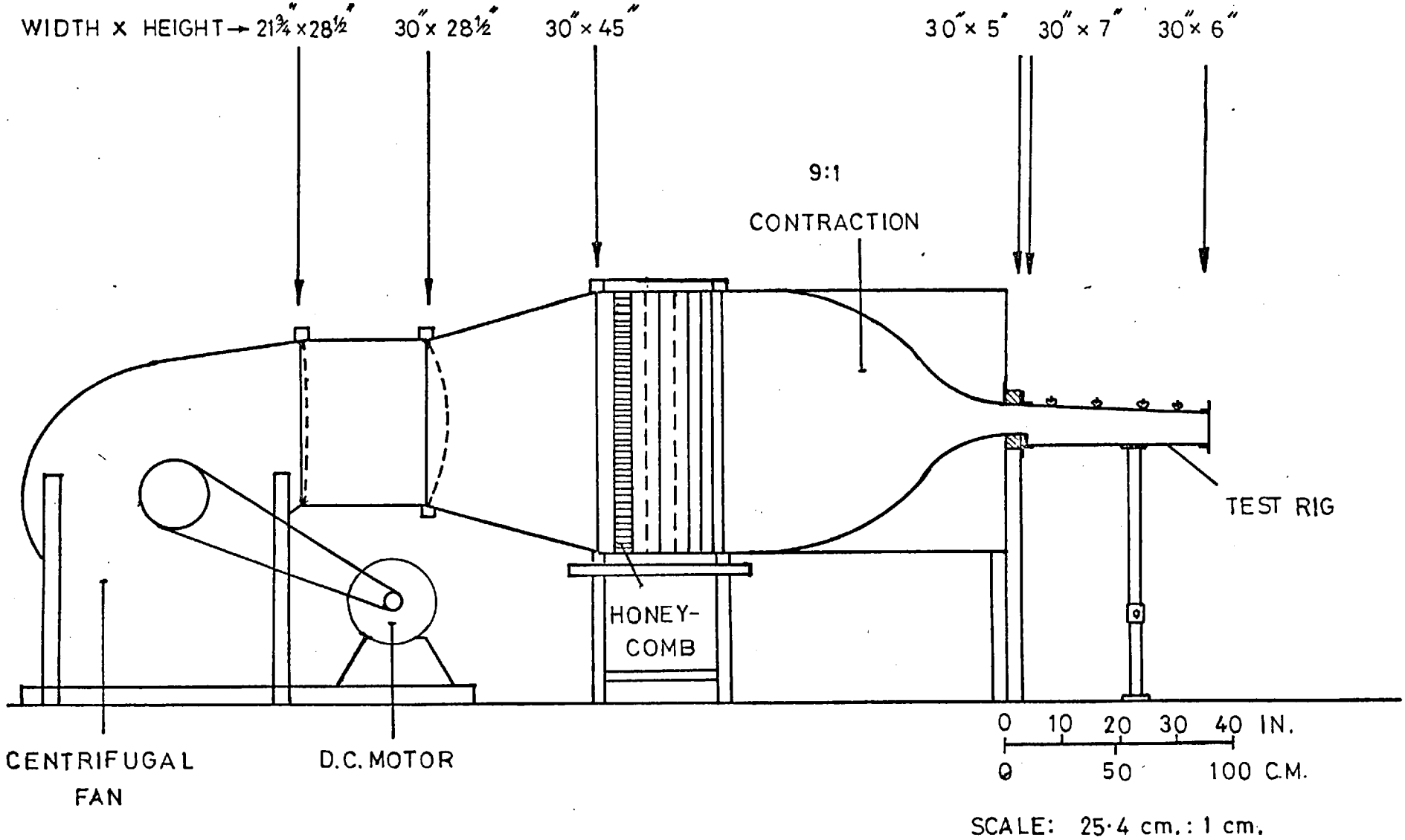
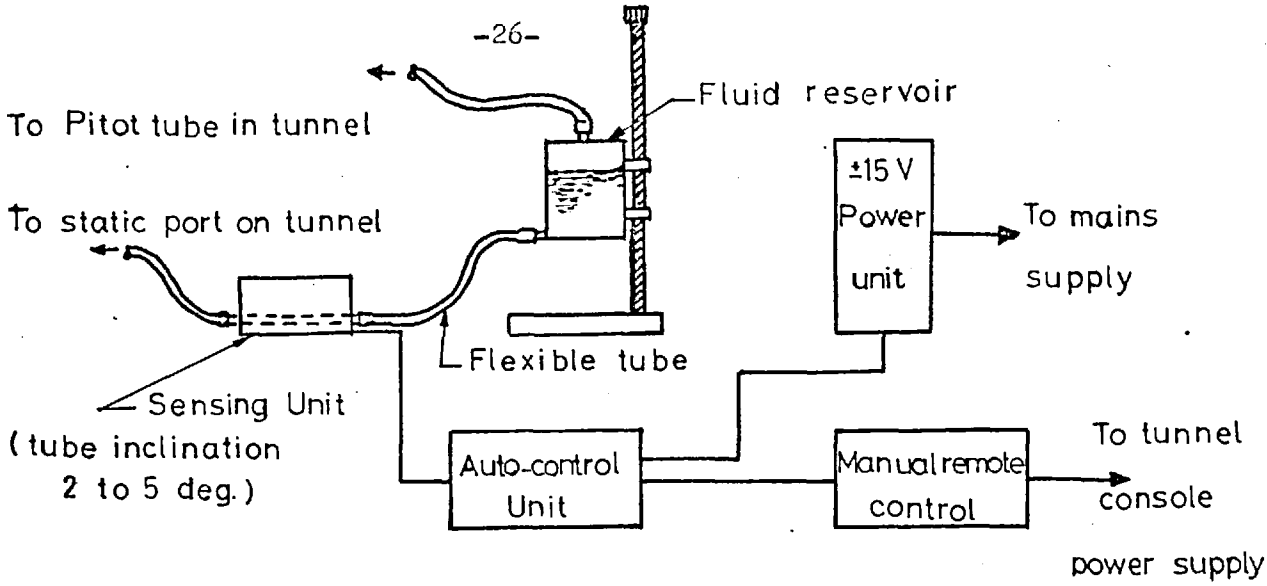
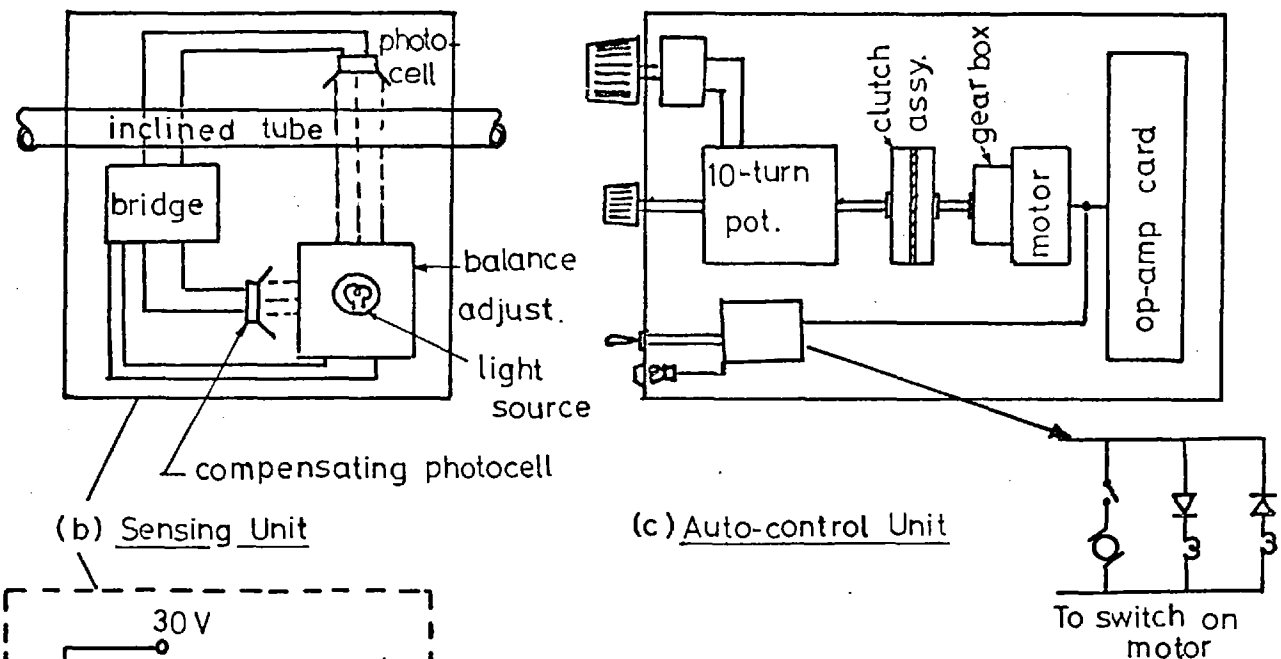


FIGURE 2.1 SIDE VIEW OF TUNNEL WITH TEST RIG,

DOTTED LINES INDICATE SCREENS

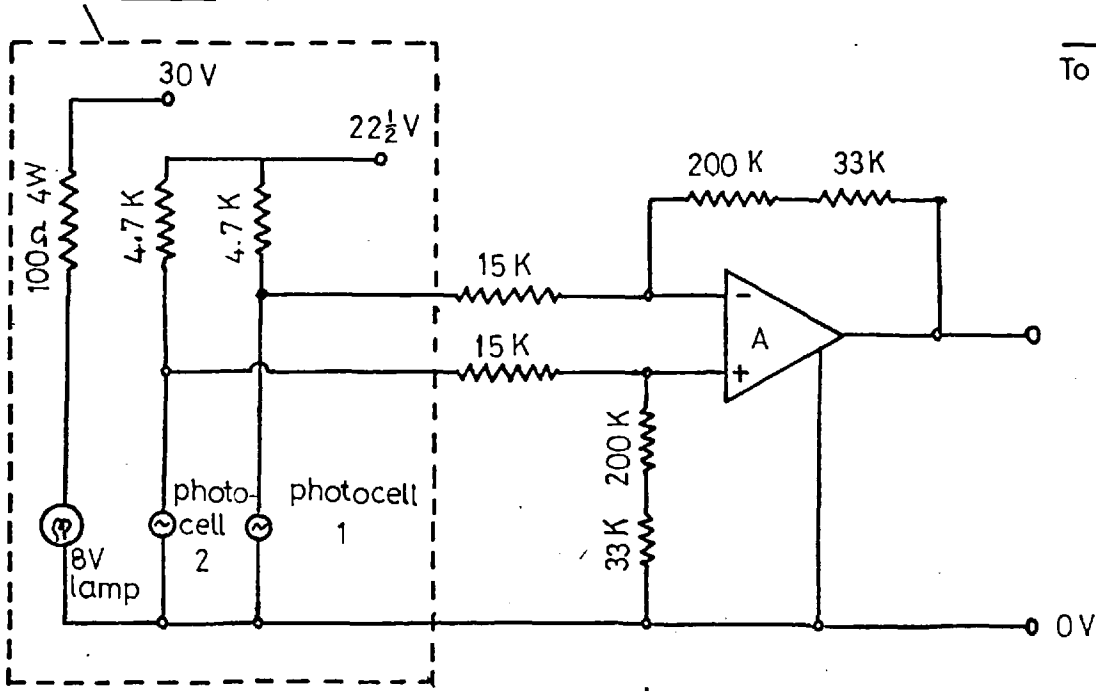


(a) General Layout



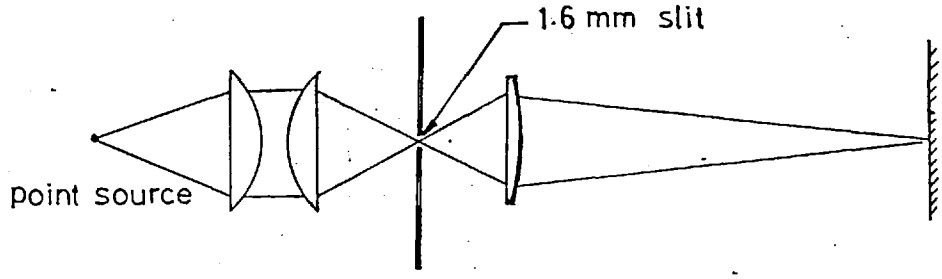
(b) Sensing Unit

(c) Auto-control Unit

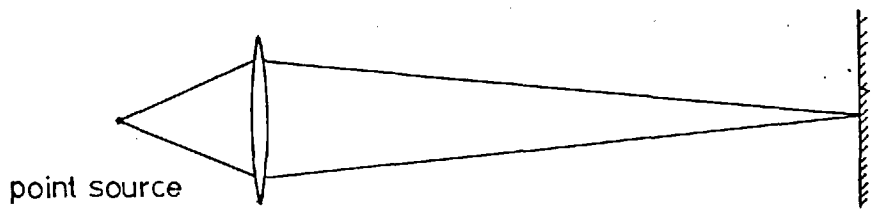


(d) Main circuit diagram

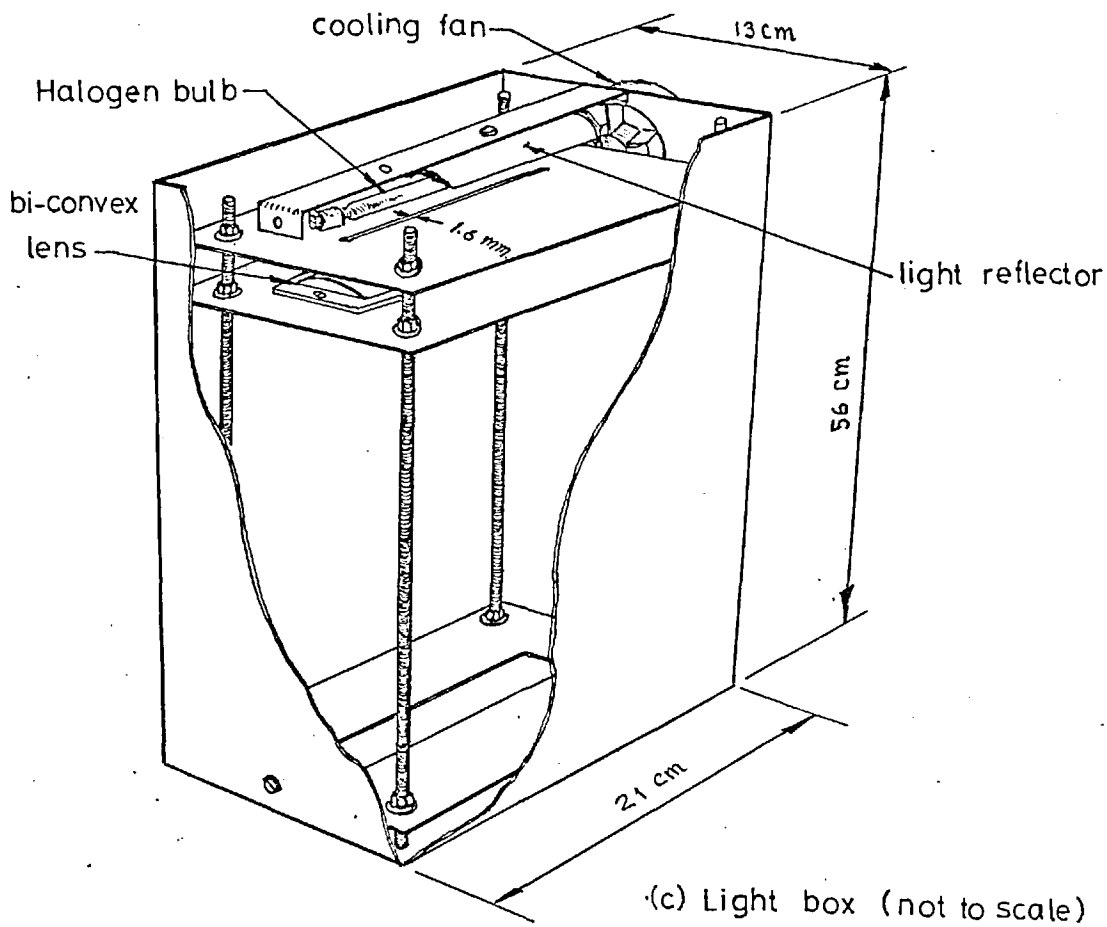
FIGURE 2.2 WIND TUNNEL AUTOMATIC SPEED CONTROL



(a) Early lens arrangement after Fiedler & Head (1966)

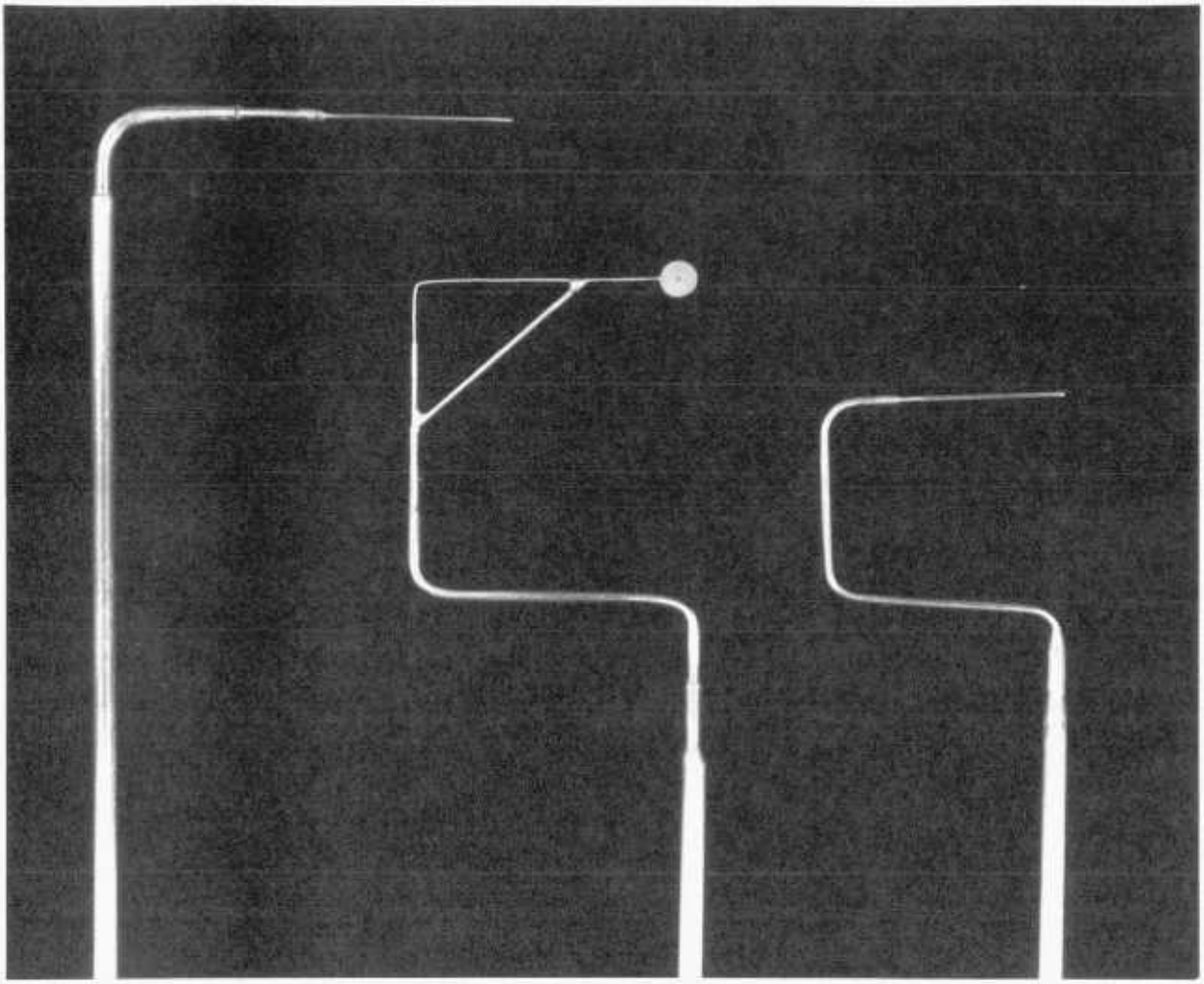


(b) Present lens arrangement



(c) Light box (not to scale)

FIGURE 2.3 LIGHT BOX AND LENS ARRANGEMENT



(a) L-shape Pitot tube (b) Disc-static probe (c) C-shape Pitot tube

(Approx. 0.8 actual size)

FIGURE 2.4 PRESSURE PROBES

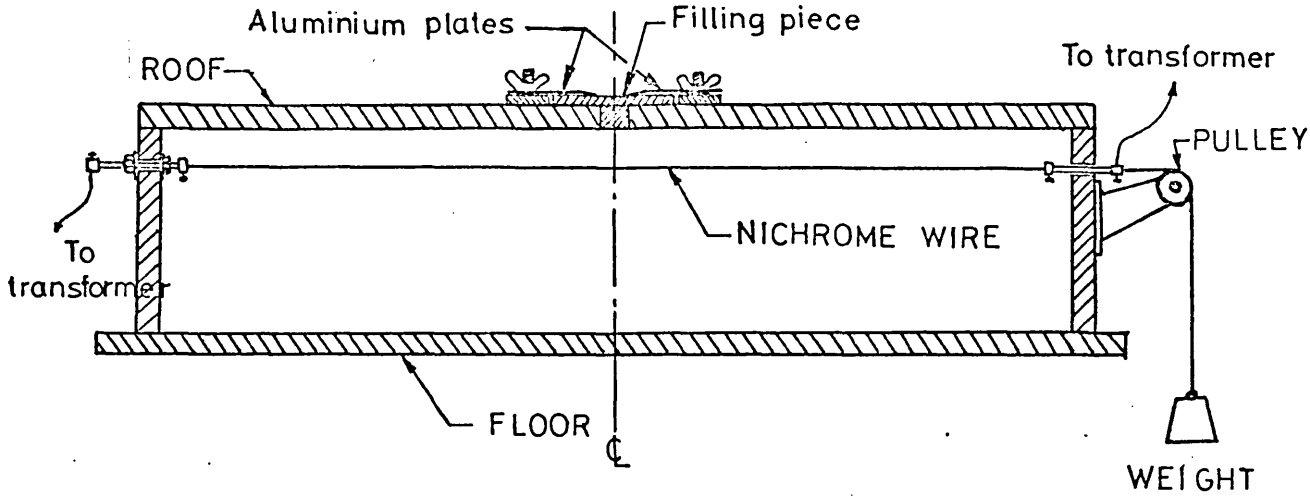


FIGURE 2.5 CROSS-SECTION OF TEST RIG SHOWING HEATED WIRE ARRANGEMENT & FILLING AT ROOF (not to scale)

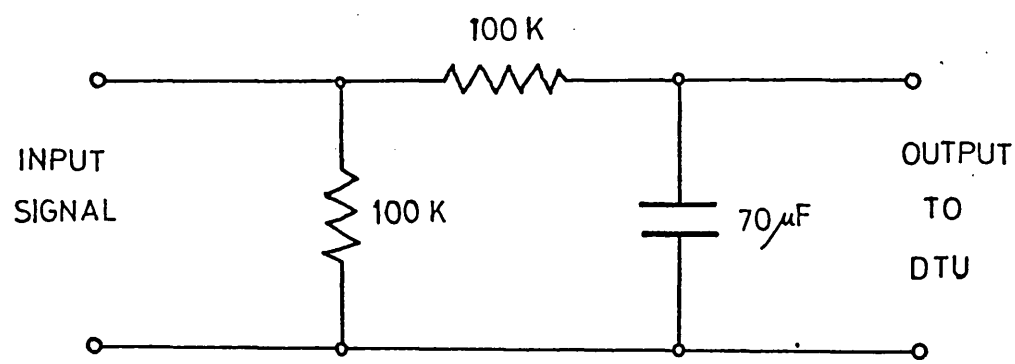
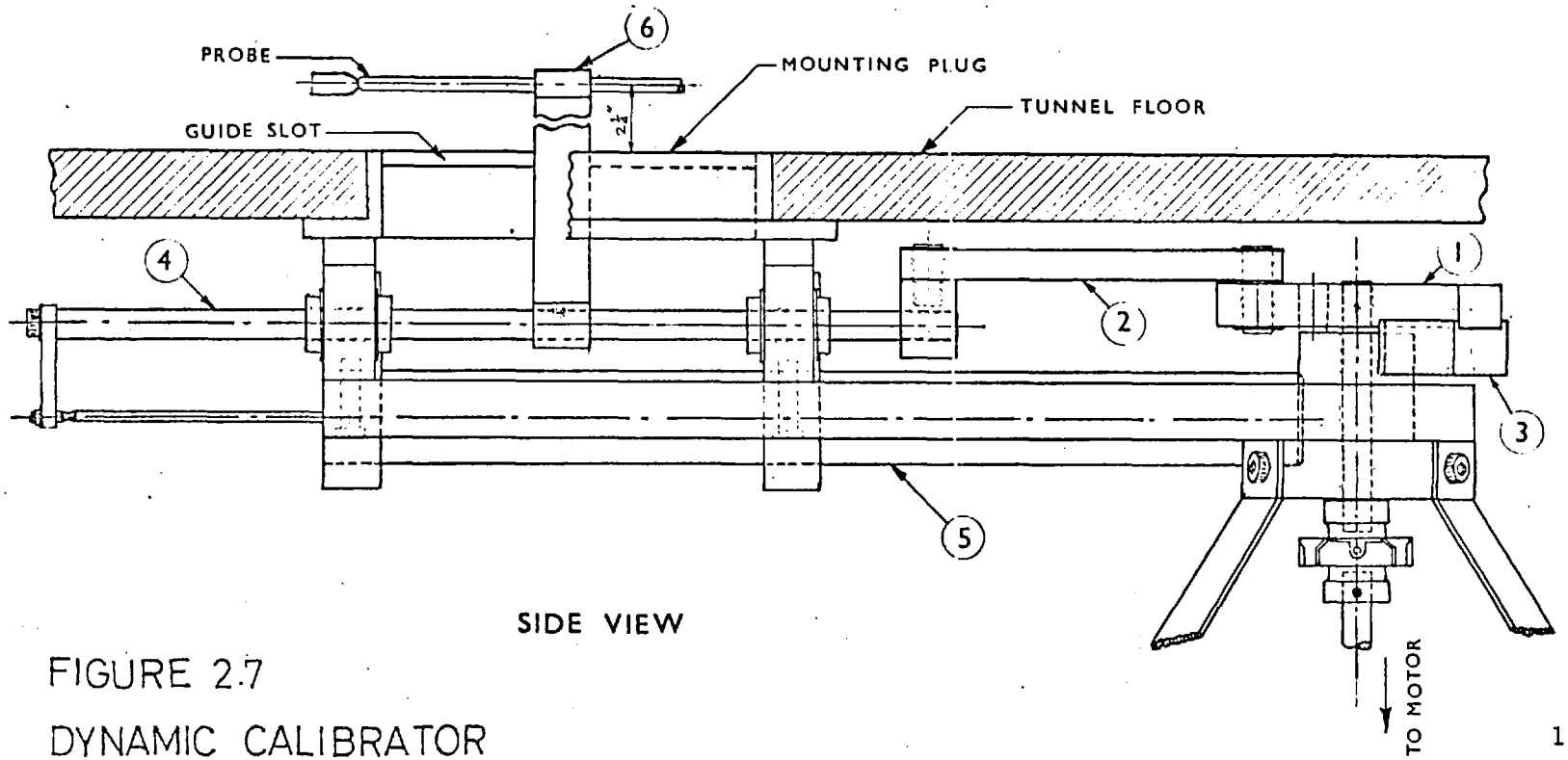


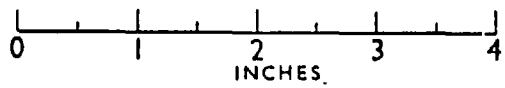
FIGURE 2.6 PASSIVE RC LOW-PASS FILTER CIRCUIT

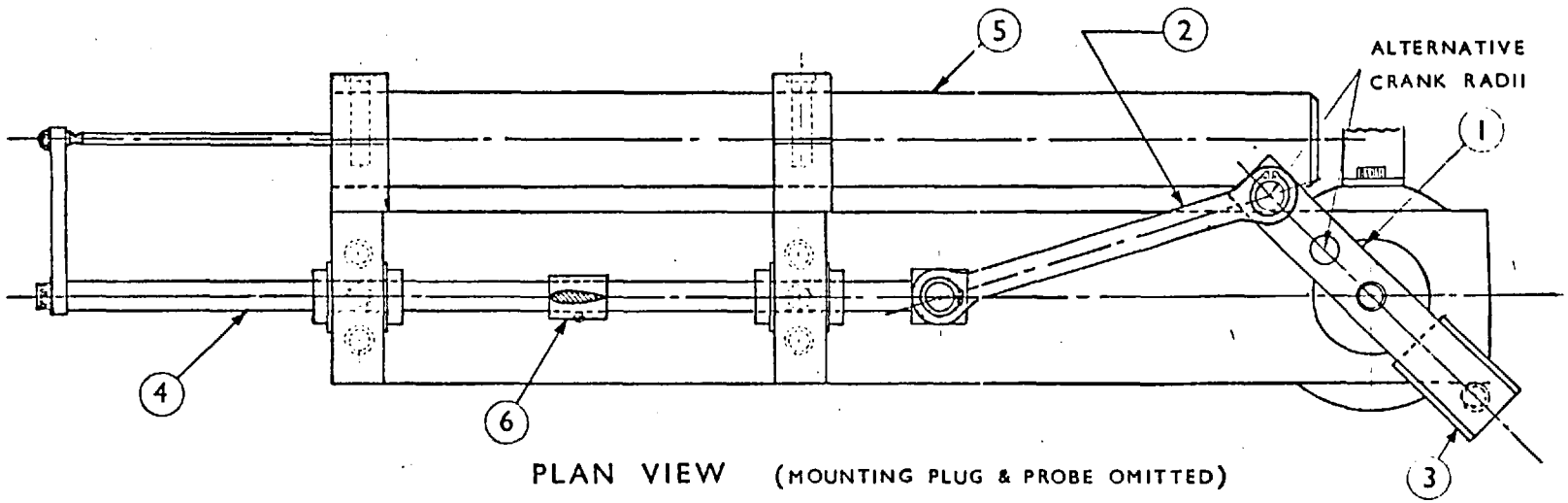


SIDE VIEW

FIGURE 2.7

DYNAMIC CALIBRATOR





PLAN VIEW (MOUNTING PLUG & PROBE OMITTED)

1. Crank
2. Connecting Rod
3. Counterweight
4. Sliding Shaft
5. Linear Displacement Transducer
6. Probe Support Holder

CHAPTER 3
THE EXPERIMENTS AND ASSOCIATED TECHNIQUES

The reference dynamic pressure of the blower tunnel was kept at 6.0cm of water for all tests unless otherwise stated; thus the reference speed of the tunnel ranged between 31.2 and 31.7 m/s depending upon the atmospheric conditions of each test. The flow temperature was recorded at regular intervals during each test using a thermocouple probe placed in the free stream at the end of the rig and connected to a Comark electronic thermometer, and the atmospheric pressure was noted on each day of the test, so that the reference tunnel speed for each test was known.

3.1 FLOW VISUALIZATION

3.1.1. Flow Study in the Smoke Tunnel

As a preliminary to the main measurements, the smoke-filled boundary layer behind a backward-facing step was studied in the smoke tunnel with the set-up as described in section 2.2.1. In particular, attention was focussed on the eddy behaviour in the recirculation and reattachment regions, to decide whether eddies were torn in half at reattachment, as reported by Bradshaw & Wong (1972) and to confirm the two-dimensionality of the mean flow already found by de Brederode (1975).

The smoke generator and light sources described in section 2.2.1 were used. The light boxes stood on the tunnel Perspex roof so that the vertical centre plane of smoke-filled boundary layer was illuminated. In some tests the span of smoke injection was about 10cm at the centre, using sticky tape to cover the other parts, in attempts to improve smoke conditions for photographing and to have clearer views of eddy behaviour in the spanwise direction. The flow speeds in the smoke tunnel were varied in the range 1 to 5 m/s.

A number of still photographs were taken during the development of the light sources, but, due to the lack of suitable light sources and/or photographic equipment, these were unfortunately not good enough for presentation. It was found profitable to place strips of mirror or silver tape on the tunnel floor underneath the light sources so that light intensity could be increased by reflection. A proper placement of photographic equipment for overall side view pictures of the boundary layer was difficult because of the limited space between the tunnel and the laboratory walls.

3.1.2 Determination of the Reattachment Line

A number of tests in the blower tunnel were devoted to an oil-flow visualization study, firstly in de Brederode's 2.54 cm (1") step test rig (Brederode, 1975), modified to provide 5.08 cm (2") step, in order to learn the technique and to decide if a new test rig was required, and finally in the present 5.08 cm (2") step test rig in order to determine the mean position of the reattachment line and to check the two-dimensionality of the reattachment region. The oil-mixture as quoted in section 2.2.2 was used in both cases with slight changes of proportion determined by trial-and-error, because of the different surface conditions in the two rigs. Oil must be applied on to the surface as economically as possible to avoid accumulation in some regions, particularly in the recirculation region where the velocity is low, as it then becomes too thick to flow freely.

A number of surface oil-flow photographs were taken and the distance of the reattachment line from the step was measured at several intervals along the span in every run. The results and discussion may be found in the next two chapters. More detail on oil-flow technique is referred to de Brederode (1975).

Since the reattachment line obtained in the oil-flow pattern was the mean line and time dependent information could not be detected by such a technique, tufts were used in some test runs to observe the fluctuating behaviour of the general flow field and the width of fluctuation band at reattachment. Tufts of about 2. 5 cm long were attached to the rig floor, spaced about 2 cm apart in the streamwise direction and about 10 cm both sides of the rig floor centre line. The same arrangements were made at the centre line of both side walls, and a few tufts were also attached to the rig floor in the reattachement region close to the side-wall corners.

3. 1. 3 Plane Mixing Layer Experiments

In some recent reports on flow visualization of plane mixing layers such as Brown & Roshko (1974) and Winant & Browand (1974), it has been suggested that this type of shear layer has more orderly and coherent eddy structure than - say - boundary layer. In our flow configuration, the shear layer close to the step somewhat resembles a free mixing layer because the laminar separation from the step shoulder rapidly becomes turbulent, but in our case there is a region of recirculation on the opposite side to the main stream rather than "still" air or a parallel stream of different velocity, and the shear layer curves towards the floor as it reattaches. Well upstream of reattachment, however, our flow may be classed as a "curved mixing layer", and it must behave in a similar manner to the plane mixing layer with regard to the eddy structure. It therefore seemed most useful to make smoke-flow visualization studies in a very-low-speed plane mixing layer, rather than trying to set up a large-scale step rig for visual studies of eddies at low speed but adequate Reynolds number.

The experiments were carried out in the roofless working section described earlier in section 2. 1. 4. Smoke-flow visualization was used with several different flow speeds to suit photography and to observe the effects of Reynolds number. The light sources used were those described in section 2. 2. 1, and they were

placed on a frame about 60 cm above the mixing layer. The heat from the light sources caused noticeable buoyancy effects, and there was some interference by the light source cooling fans which blew in opposite direction to the tunnel stream. Therefore, air above the tunnel stream was not perfectly still but behaves somewhat like a very slow and large recirculation region.

The second stage of these experiments used the shadowgraph technique in order to compare with the results of Brown & Roshko (1974) and the work was later continued by Dr. A.D. Weir of this Department. A few of the photographs taken during both stages of the experiments may be seen in I.C. Aero Report 75-03 which is presented in this thesis as Appendix I.

3.2 SURFACE PRESSURE AND THE SKIN FRICTION MEASUREMENTS

3.2.1 Streamwise Surface Pressure Distribution Measurements

The streamwise surface pressure distribution on the rig floor behind the step was measured directly from the static tapping as described in section 2.4.1, using the same equipment as for the Pitot traverse (figure 3.7). The effects of Reynolds number on the surface pressure distribution was also investigated, at an early stage, by running tunnel at several different reference speeds. The surface pressure distribution was always checked whenever the rig was re-mounted on to the tunnel after it had been removed for other users' benefit to ensure identical flow configurations for all tests.

3.2.2 Local Skin Friction Measurements

The local skin friction at the centres of five discs on the test rig floor were measured with the Stanton tube described in section 2.4.3. The calibration procedure using Preston tubes as the reference is described in the next section. Each of the five plain discs on the rig floor was replaced by the disc containing the Stanton tube in turn and its pressure difference was read off from a Combist

manometer. Note that in using the Combist manometer care must be taken to ensure that it is standing on a rigid foundation, as it was found to be extremely sensitive to any disturbance to its standing level. Using calibration curve the values of skin friction coefficients could then be easily determined.

3. 3 CALIBRATION PROCEDURES AND TECHNIQUES

3. 3. 1 Pitot Tube Calibration in Reverse Flow

Calibration of the Pitot tube in reverse flow was necessary if it was to be pointing in the conventional direction (i. e. upstream with respect to main stream) at all times even in the recirculation region. This was done in the free stream at x=15. 2 cm, y=11. 6 cm and the obtained results were plotted as shown in figure 3. 1. Yaw calibration of the Pitot tube in reverse flow was not attempted as it was later decided that more reliable results could be obtained by pointing the probe in opposite direction when measured in the recirculation region.

3. 3. 2 Disc-Static Probe Calibration

The principle of disc-static probe calibration (Bryer & Pankhurst, 1971) is to determine the constant in the expression

$$\frac{p - p_D}{\frac{1}{2}\rho U^2} = \gamma \qquad (3.1)$$

where p = true static pressure, p_D = static pressure measured by disc-static probe and $\frac{1}{2}\rho U^2$ = dynamic pressure at the calibration point.

In our case the probe was calibrated in the test rig at the point x = 60. 7 cm, y = 12. 1 cm and true static pressure, p, was measured at a point on the side wall at the same co-ordinates as the probe. The values of $p-p_D$ for various tunnel reference speeds were measured by using the MDC capacitor micromanometer, with the

probe pointing both upstream and downstream, and the typical calibration plots are shown in figure 3.2.

3.3.3 Stanton Tube Calibration

The calibration curve used here is the plot of $\tau_w/\Delta p_s$ vs. $\Delta p_s/\sigma$, as shown in figure 3.3, where τ_w = skin friction at calibration point measured with Preston tube, Δp_s = corresponding pressure difference of the Stanton tube at the same tunnel reference pressure, and $\sigma = (\rho \nu^2)/(\rho_o \nu_o^2)$, the suffix 'o' indicating the standard atmosphere values.

In the present work five different sizes of Preston tubes as described in section 2.4.3 were used in order to obtain more accurate mean value of τ_w. The calibration point was chosen at the centre of the last disc on the rig floor which was 79.8 cm from the step. At this point the flow in the inner layer should approximate to that in a conventional wall shear layer for which the universal Preston tube calibrations were derived. S.T.B. Young's (private communication) PRESTON computer program was used to evaluate the values of τ_w from Wong's Preston tube calibration chart (Wong, 1970) for all Preston tube results.

3.3.4 Hot Wire Calibrations

In the present work static calibrations of single U-wires are fitted to the law

$$E^2 = A + BU^n, \qquad (3.2)$$

with the exponent n varying between 0.4 and 0.45. With Collis & Williams' (1959) 0.45-law, the points in E^2 vs. $U^{0.45}$ plot were found to follow a gentle curved path beyond U≃22 m/s which made a straight line fitting uncertain. At one stage the law

$$E^2 = A + BU^n + CU^{2n} \qquad (3.3)$$

where n = 0.5 proposed by Davies & Patrick (Cockrell, 1972) was tried but with n = 0.45 and a curve fitting method as described in Appendix II was developed. However, this was found unnecessary in the present

work because, with the range of speeds used, the curved part was quite short. The exponent of 0.4 was found to give better straight line fit for the wires used in the present work in the speed range up to approximately 30 m/s and was therefore adopted. Typical U-wire calibration curves with and without linearizer may be found in figure 3.4(a) and 3.4(b) respectively. U-wires were always calibrated at the centre of the wind tunnel exit section with the wire in horizontal position.

The same 0.4-power calibration law mentioned above was also applied to the cross-wire calibrations which were done with the traverse gear carrying X-wires fitted to the first disc from the step, so that the probe measuring point was located at $x = 8.0$ cm, $y = 11.2$ cm. The disc mounting of the traverse gear was to provide a convenient means of X-wire yaw calibration to obtain the effective angles of the wires which were essential in data reduction. Wires were always arranged to be in horizontal planes when calibrated. Detail of cross-wire yaw response and calibration procedures are described by Castro (1973). Figures 3.5(a, b, c) show typical X-wire calibration curves.

It was found that DISA linearizers used in all hot wire work drifted considerably, thus frequent checking was necessary. In the U-probe traverse the calibration was done once each experimenting day before the commence of the traverses, while the calibration was done before and after each traverse station in the X-wire traverse.

The hot wire dynamic calibration was carried out on the first version of the dynamic calibrator as described in section 2.7 following the same principle and procedure as that of Perry & Morrison (1971), in order to determine the necessary correction, if any, due to errors caused by the differentiation of static calibration curve. This

work was temporary suspended because of poor performance of this particular calibrator until the present version of calibrator emerged. Figure 3.6 shows typical ($\partial E/\partial U$) vs. U plots from the results obtained from the original version dynamic calibrator in comparison with various static calibration laws. Dynamic calibration work done by Dr. Bruun (1975) of Southampton University with the present calibrator showed that the careful differentiation of static calibration curve and the dynamic calibration gave the same $\partial E/\partial U$ within experimental error. Therefore, no corrections due to error caused by the differentiation of static calibration curves were made in the results presented in this thesis.

3.4 MEAN FLOW MEASUREMENTS

3.4.1. Mean Velocity Profile Measurements using Pressure Probes

Figure 3.7 shows the arrangement used for the mean velocity profile measurements employing pressure probes. The traverses were done in 13 stations at x/h = 1.9, 3.4, 4.4, 5.4, 6.4, 7.4, 8.4, 9.4, 10.325, 11.325, 13.325, 14.325; the step height, h, being 5.08 cm. Throughout the Pitot tube and disc-static tube traverses, the traverse gear control potentiometer was set at 20mV = 1 mm displacement: this and the MDC capacitor micromanometer calibration, approximately 4 mV = pressure of 1 mm water, were regularly checked. Zero y was set by using a buzzer to detect electrical contact between the probe tip and the brass disc on the working section floor, or a 2.54 cm (1") slip gauge at stations where no disc was present.

Readings of about 50 points at each x station (fewer in the case of static pressure traverse because gradients were smaller), with up to 20 samples at each point in highly turbulent regions were printed and punched on paper tape for computer data processing. At the stations x/h = 1.9 and 3.4 the traverses were repeated with the probes pointing downstream to obtain values in reverse flow. This procedure was omitted for stations x/h = 4.4 and 5.4 which were also

in the recirculation region, because the total pressure profiles measured with forward-facing probes were positive everywhere.

3.4.2 Mean Velocity Profile Measurements by U-probe Hot Wire

The arrangement shown in figure 3.8 was used for all U-probe hot wire measurements. The frequency range was set at 2Hz high-pass and 20 kHz low-pass by means of the DISA auxilliary unit. The anemometer and auxiliary unit were adjusted to give unity gain and a wire overheat ratio of 0.8 was used throughout. These measurements were in fact the by-product of $\overline{u^2}$- measurements but are useful for comparison with the Pitot results. The output of the linearizer was connected, both directly and via the DISA RMS meter, to DTU input channels (figure 3.8). The same stations as for the Pitot traverse were used, except for the omission of the last one, x/h = 14.325 (due to the limitation of the traverse arrangement), and the addition of a station at x/h = 0.65. The general traverse procedure was the same as for the Pitot traverses described in the previous section.

3.4.3 Reference -Mean-Streamline Tracing

The heated wire arrangement used for the reference-streamline tracing has been described in section 2.9. A thermocouple probe fitted to the traverse gear could be traversed in the same fashion as in the Pitot and hot wire traverses described earlier. A reference ("cold junction") thermocouple was placed in the free stream at the end of the working section. The heated wire was located at x = 2.4 cm, y = 11.5 cm, so that the streamline passing through this point was close to but still above the shear layer edge at the end of the working section, and traverses were made at x/h = 1.7, 2.7, 3.7, 4.7, 5.7, 6.7, 7.75, 8.75, 9.75, 10.75, 11.75 and 12.75. Since the temperature difference at each measuring point fluctuated considerably on the differential thermometer scale, its output terminals were connected to a DVM, and about 10 samples of DVM readings at each position were taken to obtain good averages.

3.5 MEASUREMENTS OF FLUCTUATING QUANTITIES

3.5.1 Longitudinal Turbulence Intensity Using a Single-wire Probe

The method and procedure for measurements of the u-component velocity fluctuation using a single hot wire "U-probe" are described in section 3.4.2: the readings were taken simultaneously with mean-velocity profile measurements by DTU print-out and paper tape punch.

3.5.2 X-probe Hot Wire Traverse

In order to obtain v-component turbulence intensities, Reynolds stresses and higher products for energy and shear stress balance computation, "X-probe" hot wire traverses were required. In the present investigation, the planes of wires were always placed vertically with the probe axis carefully adjusted to be horizontal; the w-component of fluctuating velocity was not measured since the main interest was in uv and its governing transport equation. The traverse gear control setting and traverse procedure were the same as those described in section 3.4. Traverses were made at the same stations as for the U-probe traverses except that the first station in this case was at $x/h = 0.5$ rather than 0.65 due to the difference in lengths of the two probe supports.

Figure 3.9 shows the equipment used for these measurements. The main aim was to record linearized hot wire signals on analogue magnetic tapes for later digitizing and computer processing (described in the next section). Linearization could have been carried out in the computer but it was felt important to check the performance of the apparatus by real-time analogue measurements of $\overline{u^2}$, $\overline{v^2}$ and $\overline{uv}$ at a few traverse stations. Difficulties arose mainly from the drift of the linearized hot wire during the long time to complete one traverse; 20-second intergrating time was used for each of the 3 quantities (i.e. $\overline{u^2}$, $\overline{v^2}$ and $\overline{uv}$) in one position and in some positions several integrations were necessary. To set the PHI module "DISA test" (sum-and-difference) unit before each traverse the slopes of the linearized X-wire calibration curves were needed, and in order to set the linearizers the non-linearized

X-wire calibrations were required. Despite these drift-induced difficulties the results of careful analogue measurements at a few stations agreed reasonably well with those from digital processing of analogue tape. The latter are expected to be more accurate in principle because traverses can be completed quickly.

Analogue tape recordings were made at about 10 to 12 points in each traverse depending on the $\overline{u^2}$ distribution obtained from the U-wire measurements. The linearizers were set daily but calibrated before and after each traverse station so that mean values of the calibration could be used if necessary: wires were cleaned daily by shaking in acetone. Data amplifiers or attenuators were always set to give signal amplitudes to be recorded of about 1.5V peak-to-peak, the maximum permissible input to the tape recorder being 2V peak-to-peak. All recordings were made at a tape speed of 1.52 m/s (60 in/sec) and about 30 seconds recording time. Between each recording the recorder was run for 5-10 seconds with the input earthed so that the noise level of the recording system could be checked. A measured sine-wave signal of about 0.5V rms was recorded as a calibration signal on each channel at the start of each traverse.

3.5.3 Sampling Techniques

In the digitization of the analogue tapes an analogue replay speed of 0.38 m/s (15 in/sec), i.e. one quarter of the recording speed, was used. A sampling rate of 20,000 samples/second (10,000 per channel) was used in the present work, giving a real-time rate of 40,000/sec/channel, corresponding to 20kHz folding frequency which was the low-pass filter setting. It was found that well-converged averages could be obtained by processing about 5 seconds of real time data, taken from the later part of the analogue recording to allow the input filters of the digital system plenty of time to settle down.

The overall gain of the system, the ratio between the output voltage of analogue tape recorder when replayed and the voltage of the calibration signal, was measured for each channel to account for the variation of gain of various plug-in modules used in the tape recorder.

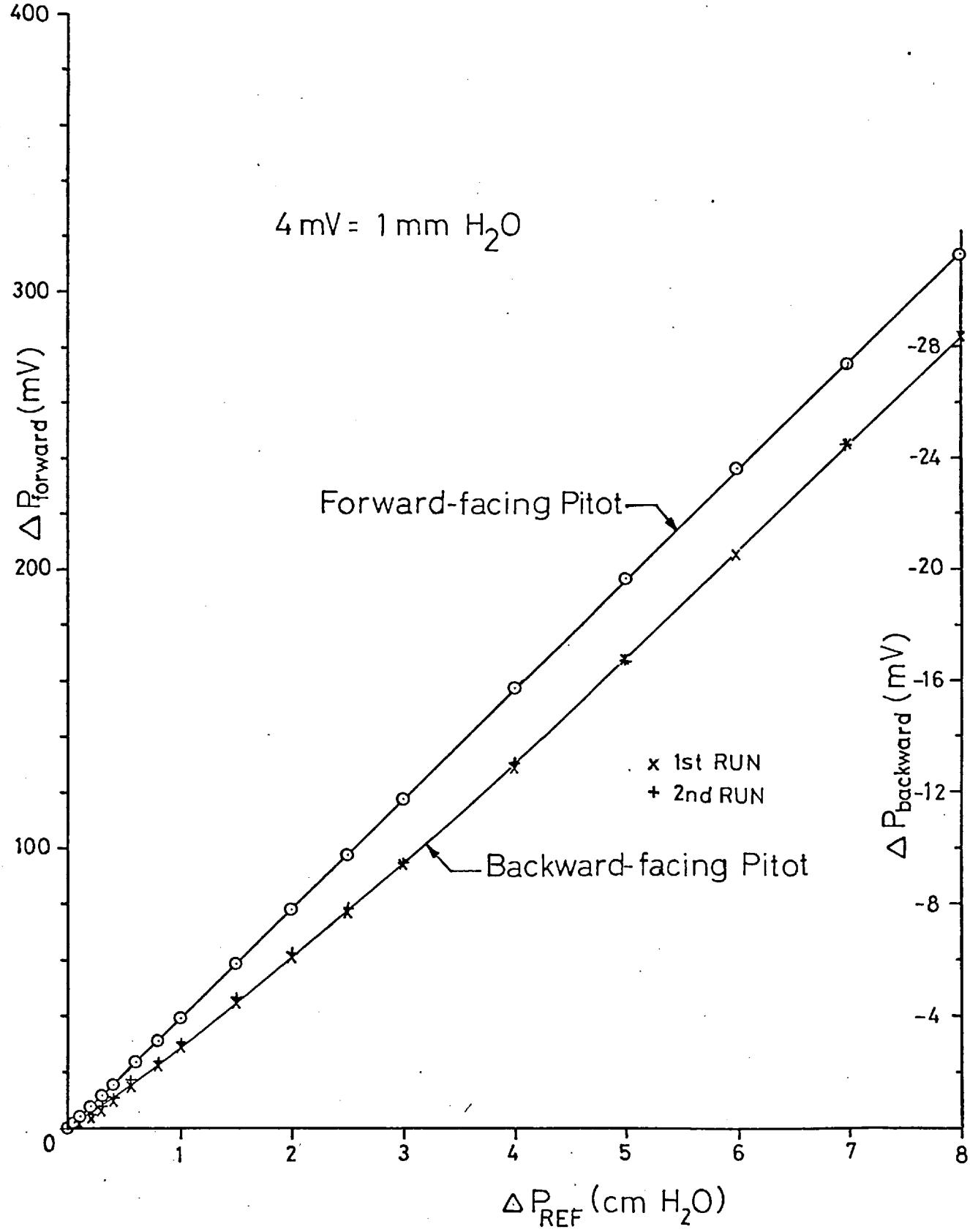


FIGURE 3.1 PITOT-TUBE CALIBRATION

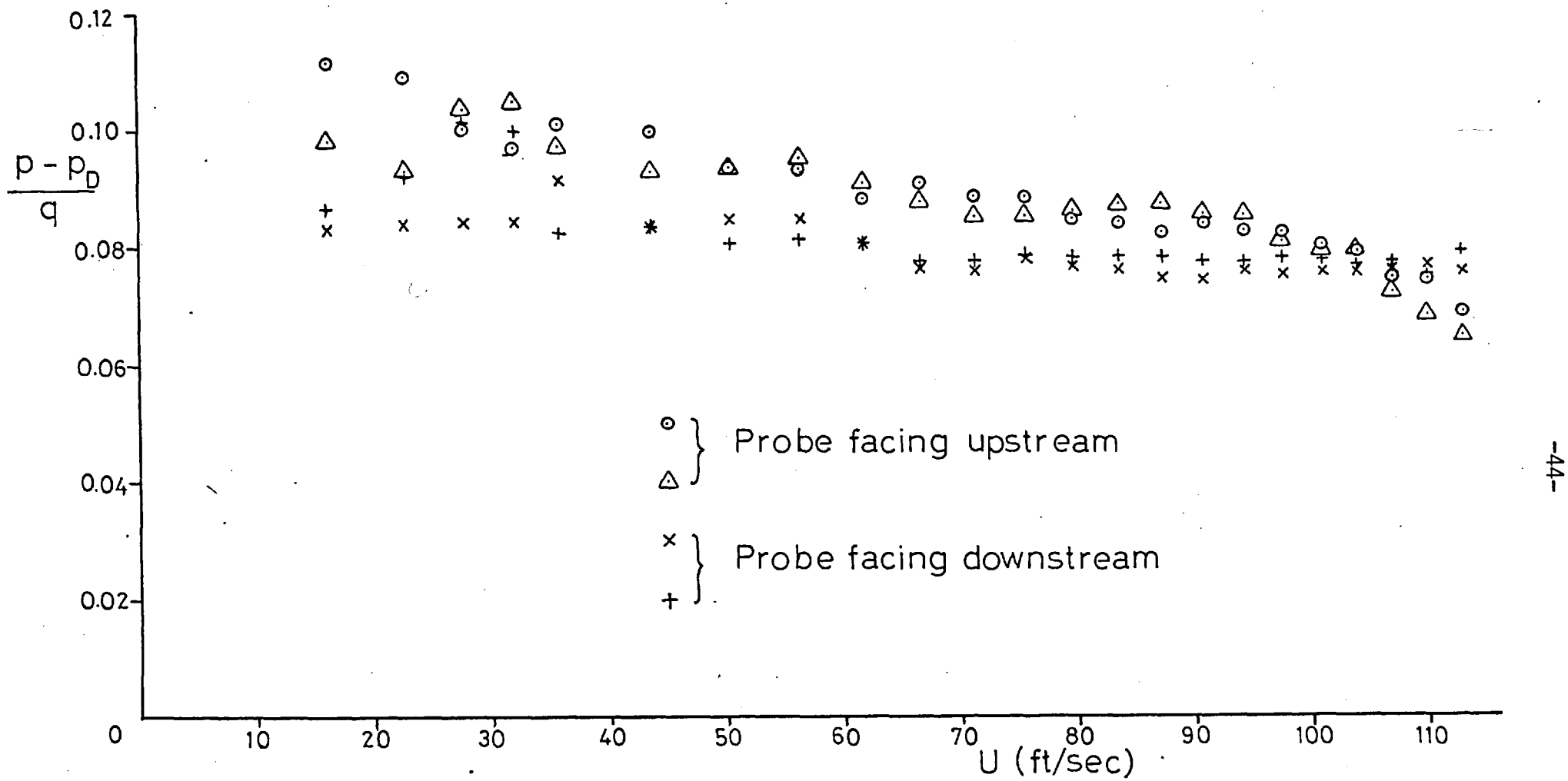


FIGURE 3.2 DISC-STATIC PROBE CALIBRATION

FIGURE 3.3 STANTON TUBE CALIBRATION

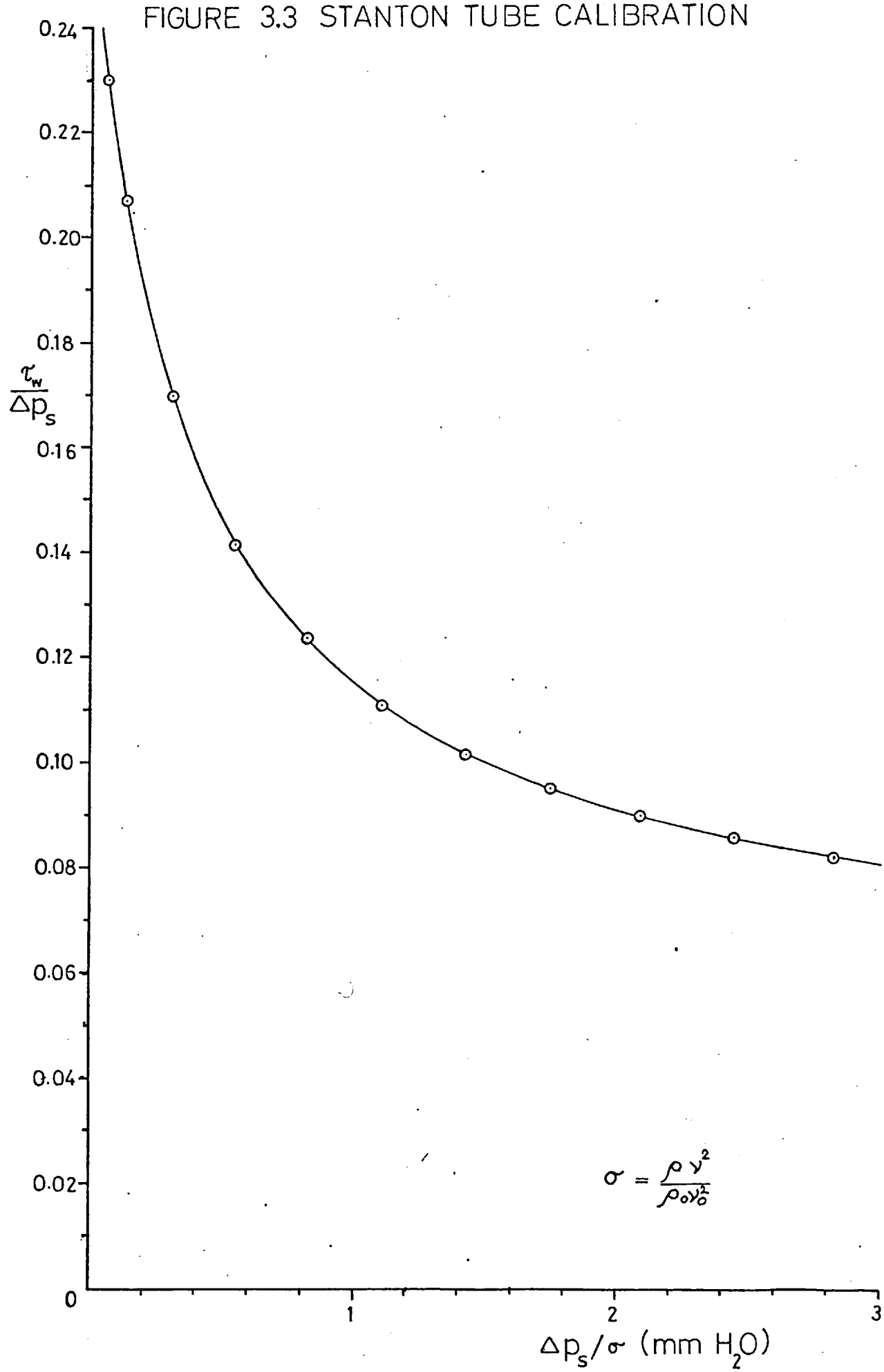
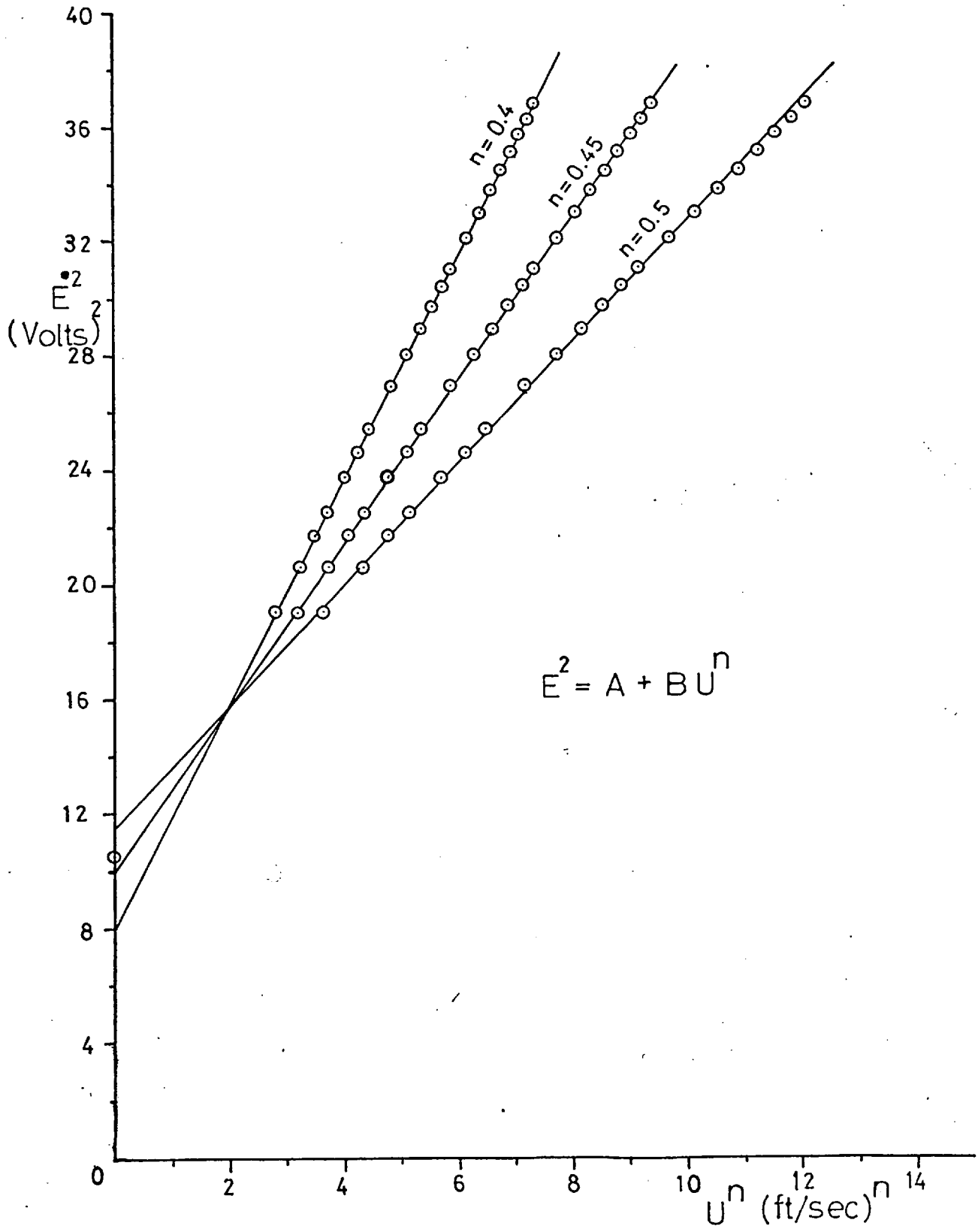


FIGURE 3.4(a)

TYPICAL U-WIRE STATIC CALIBRATION



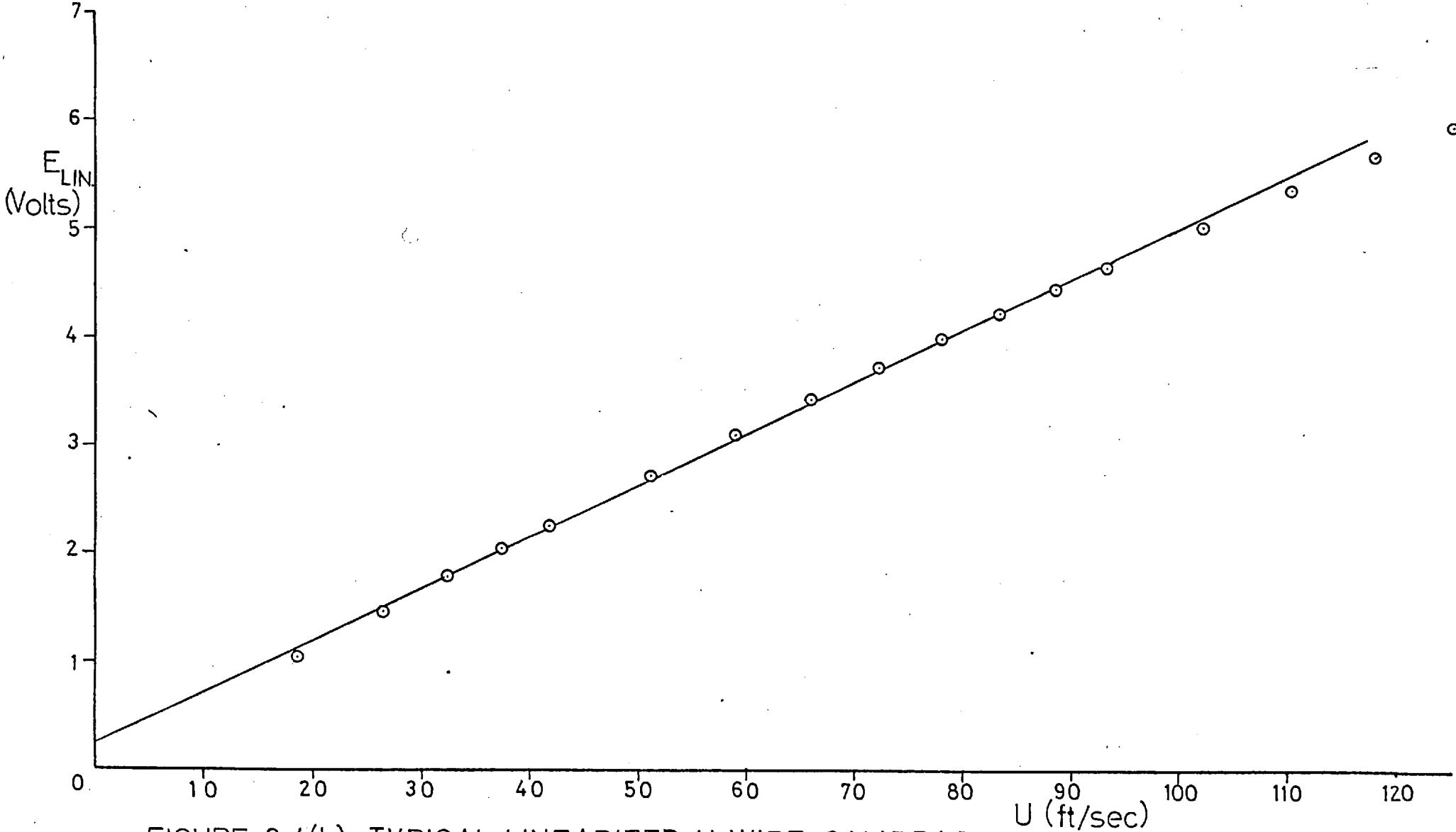


FIGURE 3.4(b) TYPICAL LINEARIZED U-WIRE CALIBRATION

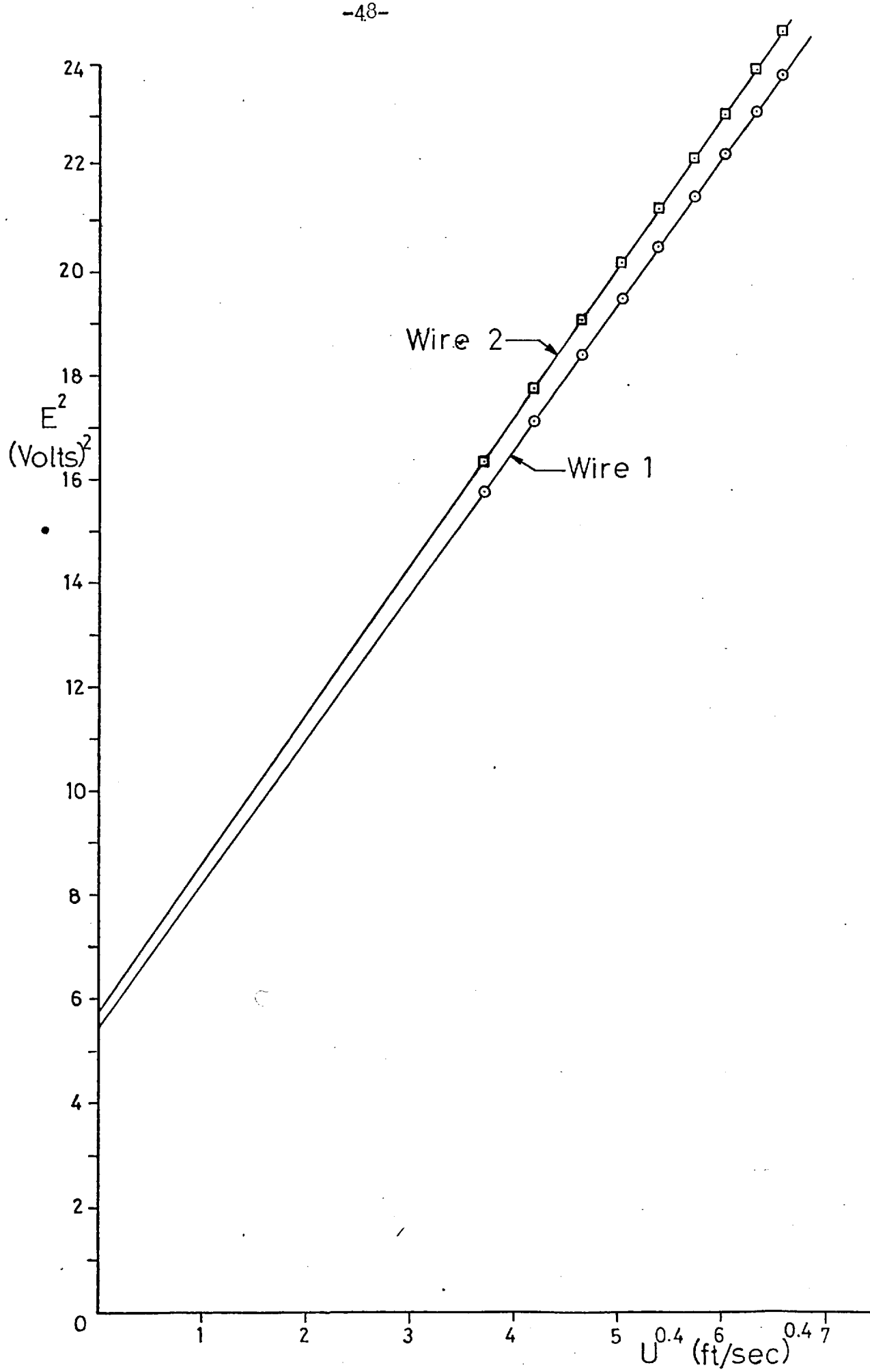
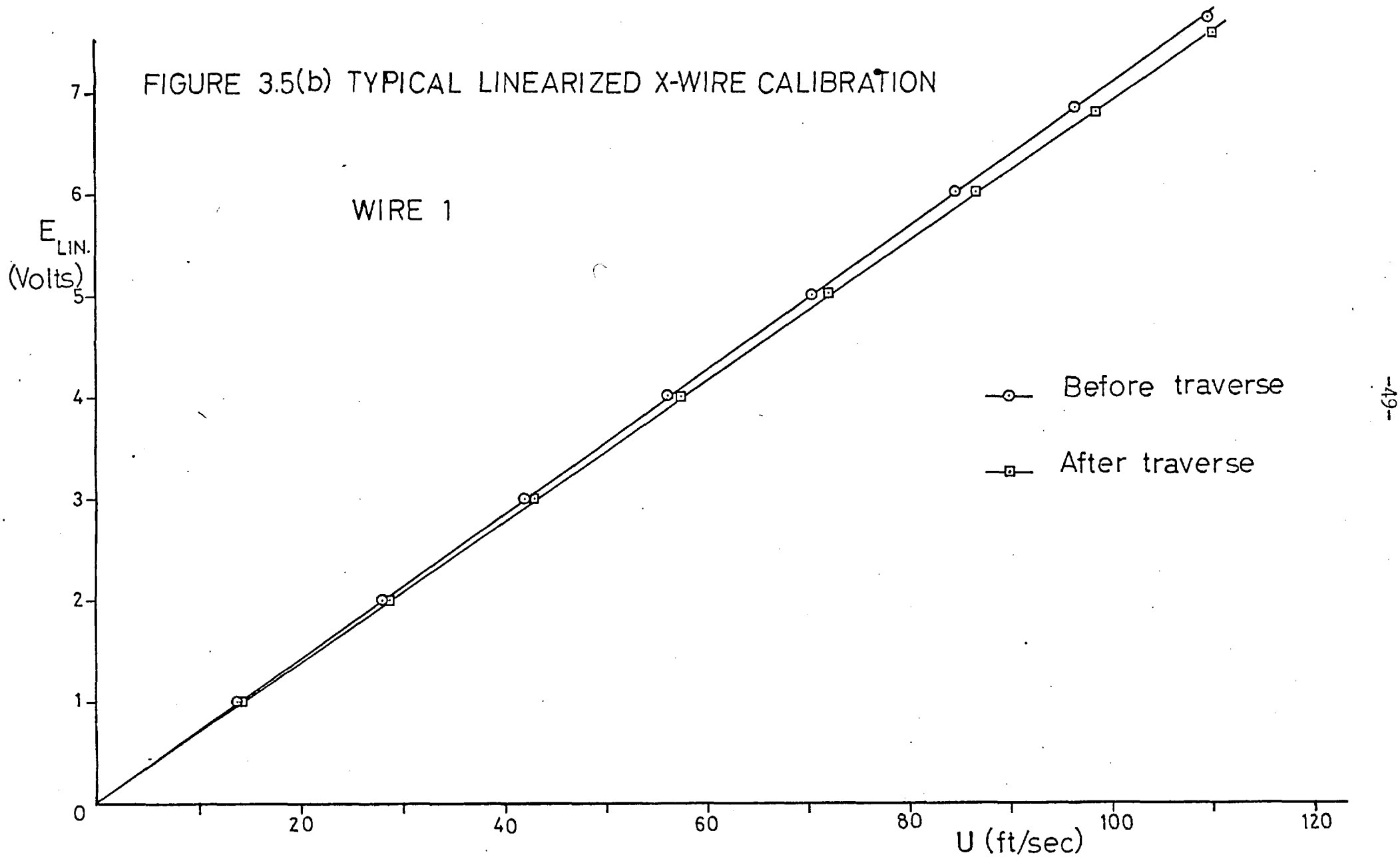
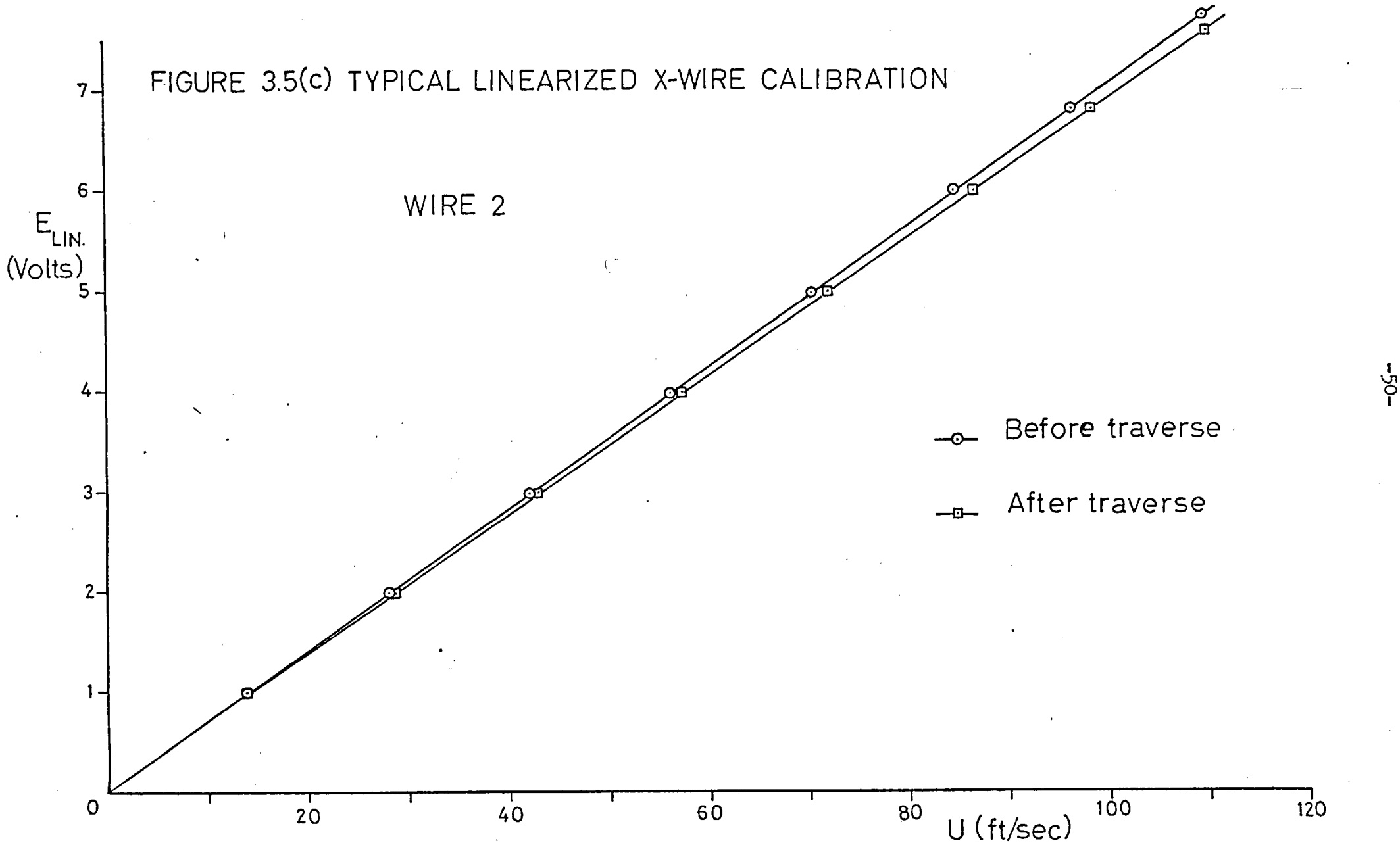
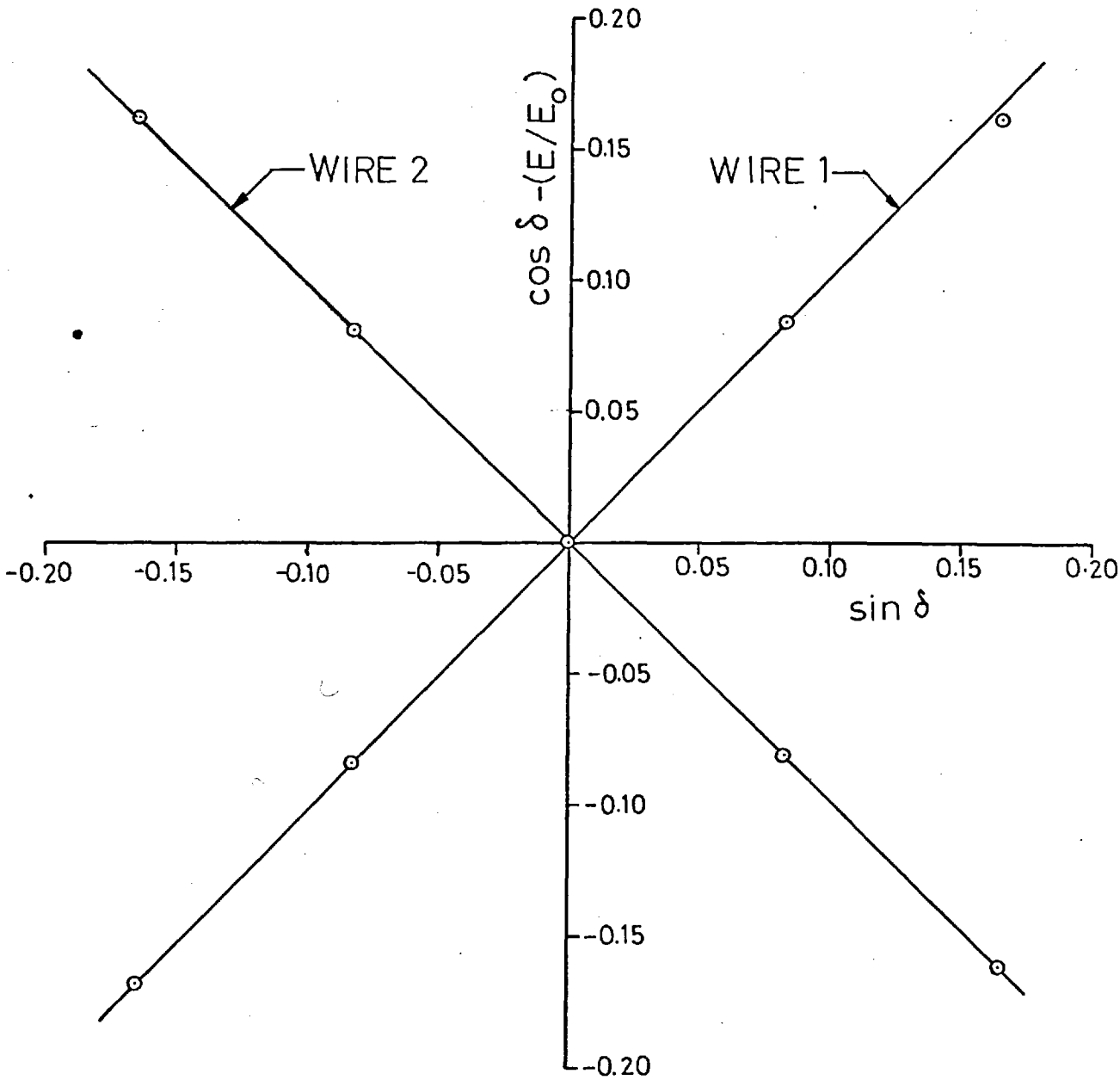


FIGURE 3.5(a) TYPICAL X-WIRE STATIC CALIBRATION


FIGURE 3.5(b) TYPICAL LINEARIZED X-WIRE CALIBRATION
WIRE 1
E LIN. (Volts)
0
1
2
3
4
5
6
7
20
40
60
80
100
120
U (ft/sec)
Before traverse
After traverse


FIGURE 3.5(c) TYPICAL LINEARIZED X-WIRE CALIBRATION
WIRE 2
E LIN. (Volts)
0
1
2
3
4
5
6
7
20
40
60
80
100
120
U (ft/sec)
Before traverse
After traverse



$\tan \psi_1 = 1.020$ $\quad \delta$ = angle x-wire made with stream direction.

$\tan \psi_2 = 0.981$ $\quad \psi$ = effective yaw angle.

FIGURE 3.5(d) TYPICAL LINEARIZED X-WIRE YAW CALIBRATION

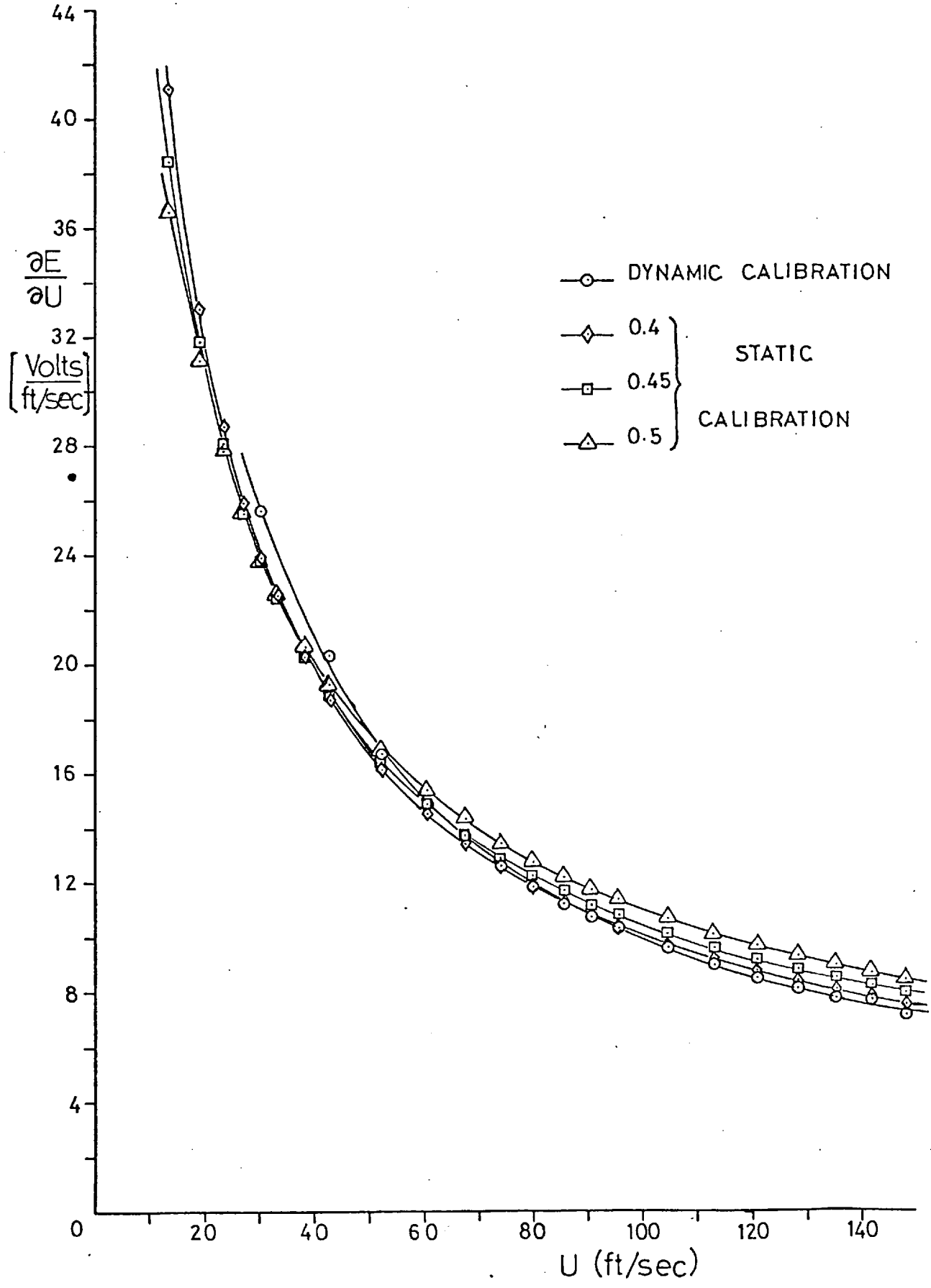


FIGURE 3.6 TYPICAL HOT-WIRE DYNAMIC CALIBRATION

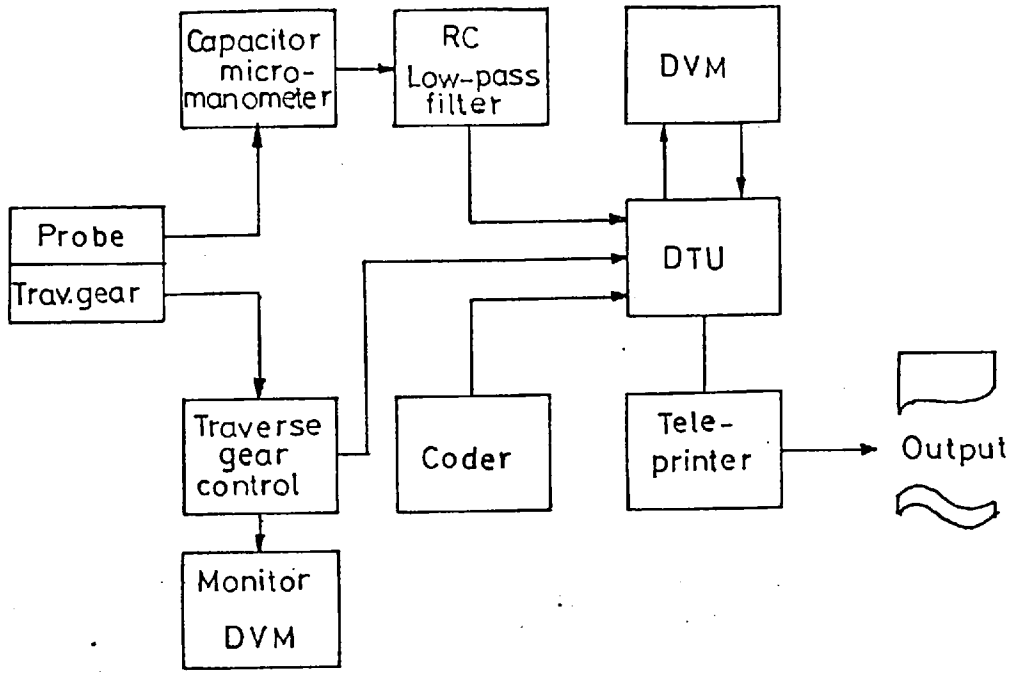


FIGURE 3.7 APPARATUS FOR PRESSURE MEASUREMENTS

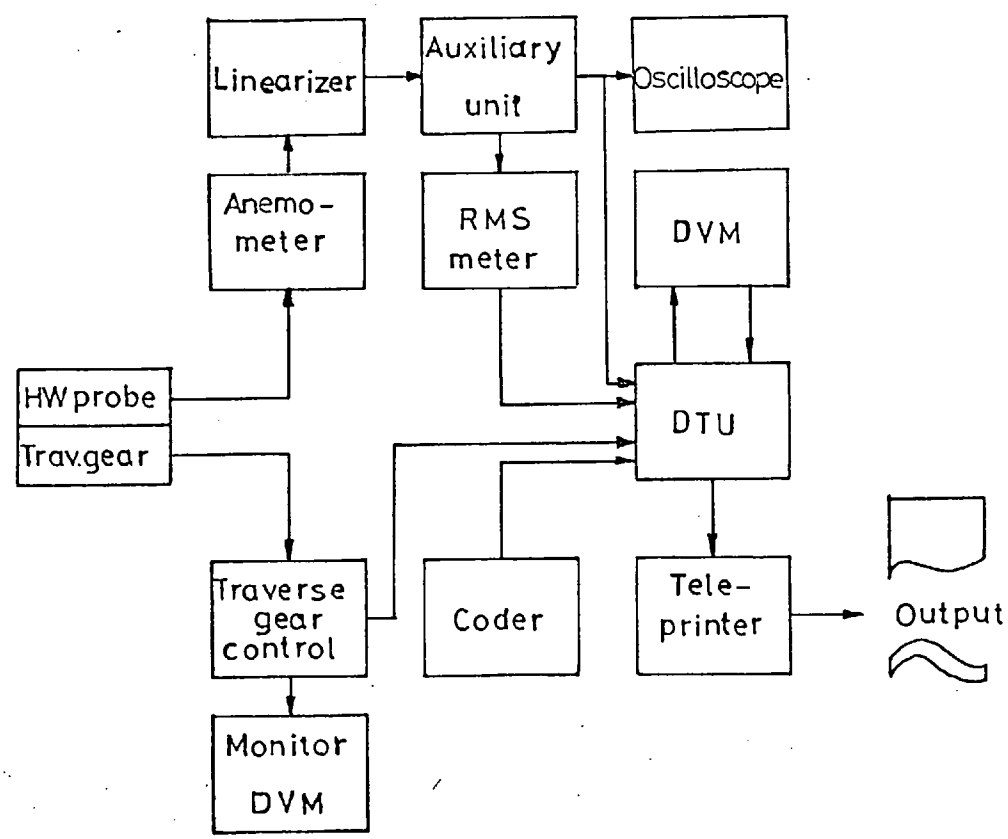


FIGURE 3.8 APPARATUS FOR U-PROBE TRAVERSE

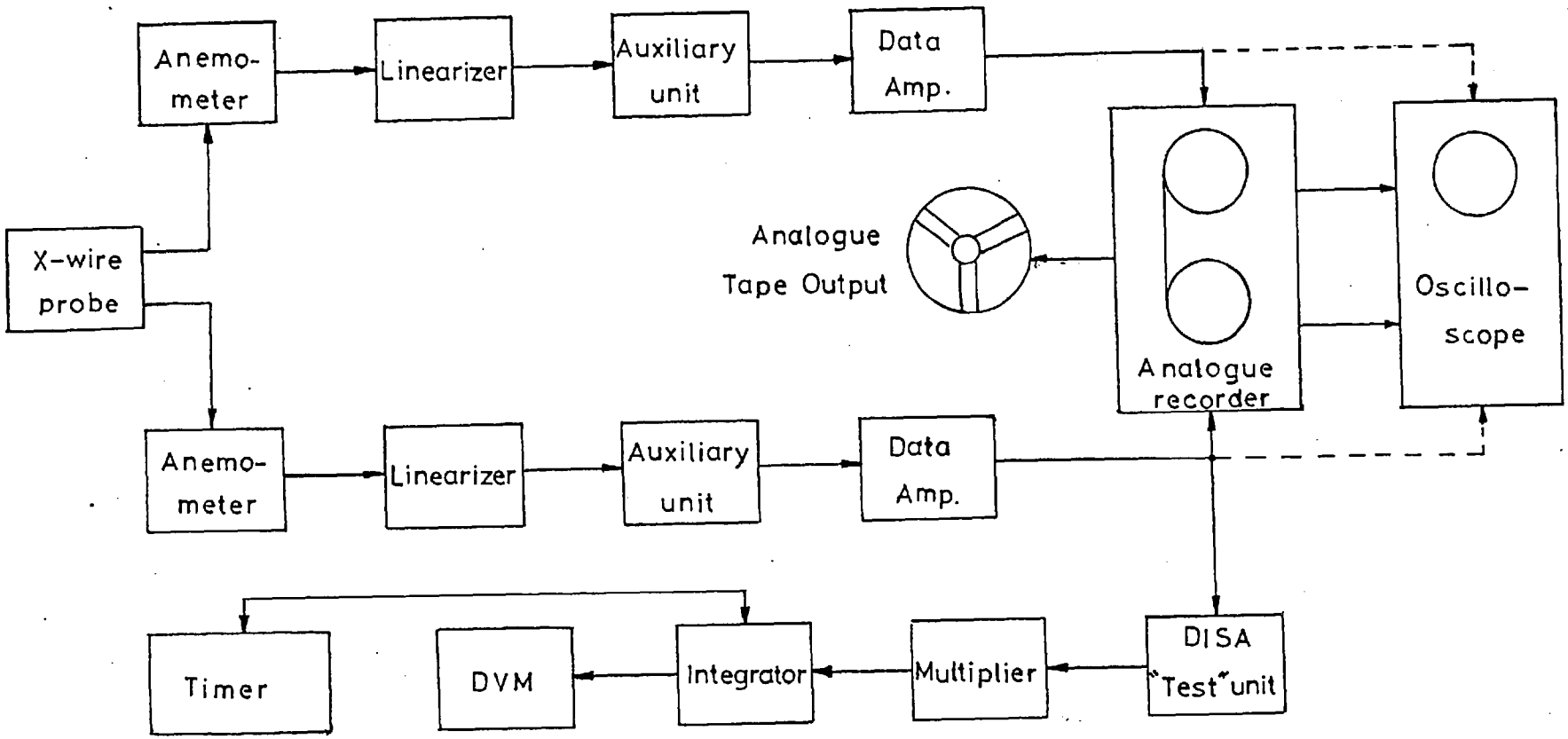


FIGURE 3.9 APPARATUS FOR X-WIRE TRAVERSE

CHAPTER 4

EXPERIMENTAL RESULTS

4.1 GENERAL FLOW BEHAVIOUR

The smoke flow visualization displayed the typical behaviour of reattaching shear layers reported by - for instance - Bradshaw & Wong (1972) and de Brederode (1975), as shown by the sketch in figure 4.1. As mentioned in section 3.1.1, our main interest was to see whether eddies at the reattaching point were actually torn in half, but the lack of suitable photographic equipment (e.g. high speed cinecamera) prevented any decisive conclusion on this point. Visual observation suggested that after arrival at the reattachment point some eddies moved upstream and some downstream alternately. This may well fit in with the fluctuation band about 4 cm wide at reattachment observed in the tuft flow visualization (section 3.1.2). Tufts in this region move to-and-fro at a roughly constant frequency so that the reattachment line moved forward and backward within this fluctuating band which could be the result of alternate movement of eddies following one another. One possible argument for this behaviour is that the entrainment of the shear layer from the recirculation region does not occur at a uniform rate and the upstream moving eddies from reattachment are the replacement of this irregular entrainment; if there were no entrainment from the recirculation region at all, eddies would all travel downstream after reattachment. Smoke injection at mid-span only, viewed from the top, showed that diffusion in the spanwise direction in the separated flow region was very slow and random, which agreed with observations made by de Brederode (1975). Secondary flow patterns were observed but details could not be seen very clearly.

Figure 4.2 shows typical reattachment - line patterns obtained from oil flow visualization. The reattachment distance was found to be 5.85 step heights from the step with repeatability in the

order of $\pm$ 0.01h, which is in the typical range reported elsewhere, e.g. Kline (1959) and de Brederode (1975), for the laminar separation - turbulent reattachment case. The reattachment line was straight over most of the span with very small wiggles, except within approximately 5 cm from either side-wall where it curved upstream (towards the step). Therefore it is safe to conclude that our flow was nominally two-dimensional at least near the centre plane: furthermore the present aspect ratio (span/step height) was 15, well above the value of 10 recommended by de Brederode (1975) as the minimum for acceptably two-dimensional flow near mid-span. The reseparation line of the slow-moving air in the recirculation region was found by oil-flow visualization to be about one step height from the step, as shown in figure 4.2 (b). For further details of surface flow patterns in the recirculation region, in particular at the step corners and on the side walls, the reader is referred to de Brederode (1975).

4.2 MEAN FLOW MEASUREMENTS

The streamwise variation of surface-pressure coefficient behind the step is shown in figure 4.3. Here the pressure coefficient is defined as

$$C_p = \frac{p - p_{ref}}{\frac{1}{2}\rho U_{ref}^2} = \frac{p - p_{ref}}{P_{ref} - p_{ref}} \qquad (4.1)$$

where p = measured pressure at surface tappings in this case, P_{ref} = reference static pressure (at 6.3 cm forward of step shoulder), U_{ref} = tunnel reference speed, P_{ref} = tunnel reference total pressure. It can be seen that the pressure distribution in the recirculation region up to reattachment has the same general shape as reported by all previous workers, for example Roshko & Lau (1965) and Tani et al (1961), namely a low pressure close to the step with a further decrease up to $x/h \simeq 3$, followed by a rapid rise to a maximum about 1 step

height behind the reattachment point ($x_r/h \simeq 5.85$). The value of peak-to-peak recompression C_p is just over 0.4 which is comparable with Wong's (1970) results. As mentioned in section 2.1.3 the rig roof was designed to simulate a streamline in an infinitely high tunnel so that C_p should tend to zero far downstream; the high C_p (but coming down towards zero) near the end of the rig suggests that the attempt was not very successful or the rig length was too short. Pressure distribution in Tani et al's (1961) results is the same order as the present results at their last measured point of about 12 step heights, whereas for all geometrical configurations of Roshko & Lau (1965) but one, C_p does not rise to a positive value.

Figure 4.4 shows pressure distribution in Roshko & Lau's (1965) reduced co-ordinates in comparison with those of Wong (1970), de Brederode (1975) and Roshko & Lau. Roshko & Lau's reduced co-ordinates are defined as

$$\tilde{x} = x/x_r \; ; \; \tilde{C}_p = \frac{C_p - C_{p\min}}{1 - C_{p\min}} \qquad (4.2)$$

where x_r is the reattachment distance. It should be noted that in Roshko & Lau's and de Brederode's cases the separation bubbles were formed on the top of the blunt leading-edge models and C_p is based on the free-stream dynamic pressure rather than the reference dynamic pressure as in Wong's and the present results. With these differences in mind, the distribution curves collapse fairly well together. The "coefficient of reattachment pressure rise"; C_{pmax}, from the lowest to the highest pressure, in our case is about 0.38 in comparison with 0.35 of Roshko & Lau (1965), 0.40 of de Brederode (1975), and 0.34 of Wong (1970).

As mentioned in section 3.2.1, the effect of Reynolds number on streamwise surface-pressure distribution was checked at a fairly early stage of the investigation, with Re_h ($U_{ref}\, h/\nu$) ranging from 6.6×10^4 to 12.1×10^4. It is presented in figure 4.5. The absolute values

of C_p in this graph are slightly different from those in figure 4. 3 due to the later slight modification of the wind tunnel exit shape. The results in figure 4. 5 show clearly that a change of about 2:1 in Reynolds number hardly has any effect on the pressure coefficient distribution, which agrees with Tani's et al (1961) conclusion.

Skin friction coefficients (based on the tunnel reference dynamic pressure) obtained by direct measurements using the Stanton tube as well as by the calculation of Coles' best fit of Pitot traverse velocity profiles (using Clauser charts as first approximation), done in VELPROF II computer program, are plotted versus x/h in figure 4. 6, with some of Wong's (1970) results for comparison. The disagreement between the present values from the two methods seems to be within the likely experimental error; so we conclude that the logarithmic law is fairly well obeyed up to a height of at least 0. 5 cm = 0. 1h, even very close to the reattachment. Wong's (1970) values are not expected to agree closely with the present results owing to the difference in pressure distribution as noted above.

The variation of the measured static pressure coefficient (defined as in equation 4. 1) across the shear layer at each traverse station is shown in figure 4. 7(a) and (b). It can be seen that the velocity profiles calculated by assuming constant static pressure equal to surface pressure would be considerably in error, especially in the reattachment region. However the variation with y is surprisingly small as a whole and the dent in each profile at $y \simeq h$ within the recirculation region may be due partly to the effects of turbulence on the disc-static probe, but the cause of wiggles above $y \simeq 1.2h$ for the first two stations close to the step is doubtful. Furthermore, the small variation in static pressure at the stations far downstream is probably due almost entirely to turbulence effects. Although a number of investigations on the error of the conventional static tube caused by turbulence intensity were made by various workers (for example Goldstein 1936, Toomre 1960, Bradshaw & Goodman 1968), no known work on the disc-static tube can be found at the present time. Since there is no simple way of investigating

the variation of static tube error with turbulence intensity, one has to be content with the suggested correction such as $\pm\frac{1}{4}(\overline{v^2}+\overline{w^2})$ (positive for small eddies and negative for large eddies) for conventional static tubes, which have poor yaw response. Similarly, it is likely that the disc-static tube which has poor yaw response in xz-plane reads very roughly

$$p - 0.1 \cdot \frac{\rho}{2}(\overline{u^2}+\overline{v^2}) - c\rho\overline{w^2} \qquad (4.3)$$

(guessed from the results of Bradshaw and Goodman, 1968). The value 0.1 has been chosen arbitrarily and the constant c is thought to be of order 1. Using numerical values at the station x/h = 12.325 where $\overline{u^2}/U^2_{ref} = 0.01$, $\overline{v^2}/U^2_{ref} = 0.0075$, at y = 0.6 h the correction in C_{p_s} according to (4.3) would be of the order -0.019 while the actual difference in C_{p_s} is about -0.020 there (assuming $\overline{w^2} = \frac{1}{2}(\overline{u^2}+\overline{v^2})$). It therefore suggests that, at the stations far downstream, the variation of static pressure with y is due entirely to turbulence intensity.

The total-pressure distribution at each traverse station is shown in terms of the total-pressure coefficient, C_{p_T}, referred to the tunnel reference dynamic pressure rather than to the free-stream dynamic pressure, i.e.

$$C_{p_T} = \frac{P - p_{ref}}{\frac{1}{2}\rho U^2_{ref}} = \frac{P - p_{ref}}{P_{ref} - p_{ref}} \qquad (4.4)$$

where P = total pressure at the point considered. Figures 4.8(a) - (c) show profiles of C_{pT} at all stations and figure 4.9 shows a contour plot in xy-plane. Only some of the experimental points are shown in the contour plot for the sake of clarity. The scatter in contour position inevitably becomes large as $\partial P/\partial y \to 0$, and smooth curves have been

drawn through the data points near the outer edge of the shear layer.

The 0.995 contour is a generalization of the usual definition of boundary layer thickness, δ_{995}: the two would coincide if p were constant and equal to p_{ref}, but the present definition is more meaningful in the presence of a transverse pressure gradient. The boundary layer seems to grow very slowly from about 1.2h at reattachment to about 1.6h at 14 step heights. Wong's (1970) results show that, with his working section of zero pressure gradient downstream of the reattachment, the growth is asymptotic ($d\delta/dx \rightarrow o$) beyond 50 step-heights, though of course the normal growth rate of a constant-pressure boundary layer must eventually be regained.

The computer program "VELPROF I" written by de Brederode (1973), with some modification to suit the present code convention, was used to process the pressure-probe data in the Department Honeywell H21 computer to obtain the velocity profiles and Clauser-chart co-ordinates for all traverse stations downstream of the reattachment. In the recirculation region, however, the results were calculated entirely by hand (i.e. using a pocket electronic calculator) because it was felt that this would be quicker than modifying the program to account for changes in probe calibration in the reversed flow region. To process the U-wire data, a small computer program was written also for the Honeywell H 21 computer. Mean velocity profiles, U/U_{ref} vs. y/h, from the Pitot and static traverses and from the U-wire traverses are presented together - for comparison purposes - in figures 4.10 (a) - (c) and contour plots of the results from the two methods are shown in figures 4.11 and 4.12 respectively. It should be noted that the reversed-flow part of the Pitot results at x/h = 4.4 was derived from the Pitot tube reversed-flow calibration and should not be taken too seriously. With regard to the single hot wire results, some linearized hot wire calibration curves (as in figure 3.4(a).) are slightly curved or, in some cases, approximate to two successive straight lines; the calibration

values used in calculating the results presented here were those obtained from best-fit straight lines done by eye, and the discrepancy between these results and those derived from the actual calibration curves was found to be negligibly small. Moreover, as the hot wire is not capable of distinguishing flow direction, data points in the recirculation region were plotted on the negative side and an approximate connecting line was drawn for each profile.

Figures 4.10 (a) - (c) show the degree of disagreement between the Pitot and hot wire results. With the exception of x/h = 5.4 (i.e. close to reattachment) all profiles show that the Pitot tube reads higher than the hot wire, especially close to the surface. MacMillan's (1956) displacement correction for shear flow was done automatically in the computer program for Pitot results, but the correction is very small because a small Pitot tube was used. The U-wire results at x/h = 9.325 should be disregarded as serious experimental error was suspected here. As usual in using hot wires for mean-velocity measurement, calibration drift is likely to have been more serious than for the Pitot. As a whole the disagreement between the two measuring methods is quite reasonable and to be expected: allowing for the experimental error, a few stations far downstream show good agreement which suggests that turbulence intensity effects on the Pitot tube may be responsible for the high velocity values. The magnitude of the increase in Pitot reading is usually taken to be simply $\frac{1}{2}\rho(\overline{u^2} + \overline{v^2} + \overline{w^2})$ as first suggested by Goldstein (1936). With the disc-static correction due to turbulence intensity as in (4.3) the measured dynamic pressure may be written as

$$(P - p)_{meas.} = (P - p)_{true} + \tfrac{1}{2}\rho(\overline{u^2} + \overline{v^2} + \overline{w^2}) + 0.1.\tfrac{\rho}{2}(\overline{u^2} + \overline{v^2}) + \rho\overline{w^2} \qquad (4.5)$$

$$\Delta\frac{U}{U_{ref}} = \frac{U}{U}_{ref}\left[\tfrac{1}{2}\left(\frac{\overline{u^2}}{U^2_{ref}} + \frac{\overline{v^2}}{U^2_{ref}} + \frac{\overline{w^2}}{U^2_{ref}}\right) + 0.05\left(\frac{\overline{u^2}}{U^2_{ref}} + \frac{\overline{v^2}}{U^2_{ref}} + \frac{\overline{w^2}}{U^2_{ref}}\right)\right] \qquad (4.5.a)$$

As a test case let us consider the point x = 5.4h, y = 0.6h where $(\overline{u^2}/U^2_{ref}) = 0.027$, $(\overline{v^2}/U^2_{ref}) = 0.0155$, $\frac{1}{2}(\overline{u^2} + \overline{v^2})/U^2_{ref} \simeq 0.0213$, $U/U_{ref} = 0.565$. Then the overestimation in U/U_{ref}, given by (4.5), is about 0.098 whereas the actual difference between the Pitot and hot-wire results is about 0.06. At the same station near the floor, the changing signs of the difference may be due to the serious error in Pitot reading at very low velocity as well as the possibility of hot wire data points to be in the negative side. This station is just ahead of the reattachment point. Near the floor - say at x = 6.4h, y = 0.1h where the turbulence intensities are much lower ($\frac{\overline{u^2}}{U^2}_{ref} = 0.0186$, $\frac{\overline{v^2}}{U^2}_{ref} = 0.0055$, $U/U_{ref} = 0.28$) - the calculated error caused by turbulence intensity is about 0.112 compared to the actual difference of about 0.05 between hot-wire and Pitot results. On the other hand, both the proximity of wall and turbulence intensity also have effect on hot-wire measurements. When neglecting third-order and higher terms, the relation for single hot-wire correction reads (Hinze 1959)

$$U_{meas} \simeq U(1 - \tfrac{1}{4}\frac{\overline{u^2}}{U^2} + \tfrac{1}{2}\frac{\overline{v^2}}{U^2}) \qquad (4.6)$$

i.e.
$$\Delta(\frac{U}{U_{ref}}) \simeq -\frac{U_{ref}}{U}(\tfrac{1}{4}\frac{\overline{u^2}}{U^2_{ref}} - \tfrac{1}{2}\frac{\overline{v^2}}{U^2_{ref}}) \qquad (4.7)$$

For the two points considered above we found: at x = 5.4h, y = 0.6h - where $U/U_{ref} = 0.5$ (hot wire results), $\Delta(U/U_{ref}) \simeq 0.002$; and at x = 6.4h, y = 0.1h, $U/U_{ref} = 0.22$, $\Delta(U/U_{ref}) \simeq -0.009$. It can be seen that in both cases the effect of turbulence intensities on hot-wire measurement is negligible compared with its effect on the Pitot results; in the second case although the turbulence intensities are small the magnitude of error is considerably increased because of low local mean

velocity and in the opposite sense to make the overall difference of about 0.118 compared to the actual difference of 0.05. We can therefore conclude that, apart from the experimental error such as hot-wire calibration drift, the main cause of the disagreement appears in the Pitot and single hot-wire results is the turbulence intensity effect: the much higher estimated error is probably caused by the assumption of constant $c = 1$ in equation (4.5). The maximum discrepancy is about 20% of the mean velocity except in the reattachment region.

"Clauser charts" (plots of U/U_e vs. $\log (U_e y/\nu)$ for all traverse stations behind reattachment obtained from the Pitot results are shown in figures 4.13(a) to (b). C_f lines are also shown so that the approximate value of skin friction at each station may be determined; these values were in fact used as the initial value input data for the computer iterative process to obtain the final values of C_f from a fit to the velocity profiles assuming Coles' constants $K = 0.41$ and $C = 5.0$. Figures 4.14(a) to (b) show individual logarithmic velocity profiles obtained from the Pitot results (U/u_τ vs. $\log y^+$; $y^+ = u_\tau y/\nu$) while in figure 4.15 all profiles were plotted on the same graph to exhibit the overall feature of the shear layer behind the reattachment. The outer regions of these velocity profiles show the trends of different adverse pressure gradient or Reynolds number effect (Duncan et al, 1970) and the data points fall surprisingly close together on a common curve in the "inner" region, indicating the degree of consistency of the results. Note that the higher values for $x/h = 6.4$ in both figures 4.14(b) and 4.15 are omitted owing to space limitation. Due to the uncertainty of some of the U-wire calibration as mentioned earlier only two logarithmic velocity profiles from the U-wire results (at $x/h = 7.4$ and 12.325) have been deduced and plotted in figure 4.14(c) in comparison with the Pitot results. The $(U/u_\tau, y^+)$ co-ordinates of the hot-wire results were first computed, using the value of C_f obtained from the

Pitot results, and plotted on the same scales as for the Pitot results. The U/u_τ scale of hot-wire results is then adjusted to fit the lowest point; the 'Cole's log-law' line is also drawn. It should be noted that no adjustment of y^+ scale has been made as it is believed to have a very small effect. The discrepancy between the two results follows closely to the linear profile plots and it is seen that C_f estimated by the hot-wire results would be about 33% lower than that by the Pitot results at $x/h = 7.4$. It is true that the Pitot results are affected more by high turbulence level but they are believed to be almost free of experimental errors.

The relative temperature distribution in the wake of the heated-wire during the reference-mean-streamline tracing are shown in figures 4.16(a) - (c) and the reference-mean-streamline itself is shown in figure 4.17. The shape of this streamline is as expected, i.e. it curves down towards the reattachment region where the shear layer is thinnest and then gradually rises downstream; this is very similar to the variation of main-stream velocity with downstream distance as shown in figure 4.18. It should be noted that close to the step the

main-stream velocity varies linearly with y due to expansion (see for example Rockwell & Fiske, 1970) and therefore in figure 4.18 the velocity ratios U_1/U_{ref} are those at y = 1.8 h.

4.3 MEASUREMENTS OF FLUCTUATING QUANTITIES

The output of the computer program used to process linearized single hot-wire data, mentioned above, also yields the longitudinal turbulence intensity, $\overline{u^2}/U^2_{ref}$. The "DIG2U" computer program (Weir & Bradshaw, 1974) was used to process digital tapes of the cross-wire data to obtain $\overline{u^2}/U^2_{ref}$, $\overline{v^2}/U^2_{ref}$, $-\overline{uv}/U^2_{ref}$, higher-order terms, intermittency factor, etc. The 'wholesale intermittency' THRESH subroutine, the same as that used by Murlis (1975), was used to compute the intermittency factor. Details of the intermittency problem and the choice of criterion function are described by Murlis. He in fact followed Castro (1973) who took the sensitised signal, $\partial uv/\partial t$, as criterion function and added as an alternative criterion function, $\partial^2 uv/\partial t^2$, to remove the effects of spurious zero values of $\partial uv/\partial t$. As to the choice of 'threshold levels', the values suggested by Murlis were originally used and later adjusted to appropriate values by using values of computer output criterions of the neighbouring point. The presentation of intermittency is postponed until the next chapter.

The quantities $\overline{u^2}/U^2_{ref}$ from both single hot wire and cross-wire results, $\overline{v^2}/U^2_{ref}$ and $-\overline{uv}/U^2_{ref}$ for each traverse station are plotted against y/h in figures 4.19(a) - (l) while contour plots of $\overline{u^2}/U^2_{ref}$ (from U-probe results and from cross-wire results), $\overline{v^2}/U^2_{ref}$ and $-\overline{uv}/U^2_{ref}$ are shown in figures 4.20 to 4.23 respectively. In the high-turbulence region the disagreement of longitudinal intensities measured by U-probe and X-probe is great, as great as 50% in some places, and the results from U-probe are higher almost everywhere.

By comparing the contour plots in figures 4.20 and 4.21, the pattern of X-probe results seems to be more orderly than that of U-probe results. As mentioned earlier, the single wire results may suffer to a certain extent from the calibration drift; the decrease in slope of the E_{lin} vs. U (which usually is the case) always yields an overestimated results. Bradbury (1975), in his paper describing a system for using both hot wire and pulsed wire anemometers in an on-line manner, shows that the normal wire measurements in high turbulence are dependent on the wire attitude; namely, the spanwise U-wire reads higher than the transverse U-wire. In our case the wire of U-probe was always placed horizontally but the wires of X-probe were placed vertically. Castro (1975), in his discussion of errors in the hot-wire measurement, concludes that it would be better to align the cross-wire probe in the mean streamline direction to help equalising the errors on either side caused by the rectifying effect of the wires. In the present results the cross-wire probe was placed in the horizontal direction and <u>not</u> in the mean streamline direction. He also remarks that cross-wire measures too low a value of the turbulence intensity which is what we find when comparing $\overline{u^2}$ - component intensity with that from U-wire results. His last remark is that even if complex calibration are made, there are bound to be significant measurement errors at intensities greater than about 30%: in the present work the longitudinal intensity in some region is as high as 63%. Furthermore, in the recirculation and reattachment regions the velocity vectors in some places are far from being horizontal and the measured values of longitudinal intensity made by a normal wire are not the true ones. For a velocity vector inclination of β to the horizontal plane, with a linearized normal hot-wire in a spanwise direction, simple derivation* yields

$$\overline{e^2} = C^2\cos^2\beta(\overline{u^2} + \overline{v^2}\tan^2\beta - 2\overline{uv}\tan\beta) \qquad (4.8)$$

where e = measured fluctuating voltage and C = linearized hot-wire calibration constant. If the velocity vector were horizontal we would

---

* I am grateful to Dr. A. J. Smits for showing me this derivation.

obtain the true value (i.e. $\beta = 0$) and the relation becomes

$$(\overline{e^2})_{true} = C^2\overline{u^2} \tag{4.9}$$

From (4.8) and (4.9) the error due to the inclination of the velocity vector (neglecting the effects of high turbulence) may be written as

$$\frac{\Delta\overline{e^2}}{(\overline{e^2})_{true}} = \frac{\overline{v^2}\tan^2\beta - \overline{u^2}\sin^2\beta - 2\overline{uv}\tan\beta}{\overline{u^2}} \tag{4.10}$$

For our worst case at $x = 5.4h$, $y = 0.6h$ ($\overline{u^2}/U_{ref} = 0.027$, $\overline{v^2}/U_{ref} = 0.0155$ and $-\overline{uv}/U^2_{ref} = 0.0095$) assuming a velocity vector inclination of 5^o, the error would be about 6%; and if $\beta = 10^o$ the error becomes about 11%.

Considering the main causes of errors in hot-wire measurements outlined above, it is no great surprise to find consistent disagreement between the results measured by two different types of probes in addition to the scatter in the results as in figures 4.19 (a)-(l). In view of calibration uncertainty of the linearized U-probe as mentioned earlier, the results by the X-probe and U from Pitot results are used in all subsequent calculation, i.e. turbulent energy and shear stress balances, and should be acceptable for comparing results at different stations and for studying dimensionless turbulence parameters such as skewness. However, these or any other hot-wire measurements in highly-turbulent flows cannot be relied on for absolute values of intensities.

4.4 THE TURBULENT ENERGY BALANCE

The turbulent energy transport equation may be written as

$$\frac{D(\frac{1}{2}\overline{q^2})}{Dt} \equiv \overbrace{(U\frac{\partial}{\partial x} + V\frac{\partial}{\partial y})(\tfrac{1}{2}\overline{q^2})}^{\text{Advection}}$$

$$= \overbrace{-\overline{uv}\,(\frac{\partial U}{\partial y} + \frac{\partial V}{\partial x}) - \overline{u^2}\frac{\partial U}{\partial x} - \overline{v^2}\frac{\partial V}{\partial y}}^{\text{Production}} - \overbrace{\frac{\partial}{\partial x}(\tfrac{1}{2}\overline{q^2u} + \frac{\overline{pu}}{\rho}) - \frac{\partial}{\partial y}(\tfrac{1}{2}\overline{q^2v} + \frac{\overline{pv}}{\rho})}^{\text{Diffusion}} - \overbrace{\epsilon}^{\text{Dissipation}} \tag{4.11}$$

for a steady two-dimensional flow when the viscous diffusion term $\nu\nabla^2\frac{1}{2}\overline{q^2}$ has been neglected.

The transverse mean velocity component, V, was required for the calculation of energy and shear stress balances and was calculated by using the continuity equation

$$\frac{\partial U}{\partial x} + \frac{\partial V}{\partial y} = 0 \qquad (4.12)$$

$$V = -\int_0^y \frac{\partial U}{\partial x}\, dy' \qquad (4.13.a)$$

$$= -\left(\int_0^{y_s} \frac{\partial U}{\partial x}\, dy' - \int_y^{y_s} \frac{\partial U}{\partial x}\, dy'\right)$$

$$= V_s + \int_y^{y_s} \frac{\partial U}{\partial x}\, dy'$$

$$= U_s \tan\psi_s + \int_y^{y_s} \frac{\partial U}{\partial x}\, dy'$$

$$= |\underset{\sim}{U}_s| \sin\psi_s + \int_y^{y_s} \frac{\partial U}{\partial x}\, dy' \qquad (4.13.b)$$

where ψ_s is the angle the reference mean streamline makes with the horizontal plane and the subscript 's' indicates the values at the reference mean streamline. U was obtained from the Pitot and static results.

Equation (4.13.a) was used to evaluate V at the stations downstream of reattachment, while equation (4.13.b) was used for the stations in the recirculation region, where integration from y = o is untrustworthy. The integrals in these equations were determined graphically since U vs. x curves needed considerable smoothing out in some places.

Knowledge of $\overline{w^2}$ is required to evaluate the Advection term, $(U \frac{\partial}{\partial x_2} + \frac{\partial}{\partial y})(\frac{1}{2}\overline{q^2})$. In the present work we did not measure the quantity $\overline{w^2}$ and therefore the usual approximate relation $\overline{w^2} = \frac{1}{2}(\overline{u^2} + \overline{v^2})$ is assumed, so that

$$\tfrac{1}{2}\overline{q^2} = \tfrac{3}{4}(\overline{u^2}+\overline{v^2}) \qquad (4.14)$$

Castro (1973) found that the difference between the measured $\overline{w^2}$ and $\frac{1}{2}(\overline{u^2} + \overline{v^2})$ is less than 10% everywhere in a plane mixing layer. A similar assumption was used in calculating the longitudinal diffusion term, $\partial(\frac{1}{2}\overline{q^2 u})/\partial x$, to give

$$\tfrac{1}{2}\overline{q^2 u} = \frac{3}{4}(\overline{u^3} + \overline{uv^2}) \qquad (4.15)$$

In determining the transverse diffusion term, $\frac{\partial}{\partial y}(\frac{1}{2}\overline{q^2 v})$, the assumption $\overline{vw^2} = \frac{1}{2}\overline{v^3}$ (Castro, 1973) was used so that

$$\overline{q^2 v} = \overline{u^2 v} + \overline{v^3} + \overline{vw^2} = \overline{u^2 v} + \frac{3}{2}\overline{v^3} \qquad (4.16)$$

Bradshaw et al (1964), in their calculation of the energy balance diffusion term, assumed $\overline{vw^2} = \overline{v^3}$ but Castro (1973) found the magnitude of $\overline{vw^2}$ to be a little more than half $\overline{v^3}$ in agreement with Wygnanski and Fiedler's (1969) results.

The pressure term, $-(\frac{\partial}{\partial x}(\overline{pu}/\rho) + \frac{\partial}{\partial y}(\overline{pv}/\rho))$, is too difficult to measure and is neglected; therefore the rate of dissipation, ϵ, which was found by difference, includes this pressure term if the latter is not negligible (see discussion below).

The normal - stress production term, $-(\overline{u^2}\frac{\partial U}{\partial x} + \overline{v^2}\frac{\partial V}{\partial y})$, may be written as $-(\overline{u^2} - \overline{v^2})\frac{\partial U}{\partial x}$ and was used in the results presented here.

Figures 4.24 (a) - (j) show turbulent energy balance at the stations where the cross-wire traverses were made. All quantities are normalized by (U^3_{ref}/h). The approximate values for a constant - pressure boundary layer are also plotted in figure 4.24 (j) (x/h = 12.325) for comparison. It should be noted that at this, the last station, the slopes of all curves plotted against x are very difficult to measure

accurately. The changes of energy scale among these figures should also be noted. Most of the dissipation-rate curves have a dent at point of maximum shear-stress production. The results of Castro (1973) show an 'out-of-balance' term in the turbulent energy balance, obtained from using measured values of diffusion and calculated values of dissipation rate by assuming ϵ to be proportional to $(\overline{q^2})^{3/2}$, which is comparable to the dent appearing in the dissipation-rate curves in our case. The discussion of energy behaviour is postponed until the next chapter.

4.5 THE SHEAR STRESS BALANCE

The shear stress transport equation may be written in similar fashion as the turbulent energy transport equation (4.11), i.e.

$$\frac{D(\overline{uv})}{Dt} \equiv \left(U\frac{\partial}{\partial x} + V\frac{\partial}{\partial y} \right)(\overline{uv})$$

$$= -\overline{v^2}\frac{\partial U}{\partial y} - \overline{u^2}\frac{\partial V}{\partial x} + \overline{\frac{p}{\rho}\left(\frac{\partial u}{\partial y} + \frac{\partial v}{\partial x}\right)} - \frac{\partial}{\partial x}\left(\overline{u^2 v} + \frac{\overline{pv}}{\rho}\right) - \frac{\partial}{\partial y}\left(\overline{v^2 u} + \frac{\overline{pu}}{\rho}\right) \quad (4.17)$$

The calculation procedure is similar to that for the turbulent energy balance described in the previous section. Figures 4.25 (a) - (j) show shear stress balances at the cross-wire traverse stations. The terms

$\left(U\frac{\partial}{\partial x} + V\frac{\partial}{\partial y} \right)(\overline{uv})$, $\overline{v^2}\frac{\partial U}{\partial y}$, $\overline{u^2}\frac{\partial V}{\partial x}$, $\frac{\partial(\overline{u^2 v})}{\partial x}$, and $\frac{\partial(\overline{uv^2})}{\partial y}$,

all normalized by U_{ref}^3/h, are plotted separately, together with the pressure stress term obtained by the difference. The discussion of the shear stress balance is in the next chapter.

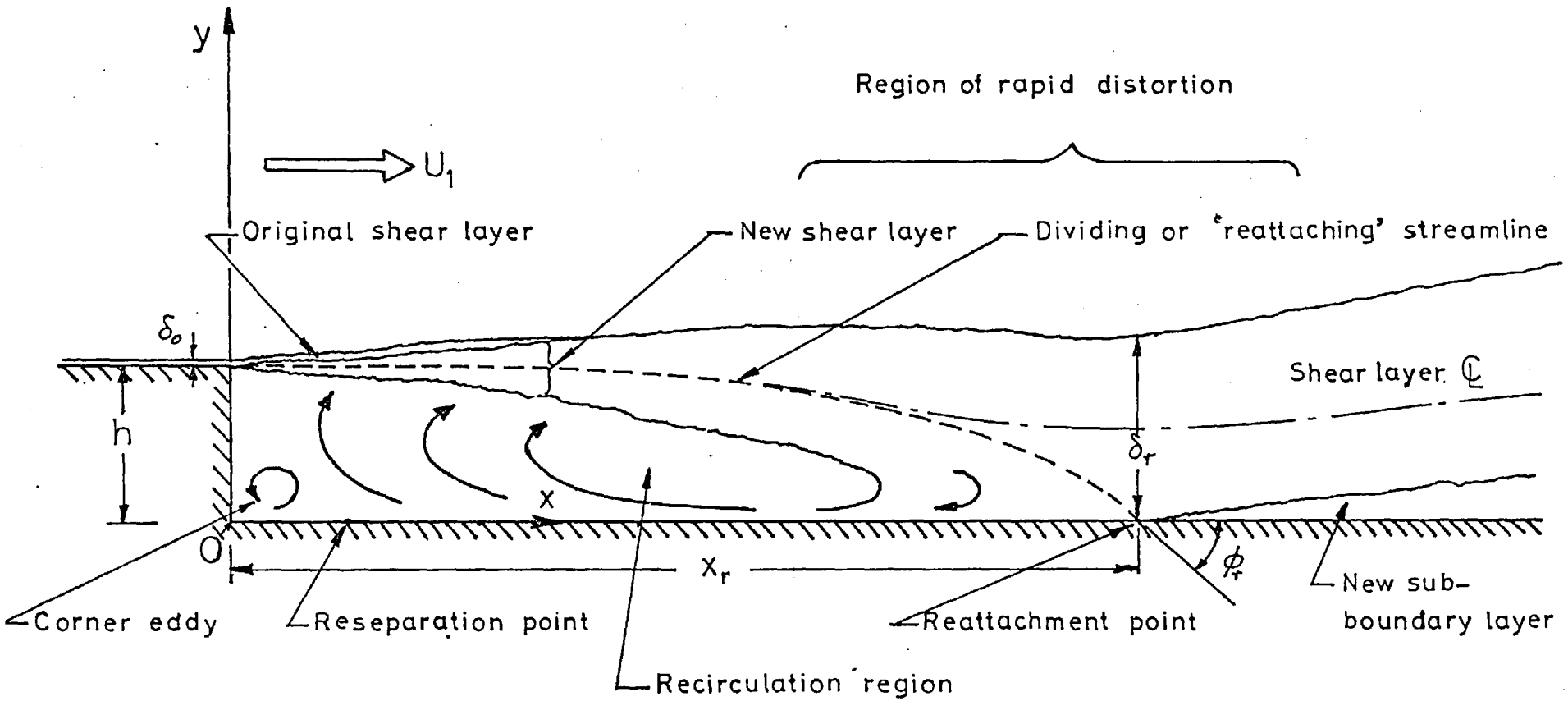
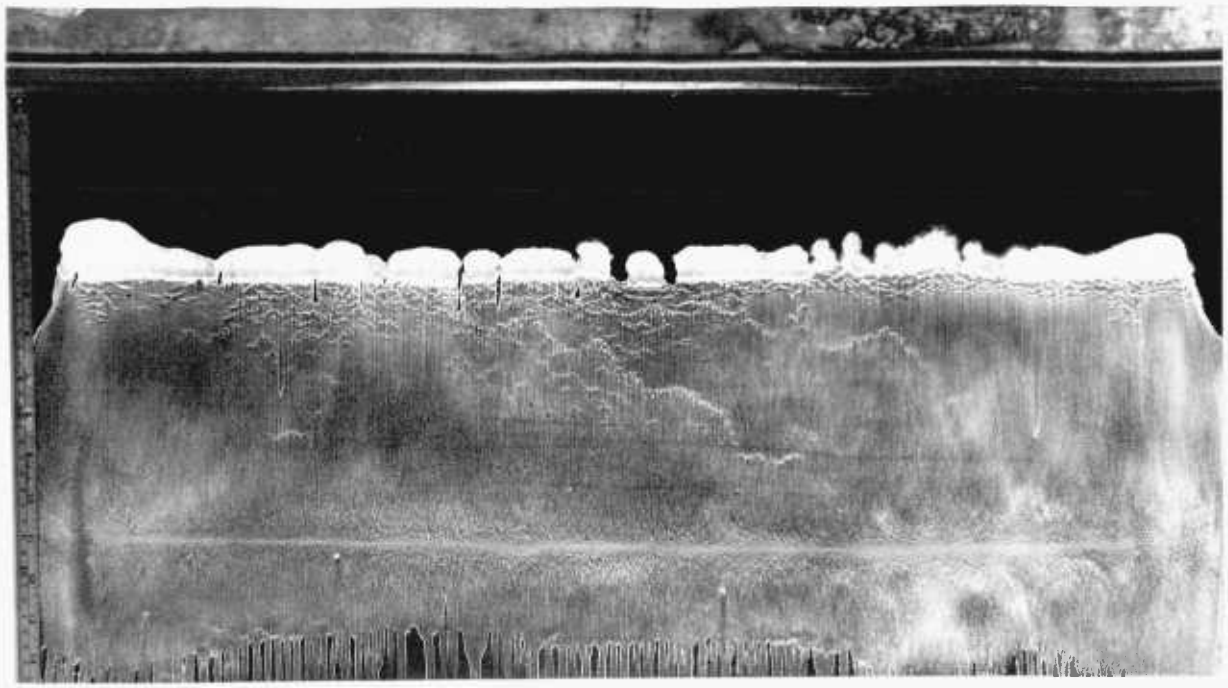


FIGURE 4.1 SKETCH OF TYPICAL REATTACHING SHEAR LAYER (Approx. half actual size)



(a) Full span

(b) Central span, also Showing approx. reseparation line.

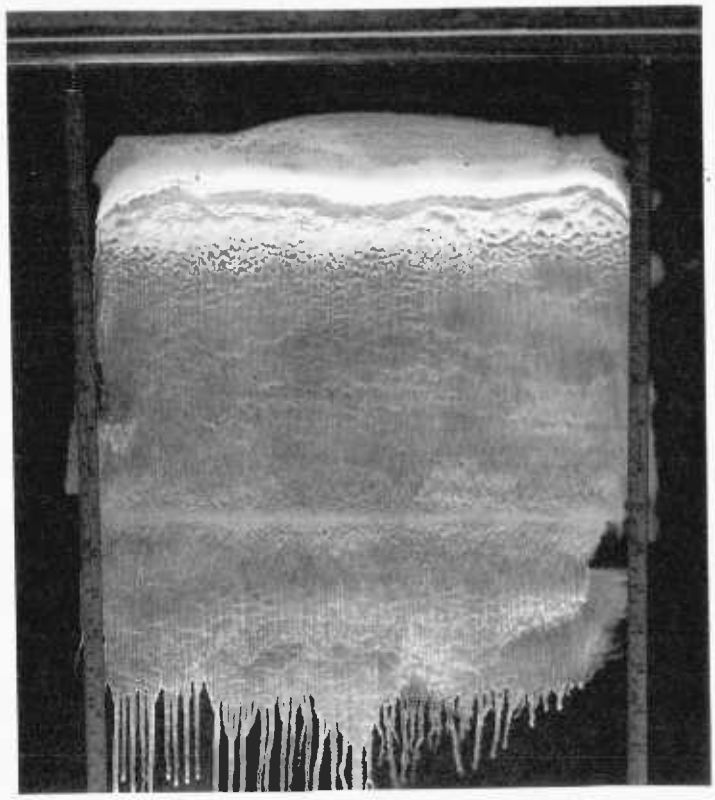


FIGURE 4.2 OIL-FLOW PHOTOGRAPHS OF REATTACHMENT LINE
(Flow from top)

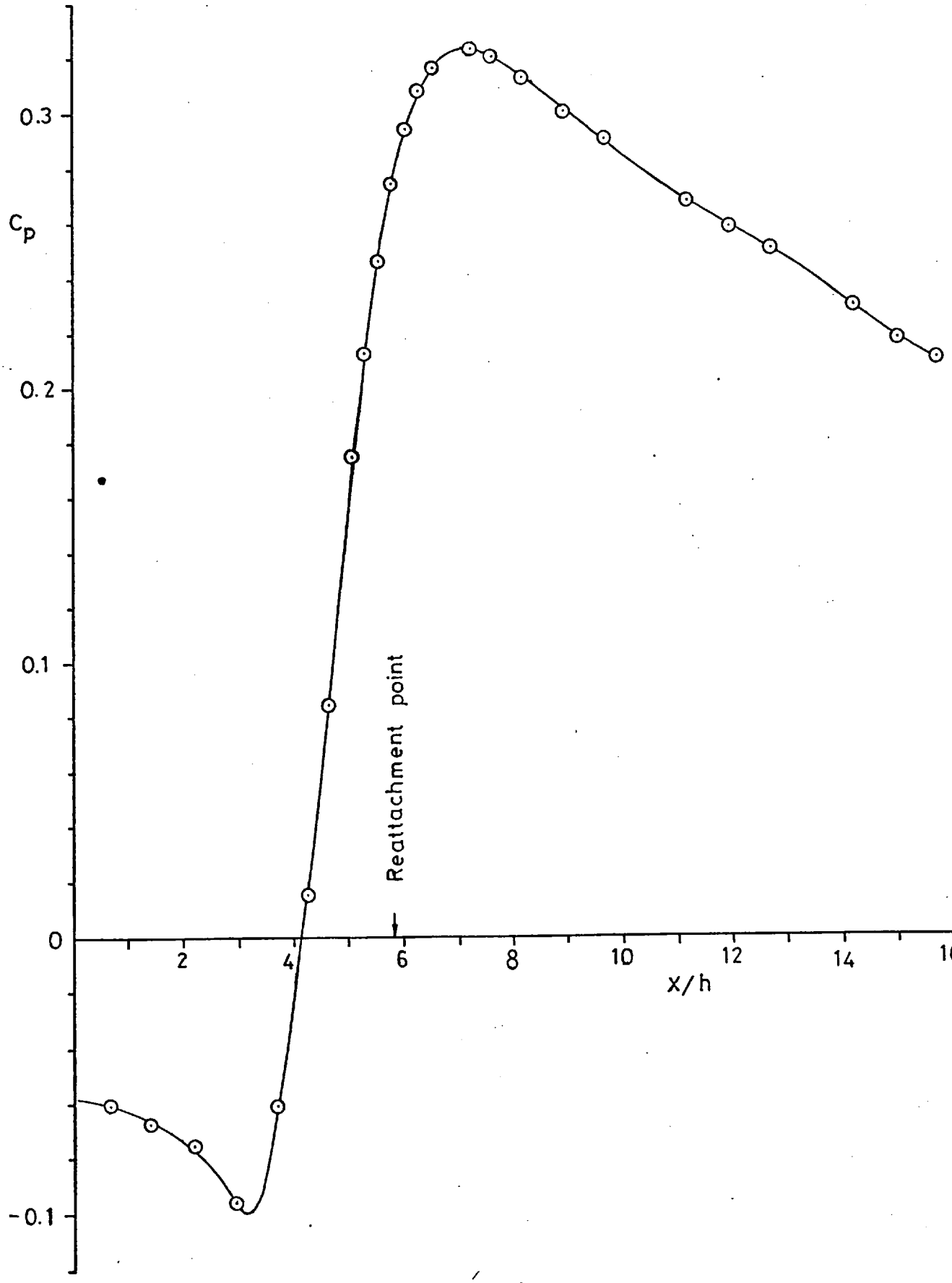


FIGURE 4.3 SURFACE PRESSURE DISTRIBUTION

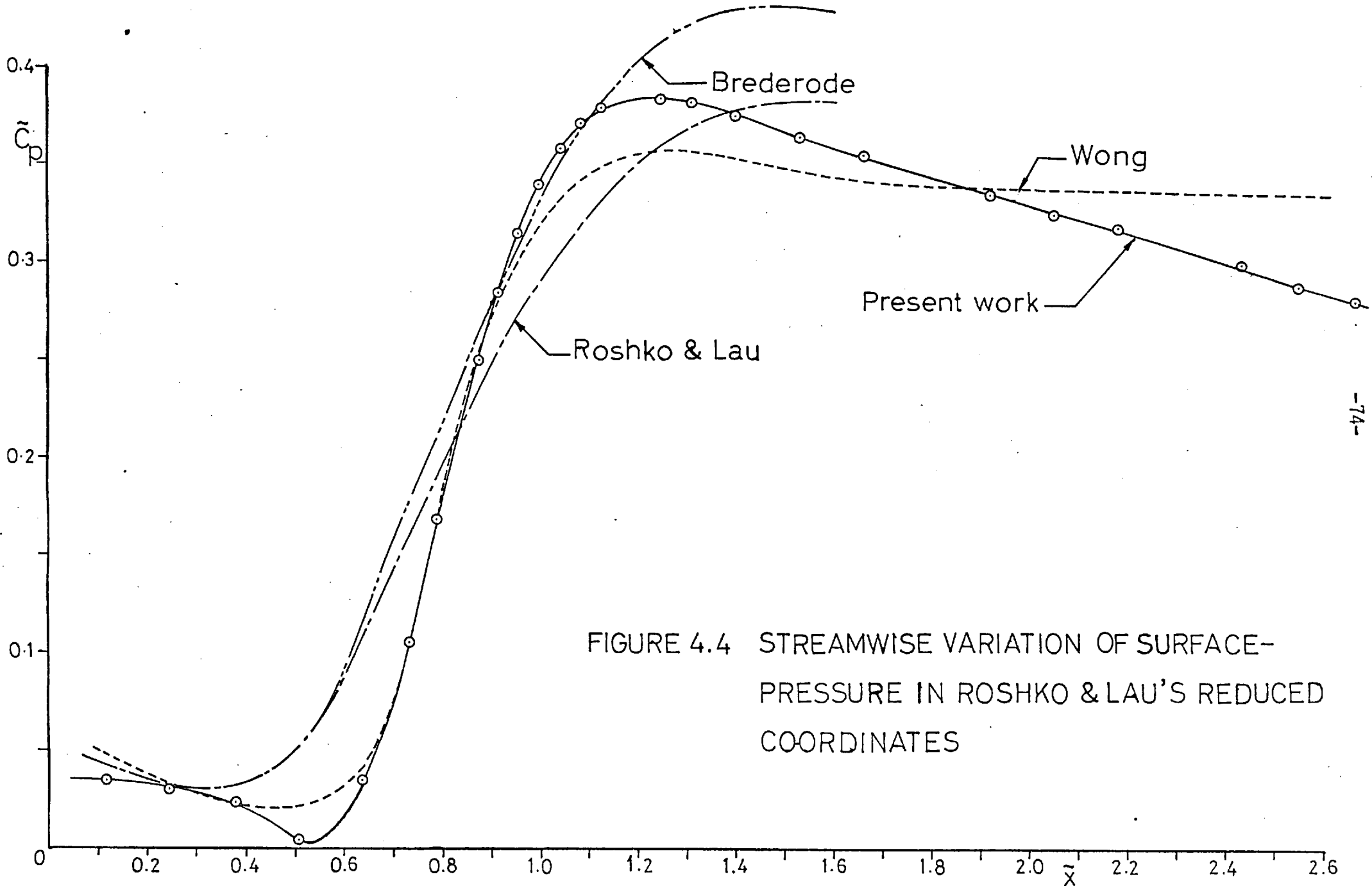


FIGURE 4.4 STREAMWISE VARIATION OF SURFACE-PRESSURE IN ROSHKO & LAU'S REDUCED COORDINATES

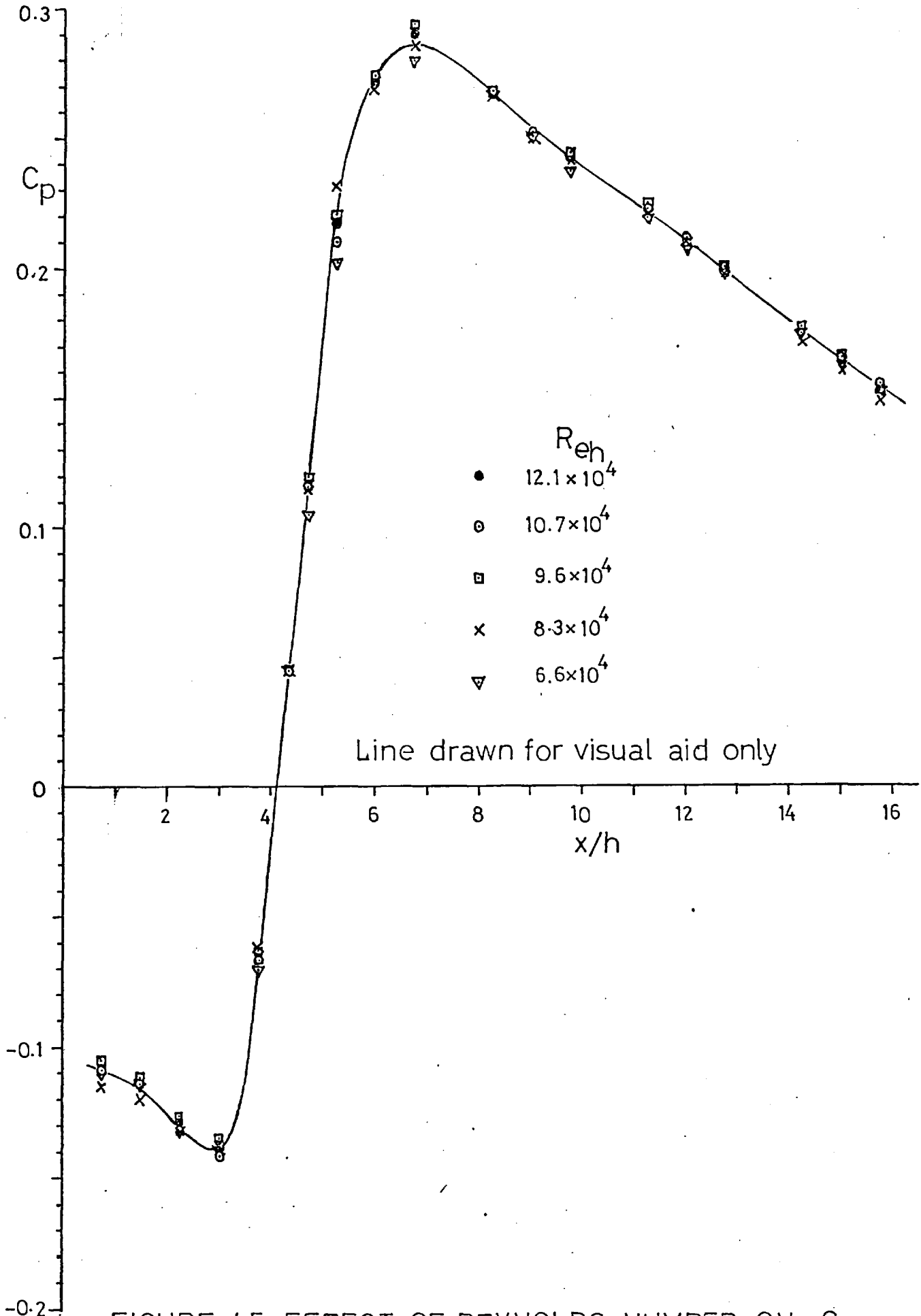


FIGURE 4.5 EFFECT OF REYNOLDS NUMBER ON C_p

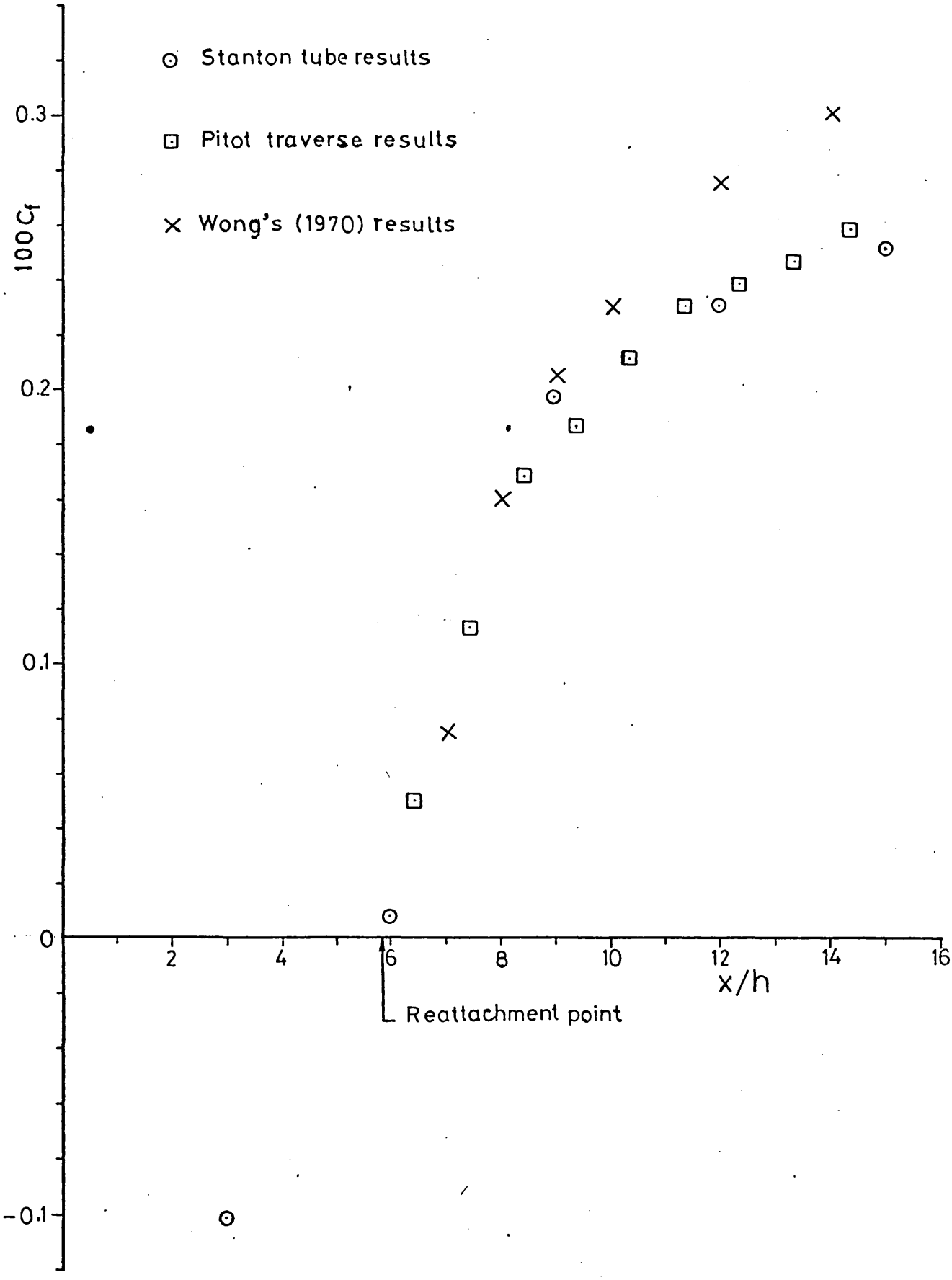


FIGURE 4.6 SKIN FRICTION COEFFICIENT

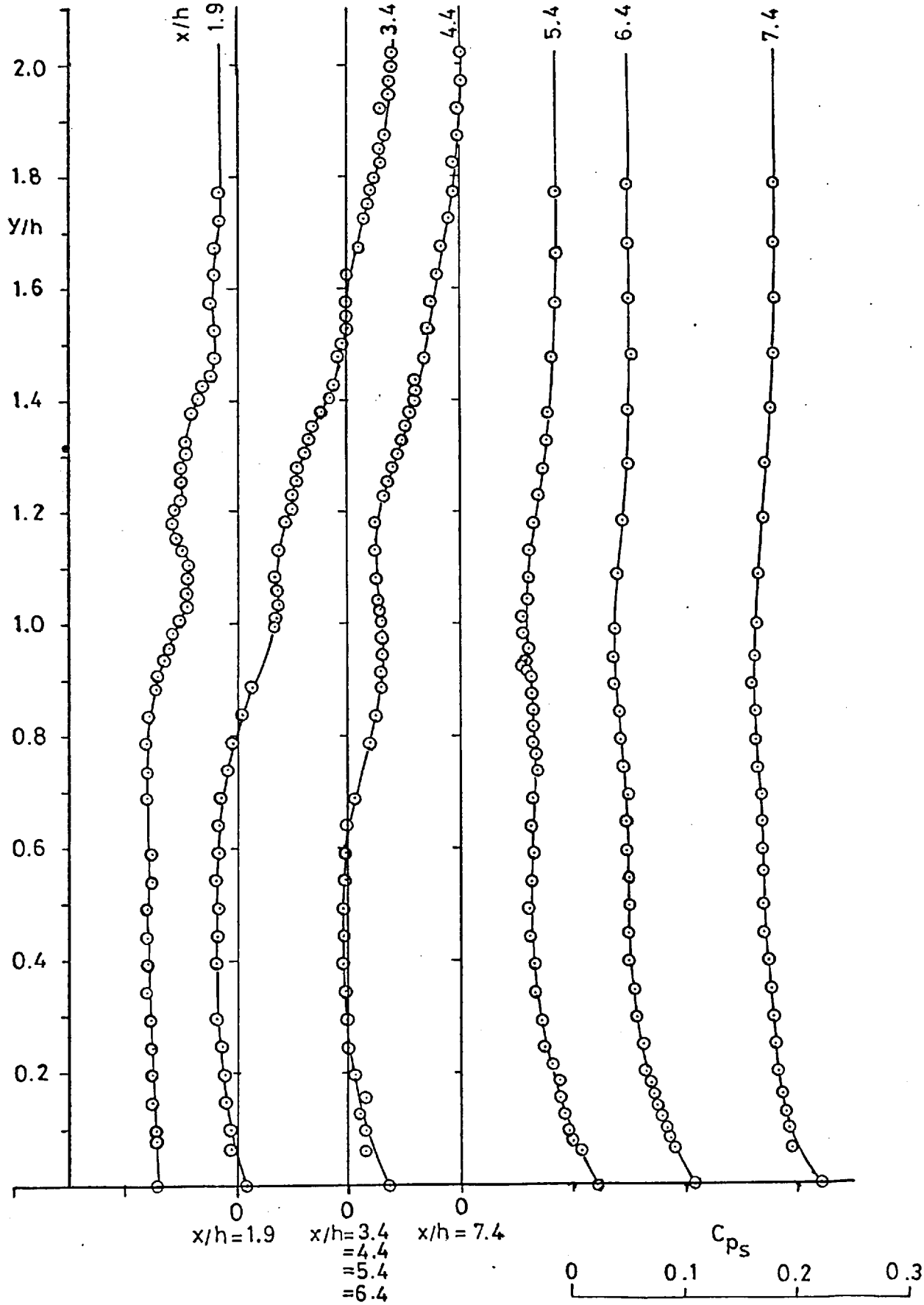


FIGURE 4.7(a) TRANSVERSE VARIATION OF STATIC PRESSURE

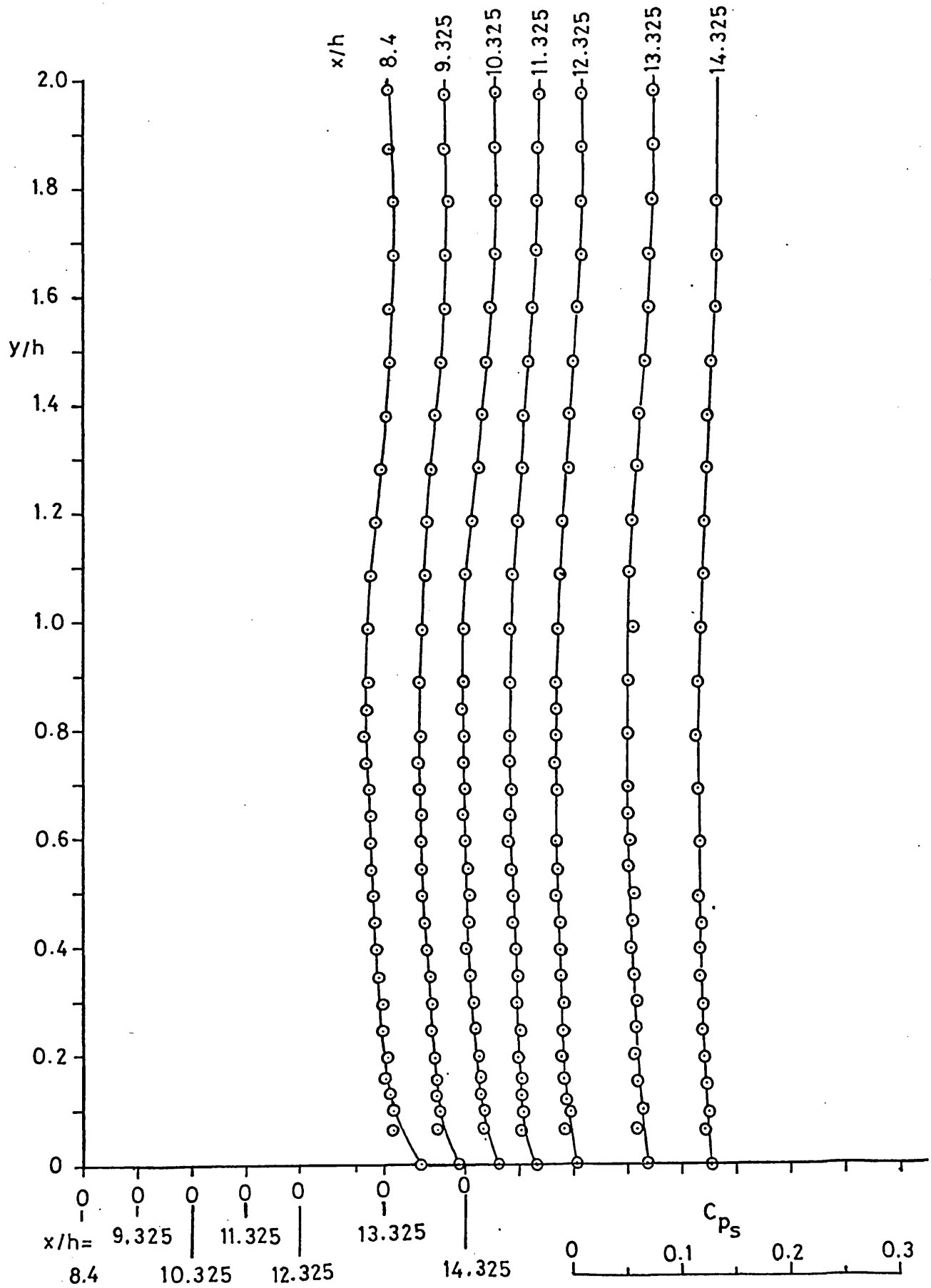


FIGURE 4.7(b) TRANSVERSE VARIATION OF STATIC PRESSURE

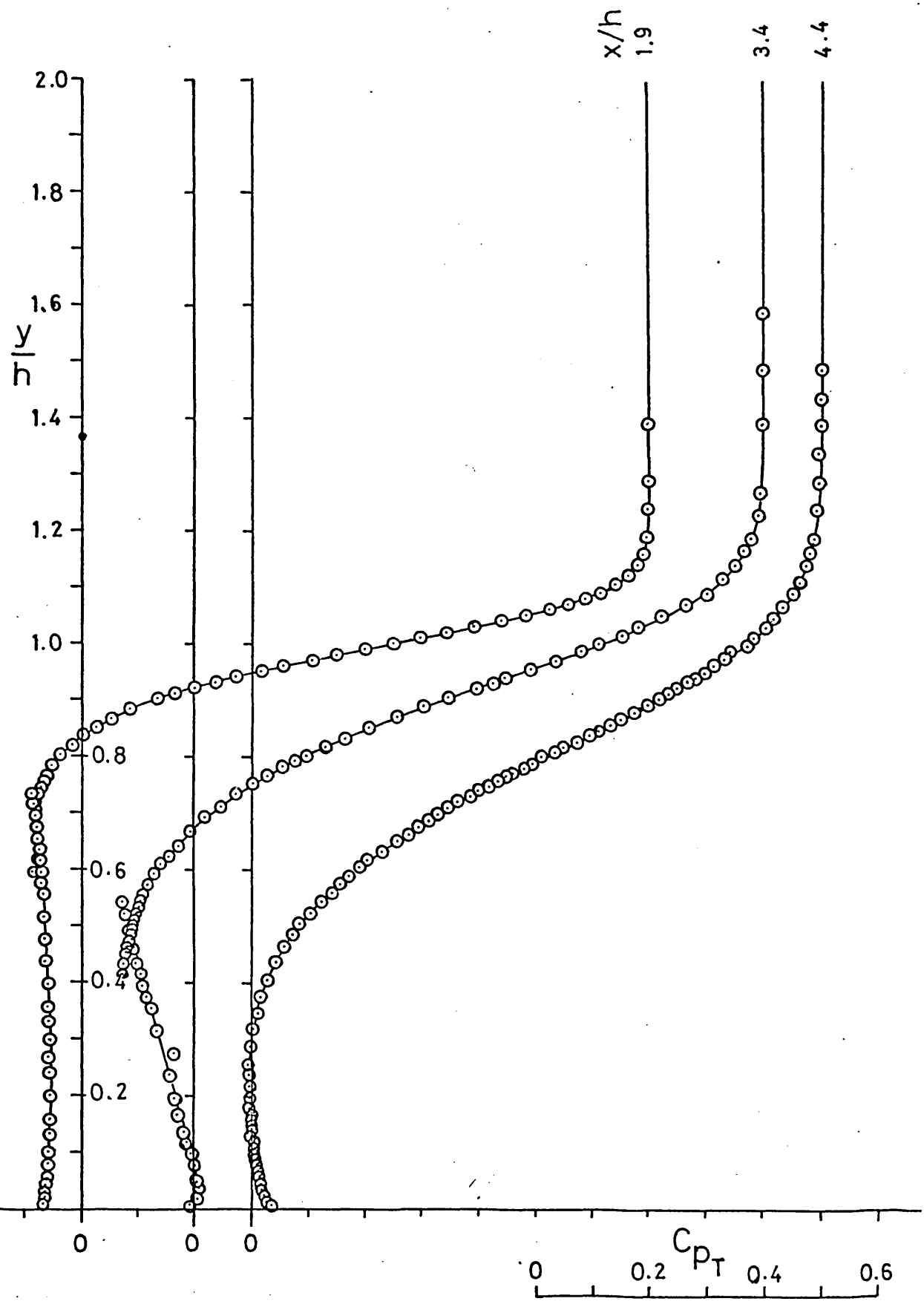


FIGURE 4.8(a) TOTAL PRESSURE PROFILES

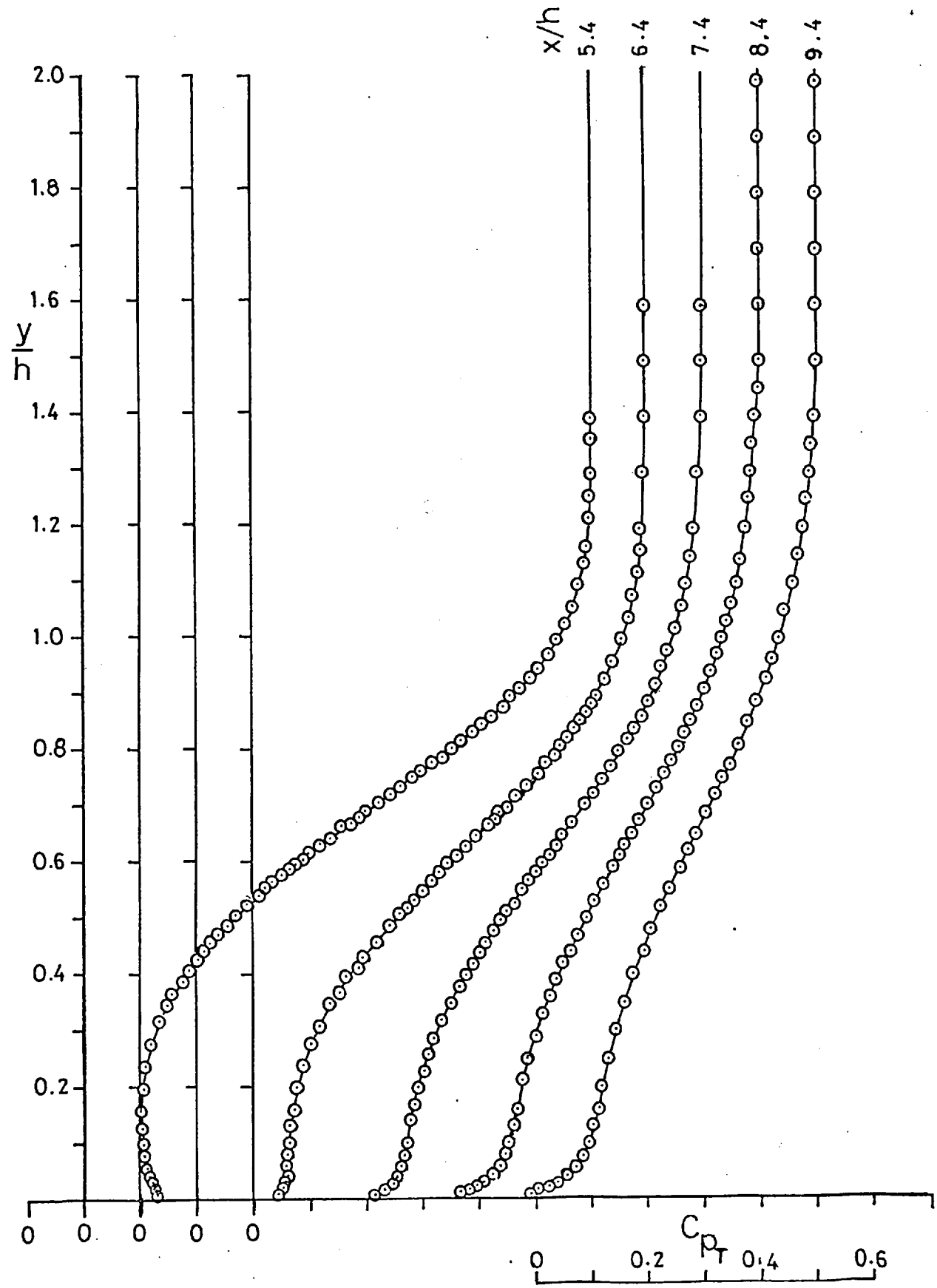


FIGURE 4.8(b) TOTAL PRESSURE PROFILES

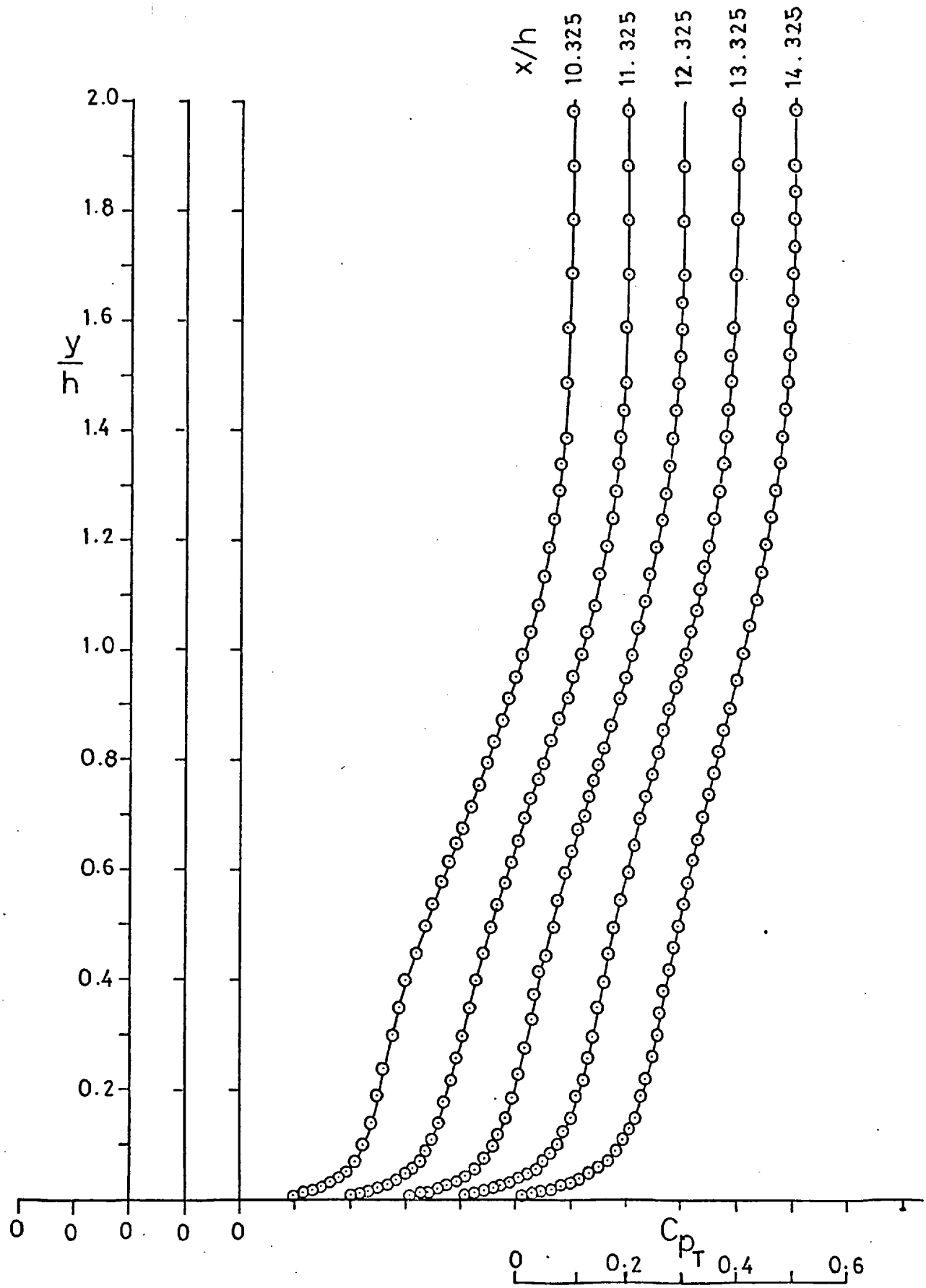


FIGURE 4.8(c) TOTAL PRESSURE PROFILES

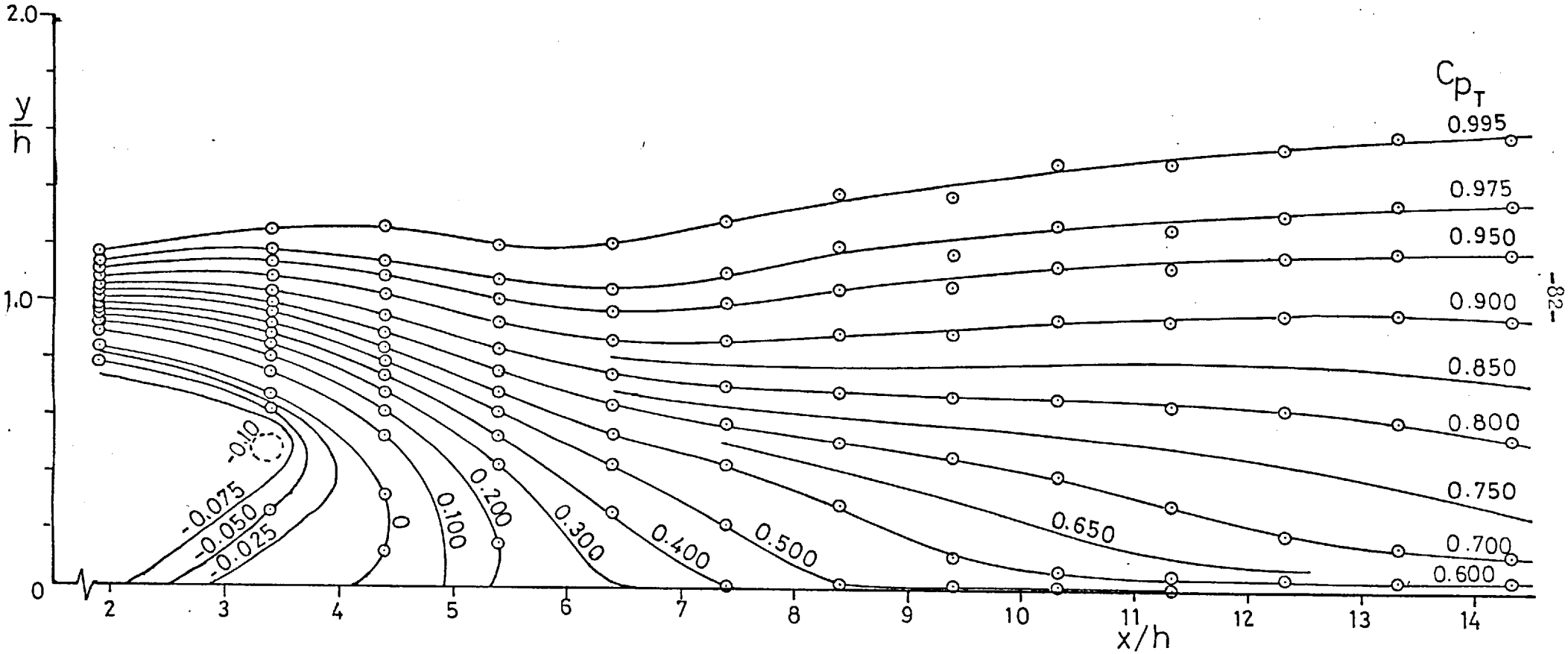


FIGURE 4.9 CONTOUR PLOT OF TOTAL PRESSURE COEFFICIENT, $C_{P_T} = \frac{P - P_{ref}}{(P-p)_{ref}}$

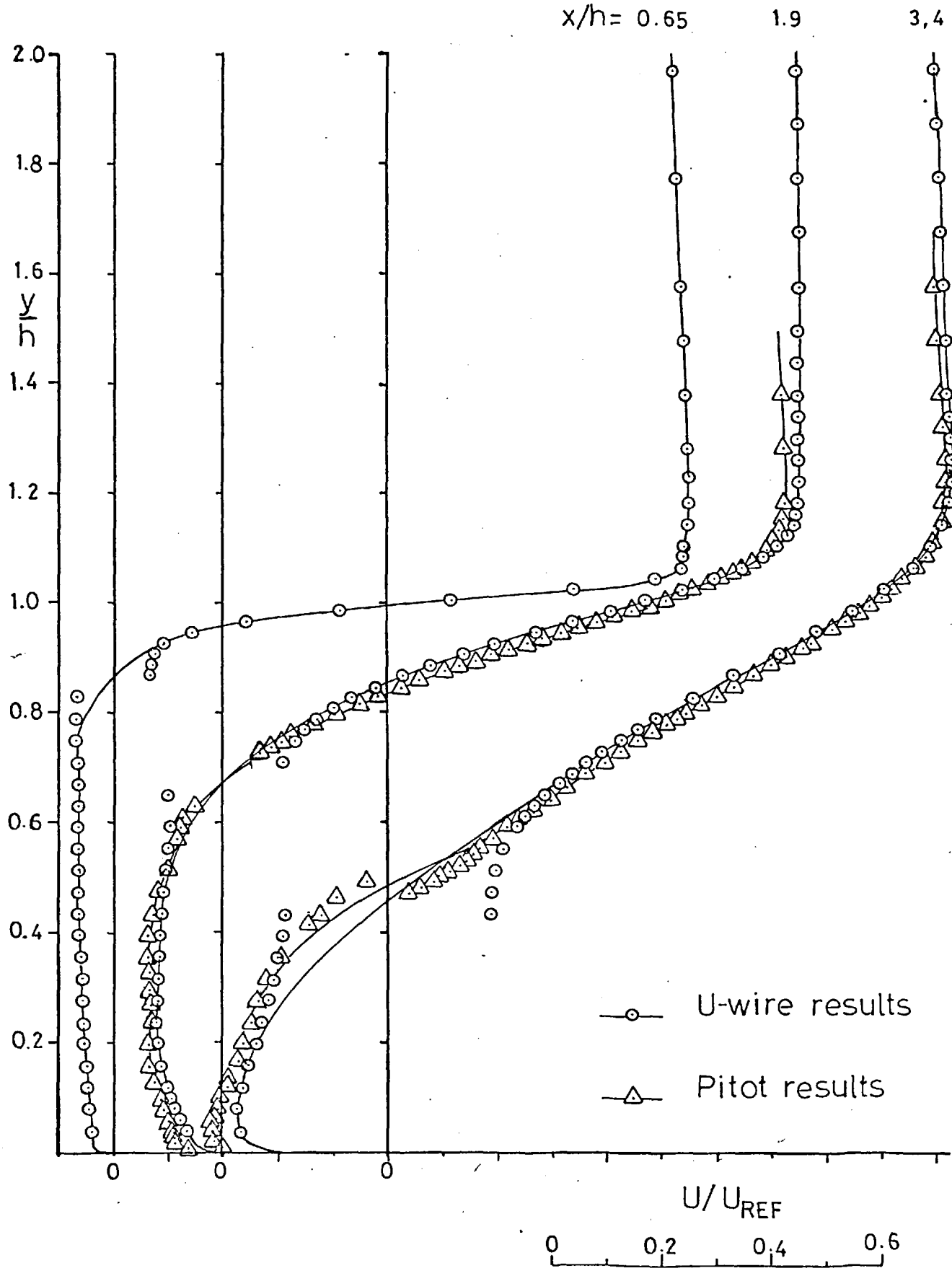


FIGURE 4.10(a) MEAN VELOCITY PROFILES

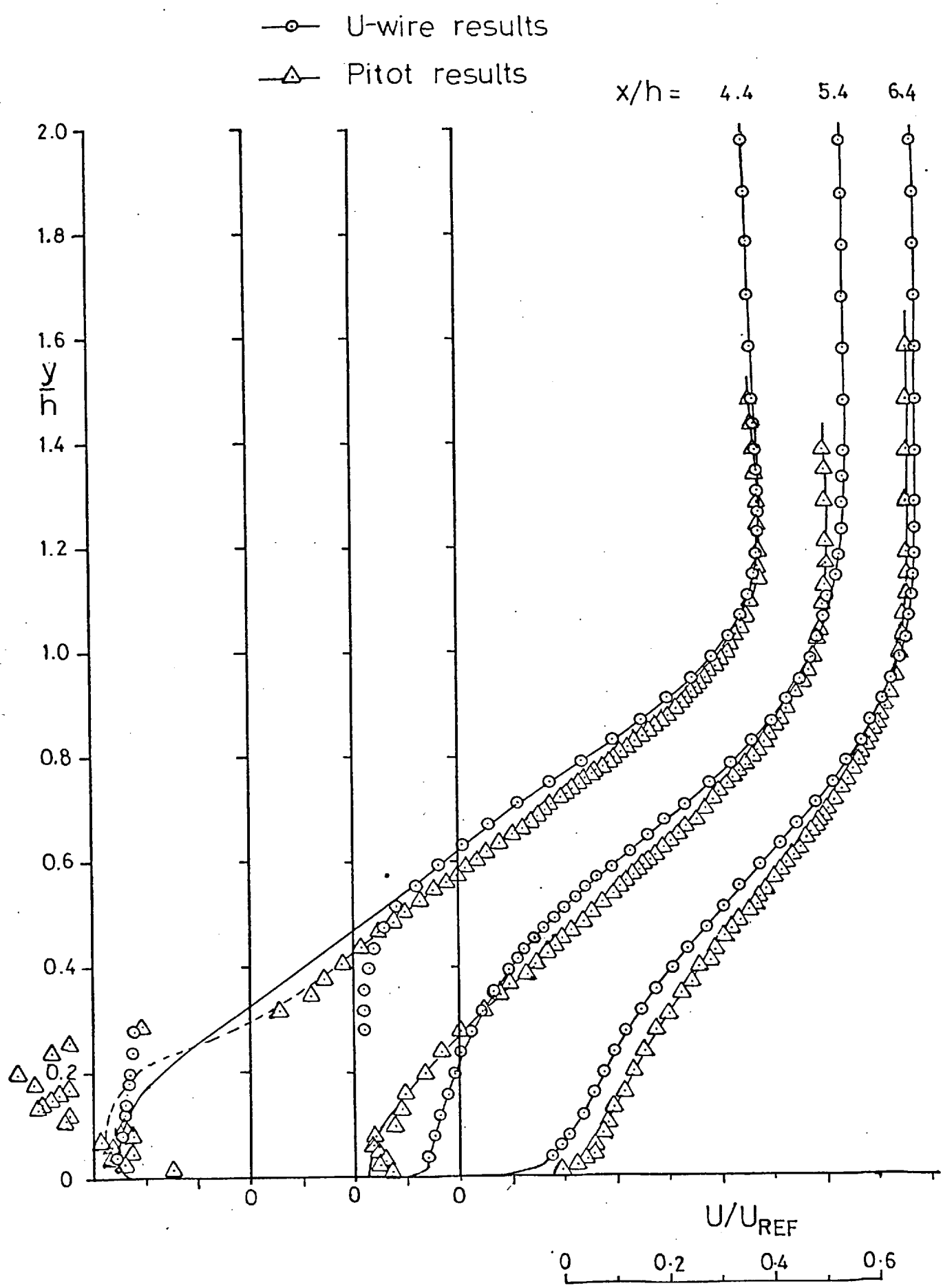


FIGURE 4.10(b) MEAN VELOCITY PROFILES

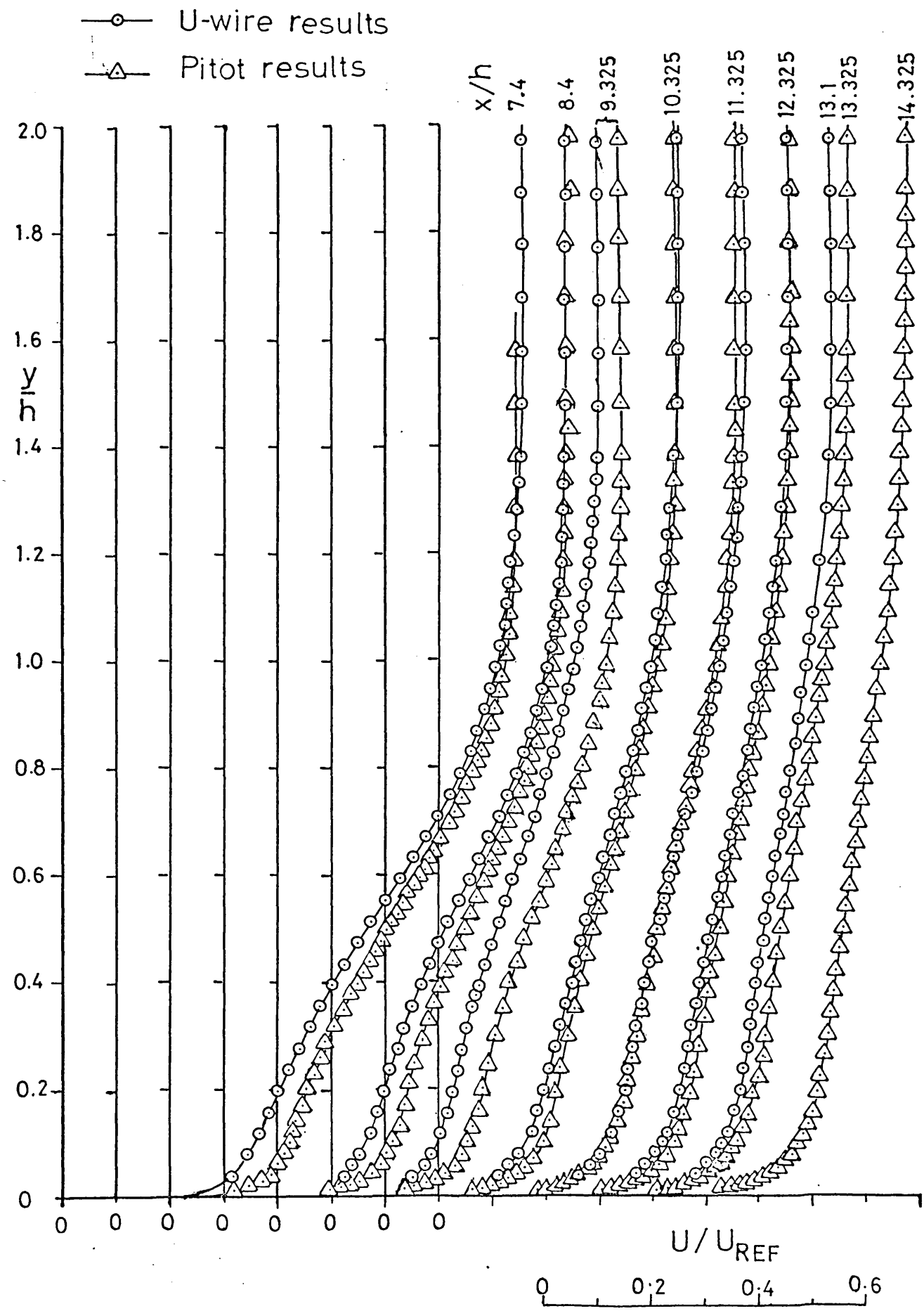


FIGURE 4.10(c) MEAN VELOCITY PROFILES

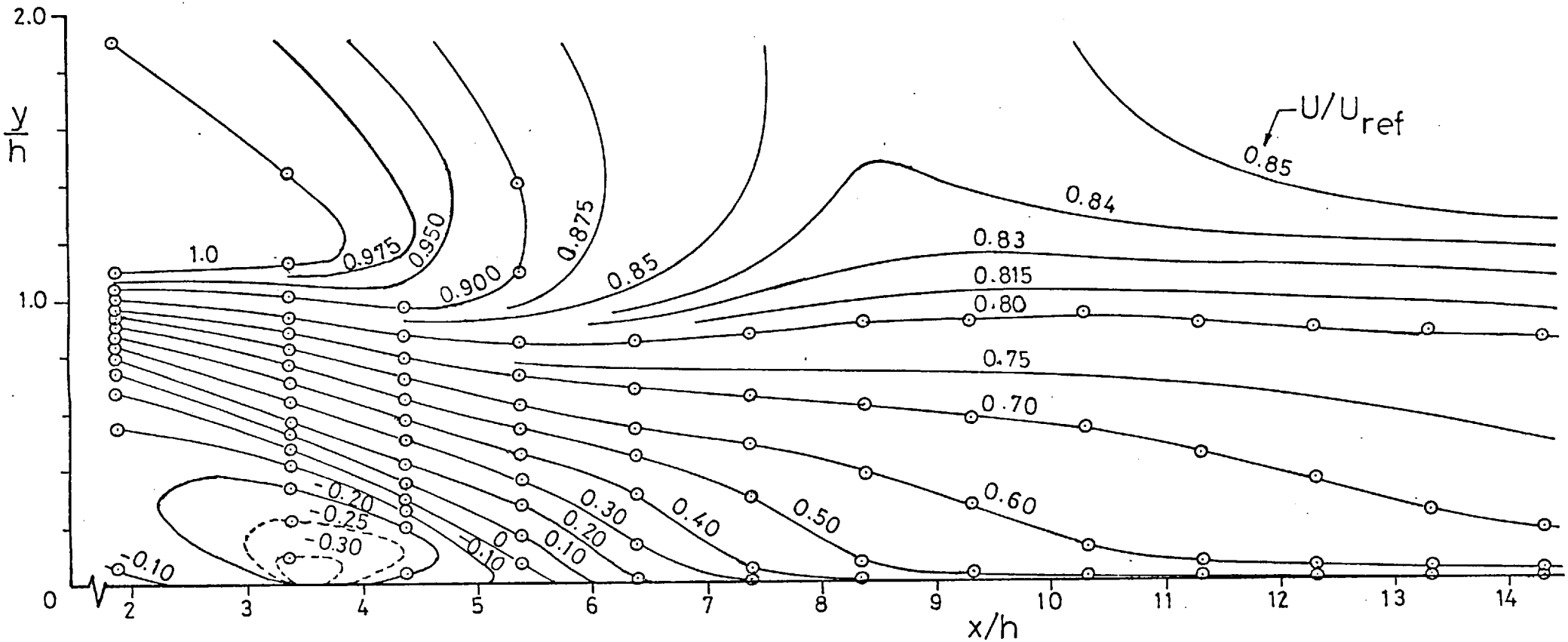


FIGURE 4.11 CONTOUR PLOT OF U/U_{ref} FROM PITOT RESULTS

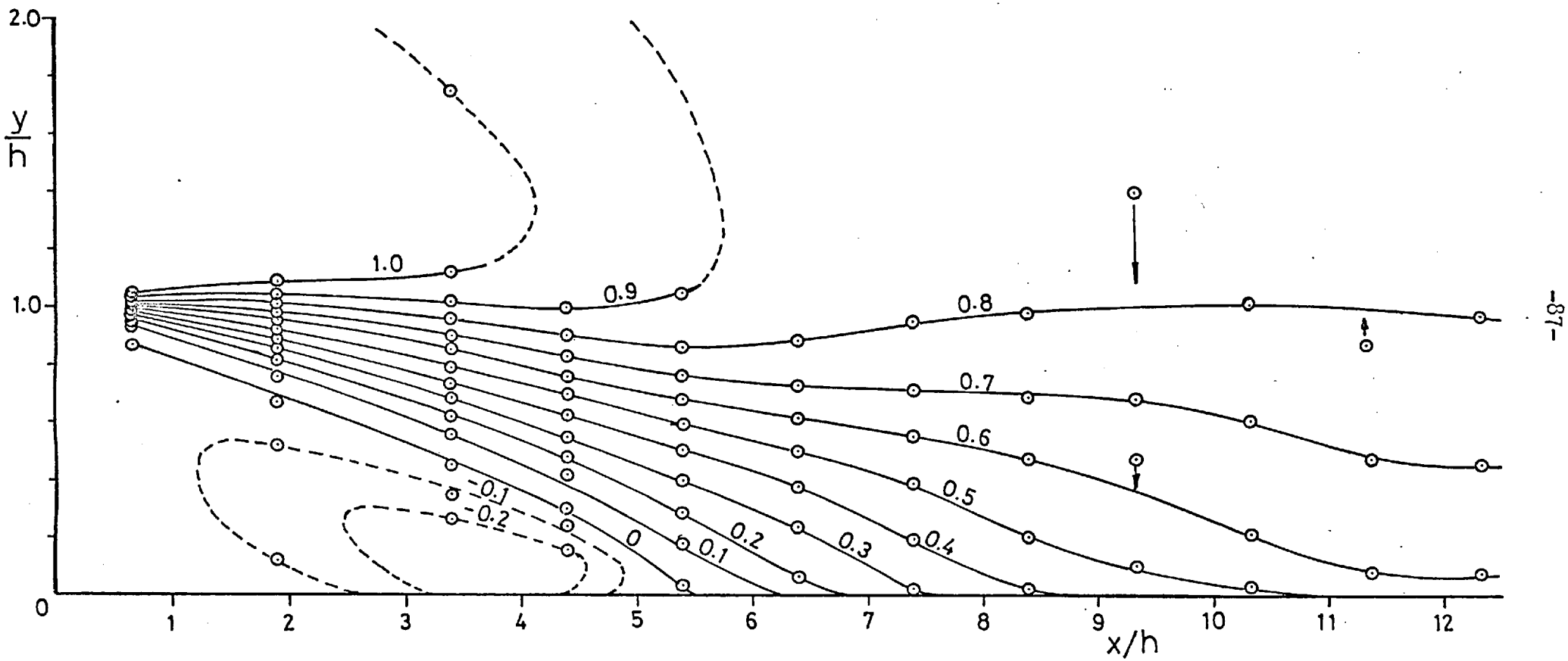
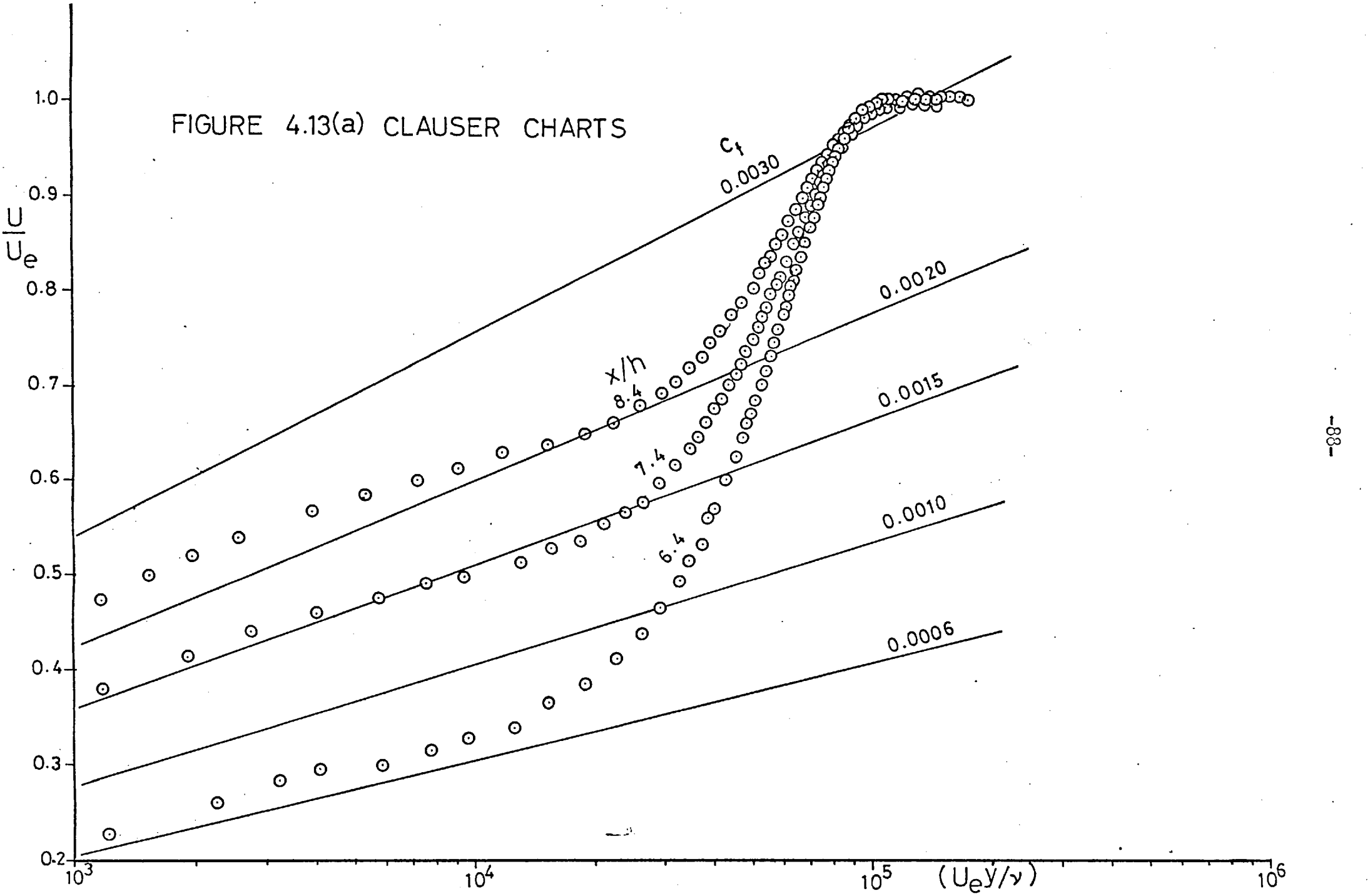


FIGURE 4.12 CONTOUR PLOT OF U/U_{ref} FROM U-WIRE RESULTS


FIGURE 4.13(a) CLAUSER CHARTS
$\frac{U}{U_e}$
1.0
0.9
0.8
0.7
0.6
0.5
0.4
0.3
0.2
c_f
0.0030
0.0020
0.0015
0.0010
0.0006
x/h
8.4
7.4
6.4
10^3
10^4
10^5
10^6
$(U_e y/\nu)$

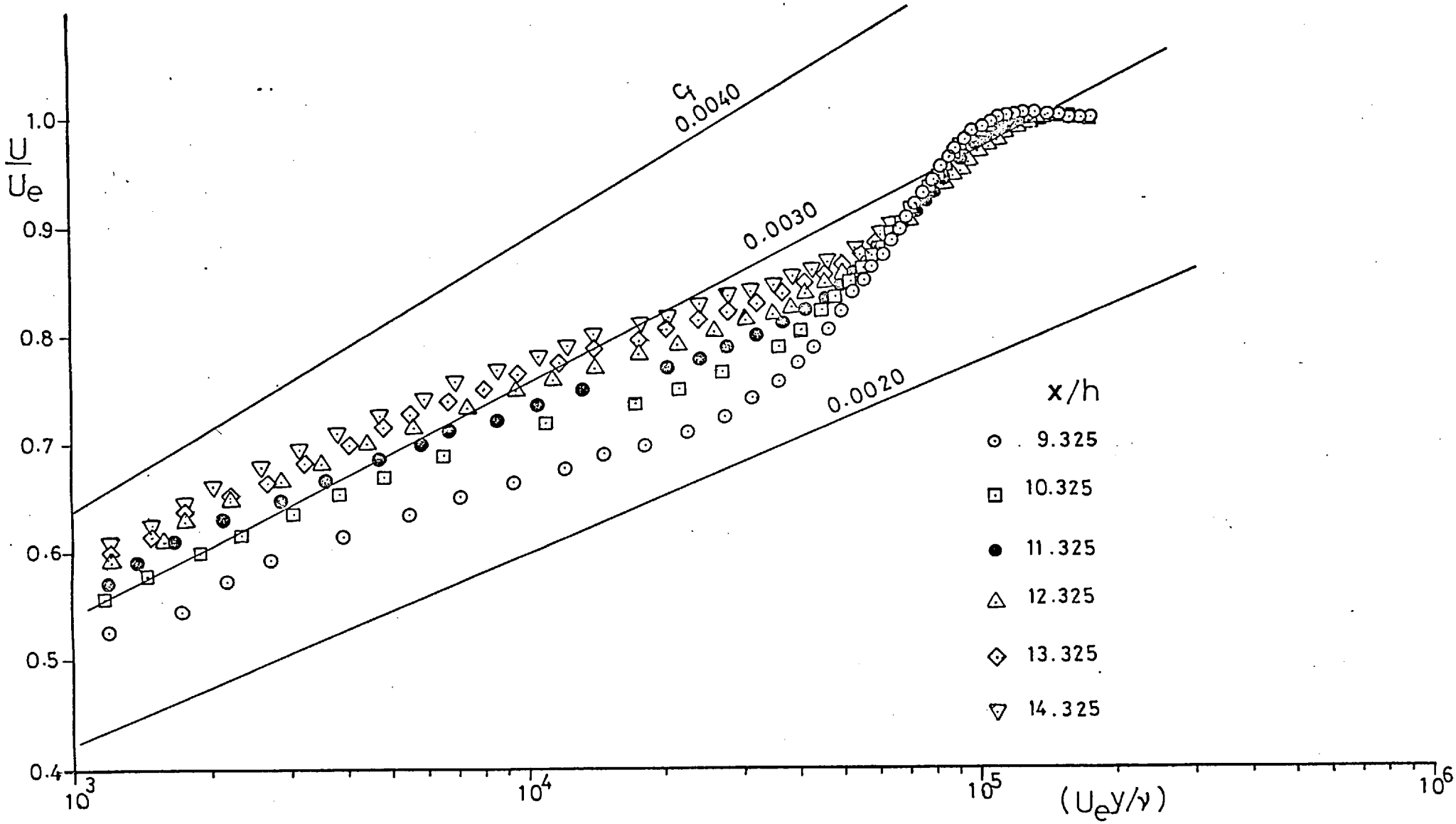


FIGURE 4.13(b) CLAUSER CHARTS

FIGURE 4.14(a) SEMI-LOGARITHMIC PLOT OF MEAN VELOCITY PROFILES

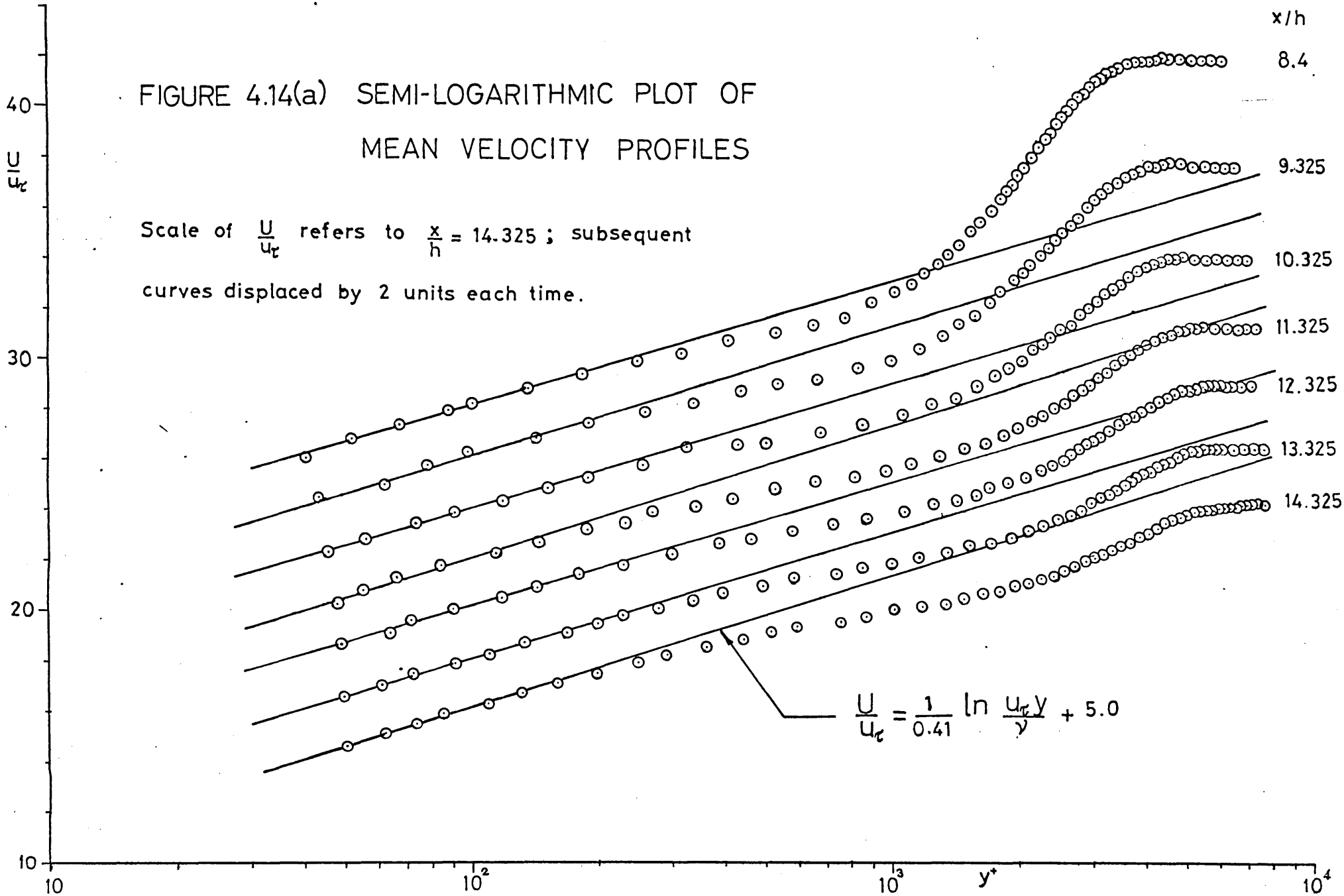
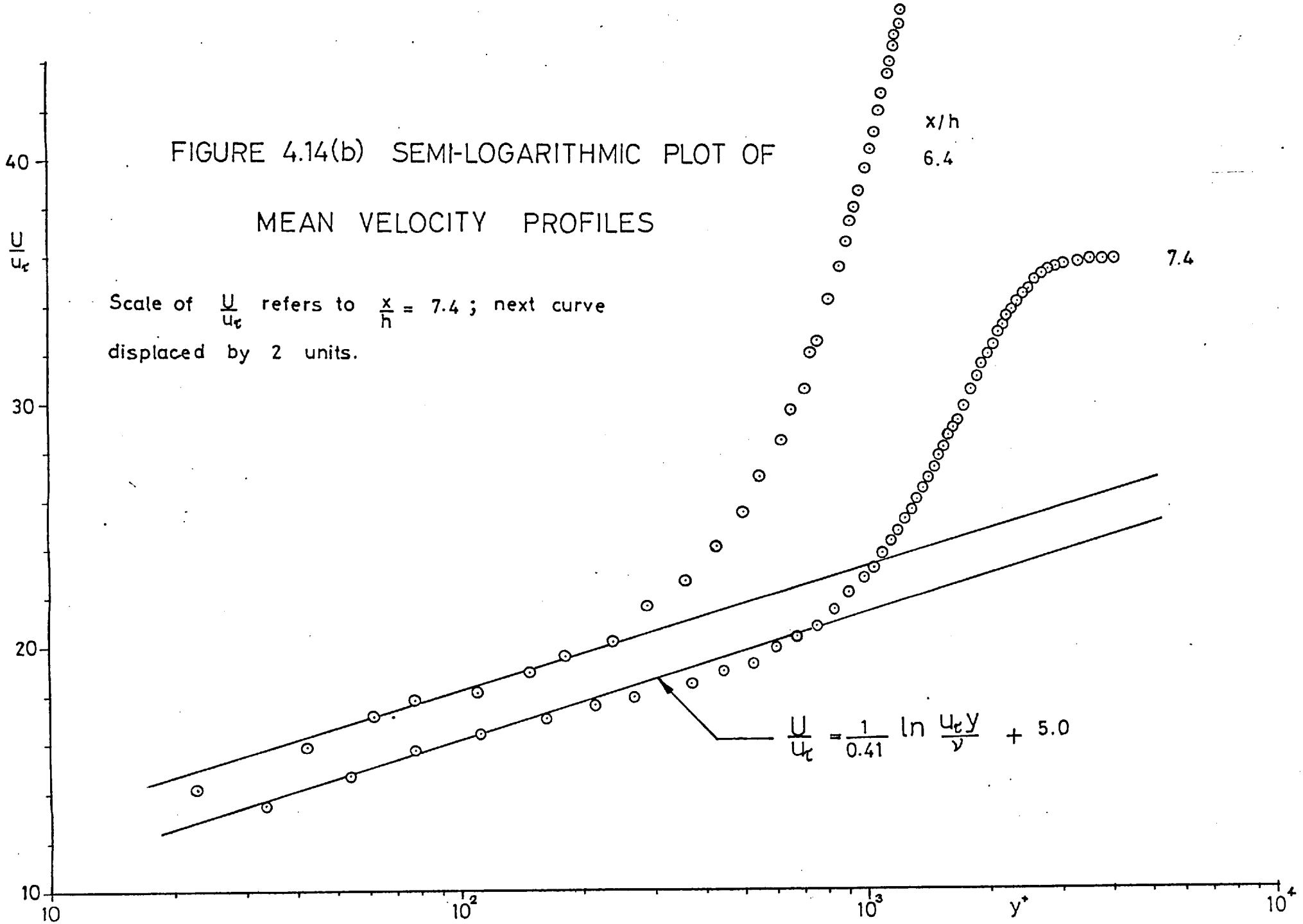


FIGURE 4.14(b) SEMI-LOGARITHMIC PLOT OF MEAN VELOCITY PROFILES

Scale of $\frac{U}{u_\tau}$ refers to $\frac{x}{h}$ = 7.4 ; next curve displaced by 2 units.



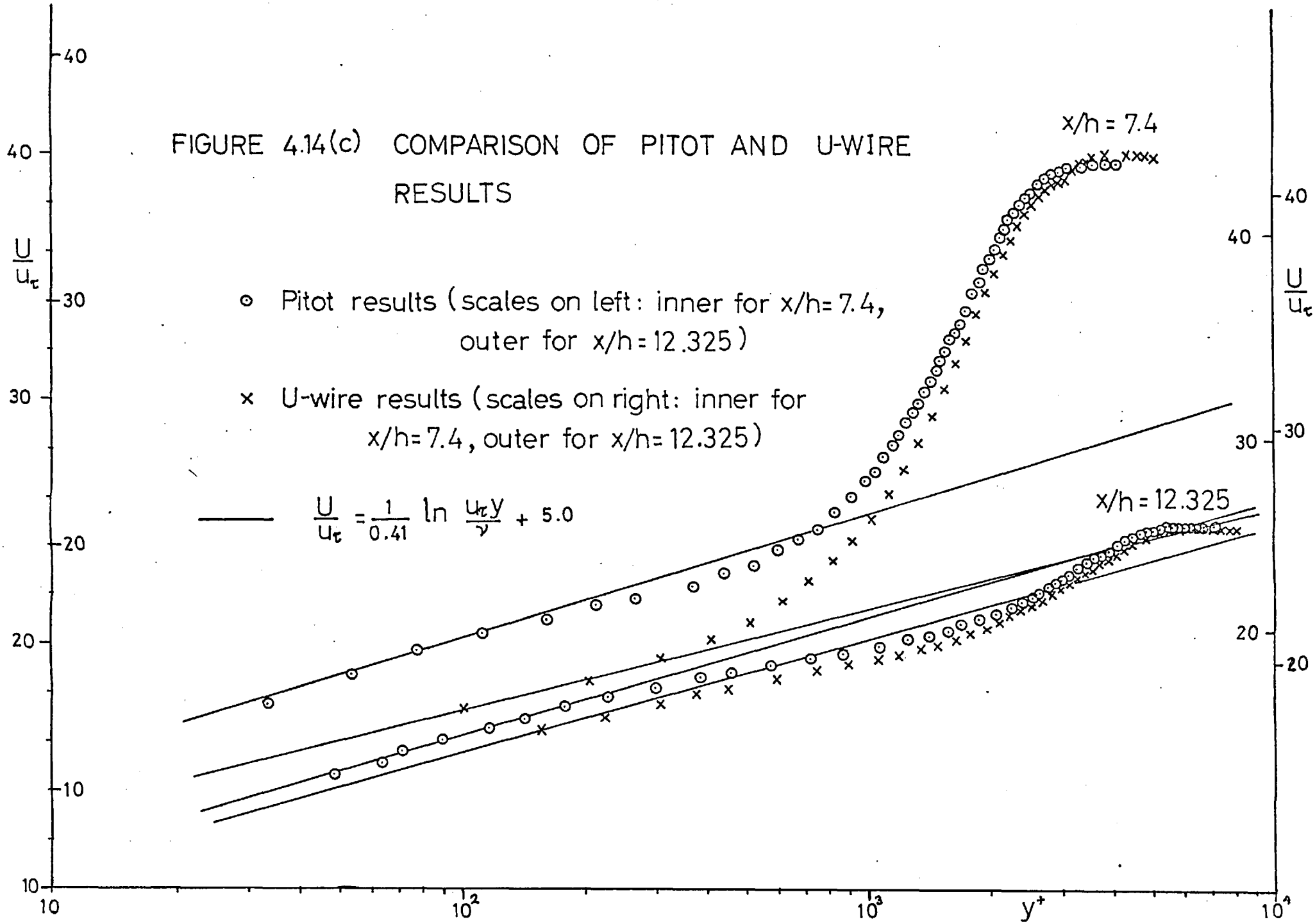

FIGURE 4.14(c) COMPARISON OF PITOT AND U-WIRE RESULTS
⊙ Pitot results (scales on left: inner for x/h= 7.4, outer for x/h = 12.325)
× U-wire results (scales on right: inner for x/h= 7.4, outer for x/h= 12.325)
$\frac{U}{u_\tau} = \frac{1}{0.41} \ln \frac{u_\tau y}{\nu} + 5.0$
x/h = 7.4
x/h = 12.325
$\frac{U}{u_\tau}$
y^+
10
10^2
10^3
10^4
20
30
40

FIGURE 4.15 COLLECTIVE PLOT OF SEMI-LOGARITHMIC VELOCITY PROFILES

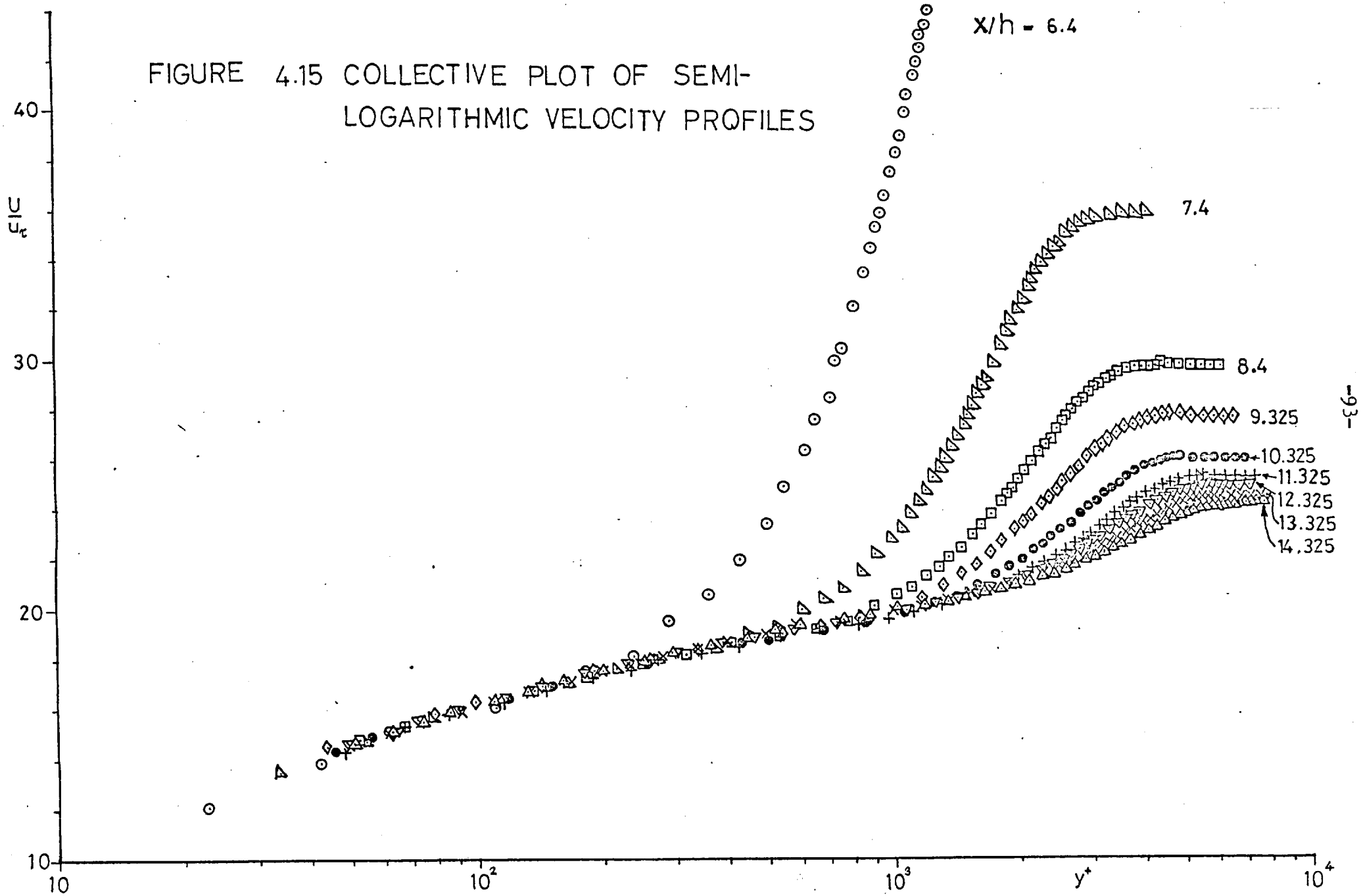


FIGURE 4.16(a) TEMPERATURE PROFILES DOWNSTREAM OF HEATED WIRE

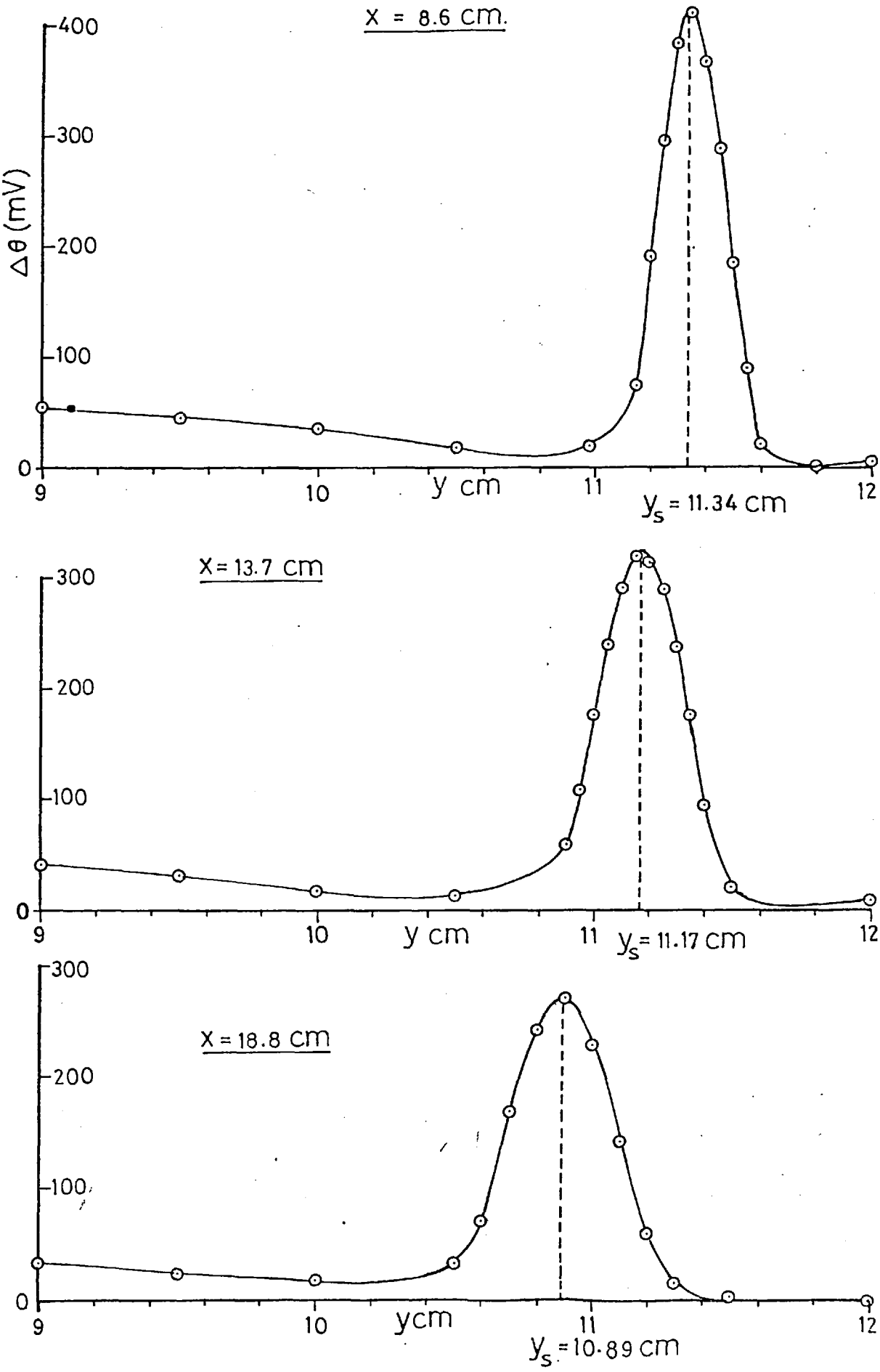


FIGURE 4.16(b) TEMPERATURE PROFILES DOWNSTREAM OF HEATED WIRE

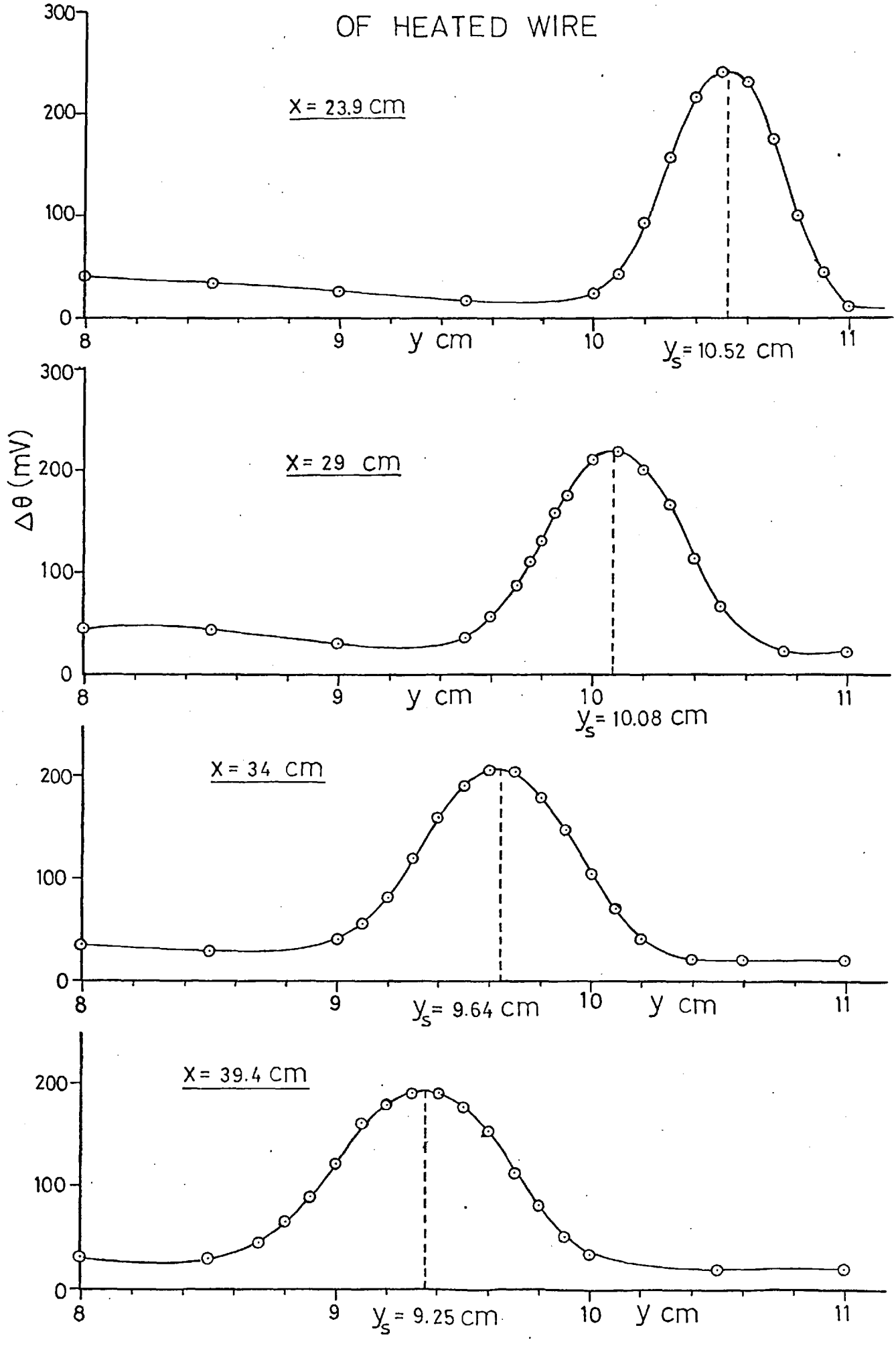
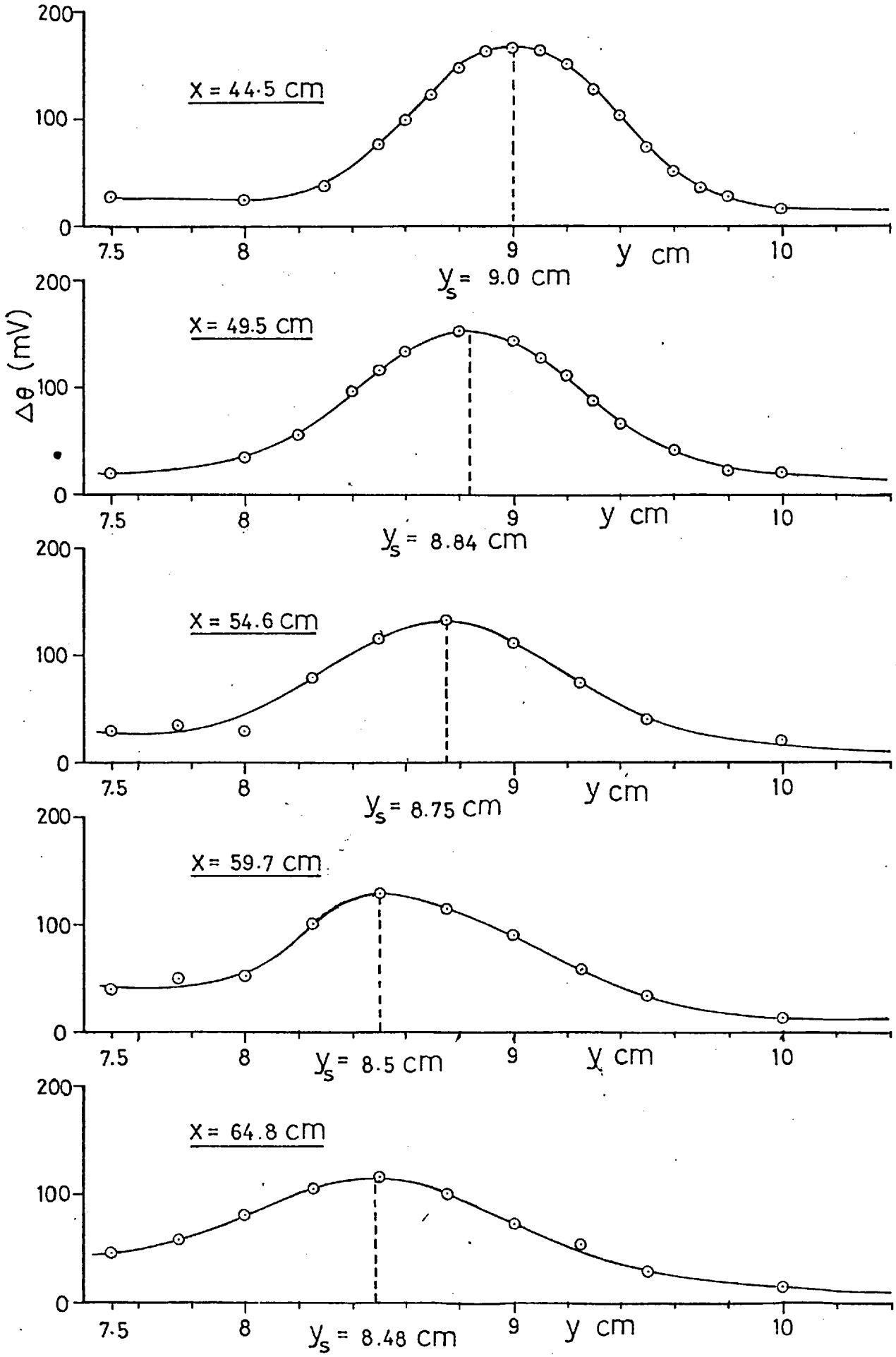


FIGURE 4.16(c) TEMPERATURE PROFILES DOWNSTREAM OF HEATED WIRE



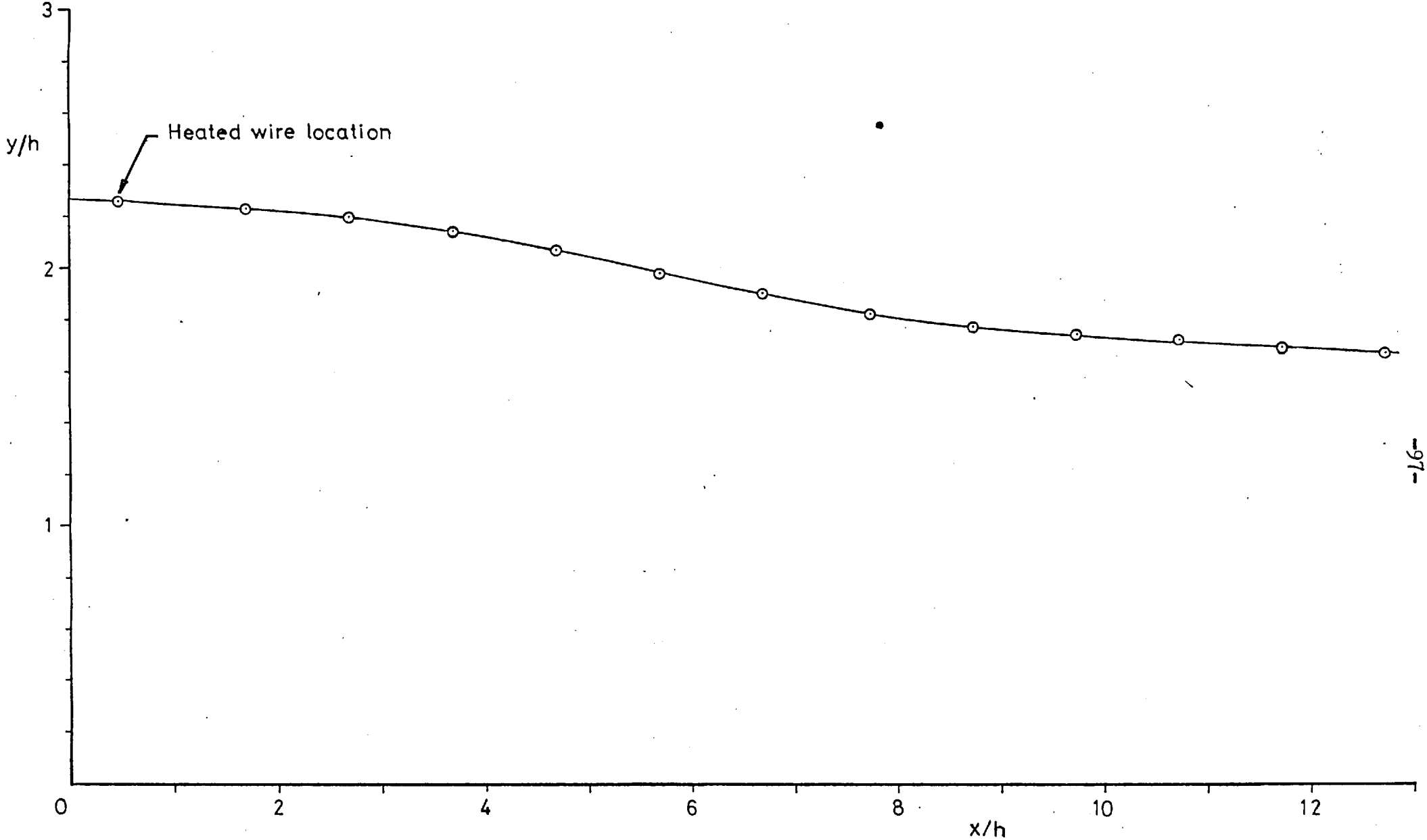


FIGURE 4.17 REFERENCE MEAN STREAMLINE

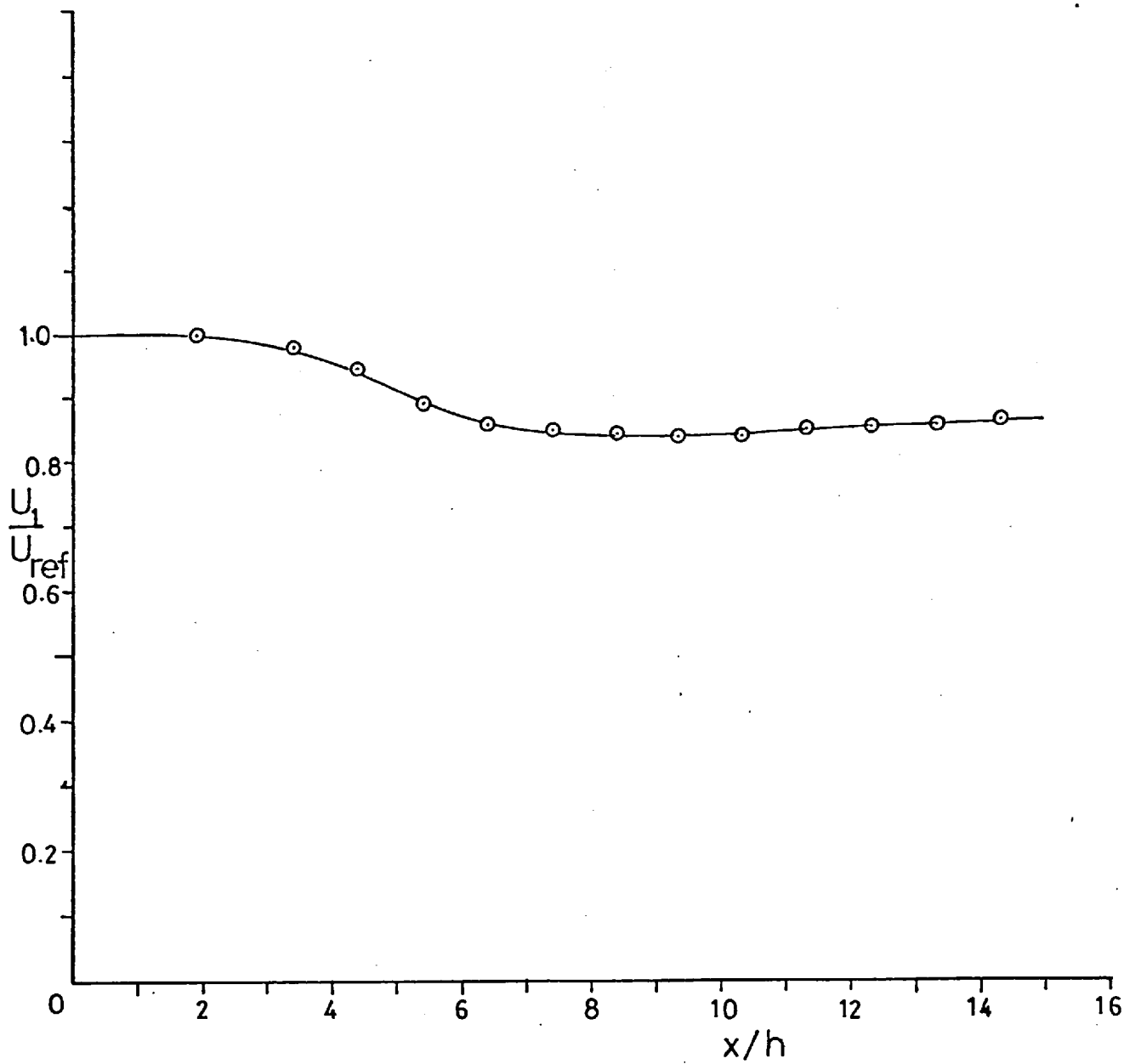


FIGURE 4.18 STREAMWISE VARIATION OF EXTERNAL STREAM VELOCITY AT $y = 1.8h$

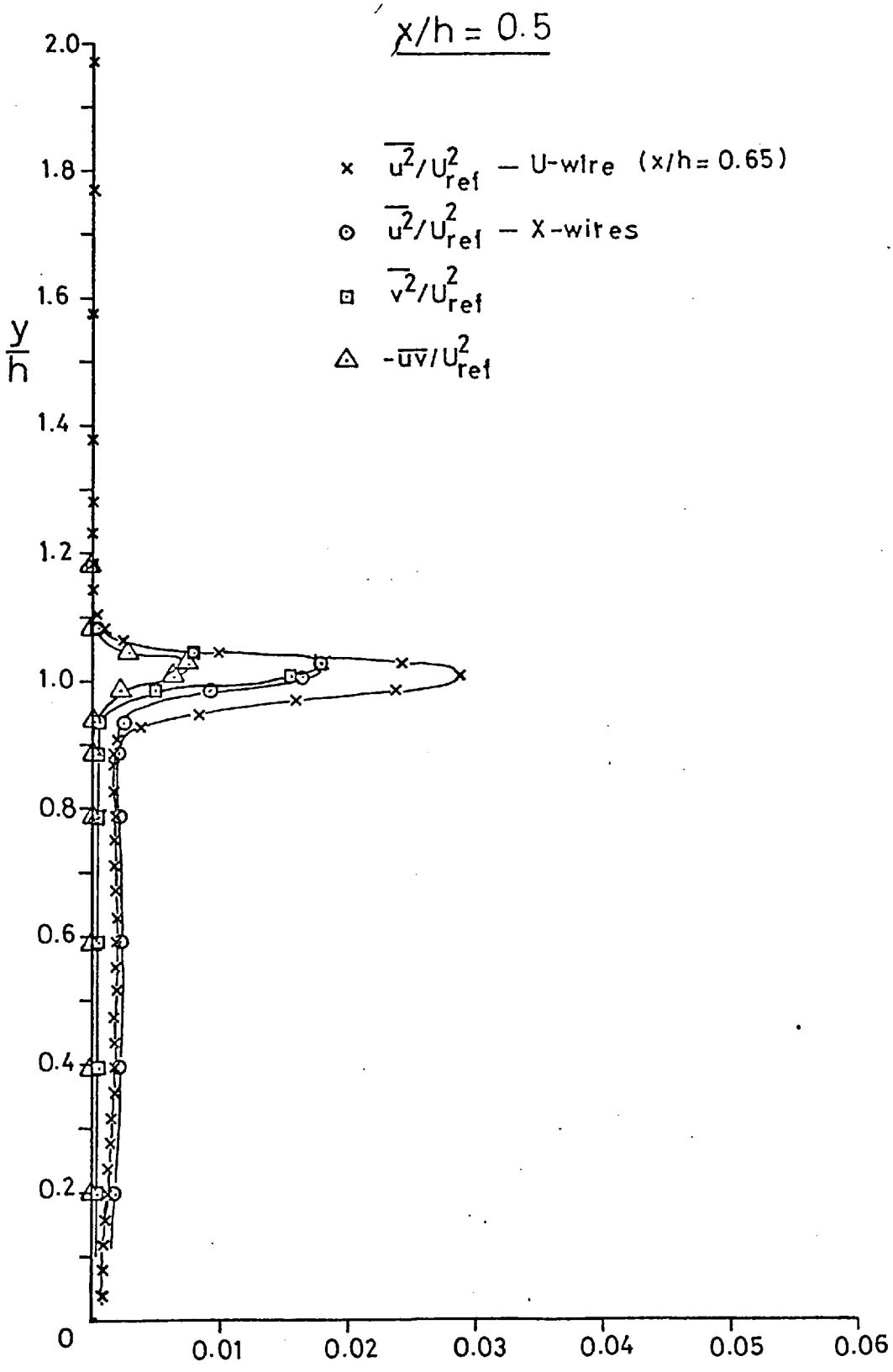


FIGURE 4.19(a) FLUCTUATING QUANTITIES

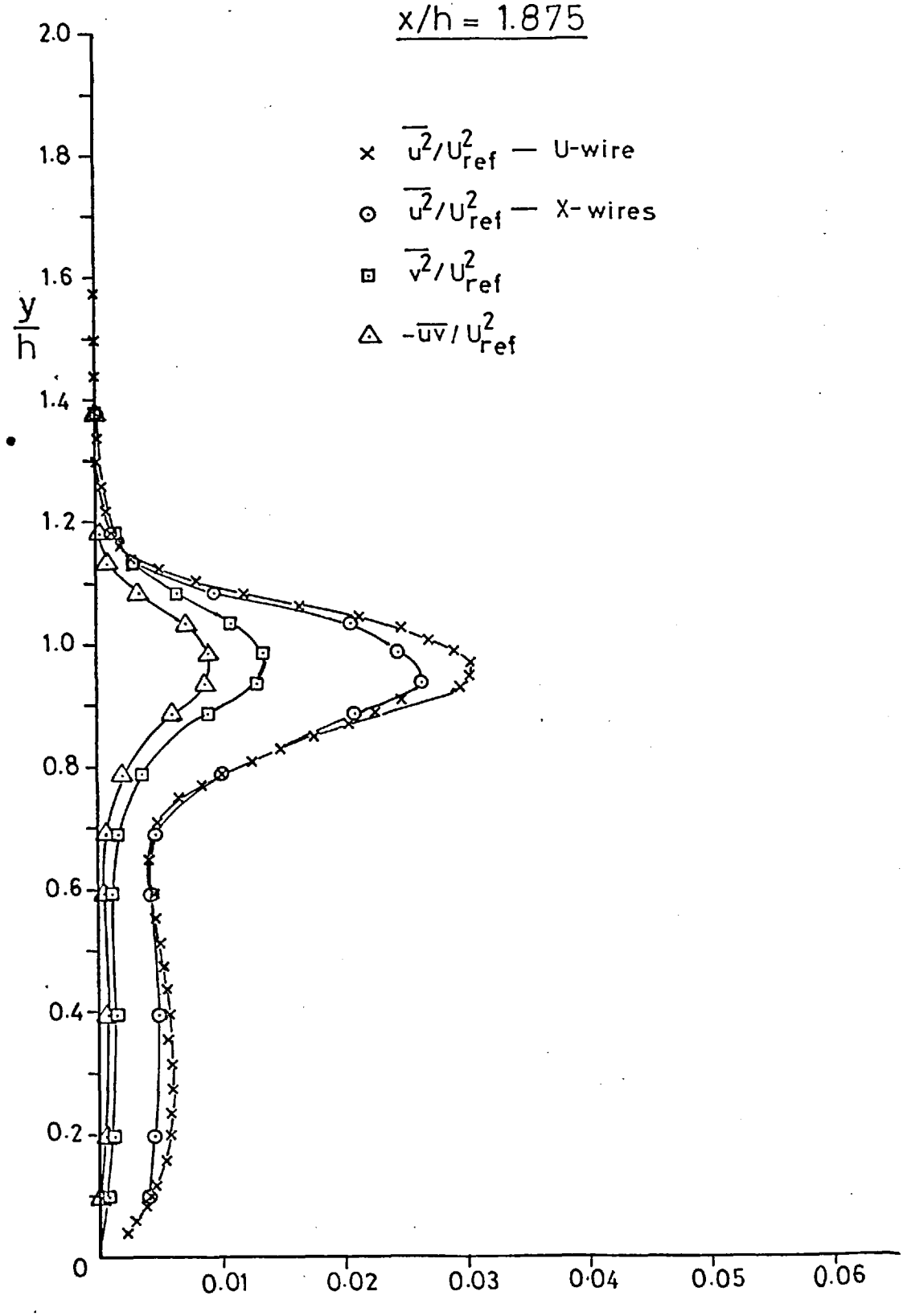


FIGURE 4.19(b) FLUCTUATING QUANTITIES

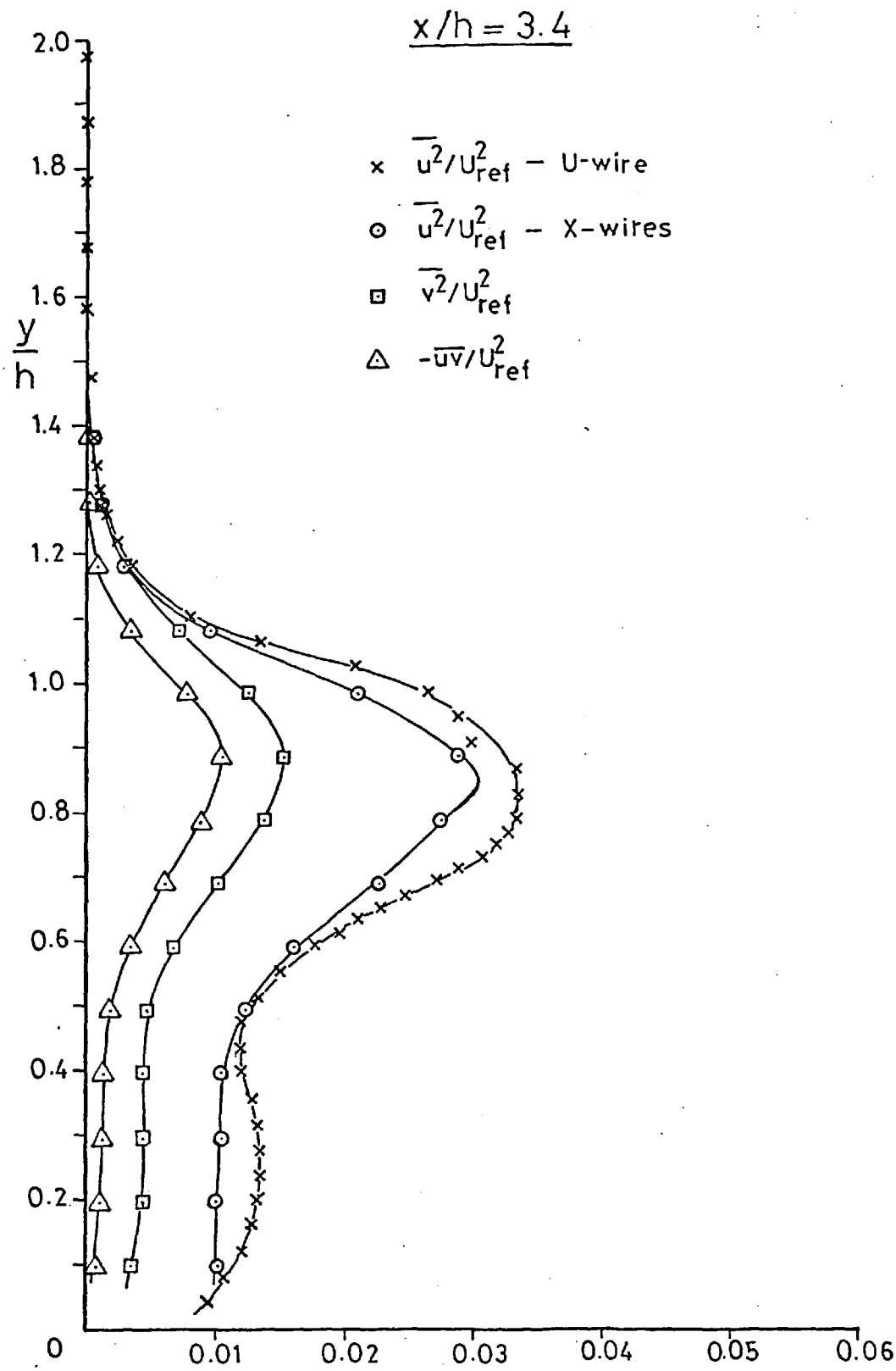


FIGURE 4.19(c) FLUCTUATING QUANTITIES

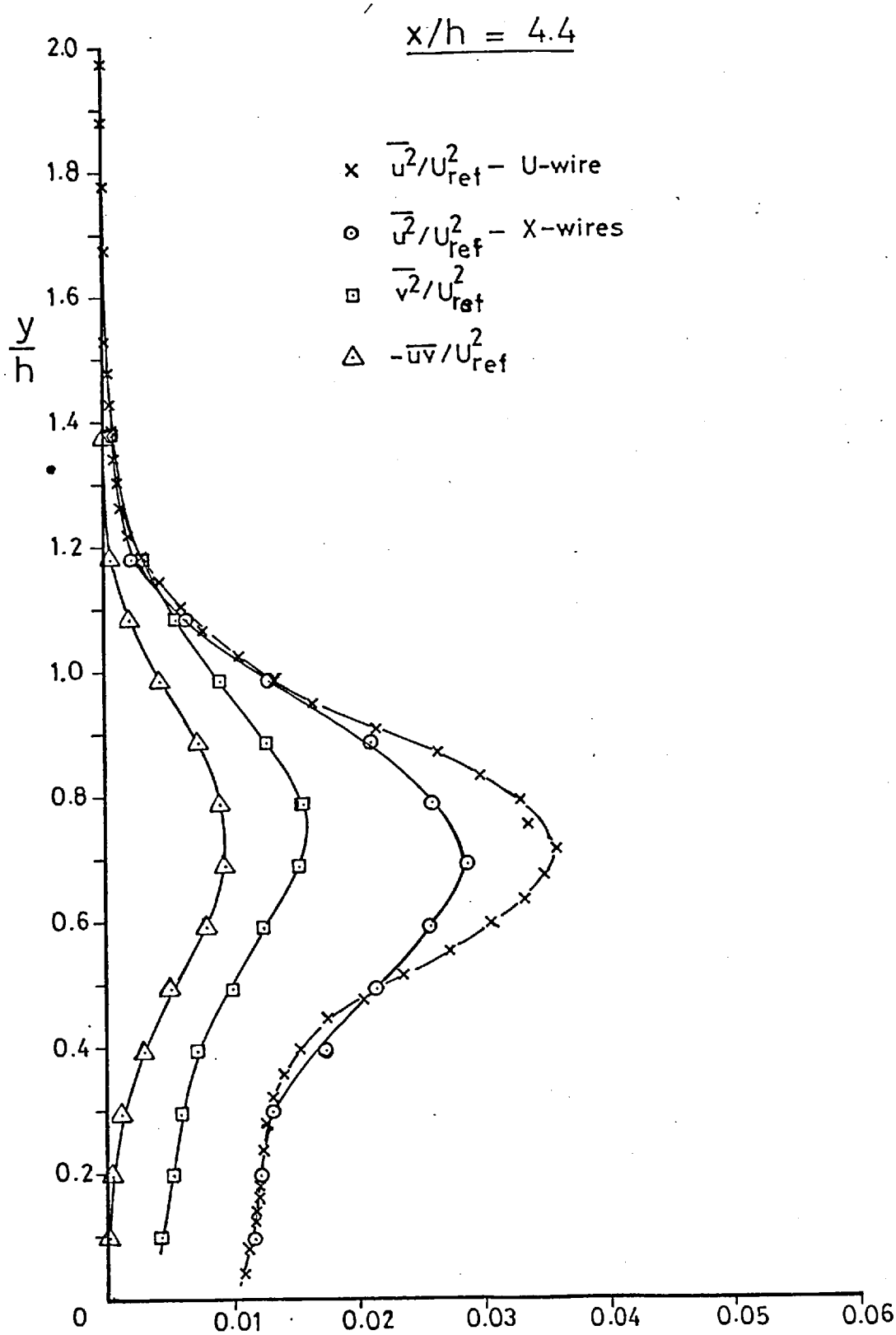


FIGURE 4.19(d) FLUCTUATING QUANTITIES

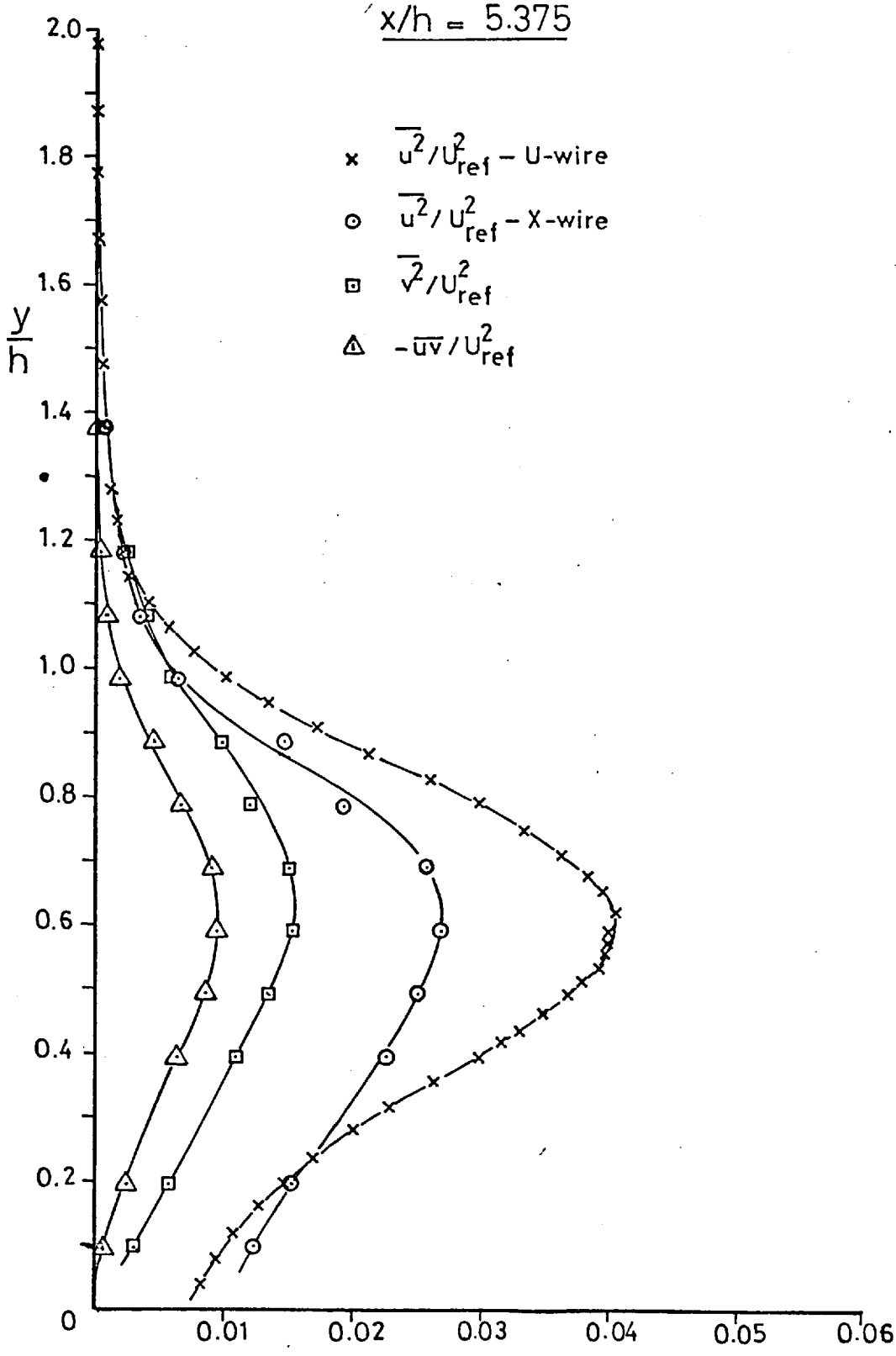


FIGURE 4.19(e) FLUCTUATING QUANTITIES

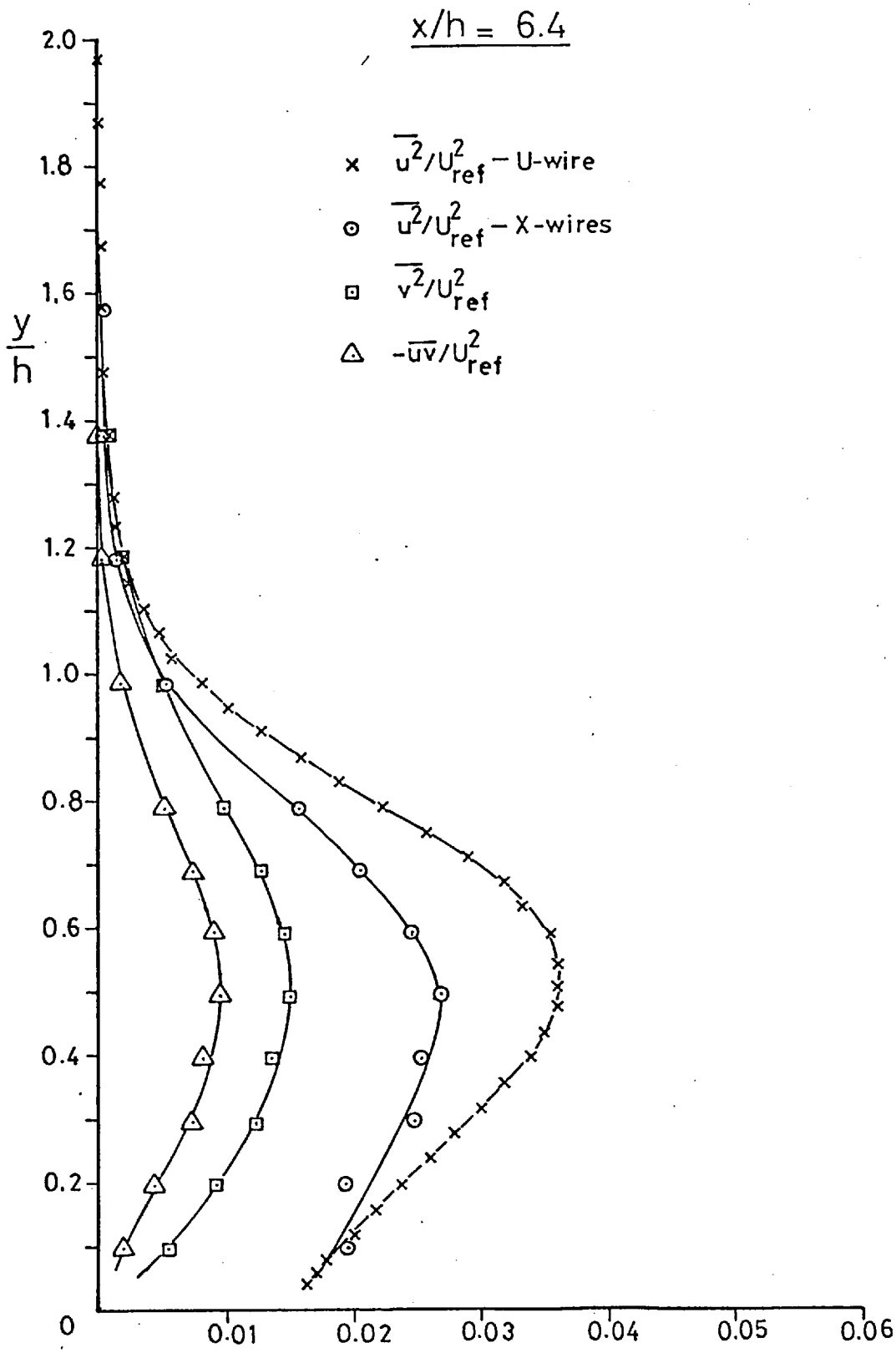


FIGURE 4.19(f) FLUCTUATING QUANTITIES

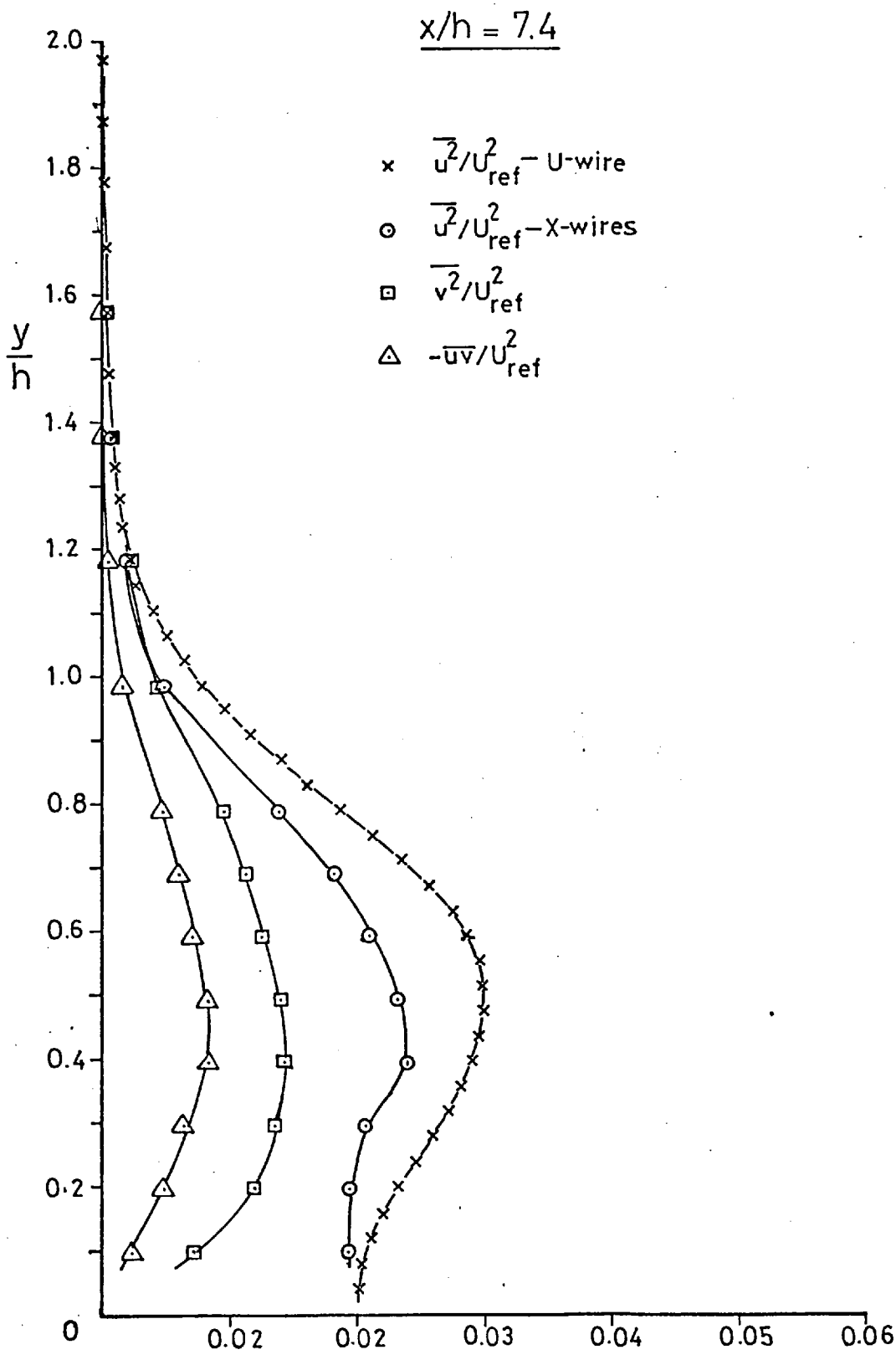


FIGURE 4.19(g) FLUCTUATING QUANTITIES

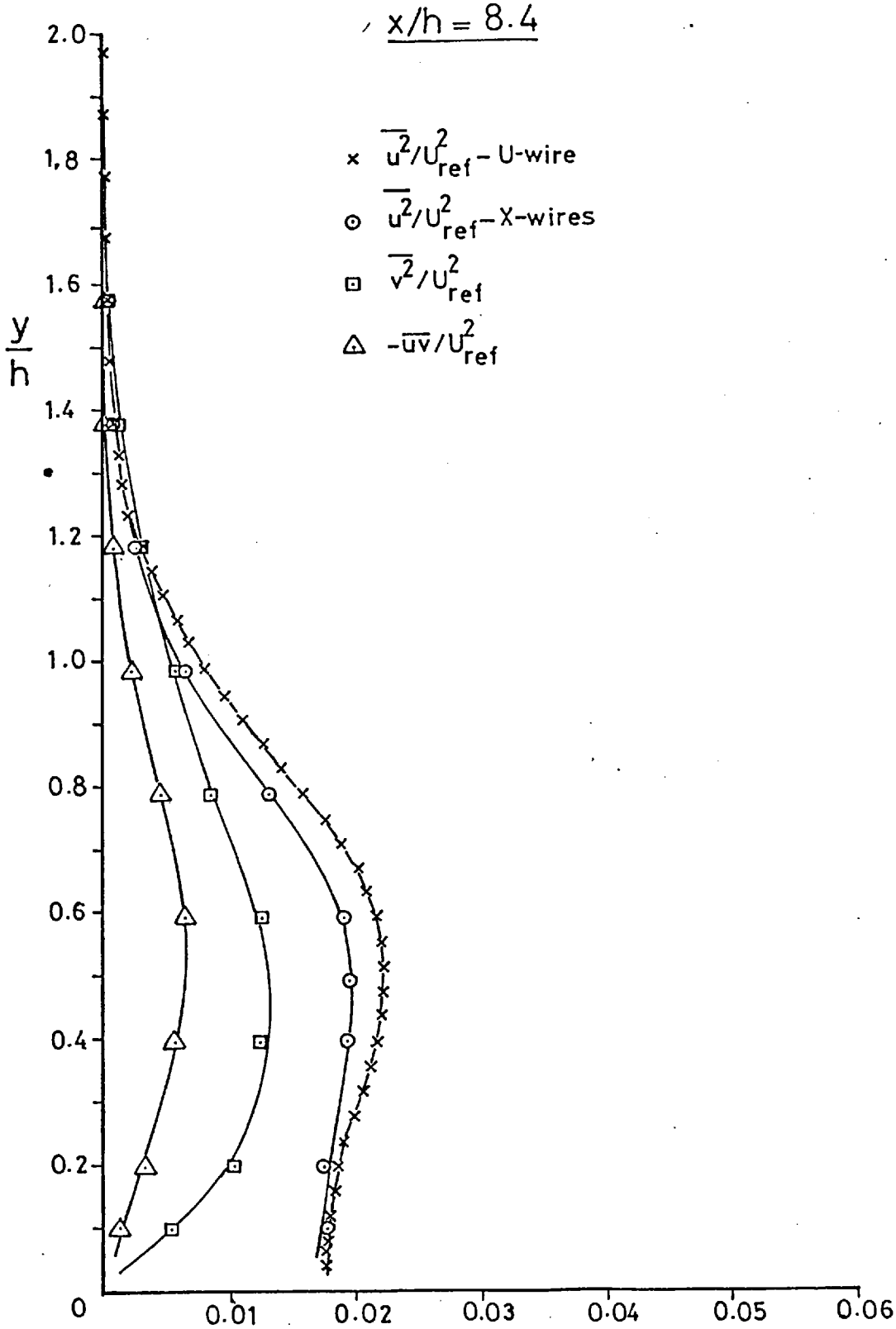


FIGURE 4.19(h) FLUCTUATING QUANTITIES

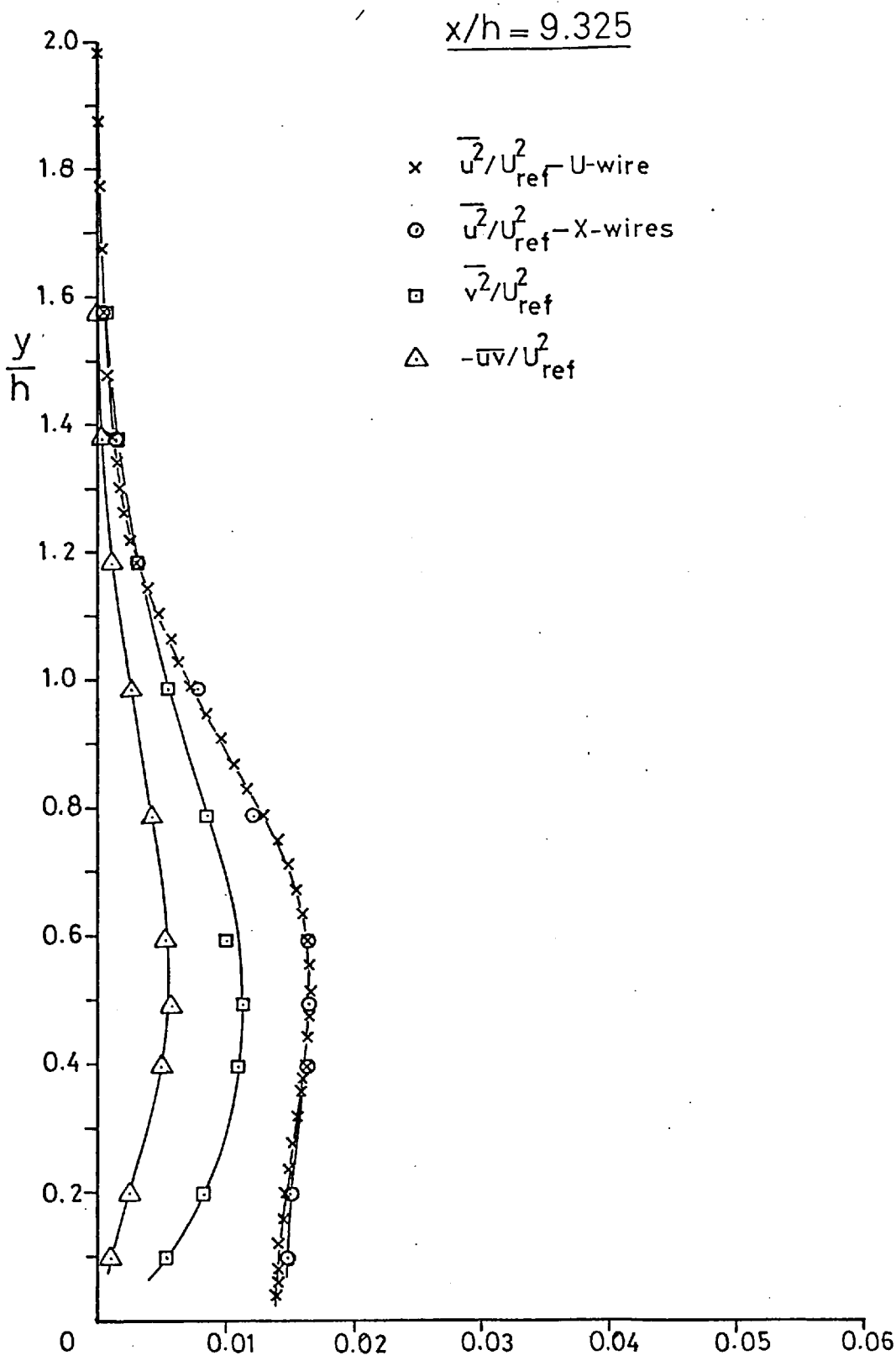


FIGURE 4.19(i) FLUCTUATING QUANTITIES

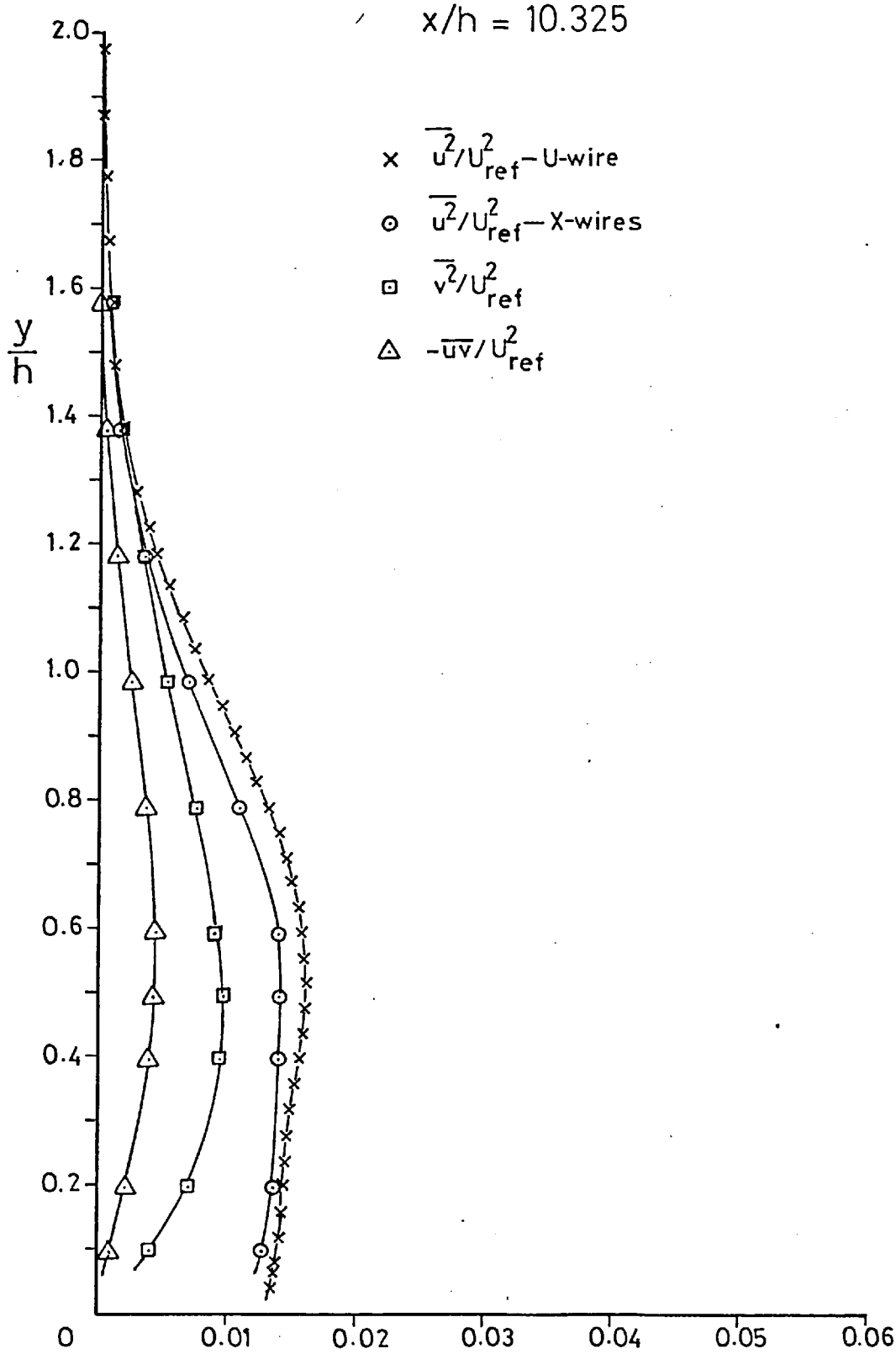


FIGURE 4.19(j) FLUCTUATING QUANTITIES

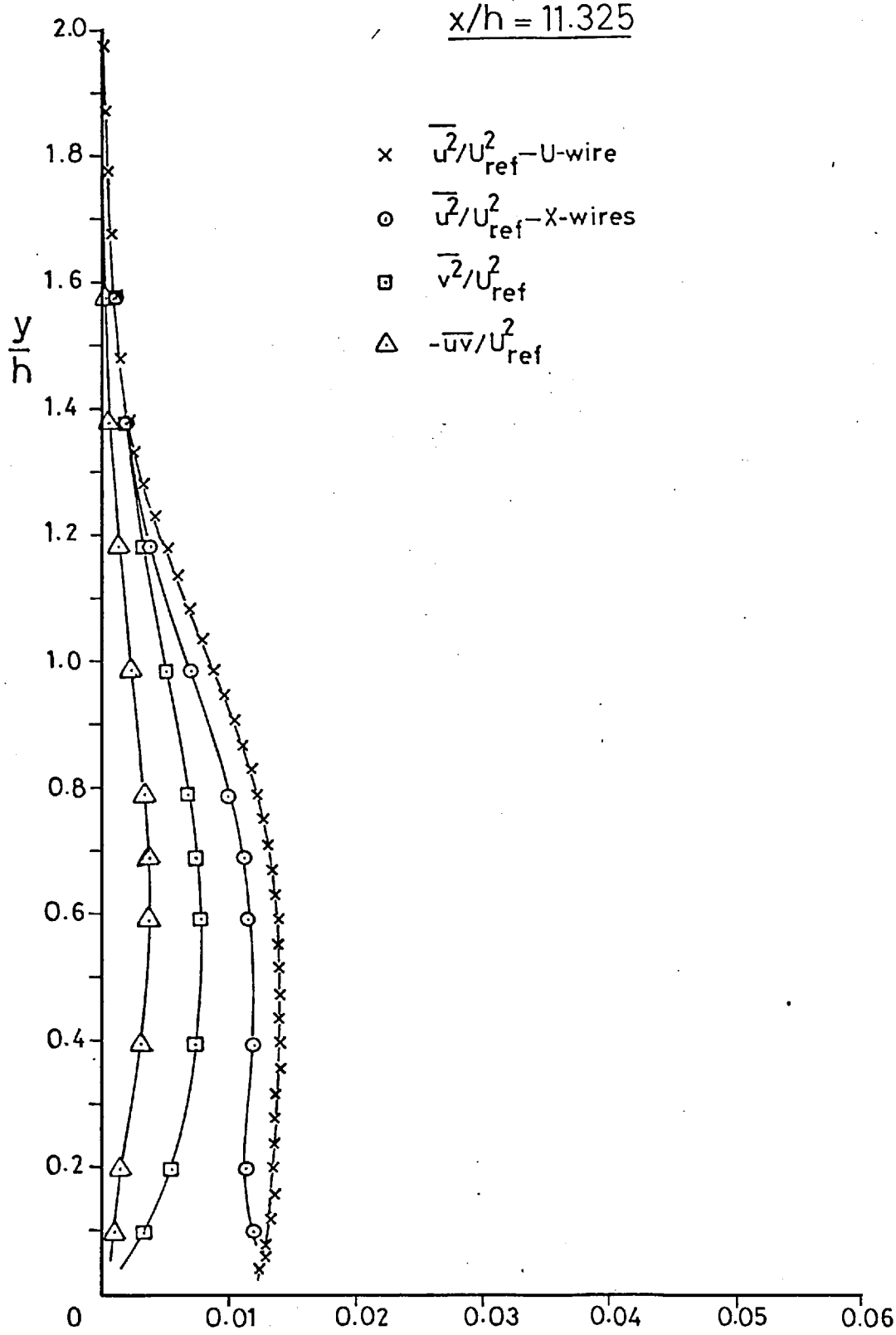


FIGURE 4.19(k) FLUCTUATING QUANTITIES

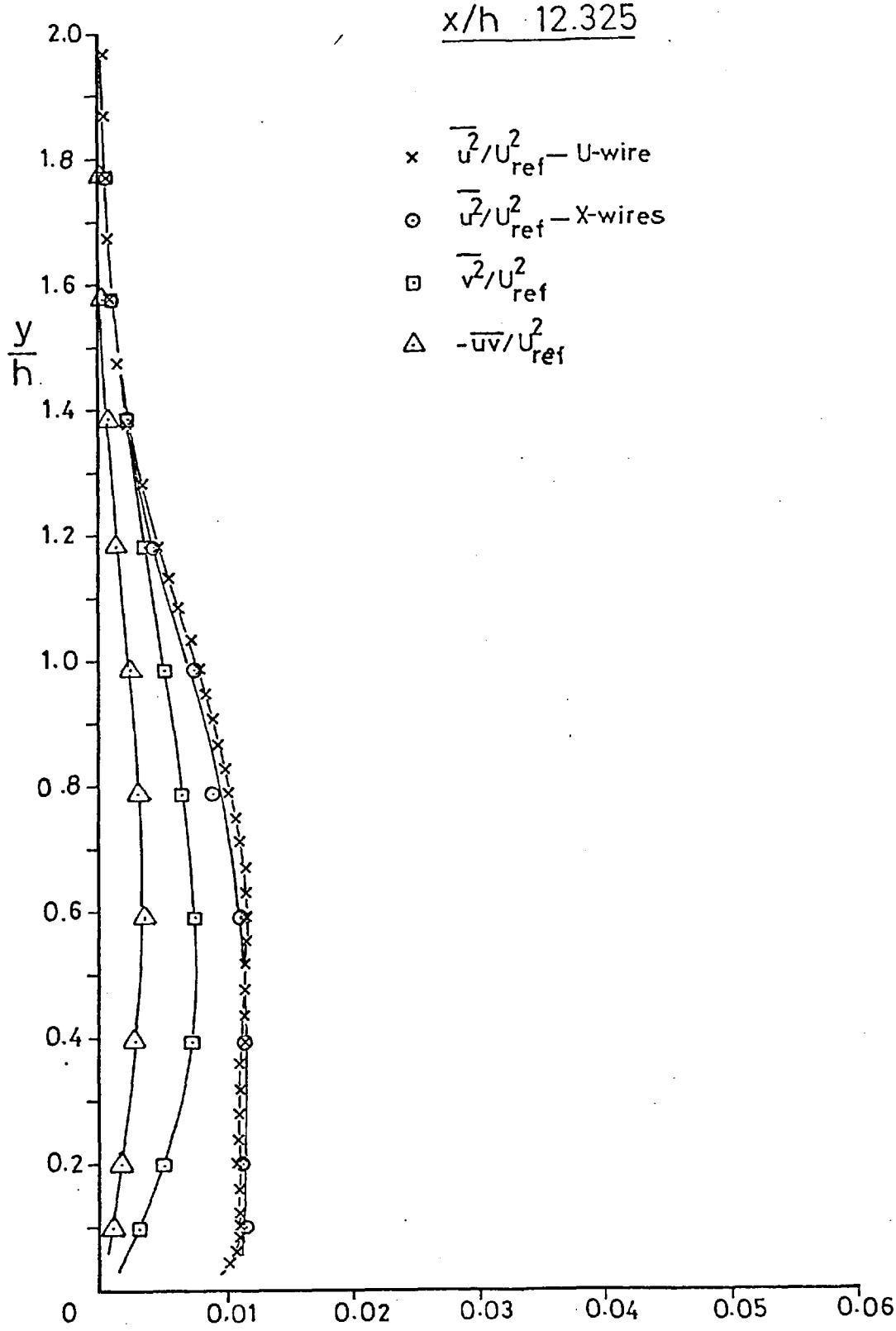


FIGURE 4.19(I) FLUCTUATING QUANTITIES

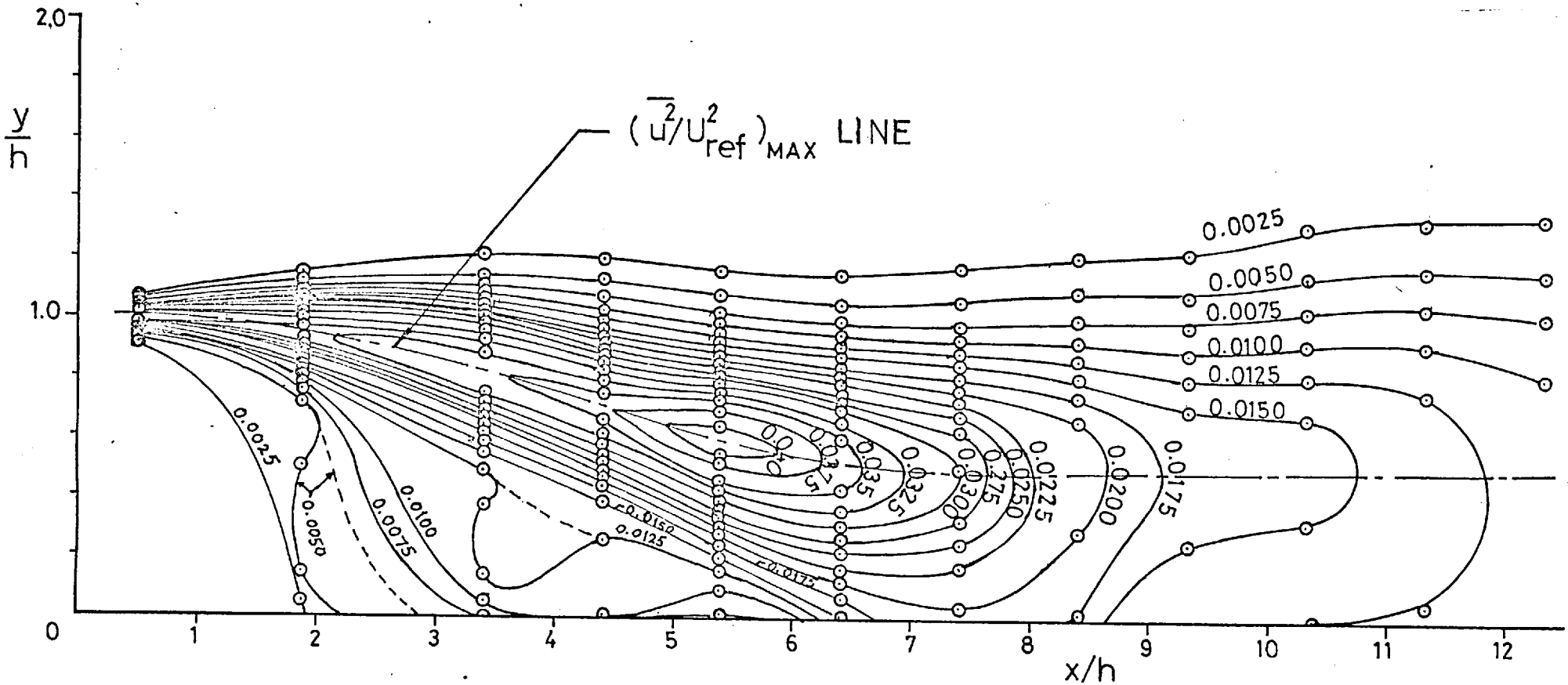


FIGURE 4.20 CONTOUR PLOT OF $\overline{u^2}/U^2_{ref}$ — U-WIRE RESULTS

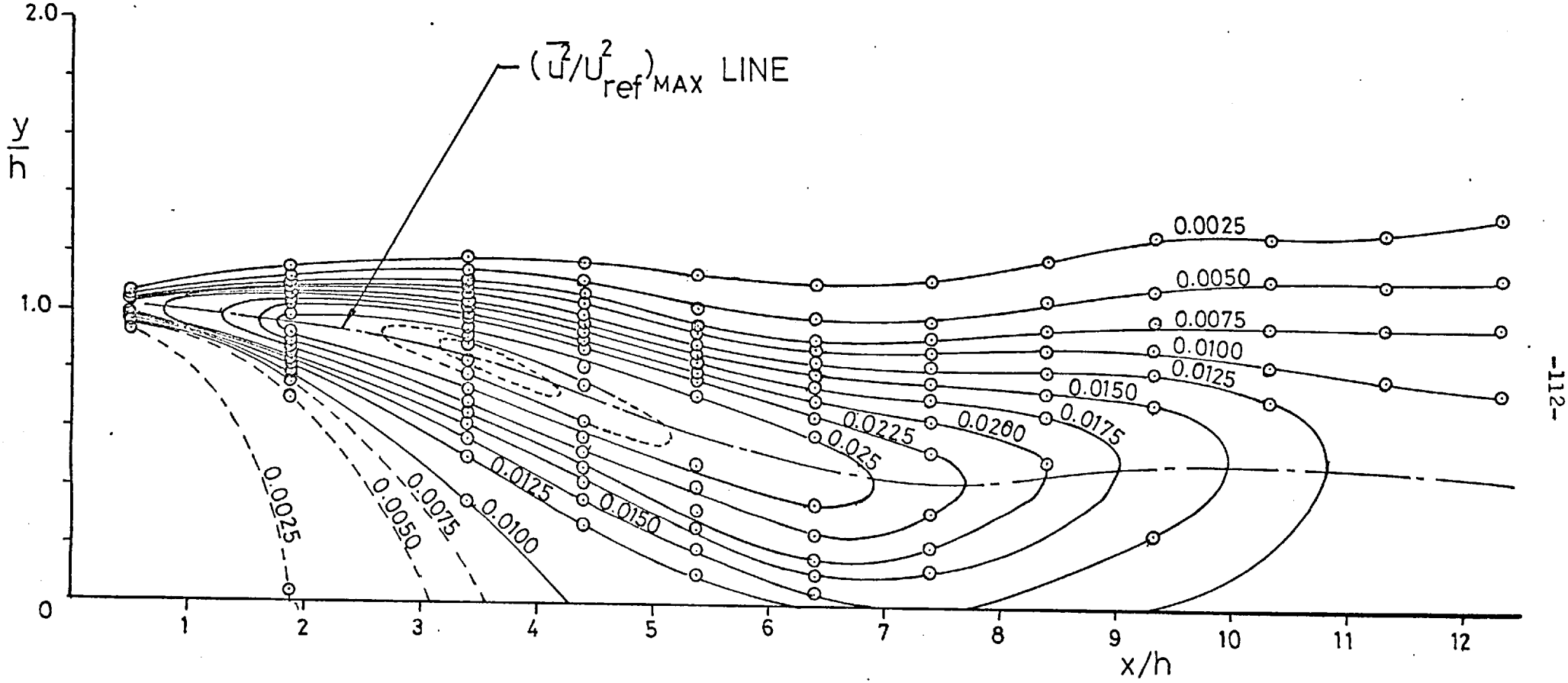


FIGURE 4.21 CONTOUR PLOT OF $\overline{u^2}/U^2_{ref}$ — X-WIRE RESULTS

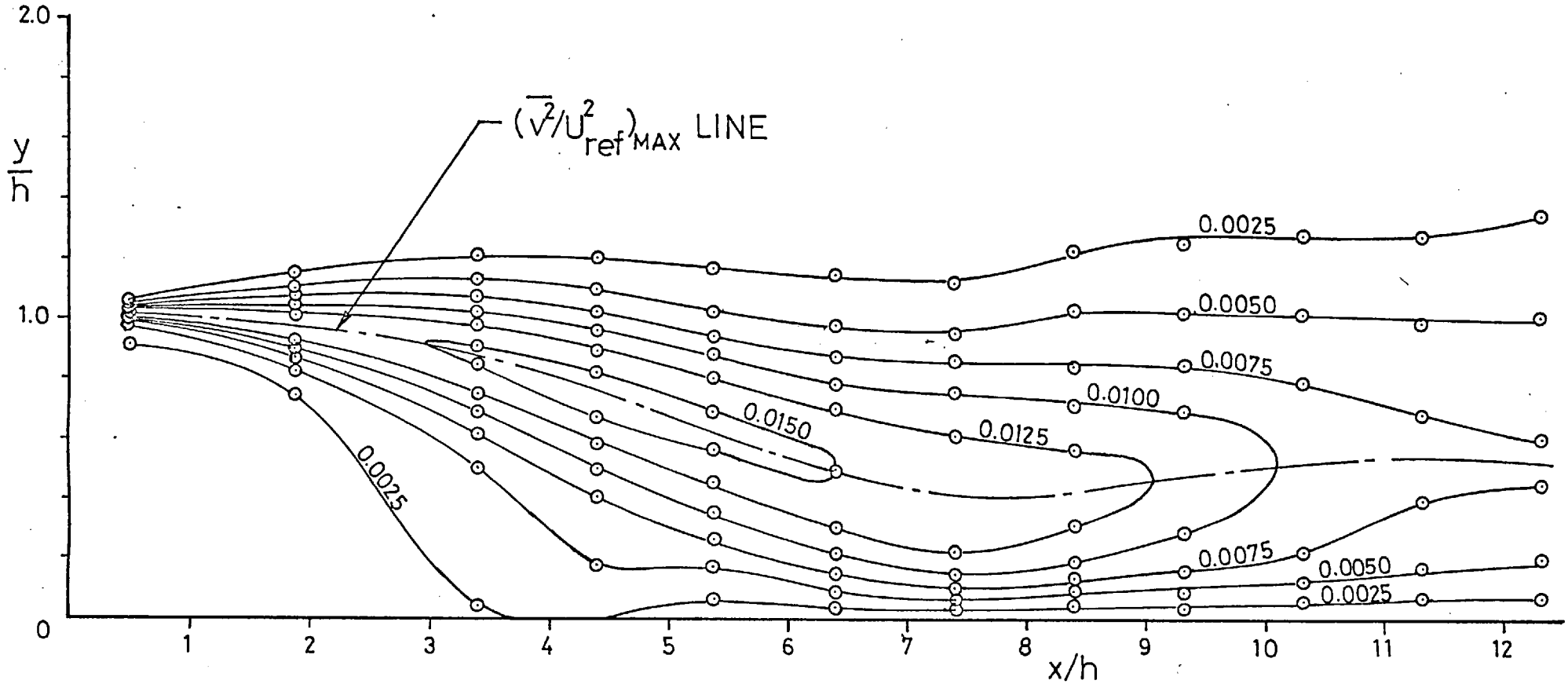


FIGURE 4.22 CONTOUR PLOT OF $\overline{v^2}/U^2_{ref}$

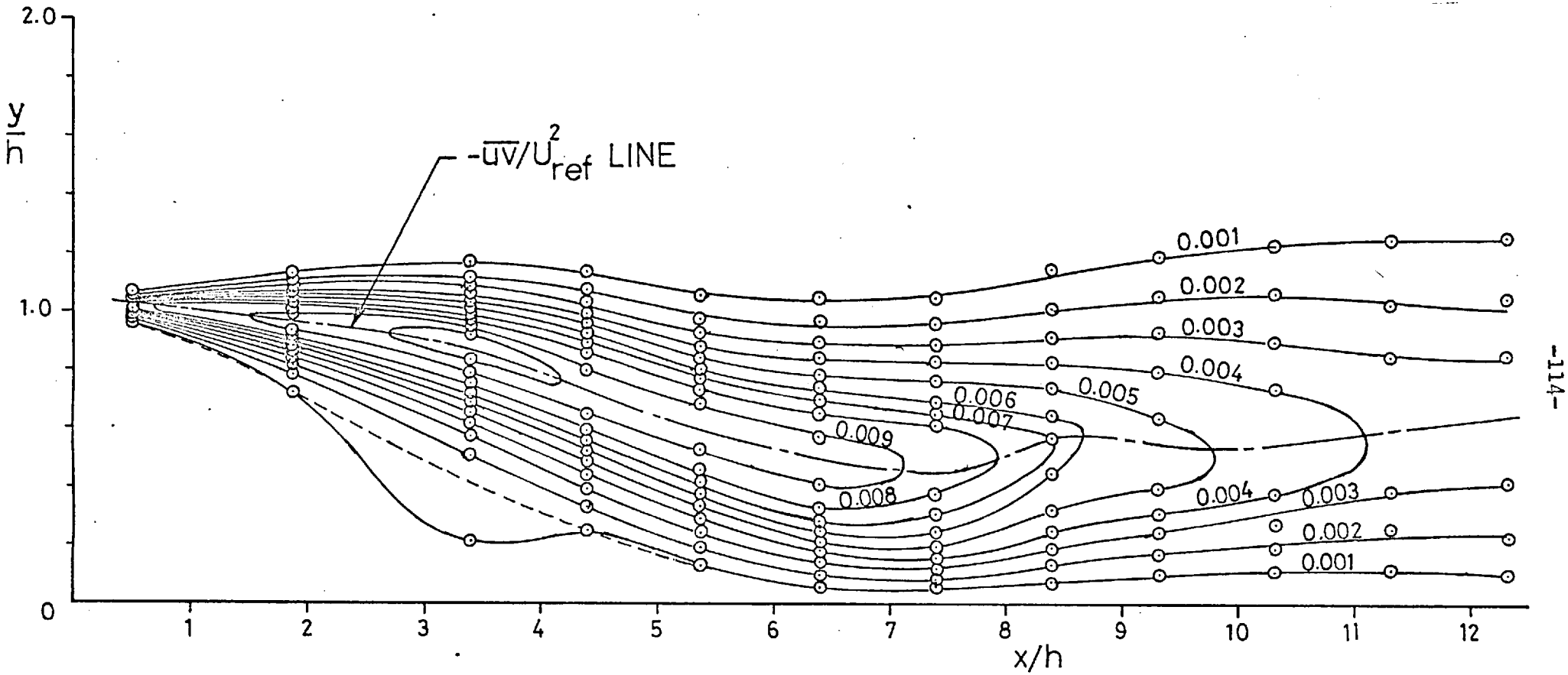


FIGURE 4.23 CONTOUR PLOT OF $-\overline{uv}/U^2_{ref}$

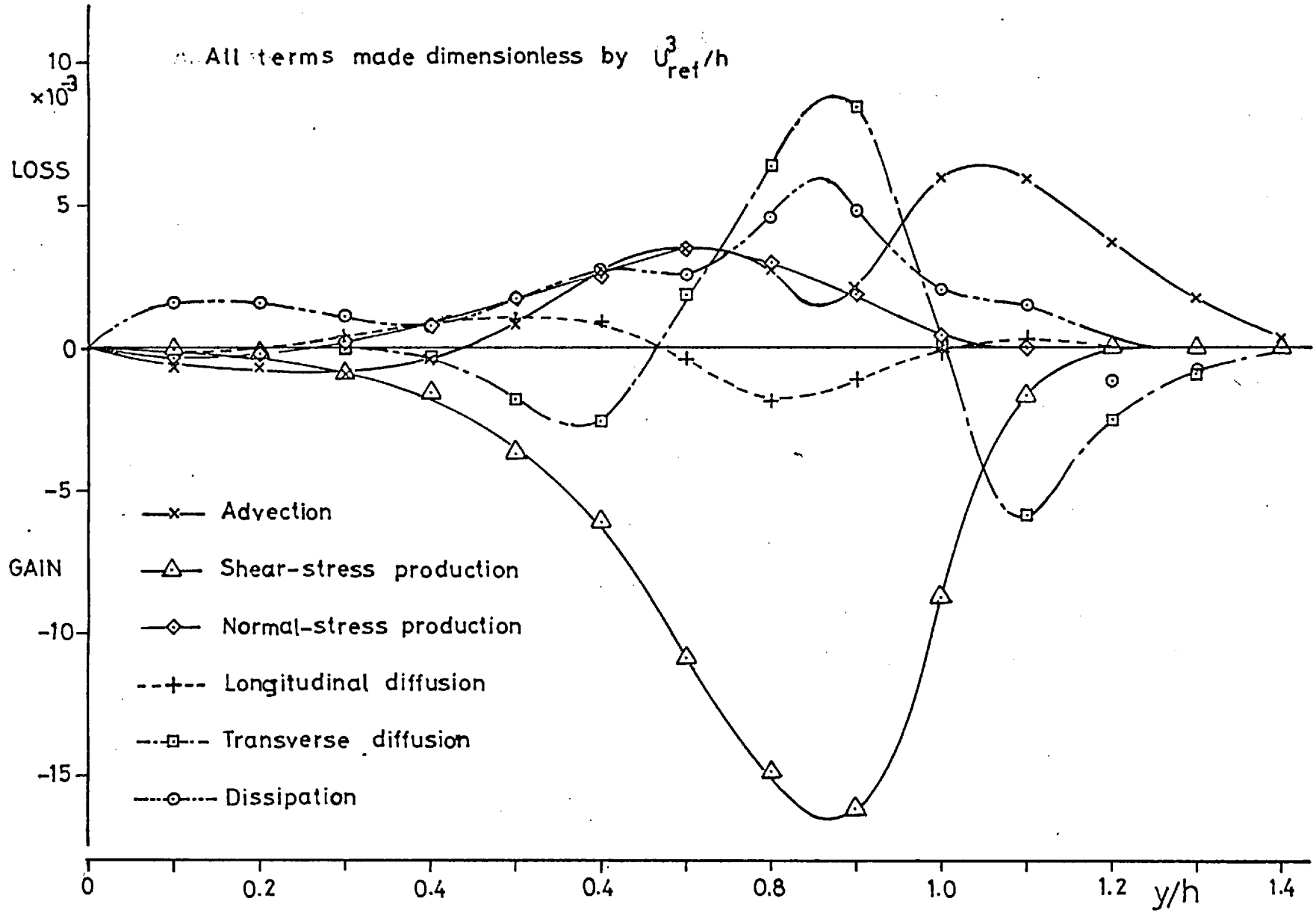


FIGURE 4.24(a) ENERGY BALANCE — x/h = 3.4

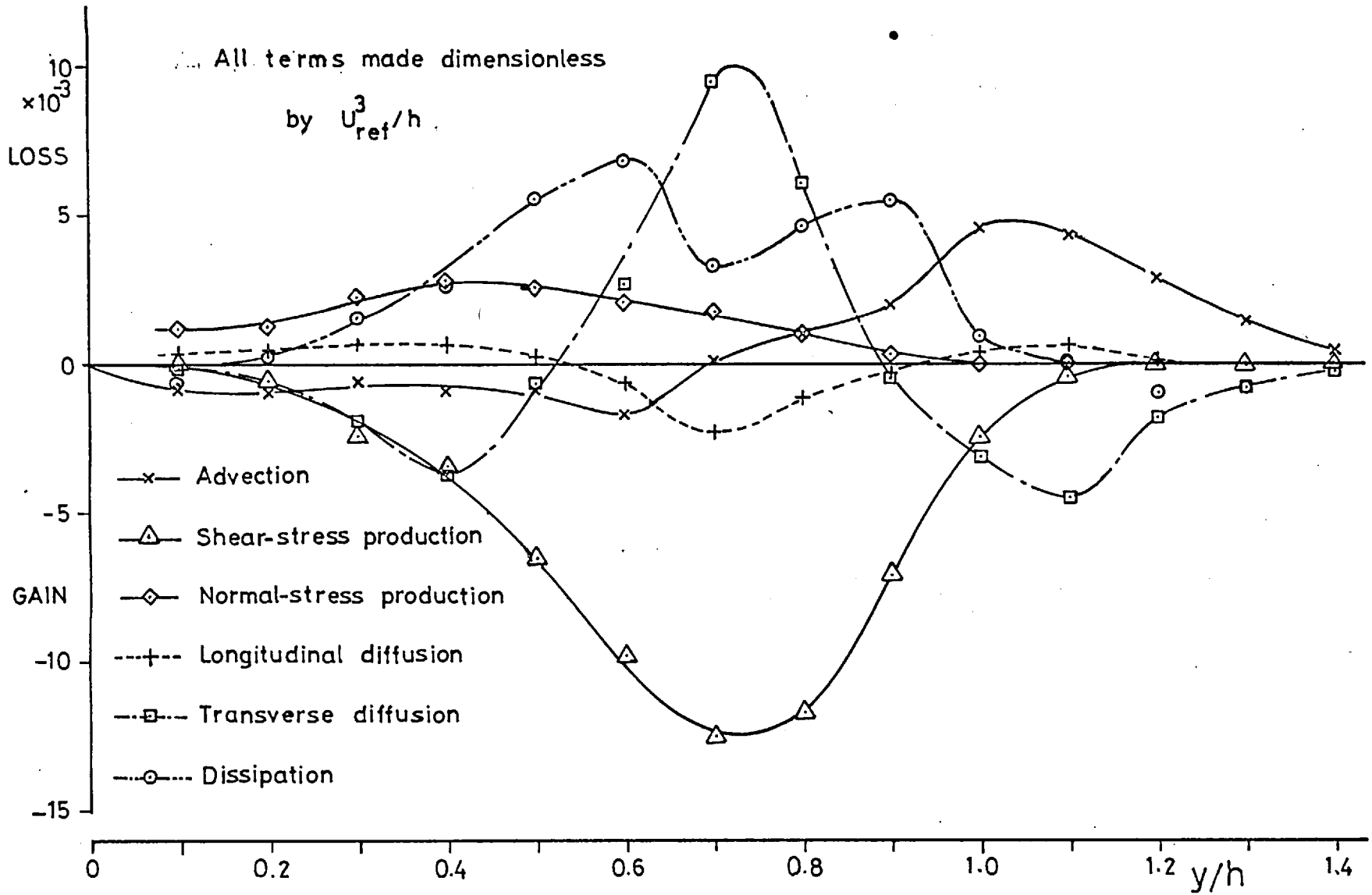


FIGURE 4.24(b) ENERGY BALANCE — x/h = 4.4

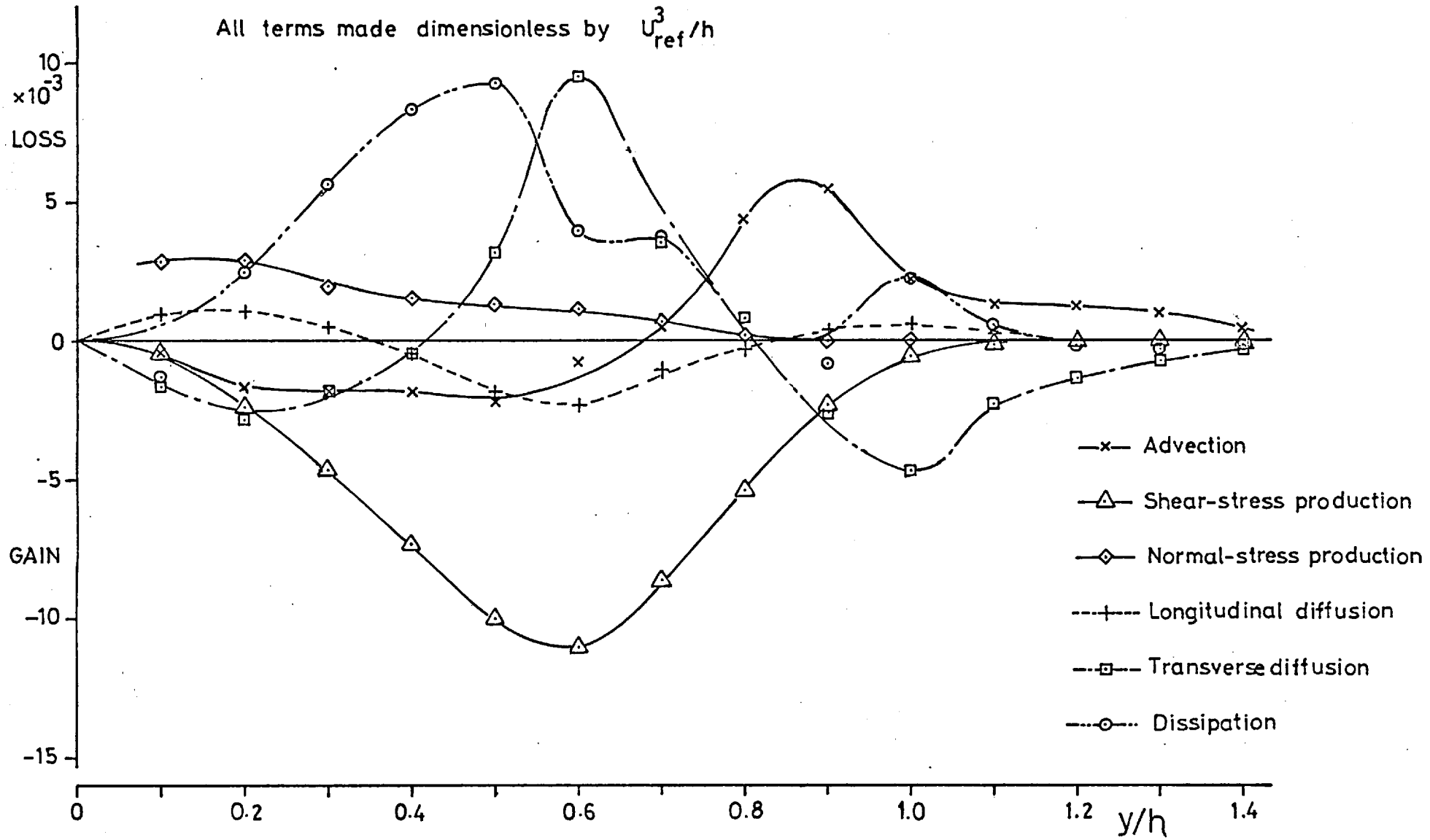


FIGURE 4.24(c) ENERGY BALANCE — x/h = 5.375

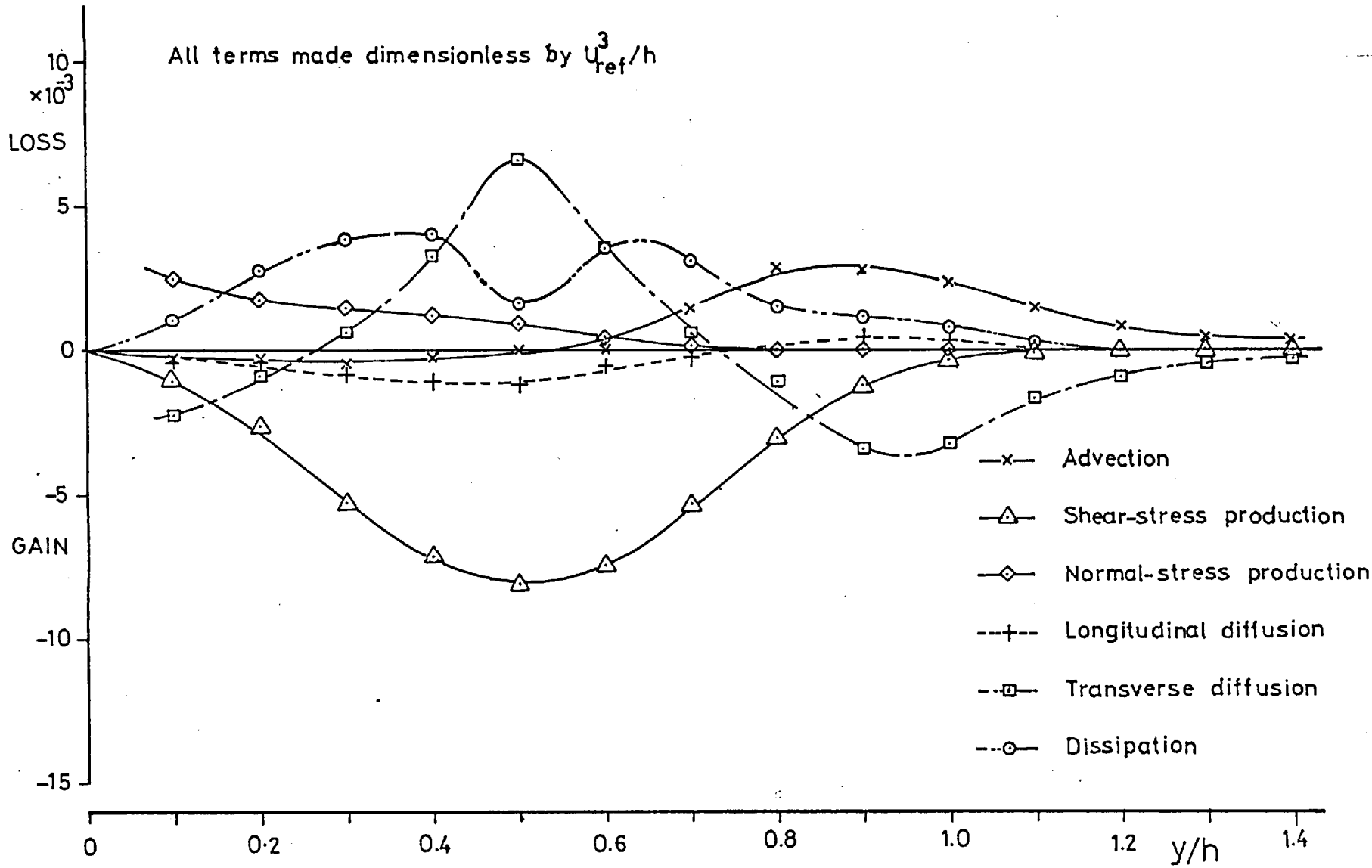


FIGURE 4.24(d) ENERGY BALANCE — x/h = 6.4

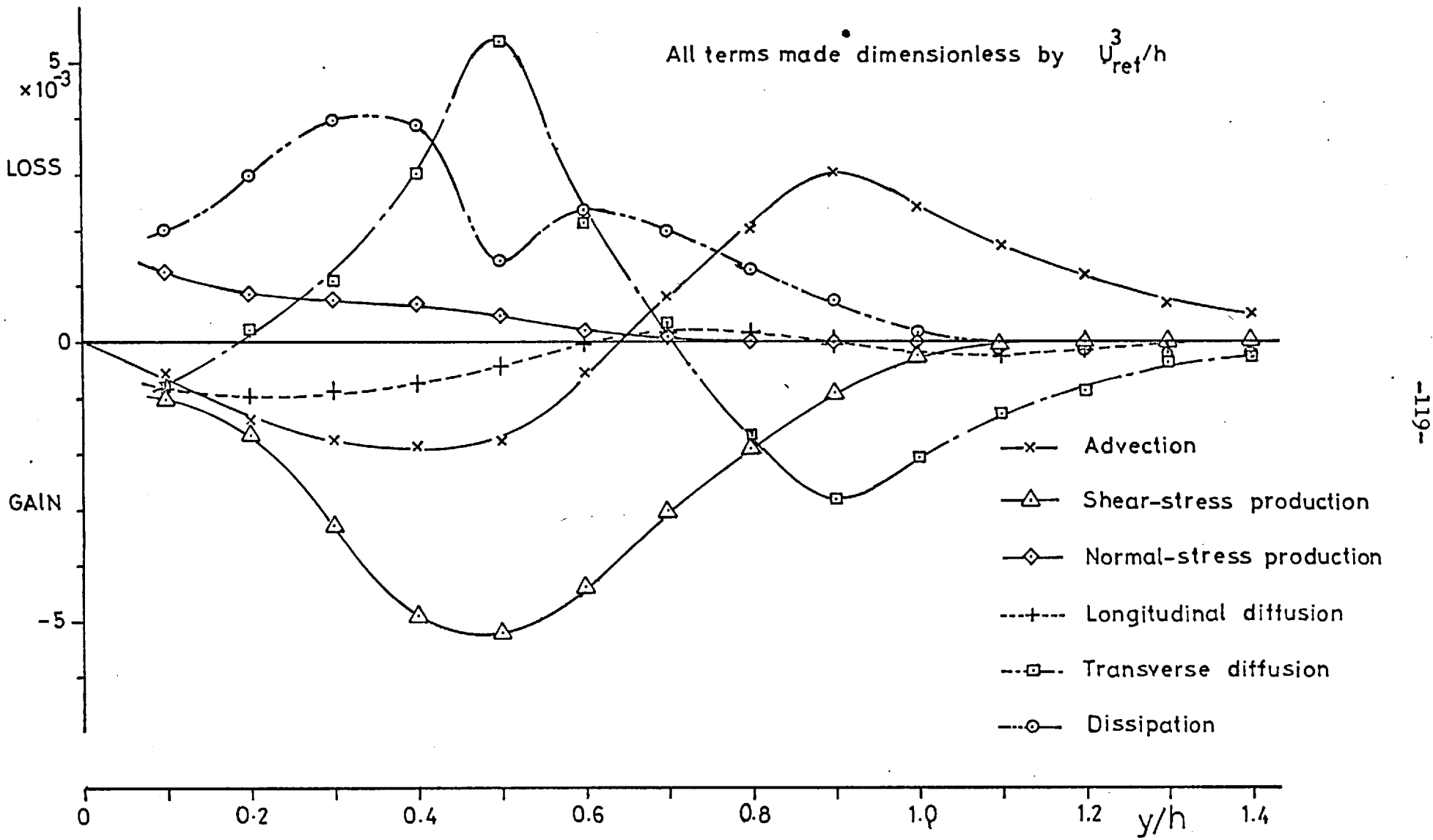


FIGURE 4.24(e) ENERGY BALANCE — x/h = 7.4

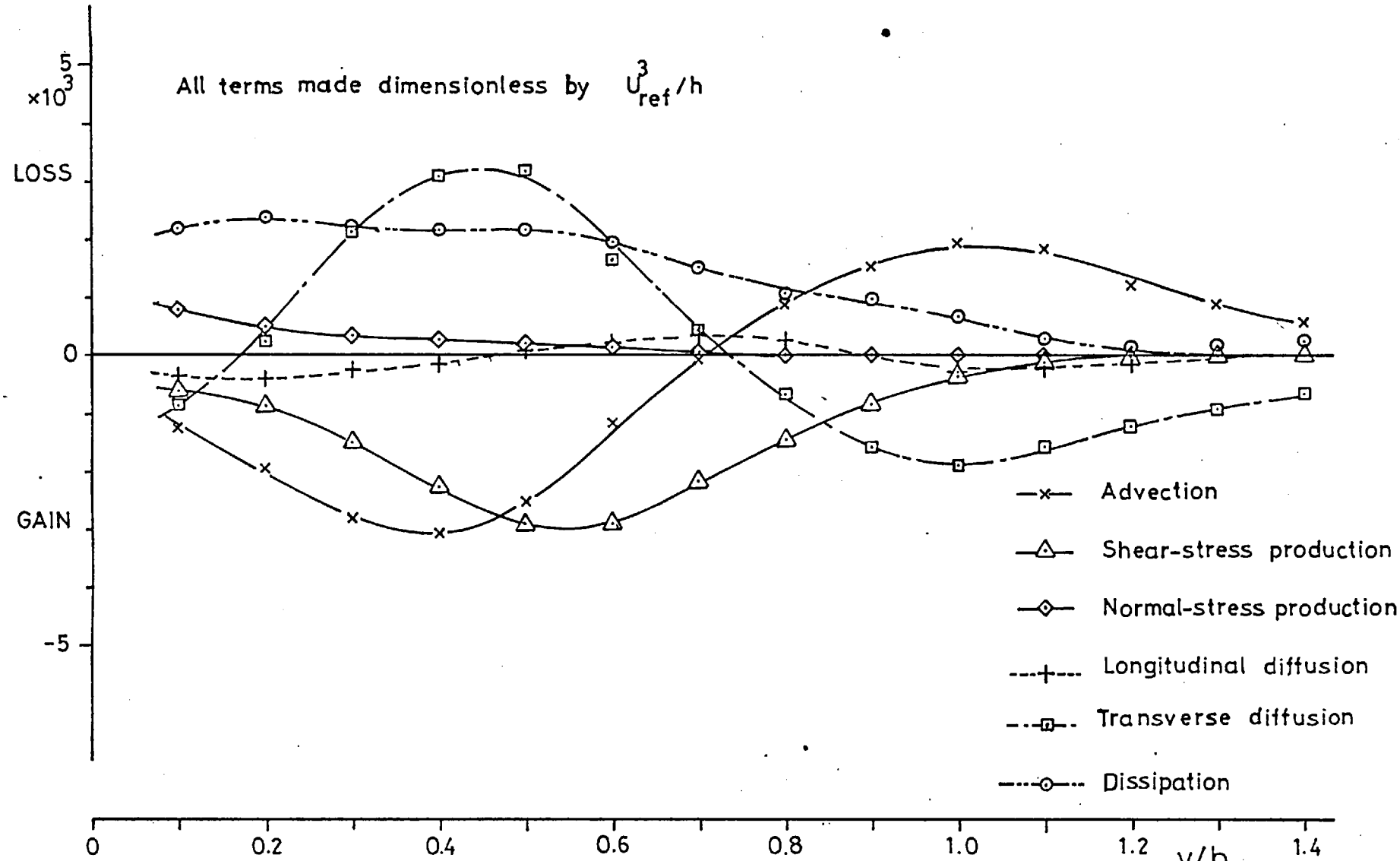


FIGURE 4.24(f) ENERGY BALANCE — x/h = 8.4

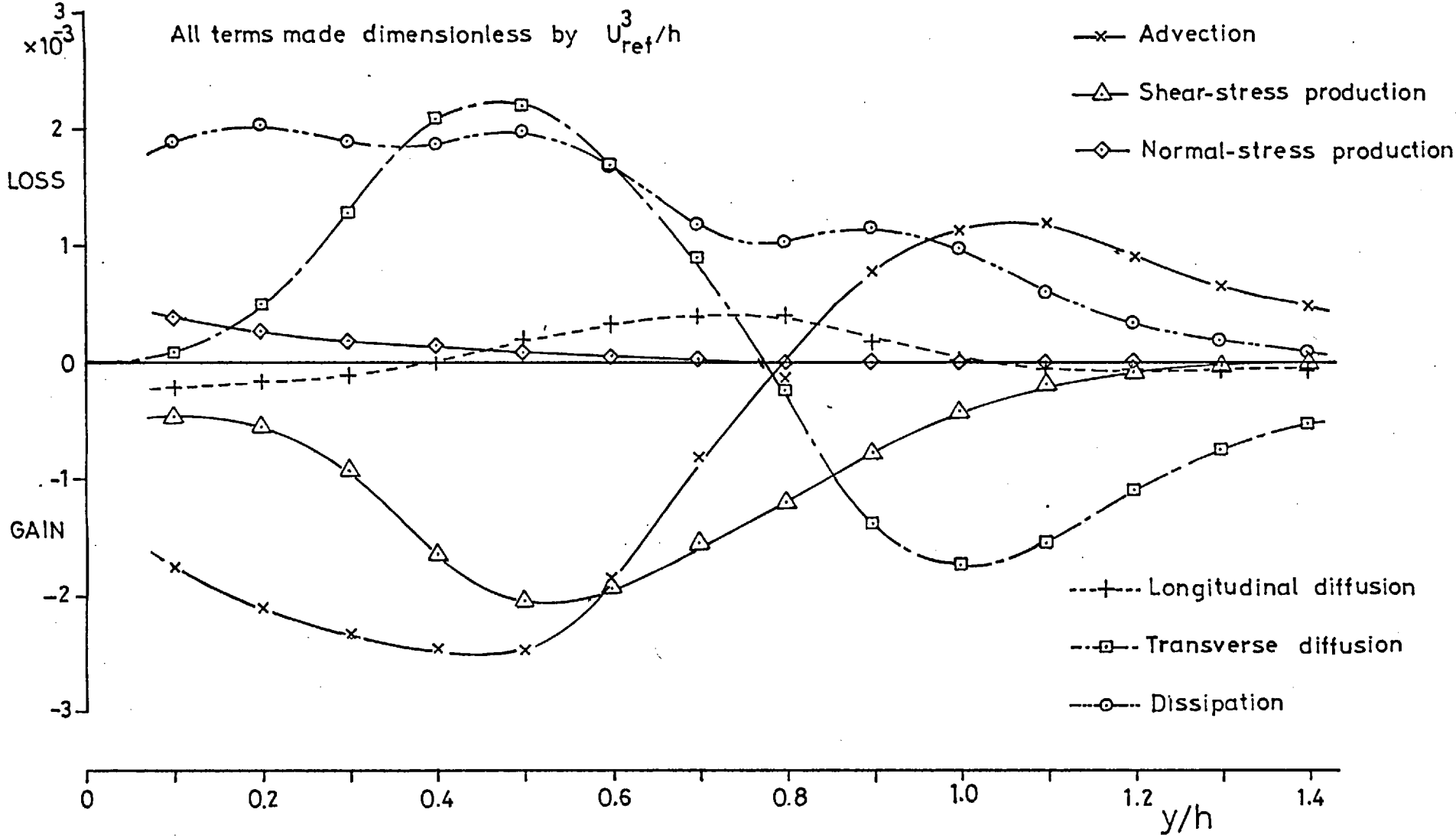


FIGURE 4.24(g) ENERGY BALANCE — x/h = 9.325

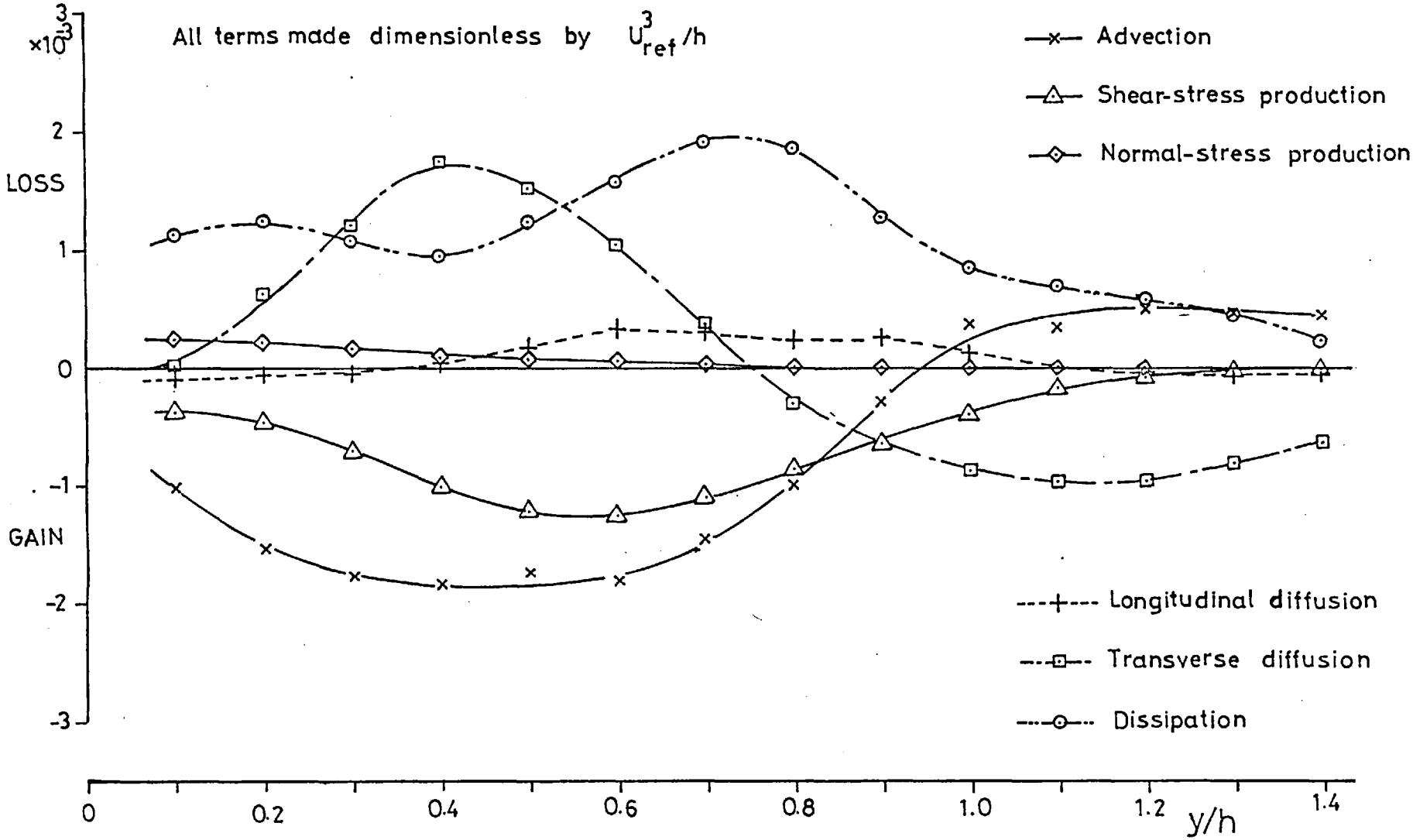


FIGURE 4.24(h) ENERGY BALANCE — x/h = 10.325

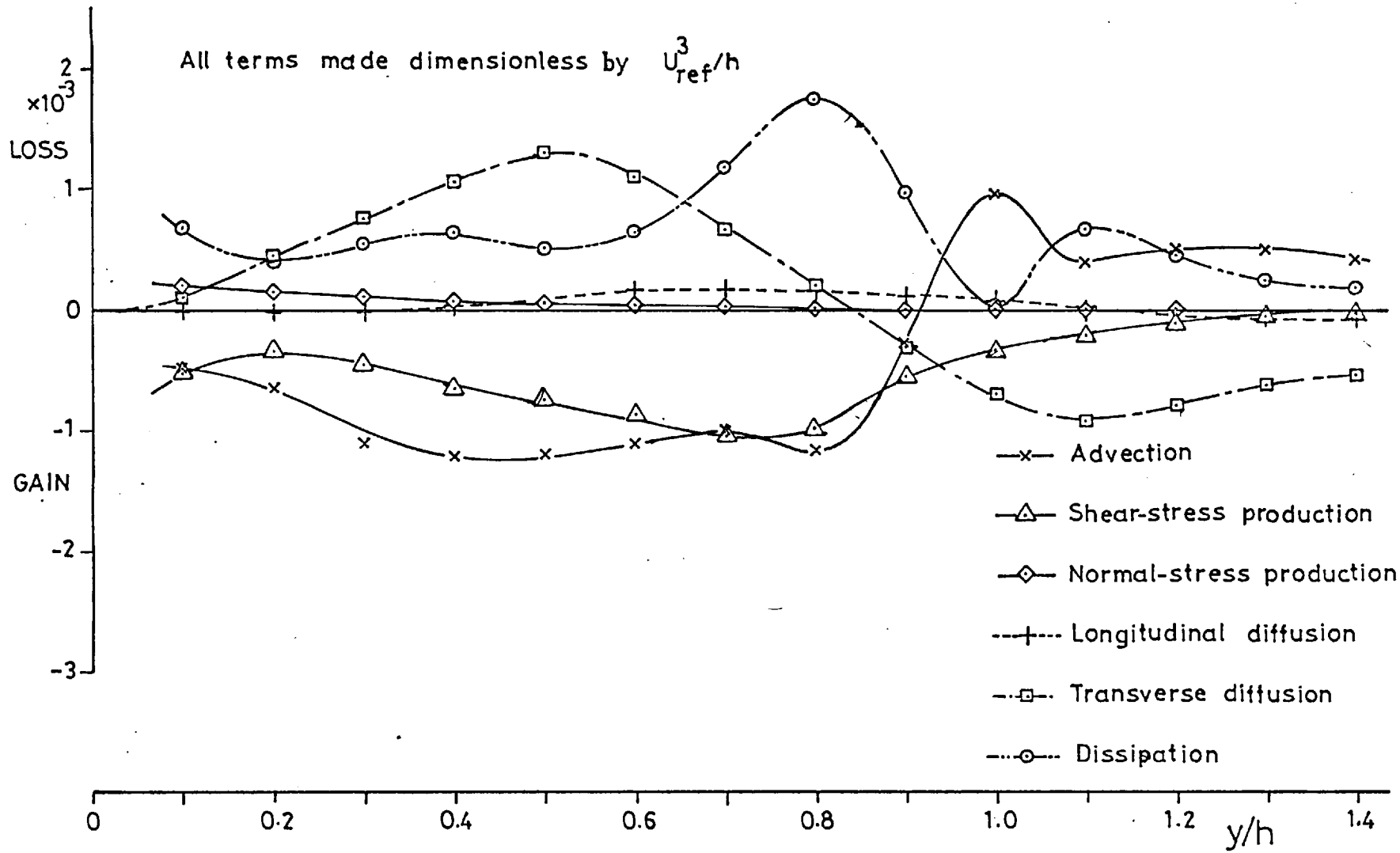


FIGURE 4.24(i) ENERGY BALANCE — x/h = 11.325

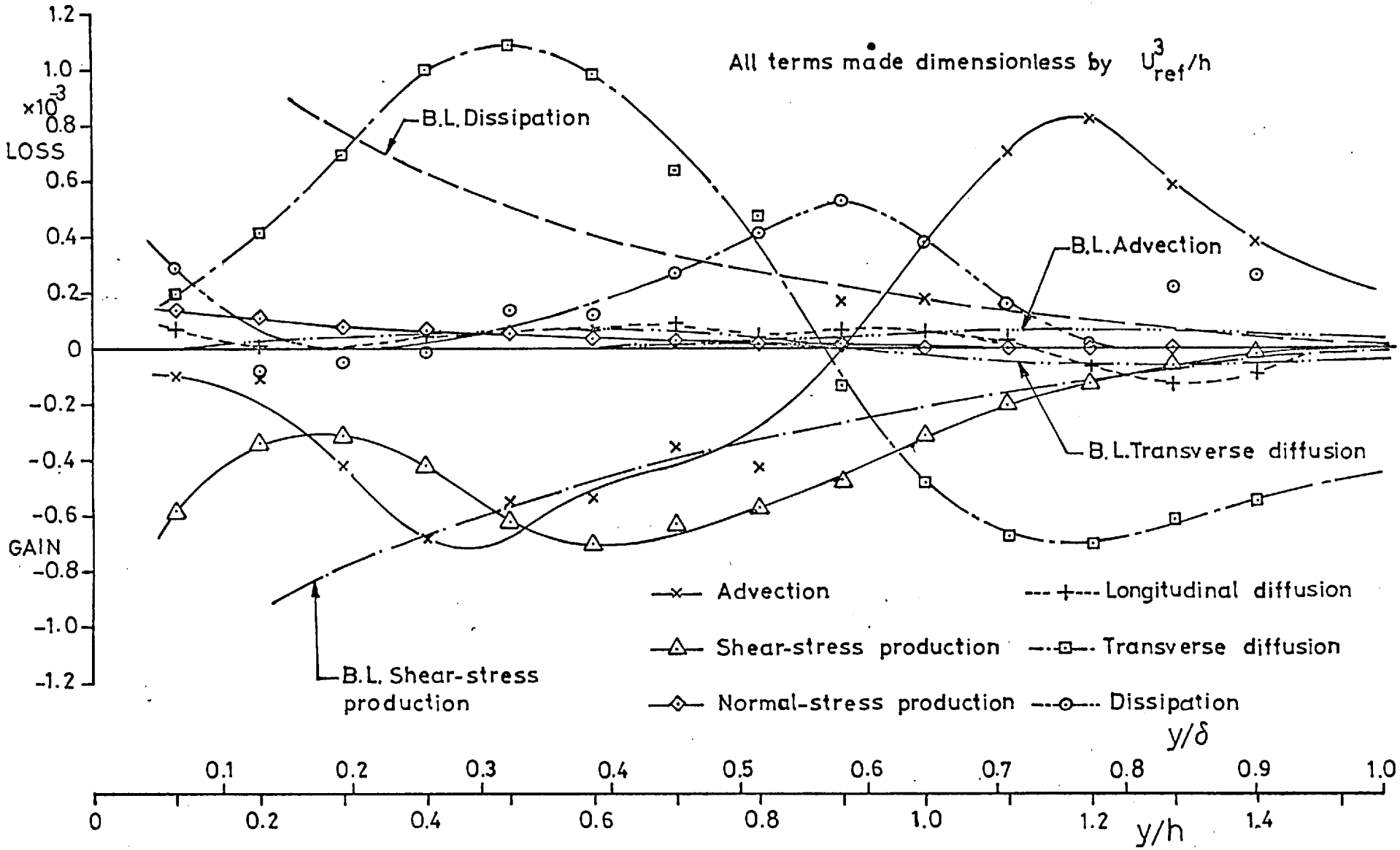
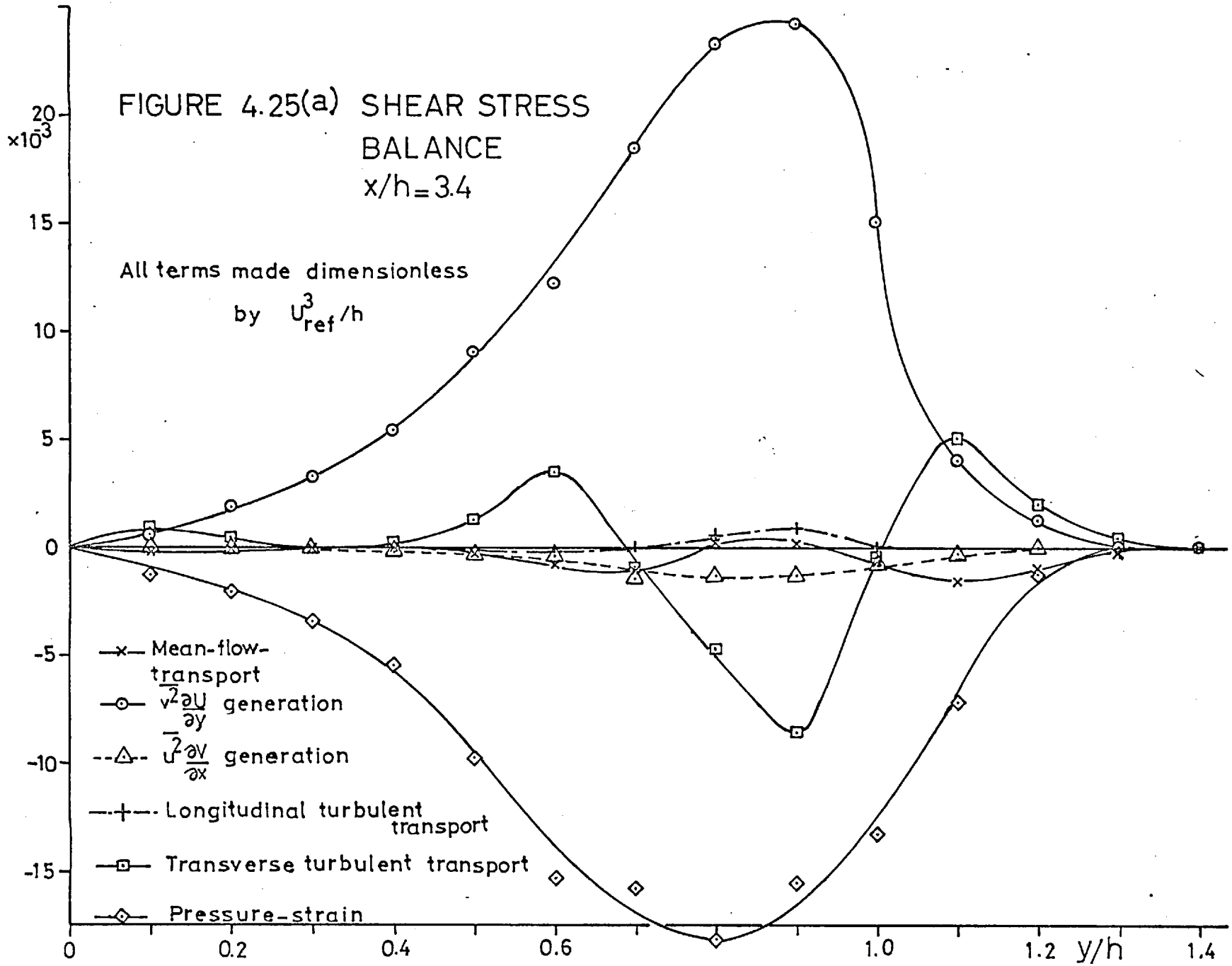
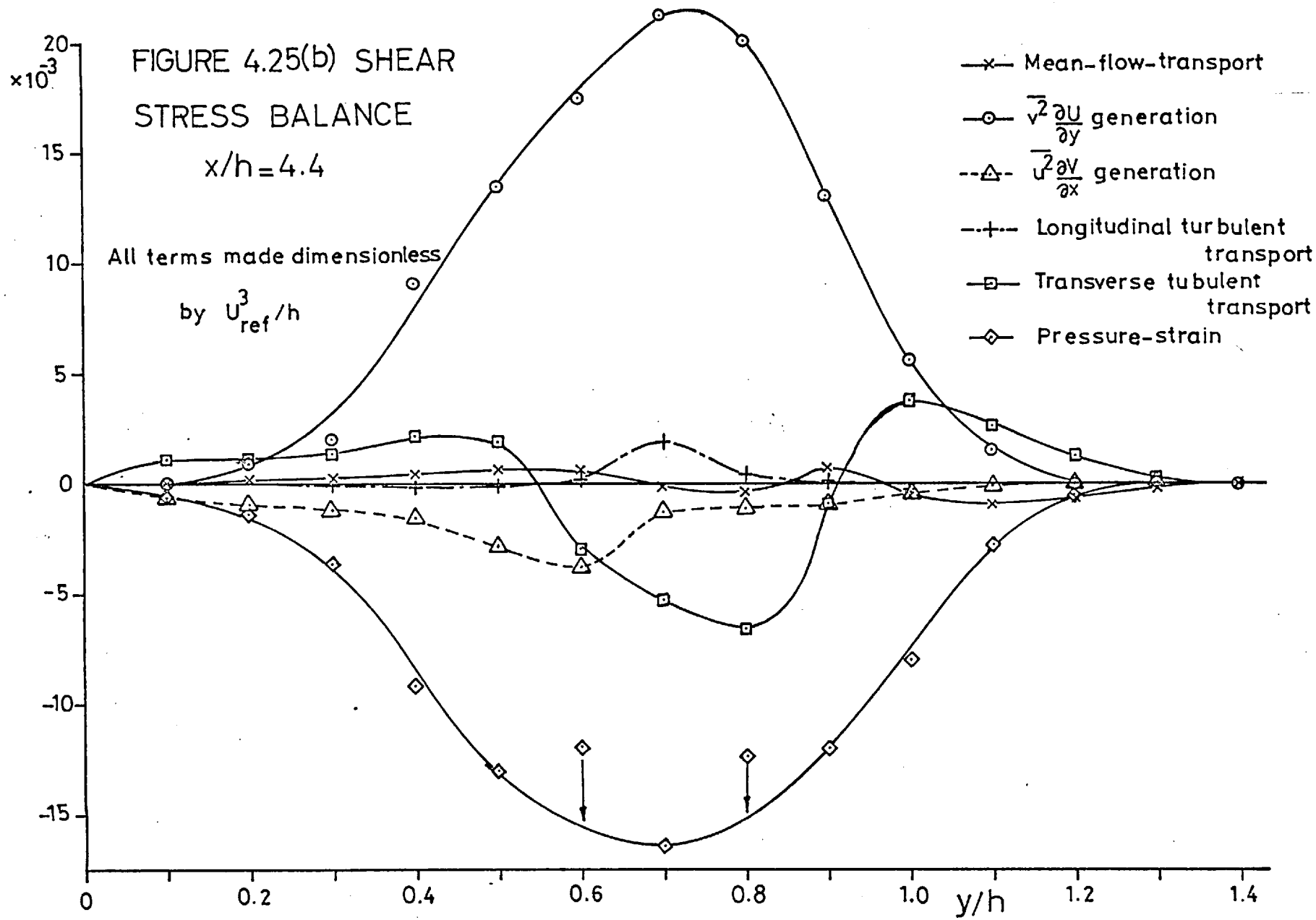


FIGURE 4.24(j) ENERGY BALANCE — x/h = 12.325


FIGURE 4.25(a) SHEAR STRESS BALANCE
x/h=3.4
All terms made dimensionless by U_{ref}^3/h
$\times 10^{-3}$
20
15
10
5
0
-5
-10
-15
Mean-flow-transport
$\overline{v^2}\frac{\partial U}{\partial y}$ generation
$\overline{u^2}\frac{\partial V}{\partial x}$ generation
Longitudinal turbulent transport
Transverse turbulent transport
Pressure-strain
0
0.2
0.4
0.6
1.0
1.2
y/h
1.4


FIGURE 4.25(b) SHEAR STRESS BALANCE
x/h = 4.4
All terms made dimensionless by U_{ref}^3/h
$\times 10^{-3}$
20
15
10
5
0
-5
-10
-15
0
0.2
0.4
0.6
0.8
1.0
1.2
1.4
y/h
Mean-flow-transport
$\overline{v^2}\frac{\partial U}{\partial y}$ generation
$\overline{u^2}\frac{\partial V}{\partial x}$ generation
Longitudinal turbulent transport
Transverse tubulent transport
Pressure-strain

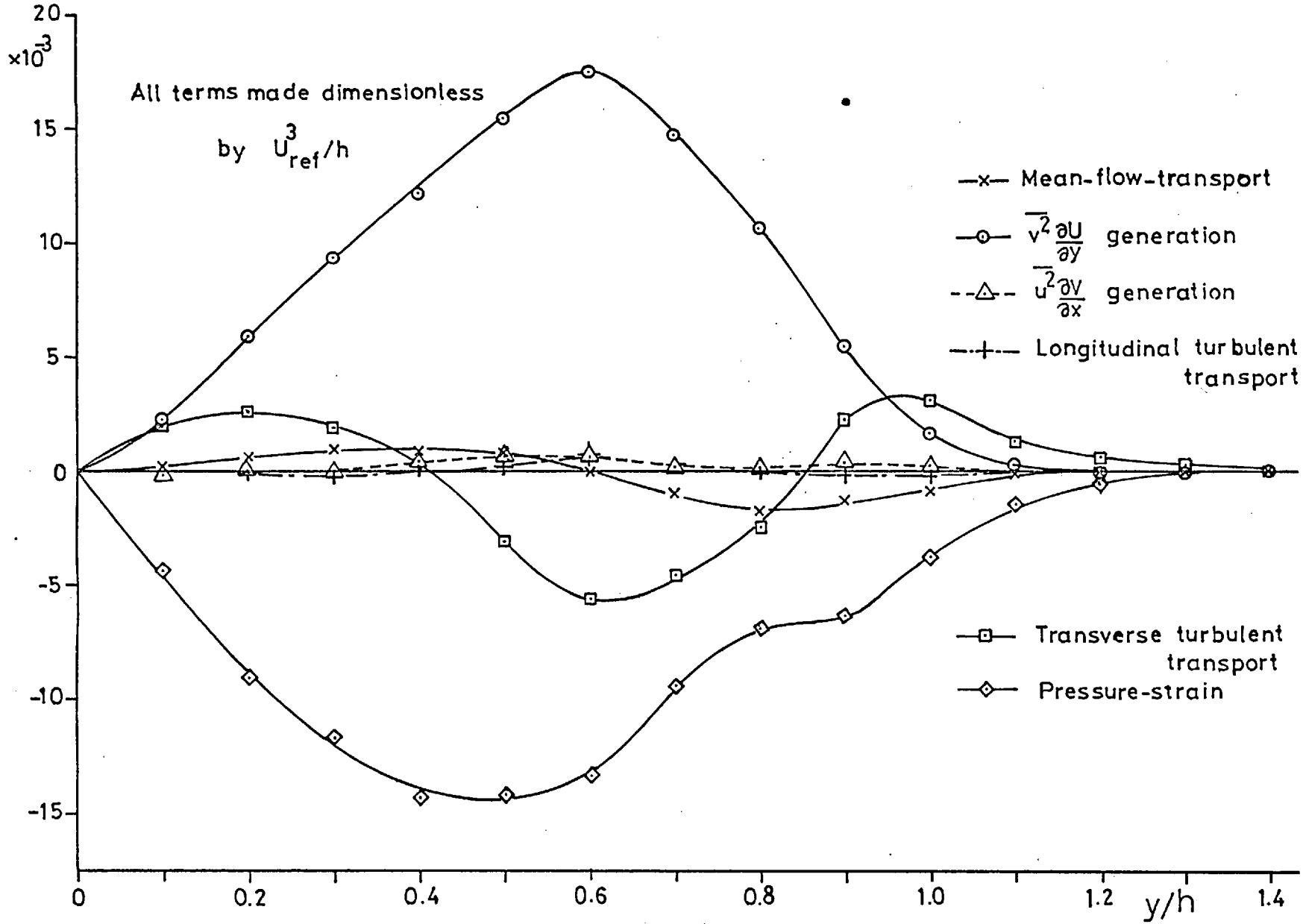


FIGURE 4.25(c) SHEAR STRESS BALANCE – x/h = 5.375

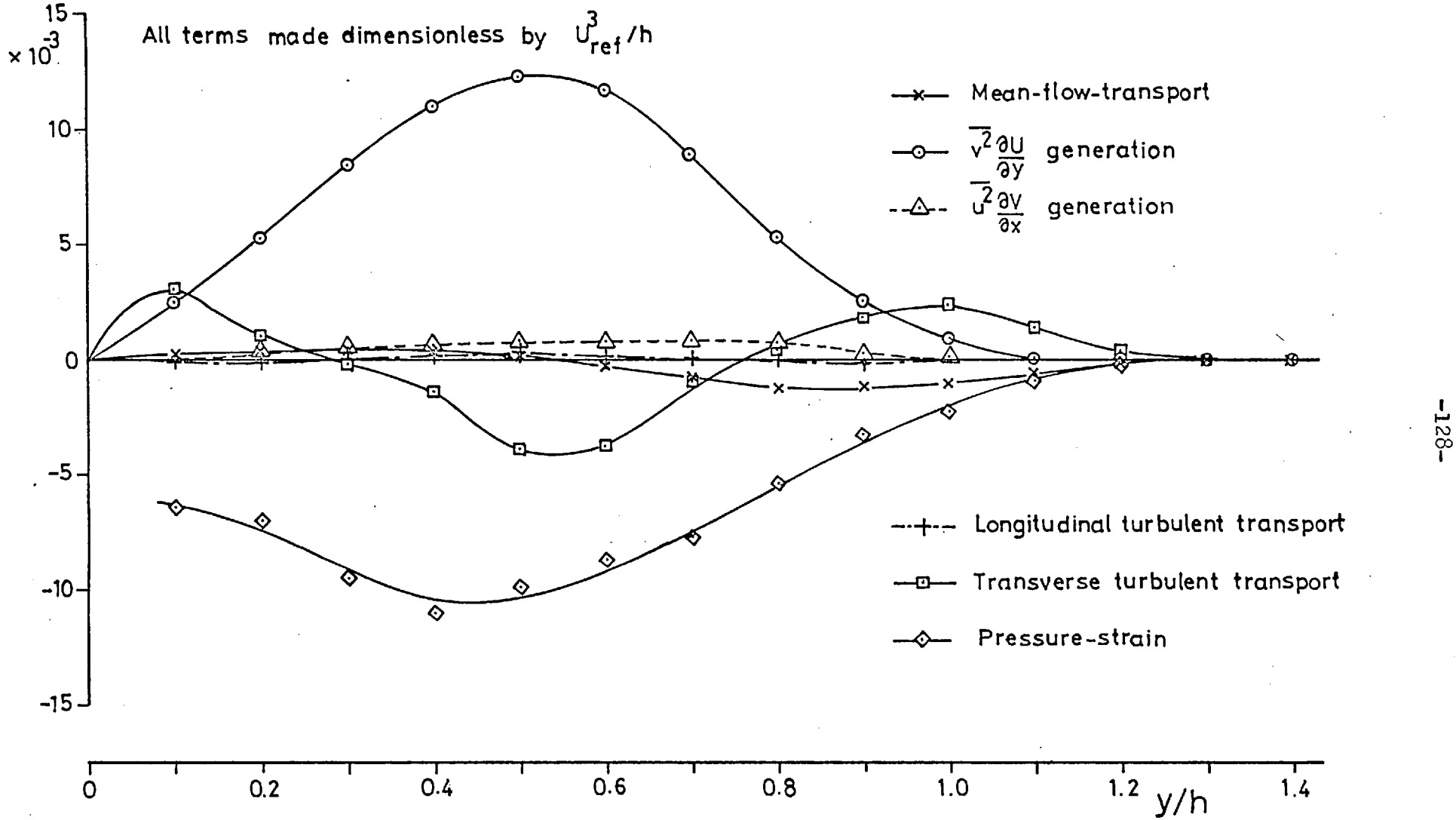


FIGURE 4.25(d) SHEAR STRESS BALANCE—x/h = 6.4

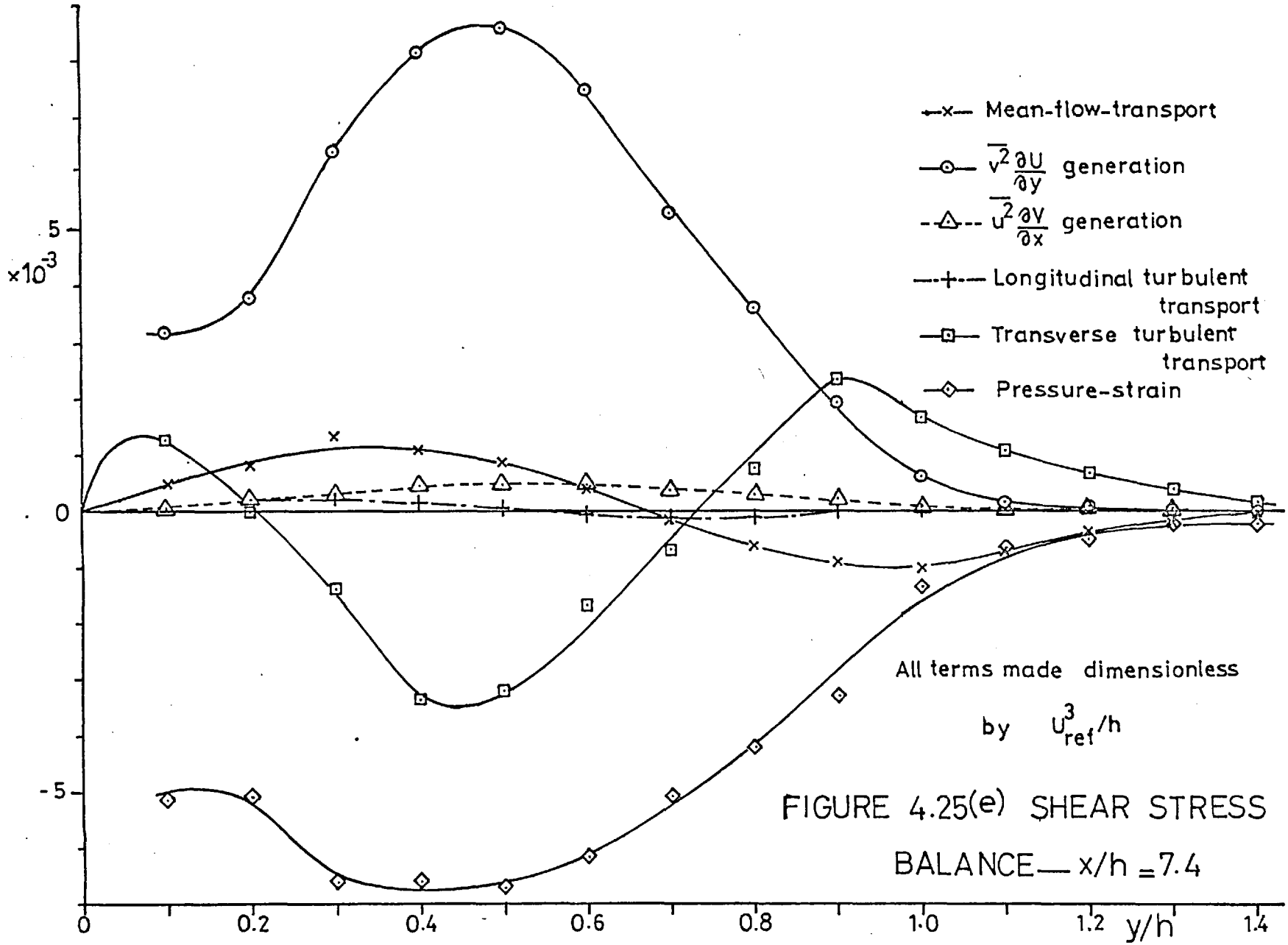


FIGURE 4.25(e) SHEAR STRESS BALANCE — x/h = 7.4

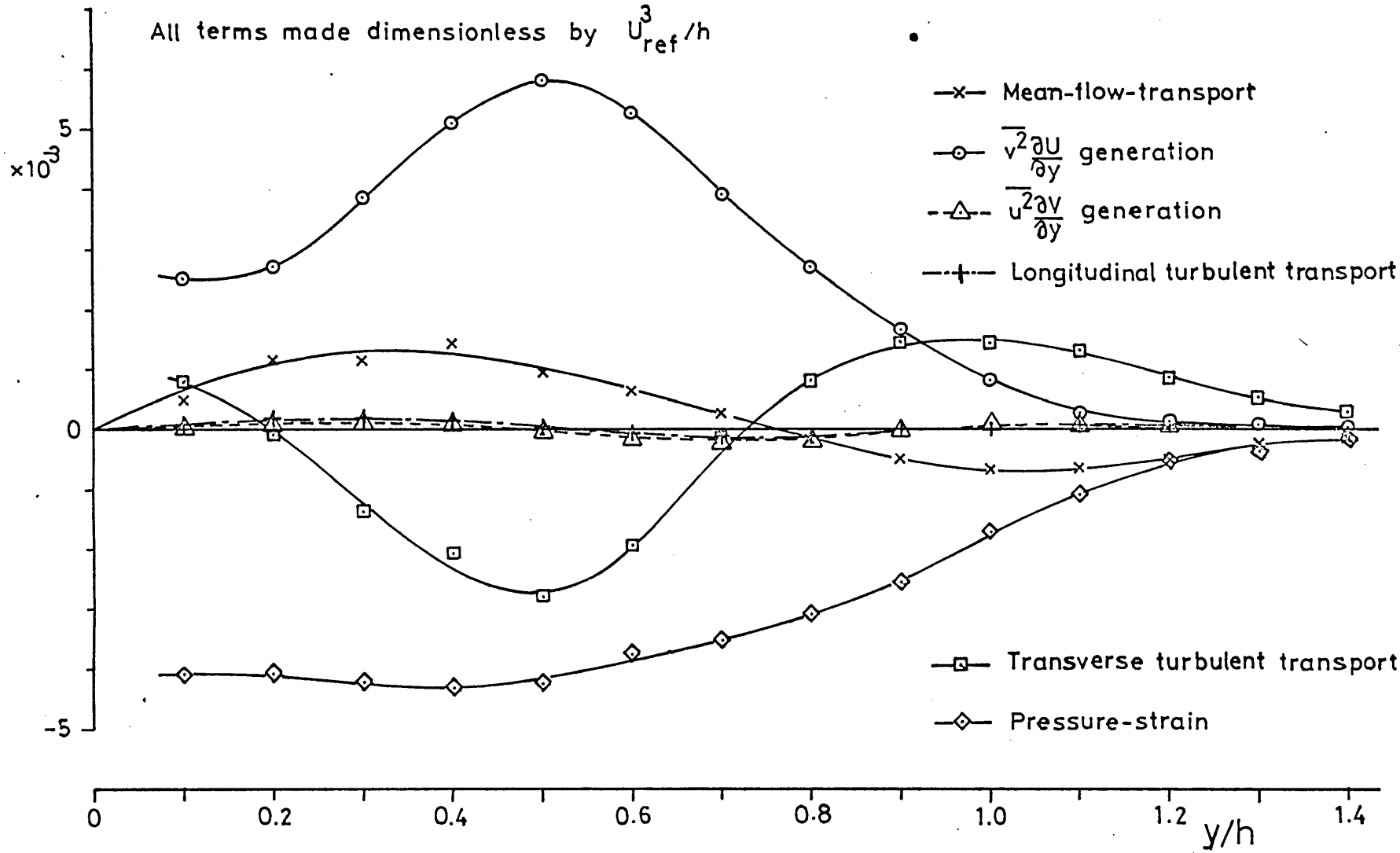


FIGURE 4.25(f) SHEAR STRESS BALANCE—x/h = 8.4

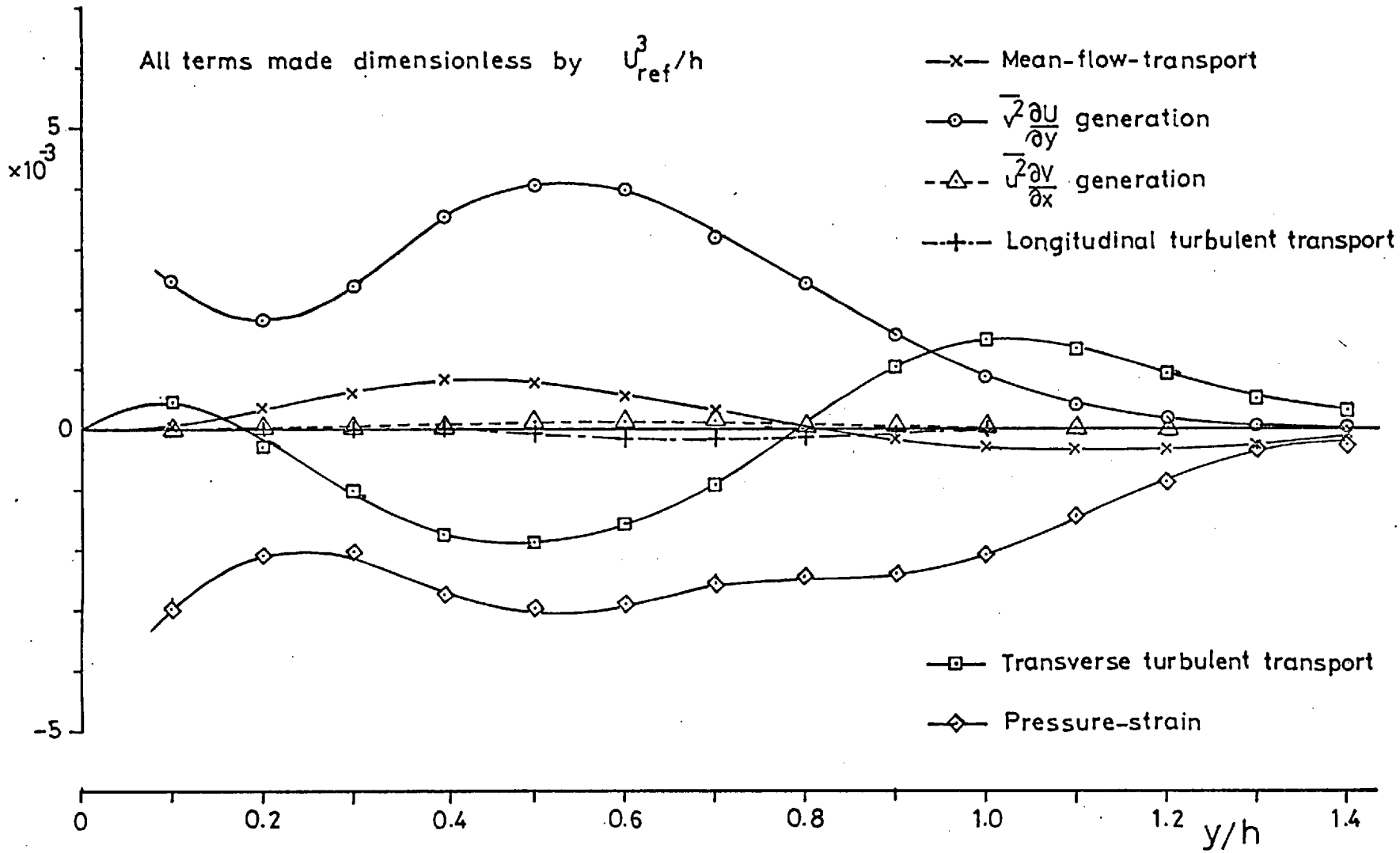


FIGURE 4.25(g) SHEAR STRESS BALANCE—x/h=9.325

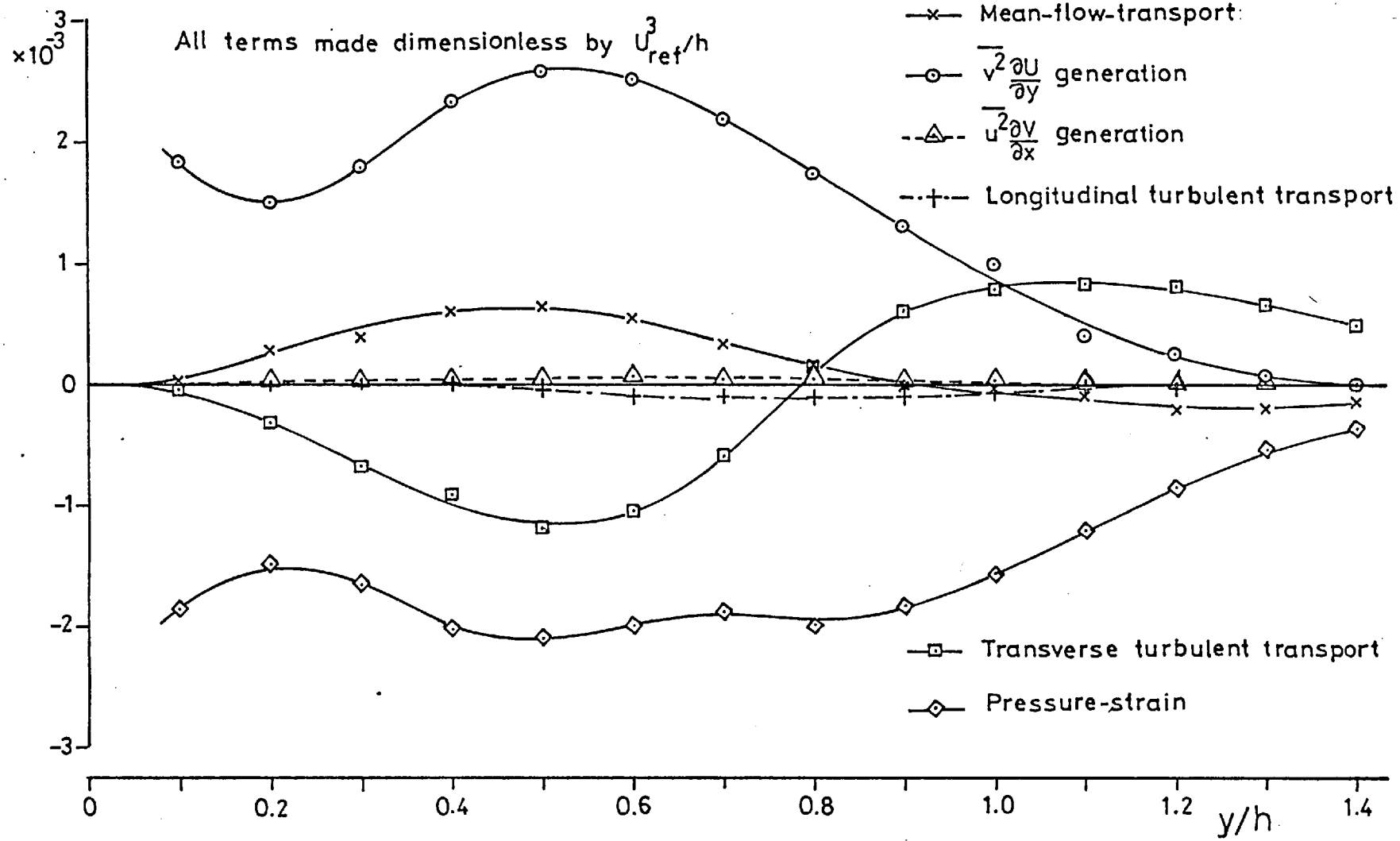


FIGURE 4.25(h) SHEAR STRESS BALANCE — x/h = 10.325

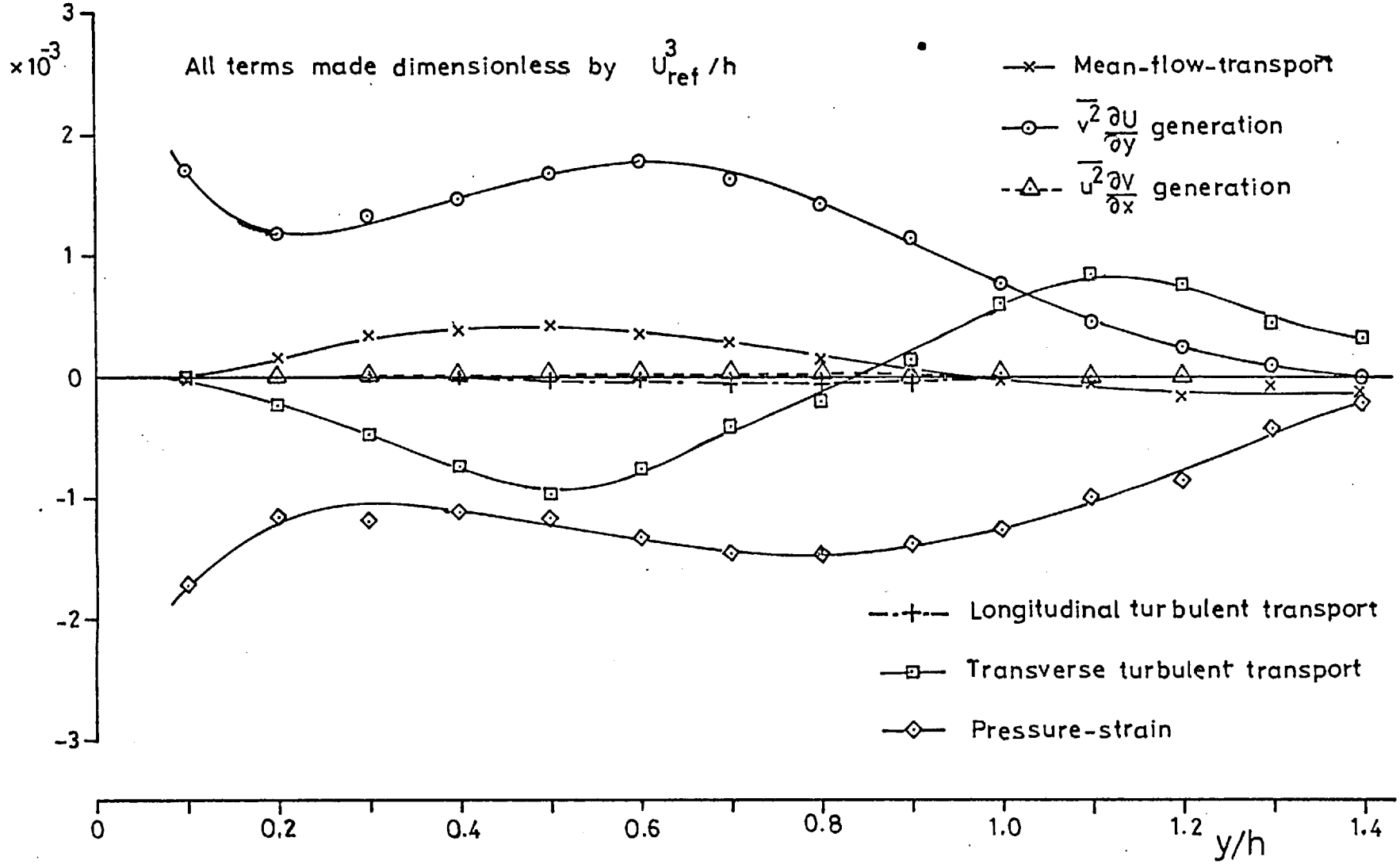


FIGURE 4.25(i) SHEAR STRESS BALANCE — x/h = 11.325

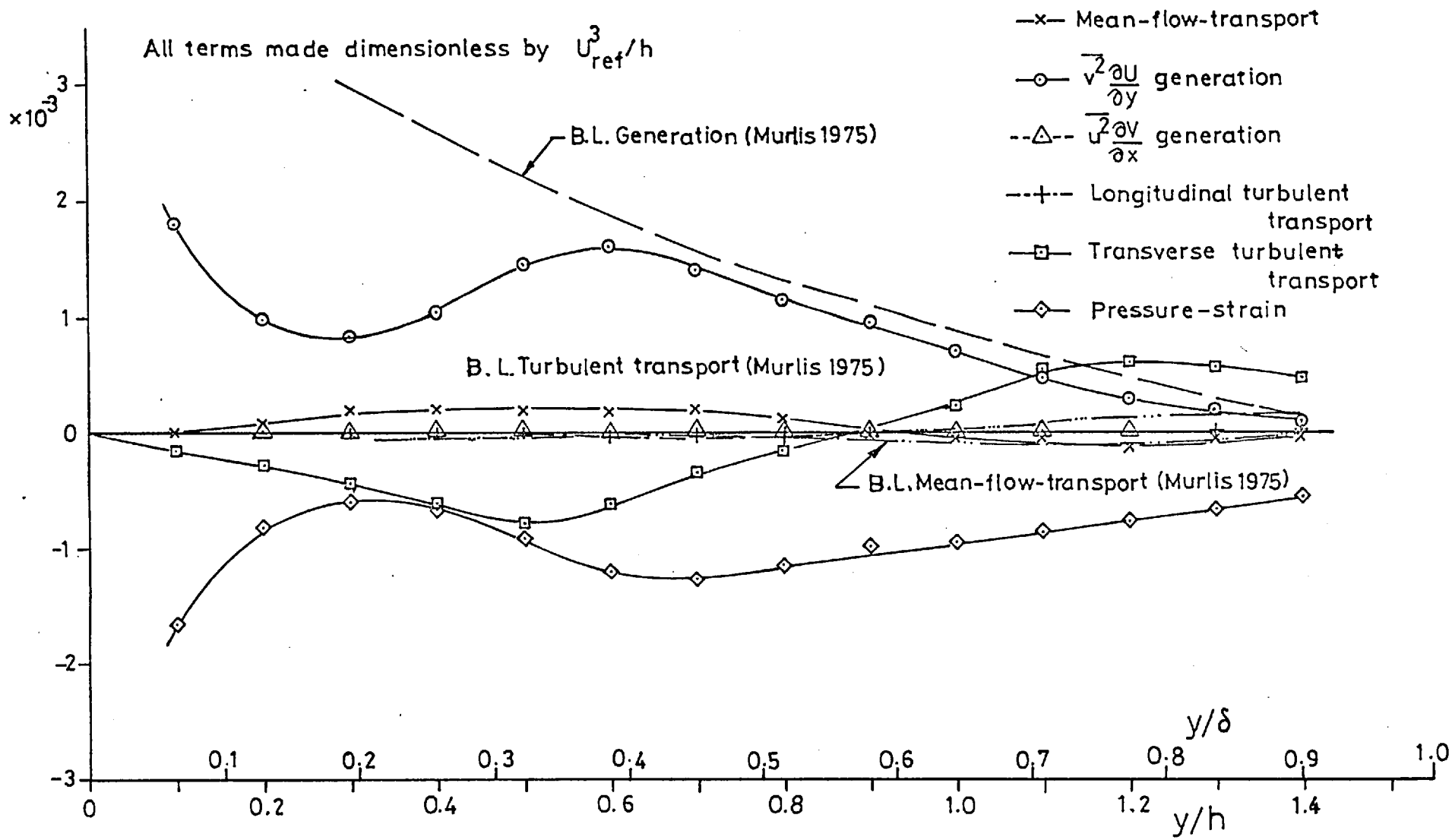


FIGURE 4.25(j) SHEAR STRESS BALANCE—x/h=12.325

CHAPTER 5

DISCUSSION OF RESULTS

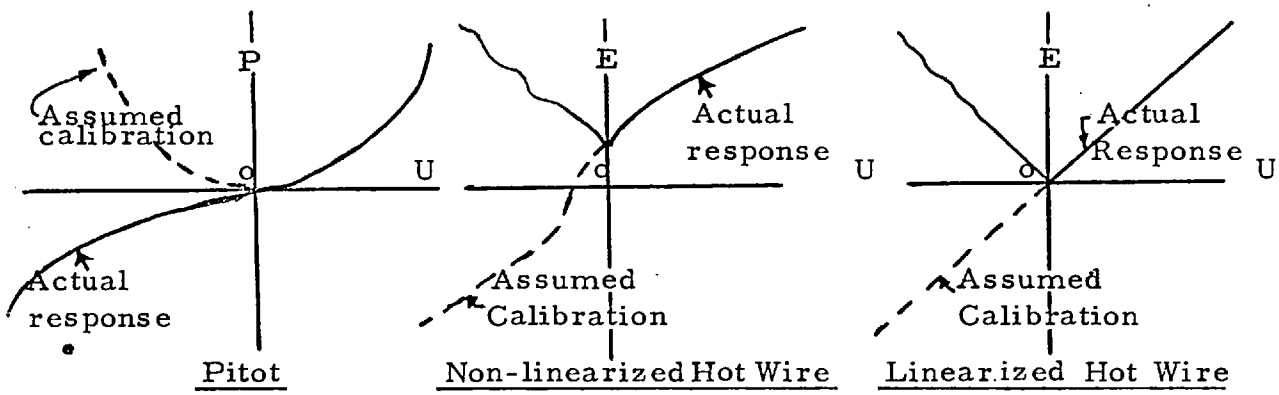
Most of the results obtained from the present work have been presented in the previous chapter with some immediate discussion. In this chapter a discussion in detail will be given, further derived results will be presented, and comparison with the results of other workers will be made when possible. As the work is a continuation of Wong's (1970) work, the discussion of the mean-flow results, which are qualitatively a repetition of Wong's, will be kept as brief as possible.

5.1. ZONES OF TRUSTWORTHY MEASUREMENTS

As already described in chapter 2, two basic types of instrument were employed in the present experiments, namely pressure probes and hot-wire probes. In the region of high turbulent intensity the accuracy of both types of instrument suffers considerably, and demarcation of the region where the results are untrustworthy is therefore necessary.

It has been shown in section 4.2. that the effect of high turbulent intensity on Pitot and disc-static probes, in measuring mean velocity, is much greater than on a hot-wire probe when the empirical formula in equation (4.5.a) for pressure probe correction is assumed, and the expression for hot-wire correction in equation (4.7) which is in effect due to cooling effects of turbulent intensity only, is used. There are, however, some other effects of high turbulent intensity, such as yaw and 'rectifying', that will lead to more significant errors in hot-wire results, and we shall return to this point shortly. Typical empirical formulae, as in equations (4.5.a) and (4.7), clearly indicate the dependence of error on local mean velocity; thus the term 'turbulent

intensity' in what follows will have the usual meaning of $\sqrt{\overline{u^2}}/U$, and not $\overline{u^2}/U^2_{ref}$ as previously used. A Pitot tube is almost as bad as a hot wire in a flow with reversals of direction, as shown in the sketches below; the results of both instruments obviously start to go badly wrong when the velocity instantaneously reverses.



Sketches showing Pitot tube and hot wire response in reverse flow

Equation (4. 5. a) for Pitot and disc-static probe correction may be written as

$$\frac{\Delta U}{U} \simeq \frac{\overline{u^2}+\overline{v^2}+\overline{w^2}}{2U^2} + 0.1 \frac{(\overline{u^2}+\overline{v^2})+\overline{w^2}}{2U^2} \quad (5.1)$$

$$\simeq \frac{\overline{u^2}+\overline{v^2}+3\overline{w^2}}{2U^2}, \quad (5.2)$$

since the second term on the right-hand-side is small compared with the other two terms. In the present results $\overline{v^2}$ in the highly turbulent region is roughly half of $\overline{u^2}$, and with the usual assumption of $\overline{w^2} \simeq (\overline{u^2}+\overline{v^2})/2$ equation (5.2) becomes,

$$\frac{\Delta U}{U} \simeq \frac{15}{8}\frac{\overline{u^2}}{U^2} \quad (5.3)$$

Using equation (5. 3) for a turbulent intensity, $\sqrt{\overline{u^2}}/U$, of 30%, the overestimation of mean velocity obtained from measurements with Pitot and disc-static probes is roughly 17%. Note that, in deriving equation (5. 2), the value of the constant c in equation (4. 5) is assumed to be unity; it has been pointed out in section 4.2. that the actual value may be less, in which case the error in mean velocity will be less than 17%.

The hot-wire results would also be greatly in error when turbulent intensity reaches a certain level regardless of the method of calibration used. Besides the nonlinear cooling effects of turbulent intensity components discussed above, Castro (1975) shows that in regions of high intensity there will be significant 'rectifying' errors, however complex the yaw-calibration, and it seems to be pointless to undertake such calibrations. As mentioned earlier, the conventional method of calibration was used in our case. Castro also points out the difficulty of assessing errors in hot-wire results; the best we can do is to define the regions where the results can be trusted quantitatively, or otherwise how large an error is to be expected in each region.

The estimates of limiting values of turbulent intensity, above which hot-wire measurements of mean velocity and turbulent intensity are unacceptably inaccurate, vary greatly from one worker to another. Hinze (1959) concludes that if errors of 10 to 20 per cent of $\sqrt{\overline{u^2}}/U$ in the measurement of turbulence are accepted, it is permissible to use the linearized small perturbation relation to measure flow with turbulent intensity of up to 20 or 25 per cent. Di Gesso (1975) quoted 20% turbulent intensity as the value above which he believes the hot-wire measurements will be unacceptably inaccurate. According to Bradbury (1975) and Castro (1975) however, the error is tolerable for a turbulent intensity less than 30 per cent. Mathew & Whitelaw (1973) also ruled out measurements in zones of turbulent intensity greater than 30% as uncertain.

As far as the mean-velocity measurement is concerned, Bradbury (1975) shows that errors estimated from a hot wire for $\sqrt{\overline{v^2}} / \sqrt{\overline{u^2}} \equiv k = 0.5$, 1.0 and 2.0 are approximately 1, 6 and 17 per cent respectively, when the apparent turbulent intensity is 30 per cent, above which errors increase very rapidly, becoming extremely large between 50 to 60 per cent intensity. In the present case k is only slightly greater than 0.5 and it is seen that even at 45% intensity the error in mean velocity is of the order of only 5%. Therefore, the mean velocity measured with a hot wire may be regarded as accurate in the regions where turbulent intensity is less than 40%, except of course when the mean velocity is near zero or reversed, provided it is free from other causes of errors. On the other hand, it has been shown that Pitot and disc-static probes are affected more by high turbulent intensity, and since all the subsequent results here are deduced from their results, the criterion of regions of reliable mean velocity measurements based on their behaviour is more appropriate. Allowing for the uncertainty in the expression for disc-static tube correction, it is probably quite safe to conclude that in the region where the turbulent intensity is less than 30% the mean velocity measured with pressure probes should be accurate to within about 15%. In the regions where mean velocity approaches zero or reverses, however, the pressure-probe results must be treated with reservation. It can be seen clearly that the unreliable region of mean velocity extends as far downstream as about 2 step heights from reattachment, and as high as about 0.7 step height above the surface at reattachment.

Bradbury's (1975) calculated results also show the errors in turbulent intensity measured with a hot wire to be about 1.5, 5 and 13.5 per cent, for k = 0.5, when apparent intensities are 30, 40 and 50 per cent respectively; the measured values are always underestimated. As in the mean velocity case, the errors in turbulent intensity increase very rapidly when the turbulent intensity is greater than 50%. It is

surprising that even with an apparent turbulent intensity as high as 50% the error is less than 15%, which seems rather too optimistic. It should be noted, however, that the errors will be slightly larger for values of k higher than 0. 5.

In general, considering mean velocity measured with pressure probes and turbulent intensity measured with hot wire and taking other possible effects - such as inclination of velocity vector in some regions, low local velocity or reverse flow etc.–into account, the following conclusion is possible. In the region where the intensity is greater than 50% - i. e part of the lower half of the free shear layer, the recirculation region and the reattachment region (shaded with slanted lines in figure 5.1.) - the results are highly unreliable and can only be interpreted qualitatively. The region outside 30% turbulent intensity contour in figure 5.1. (unshaded) may be regarded as the region of acceptably reliable measurements (systematic errors no larger than normal hot-wire traverses), whereas the results within the band of $30\% < \sqrt{\overline{u^2}}/U < 50\%$ (shaded with vertical lines in figure 5.1.) should be treated cautiously, in particular the mean velocity measured with pressure probes.

5.2. MEAN FLOW RESULTS

5.2.1. General Features of a Flow Field Involving Separation and Reattachment

Although the detailed characteristics of different flows involving shear layer separation and reattachment will differ a great deal, depending on body geometries, initial conditions at separation, streamwise pressure gradient, etc., we expect that the general features will be similar. For most flow configurations of practical interest, such as separation bubbles on aerofoils and turbine blades, the detailed characteristics are too complicated to be treated in a generalized manner; we therefore restrict our discussion to the

two-dimensional flow over a backward-facing step, the simplest geometry of all, which is the model used in the present work.

In the present experiments the initial boundary layer at separation is laminar and is very thin compared with the step height. Free shear layers are unstable at very low Reynolds numbers, however, and transition to a turbulent mixing layer follows soon after separation. Based on Bradshaw's (1966) rough criterion that the shear layer is fully developed by $x = 1000\theta_0$ from the separation point, transition in our case should be complete within about 2.2 cm (i.e. about half the step-height). Tani et al (1961), with a much thicker initial boundary layer compared with the step height, observed transition to turbulence to take place in the separated shear layer over a distance of about one step height. The thickness of initial boundary layer in relation to the step height has a great influence on the transition behaviour, and the mixing layer that follows (e.g. Crabtree (1957), Moore (1960)).

Since h/δ_0 here is quite large ($\simeq 25$), the strength of perturbation in our case falls into the 'overwhelming' category (see Bradshaw & Wong (1972) for classification of perturbations). In general, the strength of perturbation affects various parameters, such as transition distance, entrainment rate in mixing layer, reattachment distance, etc., in the recirculation and reattachment regions of flow over backward-facing step. In other words it is the factor that governs the general features and behaviour of this type of flow. Nevertheless, with 'overwhelming perturbation' it is believed that δ_0 no longer matters much; therefore we expect all flows in this category to behave in basically the same way.

The mixing layer curves towards the wall and eventually reattaches to it, forming a large recirculation region adjacent to the step corner (figure 4.1.). It was found by smoke-flow visualization of a plane mixing layer (Appendix I) that the orderly structure of eddies

generated in transition process does not seem to persist longer than a few wave-lengths; the same should be true for the moderately-curved mixing layer in the present experiments. The velocity profiles in figures 4.10(a) and (b) and the velocity contours in figures 4.11 and 4.12 show clearly the recirculation region. Although the mechanism of this separated-flow region, where reliable measurements with probes seem impossible at present, is extremely complex, its general qualitative behaviour is of interest because its influence dictates the downstream flow. Two main mechanisms in the recirculation region are the entrainment into the shear layer and the return of fluid from the reattachment point; the two are strongly correlated by mass-conservation requirements. Bradshaw & Wong (1972) conclude that the key to the behaviour of the relaxing boundary layer downstream of reattachment seems to be the rapid distortion of shear layer near reattachment, which depends on what fraction of the mass flow is deflected upstream to supply the entrainment. Brederode (1975) describes the relation between the several parameters that control the separated flow region. An increase in entrainment rate will cause the base pressure to decrease, the shear layer curvature to increase, the distance to reattachment to decrease, the attachment angle to increase and the fluid volume deflected at reattachment upstream to the recirculation region to increase. It is obvious that the attachment angle is not likely to exceed 90^{o}, thus only about half of the reattaching fluid in the shear layer, at the most, can return upstream to supply the entrainment in the recirculation region. The entrainment rate, on the other hand, depends mainly on the behaviour of the mixing layer, including the transition from laminar flow to turbulence in the present case. 'Reseparation' occurs in the recirculation region close to the step corner to form a secondary flow in the corner region, as evident from the smoke-flow and oil-flow flow visualization described earlier, but its direct effect on downstream flow is not likely to be large.

It is evident from the preceeding discussion that the ratio h/δ_o is one of the most important factors governing the separated-flow characteristics. It is probably best at this point to list all main factors, which may affect one parameter or another of the flow field, so that later discussion of other workers' results can be made more clearly; they are as follows:-

(i) Re, Reynolds number of flow, say $U_{ref}\delta_o/\nu$

(ii) δ_o/h , ratio of initial boundary layer to step height (i. e. the reciprocal of 'perturbation strength')

(iii) downstream pressure, i. e. h/(tunnel height),

(iv) geometry upstream of step, especially angle between top face and wall downstream.

Two points of interest in the reattachment region are the total layer thickness in comparison with other data and the manner which the shear layer actually reattaches. The importance of the latter is clear from the above arguments. In the present experiment the ratio of the total layer thickness at reattachment to the step height, δ_r/h, is about 1. 2 compared with the value of about 1. 5 found by Wong (1970) and Tani et al (1961). All other workers found much larger values, because the flow involved more than one separation bubble, because of the thicker boundary layer at separation or because of differences in imposed pressure gradient or tunnel height (i. e. factor (iii) listed above). The values of δ_o/h in Tani's and Wong's cases are 0. 28 and 0.12 respectively, whereas in the present case the value is 0. 04. Mueller & Robertson (1963) used a similar flow geometry but with much thicker initial boundary layer ($\delta_o/h \simeq 1.0$) and found $\delta_r/h \simeq 2.4$. The comparison suggests that the value of δ_r/h decreases with δ_o/h but increases with increasing imposed adverse pressure gradient (consider for example Arie & Rouse's (1956) results of $\delta_r/h \simeq 4.5$ for $\delta_o/h = 0$ in reattachment behind a normal plate).

Bradshaw & Wong (1972) also suggest that the eddies entering the bifurcation region (at reattachment) are themselves split, supporting their argument by the observation of decreasing length scale in the reattachment region. They further argue that if the large eddies were to be deflected alternately upstream and downstream (as was observed in our smoke flow visualization mentioned in section 4.1) rather than split one would expect strong unsteadiness to result, while McEwan (1964) found none. On the other hand, Tani et al (1961) remark that, although the pressure observed on the manometer was comparatively steady, repeated measurements sometimes yield slightly different pressure distributions, indicating the possibility of more than one type of flow pattern under the same boundary conditions. Tani et al regard this as typical of the flow separation associated with a step. This type of flow resembles the blunt trailing edge base flow with a splitter plate, which suppresses the periodical vortex shedding towards steadiness. The question arises whether the suppression is always perfect, attaining really steady flow in the separated region. Nash et al (1966) carefully surveyed the flow downstream of the step using a stroboscope and found no evidence of periodicity, but they make it clear that the term 'steady' is used for convenience and should be interpreted carefully. Mathews & Whitelaw (1973), in their plane-jet flow over a backward-facing step, found that although the problem of vortex shedding from the slot lip is diminished by the backward-facing step, the presence of periodicity due to the recirculation bubble cannot be ruled out. Mueller and Robertson (1963) conclude that variations in location of reattachment occur due to unsteadiness of the separation and wake flows. In the present experiment, manometer fluctuations, experienced while surface-pressure and the Pitot traverse readings were taken, indicate a certain degree of low-frequency unsteadiness to exist, particularly in the recirculation region and more strongly near reattachment. Thus the conclusions of ' the splitting of larger eddies at reattachment' and 'alternate deflection of eddies upstream and downstream at reattachment' seem to be equally possible, and it is

even more likely that both phenomena take place in random fashion.

Because the original shear layer in the present case is extremely thin compared with the step height, it should completely mix with the new shear layer before reattachment is reached, and no evidence of two adjacent shear layers is revealed in the velocity profiles. Downstream of the reattachment region, referred to as the relaxation region by Bradshaw & Wong (1972), we therefore have effectively a single shear layer with the possibility of developing a new sub-boundary layer on the surface as suggested by Bradshaw & Wong (fig. 4.1). The total layer thickness grows gradually downstream (see 0.995 total-pressure coefficient contour in figure 4.9). The boundary layer shape factor, $H = \delta^*/\theta$, of the present results agrees reasonably well with that of Wong (1970) where the two experiments overlap (Wong's measurements started from $x/h = 10$, whereas the last measuring station in the present work was 14.325): the slight difference is believed to result from the difference in pressure distribution downstream of reattachment in the two cases. The present results show that the value of H just downstream of reattachment is very large, which agrees with the results of Mueller & Robertson (1963), and decreases rapidly downstream. It should be realized however that the measurements in the reattachment region are hardly reliable, as pointed out in section 5.1.

5.2.2. Surface Pressure Distribution

The general shape of the surface-pressure distribution has already been commented on in section 4.2. (figure 4.3) with a short comparison of recompression Cp with other workers' results. The effect of Reynolds number on pressure distribution and the agreement of a plot of the present results in Roshko & Lau co-ordinates with others were also discussed (figures 4.4 and 4.5).

There remain a few points, with regard to surface pressure, for further discussion.

First of all the base pressure is mainly affected by all four factors listed in the previous section. Since base pressure is closely related to the entrainment rate on the lower side of the shear layer, it is expected to vary with Reynolds number at low Reynolds number, but effects will be significant only if δ_o/h is large. In the present experiment the base-pressure coefficient, which should be fairly constant over the step face, is found to be about -0.06 compared with the values of -0.07 to -0.08 of Tani et al (1961) with a laminar boundary layer at separation and δ_o/h ranging from 0.1 to 0.6. The Reynolds numbers in both cases are quite high and of the same order, i.e. $U_{ref}\,\delta_o/\nu \simeq 4200$ in the present case whereas it is about 4100 in Tani's case. In the measurements of Tani et al with a turbulent boundary layer at separation, δ_o/h ranging from 0.18 to 2.2 and Reynolds number of about 21,100, the base-pressure coefficients, C_{pb}, are still comparable in magnitude with the laminar-separation case, but have a slightly wider range, i.e. -0.06 to -0.09. It seems therefore true that there is virtually no effect of Reynolds number on base pressure at high Reynolds numbers. At low Reynolds numbers however, (Moore 1960) found that the values of base pressure on the step decreases rapidly with increasing Reynolds number based on displacement thickness at separation (laminar); for $\delta_o/h \simeq 1.0$ his results read $C_{pb} = -0.056$, -0.08 and -0.13 at $R_{e\delta^*} = 490$, 620 and 750 respectively (our $R_{e\delta^*} \simeq 1200$ and $\delta_o/h = 0.04$). The value $C_{pb} = -0.035$ of Tani et al with $\delta_o/h = 1.2$, comparable to that of Moore, show different trend from Moore's because the Reynolds number is much higher ($R_{e\delta^*} \simeq 1180$). It is thus clear that the effects of Reynolds number and δ_o/h interact strongly and must be considered together. Tani et al were able to conclude from their results that, except for a very small step height,

the base pressure is essentially the same for different step heights and boundary layer thickness; but the preceding discussions show that their conclusions only apply when Reynolds numbers are high.

On the other hand, Wong's (1970) value of the base-pressure coefficient -0.13 is much lower than the present results and those of Tani et al, when both Reynolds number and δ_o/h are of the same order ($R_{e\delta_o} \simeq 5480$, $\delta_o/h = 0.12$ in Wong's case). This is probably a result of the imposed downstream pressure gradient. This effect is also believed to be responsible for low C_{pb} of about -0.2 found by Nash et al (1966) (subsonic case with $R_{e\delta_o} \simeq 1.66 \times 10^5$, $\delta_o/h=2.4$,) and Bearman (1965) ($R_{e\delta_o} \simeq 3.5 \times 10^4$, $\delta_o/h = 0.5$). The effect of geometry upstream of the step, the last factor, listed above, may be seen for example in the results of Mueller and Robertson (1963) and Mueller et al (1964) where ledges were used instead of a backward facing step; they found C_{pb} in the range -0.3 to -0.4. Furthermore, Moore's results exhibit fairly constant pressure in the region close to the step because of prolonged laminar separated-shear-layer, whereas in the present results, in agreement with those of Wong, Tani et al and Nash et al, the pressure drops slightly just downstream of the step before it starts to rise. It is therefore clear that the various conclusions made by previous workers with regard to base pressure at the face of the step cannot apply generally, but limited to some particular conditions only. Thus, in using the existing data for any purpose, all factors as listed above must be carefully taken into account.

The study of all available data for the surface-pressure distribution downstream of a backward-facing step shows that, with the exception of the data of Tani et al, the reattachment point always lies upstream of the point of maximum pressure, i.e. the pressure recovery overshoots the value required to reattach. This is confirmed by simple momentum arguments. Tani et al (1961), without stating

means of determination, claim the reattachment distance to be 7 step heights which falls behind the point of maximum pressure for all their cases; this does not seem possible, therefore their value of reattachment distance quoted may be in error. In an attempt to correlate the reattachment position with the pressure distribution, the present author found that the reattachment position can be closely approximated by drawing a straight line through the almost linear portion of pressure rise extended to intersect with the line parallel to the x-axis passing through the point of maximum pressure, as shown in figure 5.2. The projection of the point of intersection onto the x-axis will represent the approximate reattachment point. When applying this method to the present results and those of Wong (1970), the difference between the reattachment distance determined from pressure distribution in this way and that from surface flow visualization is found to be less than 1.5%. whereas for Nash's (1966) data for $M = 0.4$ the difference is about 7.5%. For other workers' data the accuracy of the quoted reattachment distances in some cases is rather doubtful. Nash et al (1966) use 'recompression parameter', $N = \frac{Cpr-Cpb}{(-Cpb)}$, which is constant for particular conditions, to express the position of the reattachment point with respect to overall pressure rise downstream of separation; it seems to apply only in supersonic flow. The present empirical method for subsonic flow over a backward-facing step may prove useful when no facility for determining reattachment position is available, or when only rough value is required. Application of the method to the Roshko & Lau's plots in figure 4.4 confirms this idea as should be expected because their reduced co-ordinates are nothing more than generalized way of scaling. The increase in discrepancy to about 3% in Wong's case using these co-ordinates, if not due to the error in deducing the curve, reflects on the accuracy of the measured reattachment distance; for the present results it is almost exact.

5.2.3. Total Pressure Profiles

The parameter referred to in this thesis as 'total pressure coefficient', defined by equation (4.4), is the measure of total pressure with reference to the tunnel static pressure rather than the tunnel total pressure as, for example, used by Nash et al (1966); thus it tends to unity in the external stream. The individual profiles of C_{PT} shown in figures 4.8(a) to (c) show that the experimental points fall onto well-defined smooth curves, indicating a high degree of consistency of the results. If the transverse pressure gradient $\partial p / \partial y$, were zero, as it is far downstream of reattachment, the shapes of these profiles would represent the square of the velocity profiles. In using these curves it is instructive to plot contours of constant total-pressure coefficient as in figure 4.9. The 0.995 contour corresponding to the variation of boundary-layer thickness in the present context has been noted in section 4.2. Figure 4.9 shows clearly that the directions of increasing total pressure (potential lines or lines perpendicular to the constant-pressure lines - not shown) at different parts of the flow field, especially in the recirculation region, do not follow any simple pattern, except of course that, far downstream all contours tend towards the direction parallel to the wall. The number indicating the value of C_{PT} on each contour must be interpreted carefully; for example, the line $C_{PT}=0$ simply means the total pressure there is equal to the tunnel reference static pressure, and negative values merely indicate the region where total pressure falls below the reference static pressure.

5.2.4. Static Pressure Profiles

The transverse variation of the static-pressure coefficients as plotted in figures 4.7(a), (b) show that the measured values differ significantly from the corresponding values of surface pressure up to about 9 step heights downstream of the step. It should

be noted that, in the results presented here, no attempt has been made to correct for high turbulent intensity discussed in section 4.2 or any other effect, since no correction method for disc-static probe is known to the author. In general the profiles do not extrapolate very well to the surface-pressure values, except far downstream and the station closest to the step, and they have been forced to do so in most profiles. The discrepancy is large near reattachment, about 8% of C_{ps} for the worst case, and gradually decreases downstream; the good agreement at the station $x/h = 6.4$ is coincidental. The consistent scatter of the point closest to the surface in all profiles is probably caused by the effect of wall proximity and turbulence on the probe. In the recirculation region the static pressure is less than the corresponding surface pressure everywhere, but the main-stream static pressure on the opposite side of the mixing layer is greater because of streamline curvature. For the same reason the static pressure downstream of reattachment is less than the corresponding surface pressure everywhere up to about 9 step heights from the step, after which the main-stream pressure returns to more or less the value at the surface and variation across the boundary layer is almost negligibly small. Cochrane (1971) made static-pressure traverses at $x/h \simeq 2.8$ and 5.1 and found a similar variation to ours at the latter station, but the scale used in his report does not permit a worthwhile comparison.

Since part of the recirculation region from the step to about 4 step heights downsteam, where local velocity is comparatively small, involves negative C_{ps}, the assumption of constant pressure across the layer would result in a great over-estimation of mean velocity, which is probably the reason for the implausibly high velocity in this region reported by other workers, e.g. Wong (1970). The present results show that at about 4 step heights downstream of the step the largest error in static pressure caused by the above mentioned assumption is of the order of 0.04 in the region where U/U_{ref} is ranging from virtually zero to about 0.3, the overestimation in the mean velocity would thus be from about 23% to an extremely high

percentage. Taking the point x/h=3.4, y/h=0.4 as a second example, C_{ps} is less than the surface-pressure coefficient by about 0.03 which would result in the mean velocity overestimation of about 84% because the mean velocity there is very small (approx. 0.13 U_{ref}). Outside this region C_{ps} is positive everywhere, in which case the assumption would result in under-estimation of the mean velocity. The present static-pressure distribution clearly suggests that this assumption, as usually made in the case of thin shear layer, is not applicable within the region of about 9 step heights downstream of the step, if an error of less than 5% in mean velocity is required; at x/h = 8.4 the largest error in mean velocity would be roughly 6%, whereas at x/h = 9.4 it is only about 4%.

5.2.5 Mean Velocity Profiles

The individual mean velocity profiles in figures 4.10(a) to (c) are typical of flow behind a backward-facing step. The discrepancy between Pitot and hot-wire results has been discussed in section 4.2. The general shape of the profiles is comparable with all other workers' results, in particular those of Wong (1970) and Tani et al (1961). The magnitude of the reverse-flow velocity of the present results is believed to be fairly accurate, except at the station x/h = 4.4 where the reverse-flow calibration of Pitot tube was used, because the variation in static pressure across the layer has been accounted for as discussed in the previous section. Immediately downstream of reattachment the velocity profiles appear to have significant defect close to the surface, but the flow rapidly accelerates, as found in Wong's and other workers' results. This clearly exhibits the distortion of shear layer caused by the reattaching process.

The contours of constant mean velocity in figures 4.11 and 4.12 show clear demarcation of the recirculation region from the main flow as well as showing how the mean velocity varies in both longitudinal and transverse direction. It is interesting to observe the ways contours tend towards infinity in the external stream region:

the particular pattern at about 8 to 10 step heights downstream of the step is due to the streamwise variation of the main-stream velocity which decreases markedly from the tunnel exit to a minimum at about 7 step heights downstream before increasing very slowly with further distance downstream (see also figure 4.18). However, the total-pressure contour in this region is quite straight (figure 4.9).

5.2.6. Semi-Logarithmic Profiles and Skin Friction

The semi-logarithmic plots of velocity profiles deduced from Pitot and static pressure measurements, as shown in figures 4.14(a) and (b), are similar to those found by Wong (1970) whose measurements started at $x/h = 10$. The dip below the universal logarithmic 'inner law' profile, which is also noted by Wong (1970) and Bradshaw & Wong (1972), seems to start from about $x/h = 7.4$; the profile at $x/h = 6.4$ which is very close to reattachment shows no such dip. The comparison between the results made with pressure probes and hot-wire probe in figure 4.14 (c) shows that there is hardly any dip at all in the hot-wire case at $x/h = 7.4$, whereas at $x/h = 12.325$ the dip in hot-wire case is somewhat less than that in the Pitot case. Since high turbulent intensity results in an overestimation in the Pitot results but underestimation in the hot-wire results as discussed earlier, and if we assume the true profile lying somewhere in between, it is probable that the decrease in Pitot overestimation is more rapid than the decrease in hot-wire underestimation as the turbulent intensity rapidly decreases with increasing y. The skin friction coefficient plot in figure 4.6. shows that dC_f/dx is extremely large in this region; therefore about 30% error in C_f would not show serious scatter compared with other results. It is therefore rather difficult to decide which result is more reliable. However, no matter which instrument is employed the dip characteristic is still present.

The dip increases both in depth and width as the distance increases downstream, which is somewhat different from Wong's

results; this is possibly because C_f in the present results is deduced from fitting close to the surface. The same reason may also apply to the appearance of the strength of 'wake component' to become negative downstream of about x/h = 12, contrary to Wong's results of slight increase after reaching zero. The strength of the wake component near reattachment ($C_f = 0$) is of course extremely high; as noted in section 4.2, experimental points for higher y^+ of the profile at x/h = 6.4 have been omitted to suit plotting space. Full discussion of semi-logarithmic velocity profiles from downstream of x/h = 10 is given in detail by Wong (1970) and Bradshaw & Wong (1972) and the present results yield no worthwhile addition. Nevertheless, a few profiles that fill the gap between reattachment to those of Wong show similar trend to Wong's but with smaller dip and stronger wake component as noted above. Furthermore, the reasonable agreement in the values of skin friction coefficients obtained from the Stanton tube measurements and calculation using 'log-law', as observed in section 4.2 (figure 4.6), suggests the approximate applicability of the 'log-law' even very close to reattachment. On the other hand, the failure of the local-equilibrium formula in this region indicates the possibilities of the rapid change of turbulence in streamwise direction so that the length scale of the turbulence is not proportional to y, as observed by Bradshaw & Wong (1972) and Antonia & Luxton (1972).

5.3 FLUCTUATING QUANTITY RESULTS

5.3.1 Turbulent Intensities

The discrepancy between the normal-wire and the cross-wire results of $\overline{u^2}$ has been discussed in the previous chapter and the cross-wire results have been accepted as more reliable with regard to experimental errors. It can however be seen in figures 4.19(a) to (e) that the disagreement is severe mostly in the 'untrustworthy' region of measurements discussed in section 5.1 (figure 5.1). Nevertheless, qualitative information about various

quantities in this region can still be extracted. Moreover, there is encouragingly little scatter of the experimental points in all sets of results, even in the very-high-intensity region.

Close to the step ($x/h = 0.5$ in figure 4.19(a)) the region of large $\overline{u^2}/U^2_{ref}$ and $\overline{v^2}/U^2_{ref}$ is restricted to a narrow band about a step height above the surface, indicating that at about half a step height downstream of separation the free shear layer is still comparatively thin and that transition to turbulence has already taken place, which supports the comment made in the previous section concerning transition occurring very close to the separation point. It should however be realized that, although $\overline{u^2}/U^2_{ref}$ is very small in the recirculation region, the turbulent intensity in the usual context (i.e. $\sqrt{\overline{u^2}}/U$) is quite large here because of extremely low mean velocity, and would become mathematically infinite at points of zero velocity. Figure 5.3 clearly indicates that serious error in $\overline{v^2}/U^2_{ref}$ measured with the crossed wires at $x/h = 0.5$ has occurred.

As the downstream distance increases the width of the high-intensity band increases rapidly and is roughly as large as the step height at reattachment. This behaviour can be seen more clearly in the contour plots in figures 4.20, 4.21 and 4.22. Also shown in these contour plots are the loci of maximum intensity. For the normal-wire results in figure 4.20, the locus curves down from $y \simeq h$ towards the surface and reaches a constant height of $y/h \simeq 0.5$ at about 7 step heights downstream of the step, whereas the loci of both $(\overline{u^2}/U^2_{ref})_{max}$ and $(\overline{v^2}/U^2_{ref})_{max}$ from cross-wire results (figures 4.21 and 4.22) curve down in similar manner but attain the lowest height of $y/h \simeq 0.4$ at about 7.5 step heights then curve up to a constant height of $y/h \simeq 0.5$ at about 10 step heights. In view of almost constant $\overline{u^2}/U^2_{ref}$ from the surface to about $y = 0.5\,h$ in each profile downstream of $x/h \simeq 9$ (see figures 4.19 (i) to (l)), the 'maximum' should be regarded as the point where the departure from a constant value occurs, and it is not very well defined; the peak

would eventually tend to $y \simeq 0$ further downstream. Surprisingly, Bradshaw & Wong's (1972) only intensity measurements at $x/h = 10$, and Tani's (1961) last measuring station at $x/h \simeq 15$, both show distinct maximum-intensity points. Bradshaw & Wong's results shows the peak intensity to occur at $y = 0.6h$, $x/h = 10$, but at $x/h = 15$ in the measurements of Tani et al the maximum is only about $y = 0.5h$.

Figure 5.3 shows the variation of $(\overline{u^2}/U^2_{ref})$ max and $(\overline{v^2}/U^2_{ref})$ max in the streamwise direction with the values of Castro's (1973) plane-mixing layer referred to Ue at x=0 rather than U_{ref}) for comparison. It should be noted that $(\overline{u^2}/U^2_{ref})$ max from the cross-wire results is presented here. Comparison with Castro's values confirms the approximate plane-mixing layer behaviour in the region up to about 2 step heights from the step. The scatter of $(\overline{v^2}/U^2_{ref})$ max is much smaller even in the reattachment region. By comparing the two curves, it is seen that the magnitude of $(\overline{v^2}/U^2_{ref})$ max is approximately half that of $(\overline{u^2}/U^2_{ref})$ max up to the reattachment region, after which $(\overline{v^2}/U^2_{ref})$ max increases to about $\frac{2}{3}$ of $(\overline{u^2}/U^2_{ref})$ max a downstream. Both quantities decrease further downstream.

Comparison of maximum turbulent intensities with other workers' data is made in figure 5.4. The data of Tani et al (1961) and Gesso (1975) have been chosen for the purpose. Gesso, by comparing his results with those of several investigators, concludes that the conventional method of hot-wire analysis (derived for low turbulent intensity) was responsible for the wide discrepancy found in the comparison and claims the 'squared signal' analysis to offer more flexibility than the conventional analysis; but his results show even deeper dent in the plot of maximum intensity against x near the reattachment region than that in our results. On the other hand, it is surprising that the results of Tani et al show a peak in the region where a dent occurs in the present results, and the dent in their results

appears downstream of the reattachment region. It is possible that dents appearing in these results are experimental errors because of the difficulty in obtaining reliable measurements near reattachment as observed above. Although there is no way to decide which results are more reliable, they all show the same trend, i. e. the maximum intensity increases to a peak somewhere near reattachment then decreases remarkably rapidly, with the exception that Gesso's results should have the larger second hump downstream of the reattachment which does not seem very plausible. The agreement between the present results and those of Tani et al downstream of about x/h = 7, both in magnitude and shape, is considered satisfactory.

The contours of $\overline{u^2}/U^2_{ref}$ from U-probe and X-probe (figures 4. 20 and 4. 21) do not differ greatly in pattern. As expected, both show small waviness in the region adjacent to the free stream where gradients are small, just as the total-pressure contours do. For the U-probe case, the rather disordered patterns in the recirculation region and in the region close to the surface downstream of about x/h = 9 are probably an indication of experimental error. On the other hand, the X-probe results show more uniform decrease in turbulent intensity downstream of reattachment, and even with too few data points in the recirculation region the pattern suggests a gradual slope towards a region of low intensity at the corner of the step. Cochrane (1971), in his contour plot in terms of turbulent intensity percentage, found the same characteristics, but his plot shows a second small region of peak intensity, on the surface between x/h≃3 to 5 , of about $\frac{2}{3}$ the main peak intensity appearing above the reattachment region. In general Cochrane's contour pattern is more like our cross-wire results than our normal-wire results, except that the region of highest intensity in our cross-wire results is upstream of rather than above the reattachment region, whereas the location of maximum $\overline{u^2}/U^2_{ref}$ in the normal-wire results agrees with his. It is nevertheless extremely difficult to decide which set of results is more reliable because these measurements are in the 'untrustworthy' region referred to in section 5. 1.

The contours of $\overline{v^2}/U^2_{ref}$ (figure 4.23) follow closely the pattern of $\overline{u^2}/U^2_{ref}$, except in the former case there exist almost parallel contours downstream of reattachment which should eventually meet the corresponding upper contours to form closed loops far downstream.

5.3.2 Turbulent Shear Stress

Figures 4.19(a) to (l) show the general shapes of $-\overline{uv}/U^2_{ref}$ profiles at different streamwise stations downstream of the step, which resemble closely the shapes of $\overline{v^2}/U^2_{ref}$ profiles. The locus of maximum turbulent shear stress, as shown in the contour plots of figure 4.23, behaves in the same way as those of $\overline{u^2}/U^2_{ref}$ except that a kink appears after minimum distance from the surface is reached at about $x/h = 7.5$ before it starts to rise slowly. This may well be simply caused by experimental error due to difficulty in defining the maximum points of the profiles, as discussed in the previous section. The streamwise variation of the maximum shear stress, shown in comparison with other workers' data in figure 5.5 (see also the comparisons with $\overline{u^2}/U^2_{ref}$ and $\overline{v^2}/U^2_{ref}$ of the present results and shear stress of Castro (1973) in figure 5.3), suggests an almost linear rapid increase soon after transition and reaches the highest value at about $x/h = 3.5$, after which it decreases slightly to a fairly constant value in the reattachment region before further rapid decrease downstream. Its shape is quite similar to that of $\overline{u^2}/U^2_{ref}$ and its magnitude is roughly $\frac{1}{3}$ of $\overline{u^2}/U^2_{ref}$ almost everywhere.

A comparison of the present results with those of Tani et al (1961) and Gesso (1975) is of interest (figure 5.5). The results of Tani et al show an almost linear rapid increase towards reattachment point, then a sudden drop to asymptotic value at about 12 step heights downstream of the step. The peak of their curve occurs at the shoulder of the constant part of the present results, and its magnitude is much

higher than our peak value. It is unfortunate that their data does not extend further upstream beyond x/h = 4, but extrapolation seems to suggest a continuous increase all the way from the start of transition. Downstream of about x/h = 8 their values of maximum shear stress are comparable with the present results, but ours show further decrease beyond x/h = 12 rather than tending towards an asymptote as appeared in their results. In contrast, Gesso's (1975) results show a sudden decrease from a very high value of maximum turbulent shear stress at about x/h = 2 to an almost constant value from about x/h = 5 onwards. The magnitude of the constant maximum turbulent shear stress in the reattachment region is comparable with the present results. The high value near separation point may be due to the turbulent boundary layer at separation in his case. Therefore the present results seem to agree quite well, although in parts, with the two cases compared, and it may be concluded that the turbulent shear stress is large - roughly as large as in a plane mixing layer - in the mixing region nearly up to reattachment but then decreases very rapidly.

The contour plots of $-\overline{uv}/U^2_{ref}$ in figure 4.23 exhibit all the features discussed above, for instance the long strip of plateau along the locus of maximum turbulent shear stress between x/h≃4. 5 to 7 corresponds to the constant value of $\overline{uv}/U^2_{ref}$ in this region. The contour pattern also shows a very small turbulent shear stress (referred to x, y-axes) in the recirculation region and everywhere close to the surface (as it must vanish at the surface). In general, the pattern of the turbulent shear stress is similar to those of $\overline{u^2}/U^2_{ref}$ and $\overline{v^2}/U^2_{ref}$ as might be expected because uv depends on the correlation between u and v.

5.3.3 Triple Products of Fluctuating Velocity

Since in the present work only logitudinal and transverse fluctuating velocities were measured, the measured triple products as yielded by the DIG2U computer program (Weir & Bradshaw 1974) are $\overline{u^3}$, $\overline{v^3}$, $\overline{u^2v}$ and $\overline{uv^2}$, normalized as usual by U^3_{ref}. The profiles of all these products are shown in figures 5.6 to 5.9. The scatter in all cases is no more than one would expect and all profiles seem to be fairly well behaved.

Figures 5.6 (a) and (b) show $\overline{u^3}/U^3_{ref}$ at all traverse stations. Close to the step the non-zero part is restricted to a narrow region corresponding to the width of the shear mixing layer which then spreads out with the distance downstream in the same way as in the case of the turbulent intensities discussed above. The zig-zag shape with positive and negative peaks of the same order of magnitude ($x/h = 0.5$) is similar to results of other workers on mixing layers, e.g. Castro (1973). The much higher negative peak at station $x/h = 1.875$ shows that obvious error has occurred. The distance of the negative peaks from the surface varies in the same manner as those of maximum turbulent intensities and maximum turbulent shear stress, namely dipping down from about one step height close to the step to reach the minimum of about 0.75h at about 6 step heights from the step before slowly increasing downstream to attain a height of about $0.9/$ step heights at the last measuring station of $x/h = 12.325$. At the same time the height of the positive peak drops towards the surface. The magnitude of the negative peak rapidly increases to a value of about 0.2×10^{-3} at about 2 step heights and stays almost constant up to about 7 step heights, then slowly decreases to about half its value at the last measuring station; whereas the magnitude of the positive peak increases comparatively slowly towards maximum of approximately the same order then rapidly decreases and almost vanishes at about 11 step heights.

The profiles of $\overline{v^3}/U^3_{ref}$ in figure 5.7 have similar features to those of $\overline{u^3}/U^3_{ref}$ except for the reverse sign and the much smaller magnitudes. The scatter in this case is slightly worse, at a few traverse stations just downstream of reattachment, than the $\overline{u^3}/U^3_{ref}$ case. The general behaviour of $\overline{u^3}/U^3_{ref}$ discussed above applies equally well to $\overline{v^3}/U^3_{ref}$ by simply changing sign. Furthermore, $\overline{u^2v}/U^3_{ref}$ profiles as shown in figure 5.8 behave like $\overline{v^3}/U^3_{ref}$ but with larger magnitude and slightly shifted positions of peaks, whereas $\overline{uv^2}/U^3_{ref}$ profiles in figures 5.9 (a) and (b) follow those of $\overline{u^3}/U^3_{ref}$ closely except for the smaller magnitude and the disappearance of dents on positive peaks in the reattachment region. In brief, all four triple products are quite closely proportional throughout the flow, all being measures of turbulent transport by the large eddies.

The table below shows the comparison of various approximate peak values at x/h = 4.375 and 12.325 in the present work with the values found by Castro (1973) in the self-preserving region of a plane free-mixing layer. Although the mixing region in our case is curved and cannot attain the self-preserving state before reattachment, the comparison seems instructive. It shows that all values of peak triple products before reattachment in our case are higher than the

QUANTITIES	CASTRO'S RESULTS x=52.2cm (Self-preserving region)	PRESENT RESULTS	
		x/h = 4.375	x/h = 12.325
$\overline{u^3}/U^3_{ref} \times 10^3$ + MAX	2.5	1.8	0
- MAX	-1.5	-2.3	-1.0
$\overline{v^3}/U^3_{ref} \times 10^3$ + MAX	0.45	0.80	0.44
- MAX	-0.55	-0.66	0
$\overline{u^2v}/U^3_{ref} \times 10^3$ + MAX	0.6	1.0	0.36
-MAX	-0.6	-0.4	0
$\overline{uv^2}/U^3_{ref} \times 10^3$ +MAX	0.6	0.84	0
-MAX	-0.6	-0.80	-0.35

corresponding values of Castro except $\overline{u^3}$ which is the reverse, i.e. positive peak is smaller but negative peak is larger in the present case. This suggests that even close to reattachment large-eddy structure of the mixing layer is still intact. Our results also suggest that all profiles of triple products are single-sided curves at downstream of reattachment as expected when the shear layer is relaxing towards a constant-pressure boundary layer.

The triple-product profiles of Murlis' boundary layer are included in comparison with profiles at x/h = 12.325 of the present results. Since Murlis' Reynolds number is about half that of the present work the skin friction coefficient in his case will be approximately 20% higher: therefore all his values have to be scaled by $1/(1.2)^{3/2}$. The similarity in shape of Murlis' profiles and ours is striking, although his data are more scattered. It is seen that even at our last measuring station the values of triple products are still extremely large compared with those of Murlis' ordinary boundary layer (different scales used for Murlis' profiles should be noted). Our values in $\overline{u^3}/U^3_{ref}$, $\overline{v^3}/U^3_{ref}$, $\overline{u^2v}/U^3_{ref}$ and $\overline{uv^2}/U^3_{ref}$ are approximately 17, 40, 20 and 27 times those of Murlis, respectively; suggesting that relaxation of the large eddy structure to the final boundary layer state is very slow, although gross quantities like C_f appear to asymptote quite quickly.

5.3.4 Statistical Description of Turbulence

The DIG2U computer program output also includes several statistical quantities, viz. u- and v- component flatness factors ($\overline{u^4}/(\overline{u^2})^2$ and $\overline{v^4}/(\overline{v^2})^2$), u- and v-component skewness factors ($\overline{u^3}/(\overline{u^2})^{3/2}$ and $\overline{v^3}/(\overline{v^2})^{3/2}$) (Weir & Bradshaw 1974). The flatness factors are plotted against y/δ_{995} for all traverse stations in figures 5.10(a) to (d). In order to obtain reasonably large scales so that minimum values (required for intermittency factor calculation: see next section) can be determined more accurately, the higher values of flatness factors are omitted in these plots. It is interesting to note the changing

shape of the profiles from highly irregular in the recirculation region to more or less smooth profiles of typical shape far downstream. The scatter is indeed very small. Both u- and v-component behave almost the same way even in the recirculation region: the v-flatness factor is larger everywhere except at the first station close to the step and in the region near the boundary-layer edge at all other stations. Except in the recirculation region where unsystematic irregular shape is to be expected, the u-flatness factor profile of roughly parabolic-like shape starts off in a narrow region corresponding to the narrow separated shear layer, then as the distance increases downstream, the wiggling part is gradually stretched out, the parabola gets wider and shallower on the low-velocity side with the other arm remains steep, and the whole parabola slowly moves towards the surface. The drop in values of u-flatness factor on the free-stream side at $x/h = 0.5$ is curious. Just upstream of reattachment ($x/h = 5.375$) the profile shows a skewed parabolic shape with both arms are almost equally steep. Downstream of reattachment the near-surface arm gradually becomes almost flat at the last traverse station, $x/h = 12.325$. The minimum value of u-flatness factor seems to fluctuate somewhat, from place to place (figure 5.11), and is mostly smaller than the typical value of about 3 for a fully turbulent boundary layer (Murlis 1975). The locus of minimum u-flatness factor in figure 5.12 follows closely the loci of maximum $\overline{u^2}$ and $\overline{v^2}$ (see figures 4.20 to 4.22) except downstream of about $x/h = 7.5$ where the latters are higher; it is seen that the locus of u-flatness factor curves down rather smoothly towards a constant distance from the surface of roughly 0.3h. The low values of u-flatness factor obtained in the present experiment are of interest as it indicates the more orderly structure of eddies. However, the inconsistency of the results suggests that experimental error cannot be completely ruled out. In the mixing region, the minimum u-flatness factor is fairly constant at just less than 2.6

compared to the value of 2.7 found by Castro (1973).

Townsend (1956) explains that abnormally high $\overline{u^4}/(\overline{u^2})^2$ indicates high inhomogeneity in u-component turbulent intensity, but such explanation hardly throws any light on the physical behaviour of the present flow. On the other hand, if the signal has a normal (Gaussian) distribution during its 'on' periods and is 'off' for a fraction $(1-\gamma)$ of the total time, then

$$\frac{\overline{u^4}}{(\overline{u^2})^2} = \frac{3.0}{\gamma}, \qquad (5.1)$$

when γ= intermittency factor. It is obvious from equation (5.1) that a high value of flatness factor corresponds to low intermittency factor, i.e. highly intermittent motion, and vice versa. The behaviour of the u-flatness factor described above therefore suggests, on the basis of equation (5.1), that the intermittency is moderate but irregular in the recirculation region and reattachment region, and is extremely strong near the edge of the boundary layer, as expected. However in the recirculation region there are no true 'off' (non-turbulent) periods. We shall turn to the discussion of the intermittency again in the next section.

Although the v-component flatness factor, also shown in figure 5.10, has no direct bearing on the interpretation of the results except the indication of the inhomogeneity of v-component turbulent intensity, it is presented here for comparison purposes (because if γ's calculated from u - component and v-component flatness factors are not equal, both are suspect) as well as for the sake of completeness. Nevertheless, the close resemblance in its shape with that of u-flatness factor shows that $\overline{v^2}$ distribution everywhere is very much like that of

$\overline{u^2}$, except in the region close to the surface where the v-flatness factor tends to much higher value than that of u-flatness factor. Its minimum value is slightly higher than that of u-flatness factor almost everywhere and is closer to the normal distribution, which is rather surprising. Furthermore, the locus of minimum v-flatness factor (also shown in figure 5.12) does not decrease monotonically as that of u-flatness factor, but the departure is not very large.

Both u- and v-component skewness factors are plotted for each traverse station in figure 5.13(a) - (f). The most obvious features are that u- and v-skewness almost always have opposite signs and comparable magnitude and that one of their zeros coincides or lies close together. The scatter is a little worse than that of flatness factors but not too excessive. Figure 5.14 shows the loci of main zero locations of u- and v-component skewness factors, which clearly seen to behave in the same manner as the loci of minimum flatness factors, viz. curve down asymptotically towards the surface. Note that the curve in this figure is drawn for visual aid only. Above this line u-skewness factor is negative up to a certain point, whereas v-skewness factor is positive, and conversely so in the region below the line. Thus on the free-stream side region u^3 has more frequent negative values while v^3 has more frequent positive values. Close to the step, in the recirculation region, the values of both skewness factors seem to be fairly constant. Downstream of reattachment the region of positive u-skewness factor and negative v-skewness factor is restricted to a very narrow strip adjacent to the surface and their magnitudes are very small, indicating the near symmetry of probability distribution near the surface. It is also interesting to note how the shapes of u- and v-skewness factors change, and it is seen that the parabolic shape of the v-component skewness spreads with y much faster than that of the u-component.

5. 3. 5. The Intermittency

The intermittency factor, γ, defined in the usual way, at a point considered as

$$\gamma = \frac{\text{time spent in turbulent flow}}{\text{total time}} \qquad (5.2)$$

which is also yielded by DIG2U computer program when subroutine THRESH, as described in section 4. 3, is employed, is plotted against y/δ for each traverse station in figures 5.15(a) - (f). Also plotted for comparison in each figure is the intermittency factor determined from

$$\gamma = \frac{\text{minimum value of u-flatness factor}}{\text{u -flatness factor}} . \qquad (5.3)$$

Although the agreement in magnitude is poor, the profile shape of from the two definitions follows each other quite well. The value γ_{max} obtained from the relation (5. 2) is about 0. 9 in every profile, whereas that obtained from (5. 3) is nominally 1. 0. Castro (1973) in his plane mixing layer experiment, argues that irrotational fluid must sometimes reach the centre of any shear layer so in logic γ_{max} must be less than unity. One obvious reason why γ_{max} fails to reach the value of 1. 0 when using the usual definition is the behaviour of the signal chosen as turbulence criterion: as mentioned earlier, the first or second derivative of (uv) with respect to time has been chosen in our case. In using the definition (5. 3) we have forced γ_{max} to attain unity at the point of minimum flatness factor, or close to unity when no corresponding experimental point is available at minimum flatness. The approximate location of γ_{max} obtained from both methods is plotted versus distance downstream in figure 5.16, which shows similar behaviour to those of minimum flatness factors and zero skewness factors in figure 5.12 and 5.14 respectively, except the curvature of γ_{max} is much smaller close to the step. The agreement of the values of γ_{max} obtained from the two methods is reasonable. Figure 5.16

suggests that γ_{max} will eventually occur close to the surface further downstream as would be expected in ordinary boundary layer, although at our last measuring station it is still somewhat away from the surface. The effect of the proximity of solid boundary on hot-wire measurements may be partly responsible for the apparent delay.

The scatter of γ within the recirculation region is to be expected, because on the lower edge of the separated shear layer in the present case is not very meaningful, but it is interesting to note that its value is fairly constant at about 0.8. Beyond $y/\delta_{995} \simeq 1$ where γ is supposed to approach zero, the results show abnormally high values of γ in some profiles which is thought to be caused by the failure of the present computer program to discriminate irrotational signals or noise from the extremely low turbulence signals. The available noise-clip subroutine has not been used in the present results.

It is plausible to define the interface of turbulent/non-turbulent regions as the line $\gamma = 0.5$, as shown in figure 5.17 for the present results. The value of $(y/\delta_{995})_{\gamma = 0.5}$ downstream of reattachment up to near the end of our working-section is just below 0.6 and seems to be surprisingly constant, whereas the typical value of $(y/\delta_{995})_{\gamma = 0.5}$ in an ordinary boundary layer is about 0.8 (see for example Klebanoff 1955, Kovasznay et al. 1970, and Murlis 1975). It is thus clear that practically half of the shear layer downstream of reattachment contains highly intermittent eddies, and the prolonged almost constant $(y/\delta_{995})_{\gamma = 0.5}$ suggests that it will take some time to regain the value of ordinary boundary layer. This conclusion agrees fairly well with the results of Antonia and Bradshaw (1971) (also described by Bradshaw and Wong 1972) who found $(y/\delta_{995})_{\gamma = 0.5}$ of about 0.65 at the station about 30 step heights downstream of the step.

It can be shown that the experimental results of intermittency factor for ordinary boundary layer can be approximated very closely by means of the Gaussian probability distribution (Rotta 1962),

$$-\frac{\partial \gamma}{\partial y} = \frac{1}{\sqrt{2\pi}\sigma} \exp\left[-\frac{(y-\bar{y})^2}{2\sigma^2}\right], \qquad (5.4)$$

where $\bar{y}$ = mean thickness of the boundary between turbulent and non-turbulent flow. The equation (5.4) leads directly to

$$-\left(\frac{\partial \gamma}{\partial y}\right)_{max} = \frac{1}{\sqrt{2\pi}} \cdot \frac{1}{\sigma}, \qquad (5.5)$$

or

$$-\left(\frac{\partial \gamma}{\partial (y/\delta)}\right)_{max} = \frac{1}{\sqrt{2\pi}} \cdot \frac{\delta}{\sigma} . \qquad (5.6)$$

The values of the standard deviation, σ, for the measured and flatness intermittency at $x/h = 12.325$ are $0.28\delta_{995}$ and $0.25\delta_{995}$ respectively, compared with the $0.13\delta_{995}$ of Murlis (1975) and the $0.12\delta_{995}$ of Klebanoff (1955) in ordinary boundary layer. Since the standard deviation is a suitable measure of the width of the intermittency zone, i. e. of the amplitude of the waves in the free-stream boundary, our intermittency zone at $x/h = 12.325$ is practically twice of that in an ordinary boundary layer, which agrees with the comments made above with regard to the value of $(y/\delta_{995})_{\gamma = 0.5}$

Figure 5.18 shows the plots of intermittency factor versus U/U_I at $x/h = 3.4$ and 12.325 in comparison with other results. It should be noted that U/U_r is used in Castro's results: U_r is the reference velocity at the wind tunnel contraction exit. In the present results only the measured values are presented: the flatness intermittency would be slightly higher than the measured values. Within the expected experimental errors, all curves of the non-boundary-layer cases seem to collapse pretty well together and are still far distant from the boundary layer values. That the flow behind a backward-facing

step, even as far downstream as 30 step heights, is still highly intermittent in the main part of the layer, and that it will take much longer distance downstream to return to the equilibrium state of boundary layer, is once again confirmed.

5.4 THE TURBULENT ENERGY BALANCE

The discussion will be sub-divided into three distinct flow regions, viz. upstream of the reattachment region, the reattachment region, and downstream of the reattachment region. Although the names of different terms in equation (4.11) (section 4.4) are labelled, separate components of some terms rather than their sum are presented in figures 4.24(a) to (j) as tabulated below. It is probably worth mentioning that, in determining these derivatives graphically, approximate smooth

TERM	NAME
$= (U\frac{\partial}{\partial x} + V\frac{\partial}{\partial y})(\frac{1}{2}\overline{q^2})$	Advection
$-\overline{uv}\,(\frac{\partial U}{\partial y} + \frac{\partial V}{\partial x})$	Shear-stress production
$-(\overline{u^2}\frac{\partial U}{\partial x} + \overline{v^2}\frac{\partial V}{\partial y})$	Normal-stress production
$-\frac{\partial}{\partial x}(\frac{1}{2}\overline{q^2 u} + \frac{\overline{pu}}{\rho})$	Longitudinal diffusion
$-\frac{\partial}{\partial y}(\frac{1}{2}\overline{q^2 v} + \frac{\overline{pv}}{\rho})$	Transverse diffusion
ϵ	Dissipation

curves have to be drawn through scattered data points in some cases, and that the obtained values (slopes of curves) are very sensitive to the choice of these approximate curves. Because of this (among many other things) great accuracy is not to be expected. As a whole, the scatter of data points in the turbulence energy balances is not unreasonable, and certainly not more than one would expect when a graphical method is employed. The approximate streamwise variation of peak values of the main energy terms are shown in figure 5.19 , and the approximate location of these peaks in figure 5.20. Figures 5.21 to 5.24 are cross-plots, showing streamwise variation of shear-stress production, dissipation, tranverse diffusion and advection, at various values of y. Note that in conformity with Townsend (1956) energy loss is plotted upwards, energy gain downwards.

5.4.1 Upstream of the Reattachment Region

The region from the step to about 5 step heights involves a curved free shear layer and recirculation with high rate of entrainment. The resemblance of the shapes of various curves in figure 4.24(a) ($x/h = 3.4$) to those of Castro (1973) clearly suggests that the flow in this region may approximate to a plane mixing layer. However, quantitative correspondence is not to be expected, but relative magnitudes of various quantities should be sufficient for the present discussion.

Production

Castro's results show a very small loss (positive) of energy due to normal-stress production restricted to a narrow region near the 'still air' edge of the layer, whereas in our case (figure 4.24(a)) a comparatively large loss spreads from about $y = h$, with maximum at about $y = 0.7h$, down to approximately $y = 0.3h$ in the recirculation

region. Since the shear layer in this region is inclined to the x, y - axes with respect to which shear-stresses are evaluated, therefore, some of the normal-stress production would, in fact, be the component of shear-stress production in axes aligned with the shear layer. Strong entrainment, as well as reverse flow, may also be partly responsible for this apparent large loss of energy, as compared with that of the plane mixing layer. As the distance increases downstream towards reattachment, the magnitude of energy loss, due to normal-stress production, decreases only slightly, but the location of the maximum moves rapidly towards the surface and the spread extends down to the surface (figures 4. 24(b) and (c).

- The shear-stress production, whose profile is almost symmetrical about the centre of the shear layer, is the dominant source of turbulent energy as in Castro's results. Even if the two components of production in the present results were summed, the shape of the overall production profile would, more or less, retain its symmetry. The peak gain of energy due to shear-stress production decreases rather rapidly downstream towards reattachment, i. e. at almost constant rate of about $\frac{1}{3}$ of its initial value within 2 step heights (figure 5.19), and its location moves towards the surface (figure 5. 20). The symmetry is retained throughout this region with broader distribution across the layer corresponding to the increasing thickness of the shear layer. As we do not have data close to the step, the peak of the shear-stress production close to the step suggested by figure 5.19 cannot be investigated. It is presumably associated with transition rather than with the recirculating flow. Although the streamwise variation has very little meaning in this region because the shear layer is inclined to the axes, it is interesting to notice a very rapid increase of shear stress production along the y = constant lines, reaching maximum near reattachment, in the lower part of the layer up to about y/h = 0. 6, and a rapid decrease in the upper part

of the layer (figure 5.21). This merely indicates that the region of high shear-stress production moves towards the surface as the free shear layer curves down to reattach. Figure 5.25 shows rather slow streamwise decrease of total production across the layer, $\int_0^\delta \overline{uv}(\frac{\partial U}{\partial y} + \frac{\partial V}{\partial x})dy/U_{ref}^3$ towards reattachment at almost constant rate, which is the same trend as the streamwise variation of peak shear-stress production except that the latter decreases more rapidly. Although the way in which the curve would extrapolate towards the step is unknown, it clearly demonstrates that the separated-flow region involves very high energy production.

Dissipation

The peak energy loss due to dissipation in Castro's plane mixing layer results is about 0.78 of the peak gain by production, which is very high compared with the value of about 0.39 at $x/h = 3.4$ in our results. As mentioned in section 4.4 his results show a considerable 'out-of-balance' term in the central part of the layer; the dissipation to production peak ratio would reduce to about 0.53 if the 'out-of-balance' peak were added to the dissipation peak, which is still rather higher than our value. The addition of 'out-of-balance' term to the dissipation profile of Castro would also cause dents on both sides of the peak similar to that which appears in our dissipation profile in figure 4.24(a). However, it should be noted that, since dissipation in the present results is determined by difference, the neglect of the pressure diffusion terms, $\partial(\overline{pu}/\rho)/\partial x$ and $\partial(\overline{pv}/\rho)/\partial y$, and the errors produced by graphical differentiation in determining all other terms may accumulate to result in somewhat erroneous value of dissipation. We shall return to the discussion of pressure diffusion shortly. A few data points of dissipation on the energy-gain side near the high-velocity edge clearly demonstrate errors of this sort. That the ratio of dissipation peak to production peak at $x/h = 4.4$ is about 0.55, comparable to the corrected value of Castro, and that the total dissipation

in figure 5.25 increases towards reattachment seem to confirm that dissipation at x/h = 3.4 is in serious error. The same reason probably applies to the apparent sudden increase of peak dissipation at x/h = 5.375 and the apparent further increases in the total dissipation across the layer. The odd behaviour of the total advection across the layer in this region, as seen in figure 5.25, may be responsible for the error. Furthermore, the comparatively high dissipation in the recirculation region at x/h = 3.4, which is unlikely, is also doubtful. Because of the very high degree of uncertainty in the dissipation obtained, it seems pointless to pursue the discussion of dissipation in this region further.

Diffusion and Advection

The similarity between transverse diffusion profile of the present results at x/h = 3.4 (figure 4.24(a)) and that of Castro, both in shape and in relative magnitude, is striking. The results show that approximately half of the energy gained by production in the central part of the shear layer in this region is balanced by transverse-diffusion energy loss, while the outer parts of the layer energy is gained by transverse diffusion, slightly more on the high-velocity side than the low-velocity side. The advection, which again follows closely the shape of Castro's results, but with somewhat higher relative magnitude, mainly balances this transverse-diffusion energy gain, particularly at the high-velocity side. In Castro's results the advection in the central part of the layer comes down to near zero, but the sparseness of our results in that region makes decisive conclusion rather difficult. There is a small advection gain in the recirculation region in our results.

Despite fairly good agreement in transverse diffusion and advection between the present results and those of Castro, the longitudinal diffusion in both results are greatly different. Castro's results

show very small gain (inner part) and relatively larger loss (outer part) of the energy due to longitudinal diffusion on the 'still-air' side of the layer, whereas in our results there appears to be a comparatively large gain across the central part of the layer with moderate loss at low-velocity edge and very small loss at high-velocity edge.

The transverse diffusion at $x/h = 3.4$ fails to integrate to zero by about 5% of the area under the shear-stress production profile compared with 14% found by Castro. It should be noted, however, that there remains small negative transverse diffusion beyond $y/\delta_{995} = 1$, therefore, the residue of integration would be slightly less if it is integrated to infinity. The total advection across the layer at this station is absurdly high (figure 5.25) and thought to be in error because of high unreliability of mean-velocity measurements, as well as of graphically computed V, $\partial(\frac{1}{2}\overline{q^2})/\partial x$ and $\partial(\frac{1}{2}\overline{q^2})/\partial y$ in this region.

As the distance increases downstream, both longitudinal and transverse diffusion hardly change shape or magnitude, except that the gain by longitudinal diffusion becomes slightly larger. Figure 5.19 shows that peak transverse diffusion (loss peak only) slowly rises to maximum about one step height upstream of reattachment then drops slowly towards reattachment. The residues of integration at $x/h = 4.4$ and 5.375 are very small, i. e. 3% and 2% of the total shear-stress production, respectively. The location of the positive transverse-diffusion peak in this region is more or less identical with that of the shear-stress production peak as can be seen in figure 5.20. Assuming advection at $x/h = 3.4$ is in error as commented above, the region of advection gain on the surface side seems to have constant thickness of $y/h \simeq 0.7$ upstream of reattachment. The magnitudes of both loss and gain peaks of advection increase only slightly as the distance approaches reattachment. Disregarding the first point (i. e. at $x/h = 3.4$) of the total advection plot in figure 5.25, the total advection

across the layer seems to increase fairly slowly towards a constant at reattachment. The streamwise variation of advection at constant y is shown in figure 5.24, but no worthwhile discussion can be made because the layer is inclined as noted above.

5.4.2 The Reattachment Region

Consider figures 4.24(c) and (d), x/h = 5.375 and x/h = 6.4, which are immediately upstream and downstream of reattachment, respectively. The decrease in peak shear-stress production with distance downstream when passing through reattachment is more or less at the same rate as that in the upstream region, as clearly shown in figure 5.19. The shape of shear-stress production profile is unchanged by the reattachment process. At reattachment, the total shear-stress production across the layer decreases slightly more rapidly than that in the upstream region (figure 5.25). The normal-stress production at the two stations considered differ slightly in shape and magnitude. The total normal-stress production across the layer decreases a little when passing through reattachment.

The dissipation profile at x/h = 6.4 has a dent at the central part of the layer similar to those at x/h = 3.4 and x/h = 4.4, which makes the single hump feature of profile at x/h = 5.375 rather suspicious. Across reattachment, both the peak dissipation and the total dissipation across the layer appear to drop rather rapidly, but reservation must be made because of the unreliability of the computed dissipation in the upstream region as noted above.

For transverse diffusion, peak energy loss at x/h = 6.4 is about $\frac{2}{3}$ of that at x/h = 5.375, and the gain region close to the surface of the downstream station becomes much narrower, because part of fluid

volume is deflected upstream. Just downstream of reattachment ($x/h = 6.4$) the low-velocity side energy loss region of longitudinal diffusion vanishes completely and its energy gain magnitude is markedly less than that of the upstream station.

Downstream of reattachment at $x/h = 6.4$ the advection gain on the lower half of the layer drops to near zero, while the peak loss decreases to about half of that at $x/h = 5.375$. The total advection across the layer is fairly constant across reattachment (figure 5.25).

It is, therefore, apparent that reattachment involves rather rapid decrease in peak values of all main energy terms and the change in distribution shape of some terms. The total values across the layer of production and dissipation also drop rapidly across reattachment. The complex pattern of streamwise variation at constant y appearing in the region approaching reattachment for all terms (figures 5.21 to 5.24) is to be expected because the shear layer here is highly curved, and it should not be taken too seriously.

5.4.3 Downstream of the Reattachment Region

Since after reattachment the shear layer is expected to relax towards equilibrium boundary layer far downstream - over 50 step heights, according to Bradshaw and Wong (1972) - the main interest is to see how the energy-balance terms behave in this relaxation region, and, in particular, to see if the energy development is asymptotic towards equilibrium condition. Although the length of the present working section is far too short for the shear layer to attain an equilibrium state, it is hoped that, at least, an indication of asymptotic tendency should appear; thus, typical values of the main energy terms in equilibrium flat-plate boundary layer with zero pressure gradient, from Klebanoff (1955) as

reproduced by Bradshaw (1967), are also included in figure 4.24(j) (Energy balance of our last measuring station) for comparison. The high-Reynolds-number results of Murlis (1975), who used the same tunnel as, and similar apparatus to, the present experiment, compare reasonably well with these typical values. Murlis explains the slightly higher values of his results compared to those of Klebanoff, as the effect of Reynolds number. Nevertheless, the question of energy distribution across the layer rather than absolute values seems to be more relevant in the present discussion.

Production

Downstream of reattachment the peak shear-stress production decreases further at almost the same rate as in the upstream region up to about x/h = 8, downstream of which the decrease is very slow and asymptotic towards a small value (figure 5.19). The total shear-stress production across the layer also continues decreasing downstream of reattachment, but the decrease is more rapid than in the upstream region again up to about x/h=8; the slow asymptotic decrease further downstream follows closely that of the production peak. Since the shear-stress production is the product of $(-\overline{uv})$ and $(\partial U/\partial y + \partial V/\partial x)$, it should be interesting to see which term falls faster than the other. Figure 5.26 shows a comparison between the streamwise variation of $(-\overline{uv})_{max}$ and $(\partial U/\partial y + \partial V/\partial x)_{max}$. Although upstream of reattachment the peak location of the two terms may be far apart in some places, their peaks are close together near the surface downstream of reattachment, so that general behaviour may be extracted from the consideration of these peak values. It is clearly seen in figure 5.26 that from x/h=6 to x/h=7 $(\partial U/\partial y + \partial V/\partial x)_{max}$ drops very rapidly while $(-\overline{uv})_{max}$ only just starts to drop, whereas between x/h=7 to x/h=9 $(-\overline{uv})_{max}$ decreases much more rapidly than $(\partial U/\partial y + \partial V/\partial x)_{max}$; in agreement with the almost constant drop of shear-stress production peak between x/h=6 to x/h $\simeq$ 8.5, as noted above. Downstream of x/h=9 the $(-\overline{uv})_{max}$ drops further

almost at a constant rate while $(\partial U/\partial y + \partial V/\partial x)_{max}$ decreases very slowly towards asymptotic value.

The location of the production peak (figure 5.20) is almost at a constant distance of about y/h = 0.5 from the surface from x/h = 6 to x/h = 8; downstream which data points appear to be excessively scattered and departing from the surface. Here the location of peak loses its meaning when the shear layer ceases to resemble a plane mixing layer and approaches an ordinary boundary layer. With regard to the shape of shear-stress production profile, its symmetry is gradually lost downstream of reattachment, at the surface the value departs from zero soon after reattachment, rising toward a high value near the surface at last station (x/h = 12.325). Figure 5.21 shows that shear-stress production at all y decreases asymptotically to a low value, but it is not clear how these curves will eventually adjust themselves to typical equilibrium values.

Dissipation

Downstream of reattachment the dissipation behaves, if the results can be trusted at all, rather peculiarly. At x/h = 6.4 and x/h = 7.4 there remains a dent in the central part, and dissipation on the surface side is higher. Peak dissipation drops rapidly in this region, after which it decreases very slowly (figure 5.19). Further downstream at x/h = 8.4 and x/h = 9 325 the shape of the dissipation profile relaxes towards the typical shape of dissipation in an equilibrium boundary layer as shown in figure 4.24(j), but from x/h = 10.325 onward, the dissipation on the surface side decreases and there appears a peak on the high-velocity side. It is very unlikely that the dissipation vanishes near the surface, as seen in figure 4.24(j); therefore, serious error due to over-estimation of other terms, in particular the transverse diffusion, is

thought to be responsible. The streamwise variation of dissipation at different y in figure 5.22 also shows peculiar behaviour: and in view of uncertainty of the results obtained by difference, no attempt has been made in smoothing the curves shown. The total dissipation across the layer shown in figure 5.25 seems to decrease very slowly downstream of reattachment except at the last two measuring stations where serious error is suspected, as noted above.

Diffusion and Advection

Peak loss of energy due to transverse diffusion decreases more slowly than dissipation in the region immediately downstream of reattachment, but the rates of decrease with respect to the streamwise distance in the two cases are almost the same downstream of about $x/h = 8$. The location of the transverse-diffusion positive peak is identical with that of shear-stress production up to about $x/h = 7.5$ (figure 5.20), downstream of which the former is closer to the surface than the latter. The transverse-diffusion gain region adjacent to the surface becomes gradually narrower until it vanishes completely at about $x/h = 9.325$. Further downstream the shape of the transverse diffusion profile is like a distorted sine-wave, similar to that of equilibrium boundary layer, but the magnitude is about 20 times larger. The streamwise variation of the transverse diffusion at different y decreases slowly towards zero. Here again no attempt has been made to smooth the curves.

Near $y=\delta$ the magnitude of advection gain increases up to about $x/h = 9$ before it gradually decreases. Downstream of $x/h = 8$ the shape of the advection profile is almost an image of transverse diffusion. At the last measuring station ($x/h = 12.325$) the magnitude of advection is comparable with transverse diffusion (both are much larger than the values in the equilibrium boundary layer). The total advection across

the layer falls rather rapidly from $x/h \simeq 6.5$, becoming negative (gain) at about $x/h = 8$, to $x/h \simeq 9$, after which it stays almost constant. The value close to zero of last data point is suspected to be in error.

5.4.4 Overall Features of Turbulent Energy Balance

From the above discussion, it is clear that upstream of reattachment the energy gain in the high-intensity region is dominated by shear-stress production which is balanced mainly by transverse diffusion and dissipation: the two are comparable in magnitude. This closely resembles the typical turbulent energy balance in a plane mixing layer, as demonstrated by the results of Castro (1973). Also included in figure 5.20 are the values of the total production, the total dissipation and the total advection across the plane mixing layer in Castro's (1973) results. Allowing for suspected errors in dissipation and advection at $x/h = 3.4$, as pointed out above, the agreement in order of magnitude is surprisingly good, despite the fact that measurements were taken in highly unreliable region. The reattachment region involves a marked decrease of all terms. In the relaxation region downstream of reattachment, the decay of all energy-balance terms is relatively slow but they seem to tend monotonically to the values for an equilibrium boundary layer downstream. The results show that at about 12 step heights from the step the energy balance is still far from that of a typical equilibrium boundary layer, therefore, one could not possibly apply a boundary-layer calculation method, so close to reattachment, without altering the empirical constants.

5.5 SHEAR STRESS BALANCE

In the shear-stress transport equation (4.17) the destruction of shear stress by viscous forces, $\nu(u\nabla^2 v + v\nabla^2 u)$, which is always very small in high-Reynolds-number flows, except in the viscous sublayer,

has been neglected. The transport of turbulent shear stress along a mean streamline term $(U\partial/\partial x + V\partial/\partial y)(\overline{uv})$, more simply called the 'mean-flow-transport' term. is plotted in figures 4. 25(a) to (j) as 'positive $\overline{uv}$' rather than negative, and all other terms are plotted with the same sign convention. The two components of the generation of turbulent shear stress term, $\overline{v^2}\partial U/\partial y$ and $\overline{u^2}\partial V/\partial x$ are plotted separately. The transport by fluctuating longitudinal and transverse velocity terms, $\partial\overline{u^2v}/\partial x$ and $\partial\overline{uv^2}/\partial y$ (more simply turbulent transport) are also plotted separately, with transport by pressure-fluctuation terms, $\partial(\overline{pv}/\rho)/\partial x$ and $\partial(\overline{pu}/\rho)/\partial y$, neglected as being very small compared with other terms. Finally, $\overline{\frac{p}{\rho}(\partial u/\partial y + \partial v/\partial x)}$, which is the redistribution by pressure fluctuations or simply the pressure-strain term, is obtained by difference, as already mentioned in section 4. 5.

We shall divide the discussion into three regions as we have done in discussing the turbulent energy balance in the previous section. The scatter of data in figure 4. 25 is not excessive, but high accuracy is again not to be expected owing to the graphical differentiation method used. However, the results are believed to represent the broad general features of shear stress development in the present flow field.

5. 5. 1 Upstream of the Reattachment Region

The similarity in shape of various corresponding profiles between the present results at x/h = 3. 4 (figure 4. 25(a)) and those of Castro (1973) is remarkable, confirming the approximation to a plane mixing layer, as found when comparing the turbulent energy-balance terms in section 5. 4. 1. It should be noted that signs of all terms in the present presentation and Castro's are opposite. Figure 4. 25(a) to (c) show clearly that in this region the $\overline{v^2}\partial U/\partial y$ generation term and pressure-strain term are dominant, with a moderate transverse turbulent transport

term. All other terms are exceedingly small compared with the generation term. The transverse turbulent transport profile in our case at x/h = 3.4 seems to be more peaky than that of Castro, but flattening with distance downstream. The peak values of the main generation and pressure-strain terms decrease almost uniformly as the downstream distance increases towards reattachment, but their general profile shapes are retained. The marked increase in magnitude of $\overline{u^2}\partial V/\partial x$ term and the inconsistent change of other small terms is likely to be the result of experimental error rather than a real trend: although $-\partial V/\partial x$ is expected to increase (see figure 4.17), the rise actually found is implausibly sudden.

5.5.2 The Reattachment Region

Across reattachment (figures 4.25(c) and (d)) the proportion of the contributions from each of the term remains practically unchanged, but peak values of the main term decrease rather more rapidly than in the upstream region. Just downstream of reattachment the pressure-strain term close to the surface begins to depart from zero. In general, it is seen that the changes of all terms in the shear stress balance are more gradual than in the turbulent energy balance discussed in the previous section.

5.5.3 Downstream of the Reattachment Region

In the relaxation region downstream of reattachment (figures 4.25(d) to (j)), $\overline{v^2}\partial U/\partial y$ generation term and pressure-strain term still dominate, but transverse turbulent transport gradually offers more contribution as the distance increases downstream. The $\overline{v^2}\partial U/\partial y$ generation profile and pressure-strain profile are almost the image of each other about the transverse-distance axis far downstream. Mean-flow-transport term increases its proportion gradually and becomes quite

noticeable soon after reattachment. The transverse turbulent transport term behaves very much like the transverse diffusion term in the energy balance, i. e. the positive region close to the surface becomes gradually narrower and completely vanishes at about x/h = 10, downstream which its profile is rather like a negative sine-wave. The values of generation, turbulent transport and mean-flow transport in the equilibrium boundary layer from the results of Murlis (1975) at high Reynolds number are also included in figure 4. 25(j), which is our last measuring station, for comparison. His values have been scaled to base on the step height of the present experiment. Murlis also points out the unreliability of his results due to a high degree of scatter in graphical differentiation· therefore, agreement in detail is not to be expected. Note that Murlis does not plot the pressure-strain term for the reason that it would be almost the image of the main generation term. The remarkable agreement in the main generation term of the two results in the outer part of the layer is probably a coincidence. Both mean-flow transport and transverse turbulent transport terms in our case are much higher than those of Murlis. At his upstream station, Murlis's results show a positive mean-flow transport region similar to those in our results, but this vanishes completely at his last station. Therefore, the state of most terms in the shear stress transport equation at the last measuring station once more confirms the conclusion drawn earlier, in discussing the turbulent energy balance, that at about 12 step heights from the step the shear layer in the present study is still far from equilibrium, but indicating a tendency towards that state. It should be noted that $\overline{u^2}\,\partial V/\partial x$ generation term and longitudinal turbulent transport term practically vanish downstream of about x/h = 11.

5. 5. 4 Overall Features of Shear Stress Balance

It is evident from figure 4. 25(a) to (j) that the generation

and pressure-strain terms dominate throughout the flow field, with the transverse turbulent transport term being the next significant term. In passing through the reattachment region changes in all terms are more gradual than those of turbulent energy terms. The decay process in the relaxation region is rather slow, but almost uniform. It should be noted, however, that part of the pressure-strain term is associated with the mean velocity gradient, as can be seen by considering the Poisson equations for the pressure fluctuation (e. g. Crow 1968), thus cancels part of the generation.

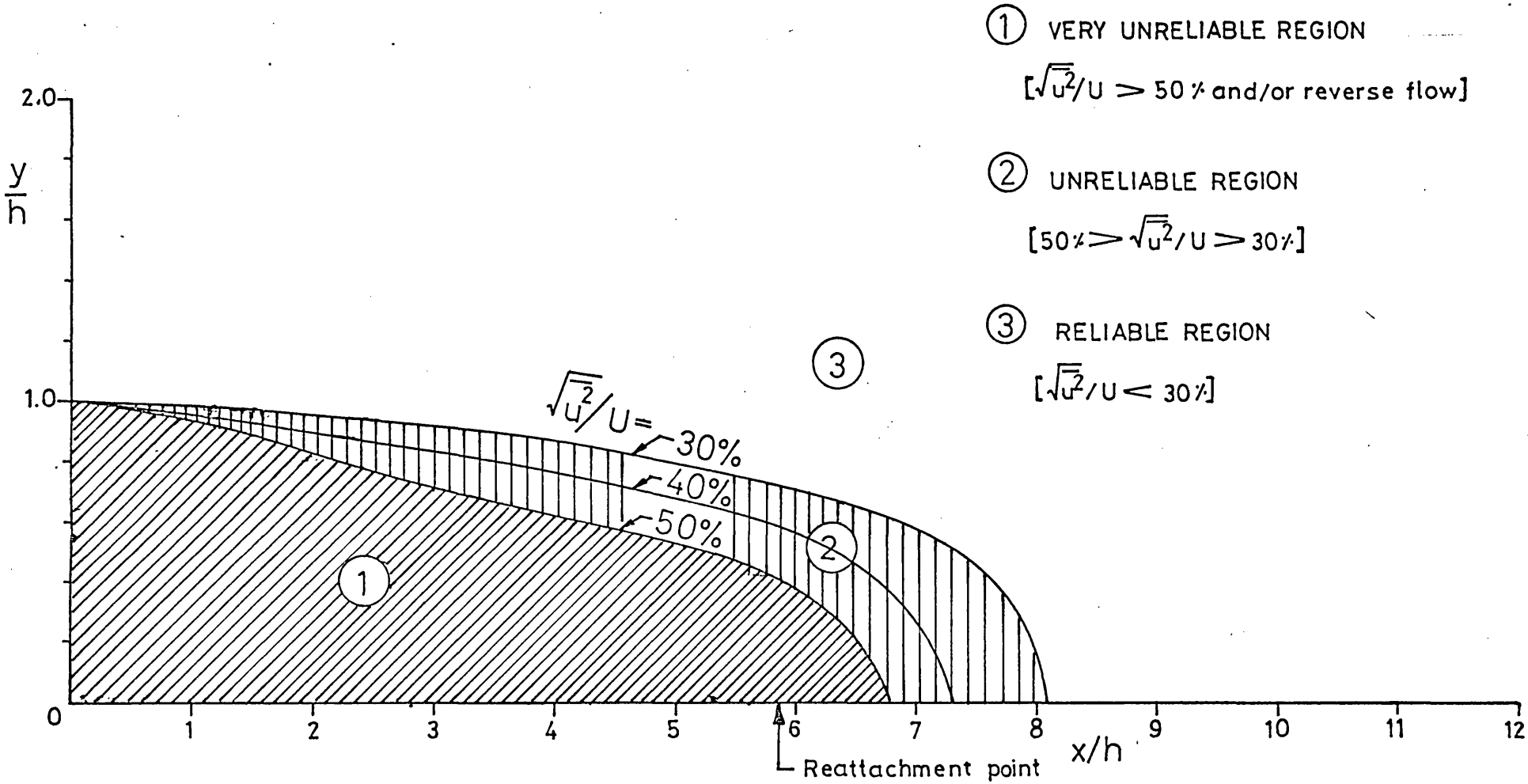


FIGURE 5.1 DEMARCATION OF RELIABLE REGION OF RESULTS

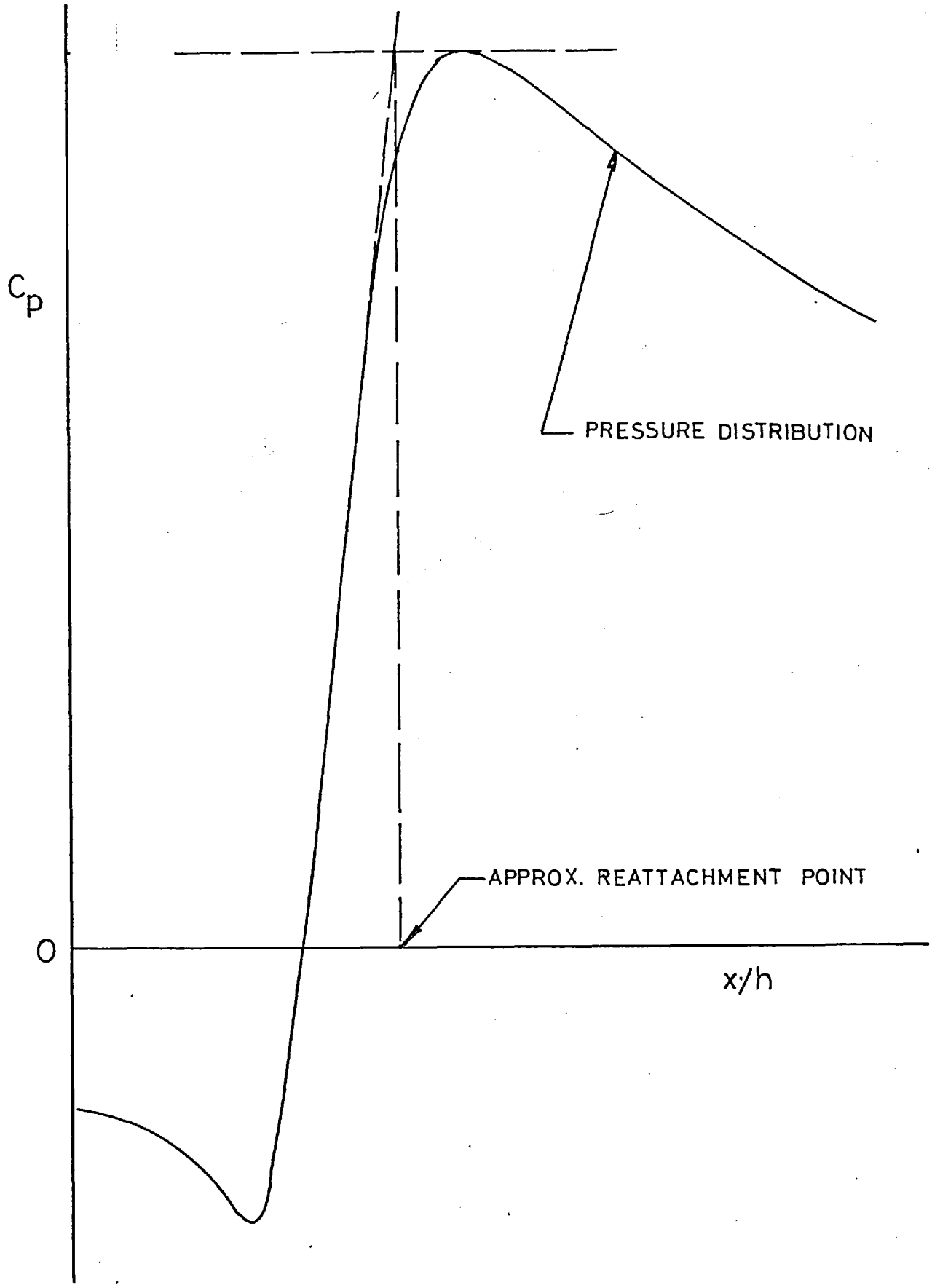


FIGURE 5.2 METHOD OF APPROX. REATTACHMENT LOCATION DETERMINATION FROM PRESSURE DISTRIBUTION

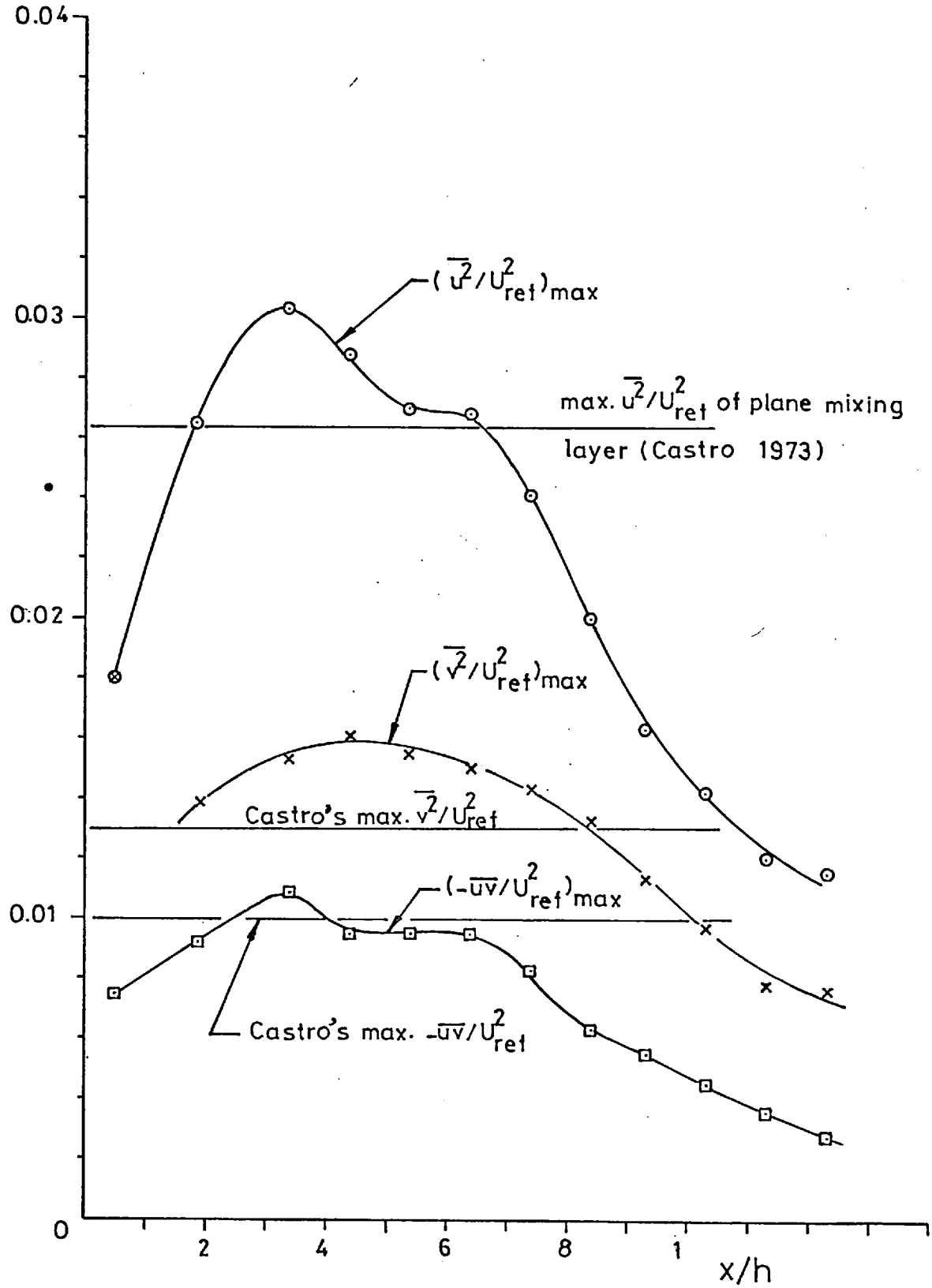


FIGURE 5.3 STREAMWISE VARIATION OF MAX. $\overline{u^2}/U_{ref}^2$, $\overline{v^2}/U_{ref}^2$ & $-\overline{uv}/U_{ref}^2$

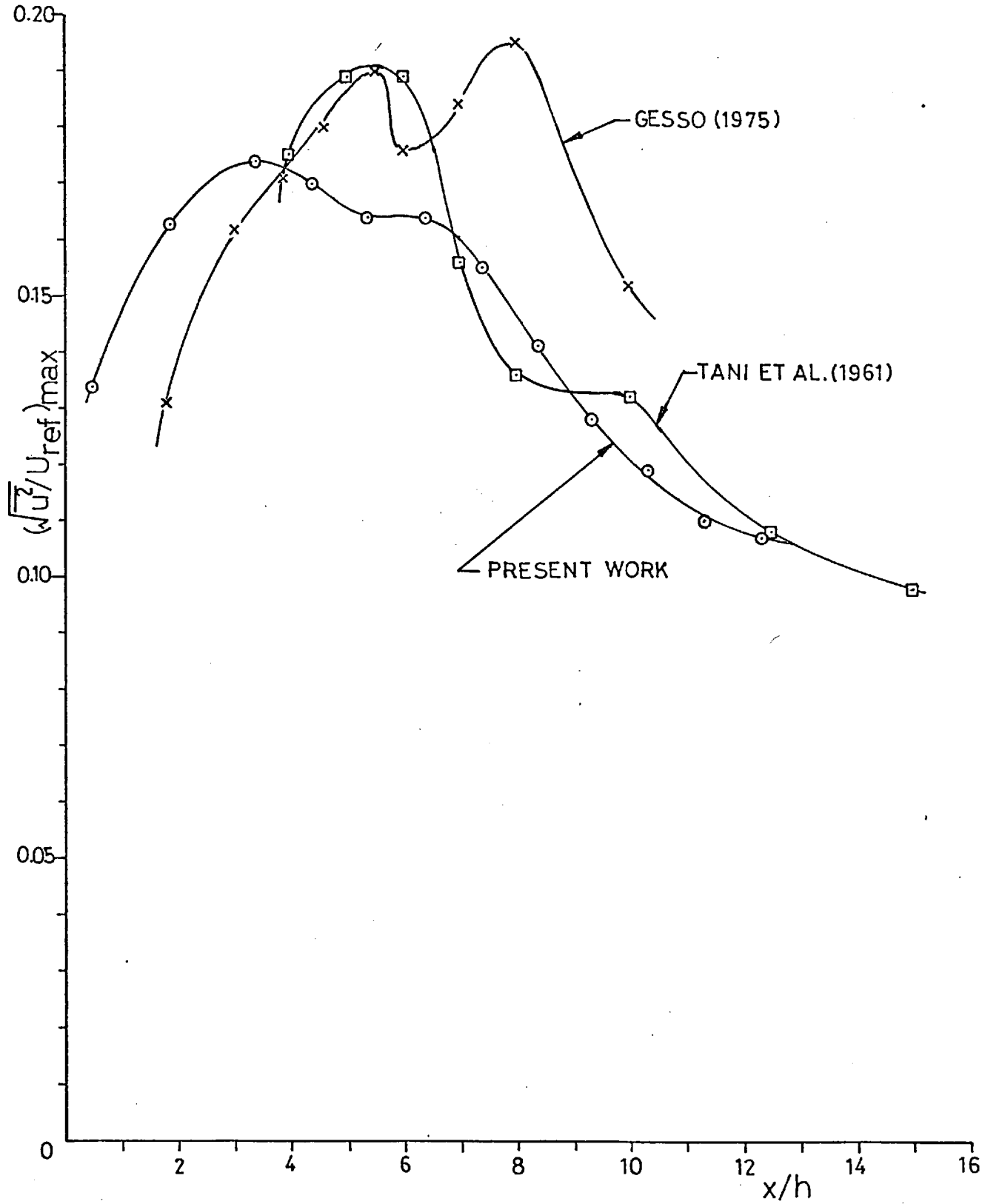


FIGURE 5.4 COMPARISON OF MAX. TURBULENT INTENSITIES WITH OTHER WORKERS' DATA

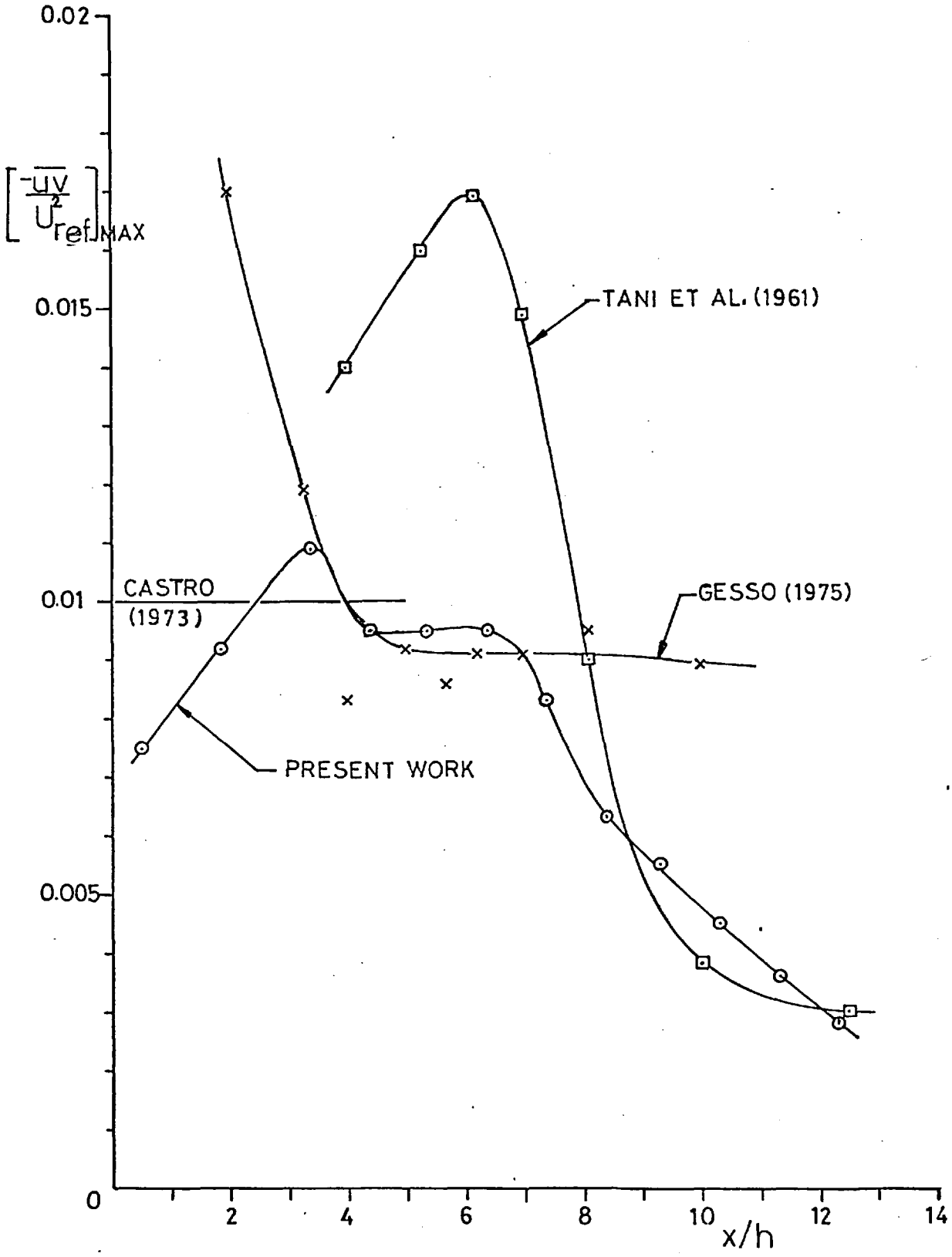


FIGURE 5.5 MAXIMUM SHEAR STRESSES

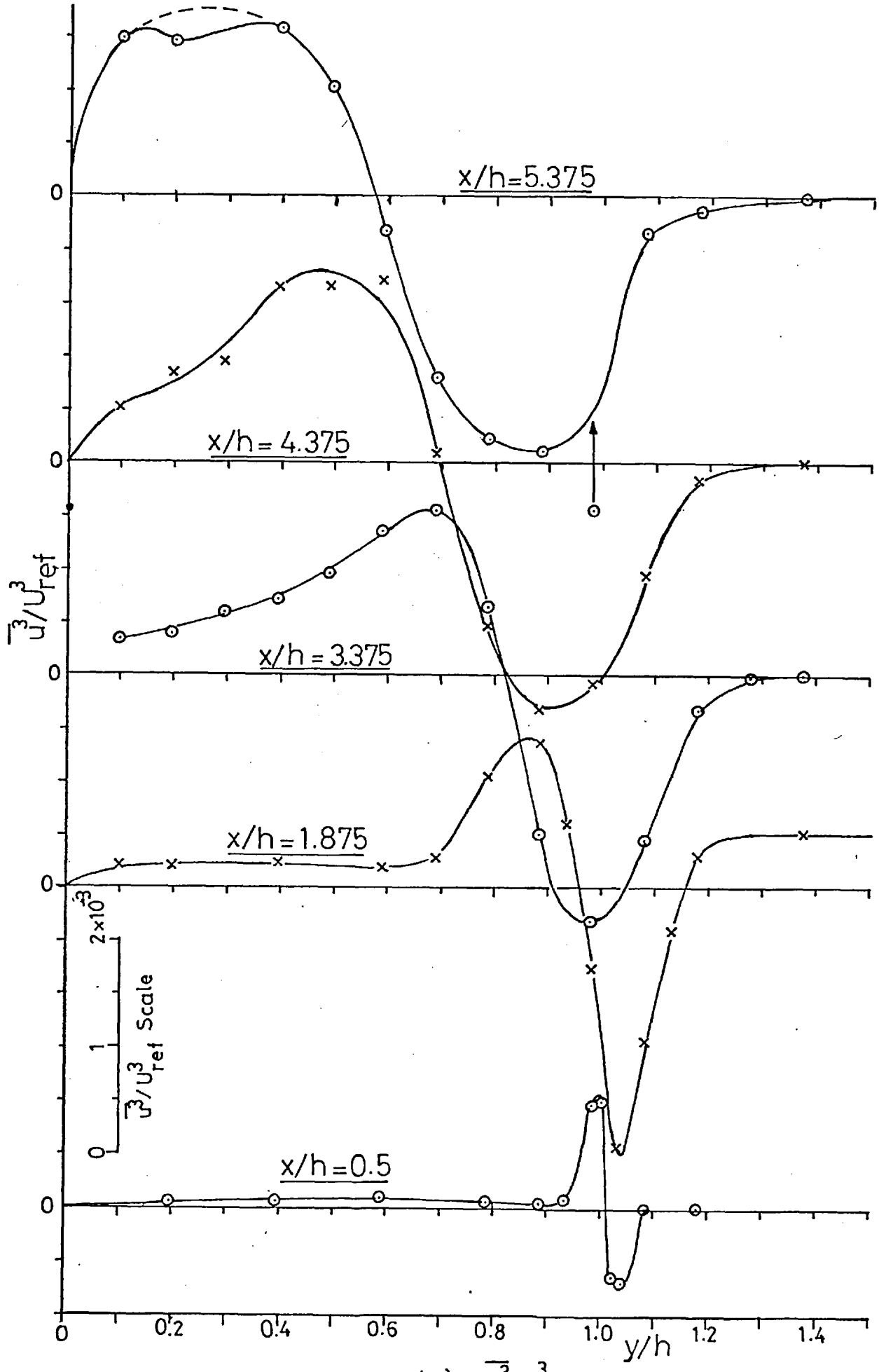


FIGURE 5.6(a) $\overline{u^3}/U_{ref}^3$ vs. y/h

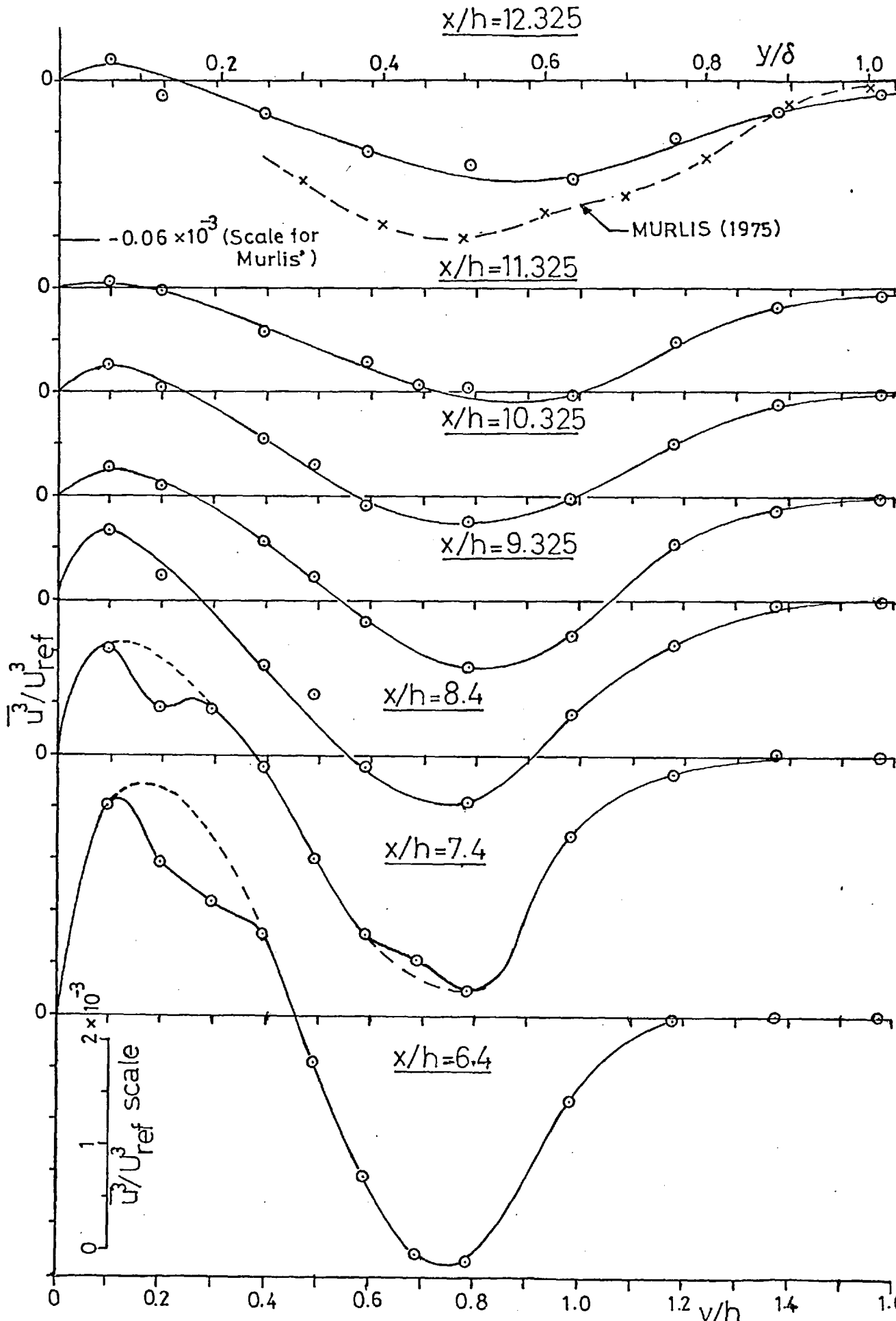


FIGURE 5.6(b) $\overline{u^3}/U_{ref}^3$ vs. y/h

FIGURE 5.7 $\overline{v^3}/U_{ref}^3$ vs. y/h

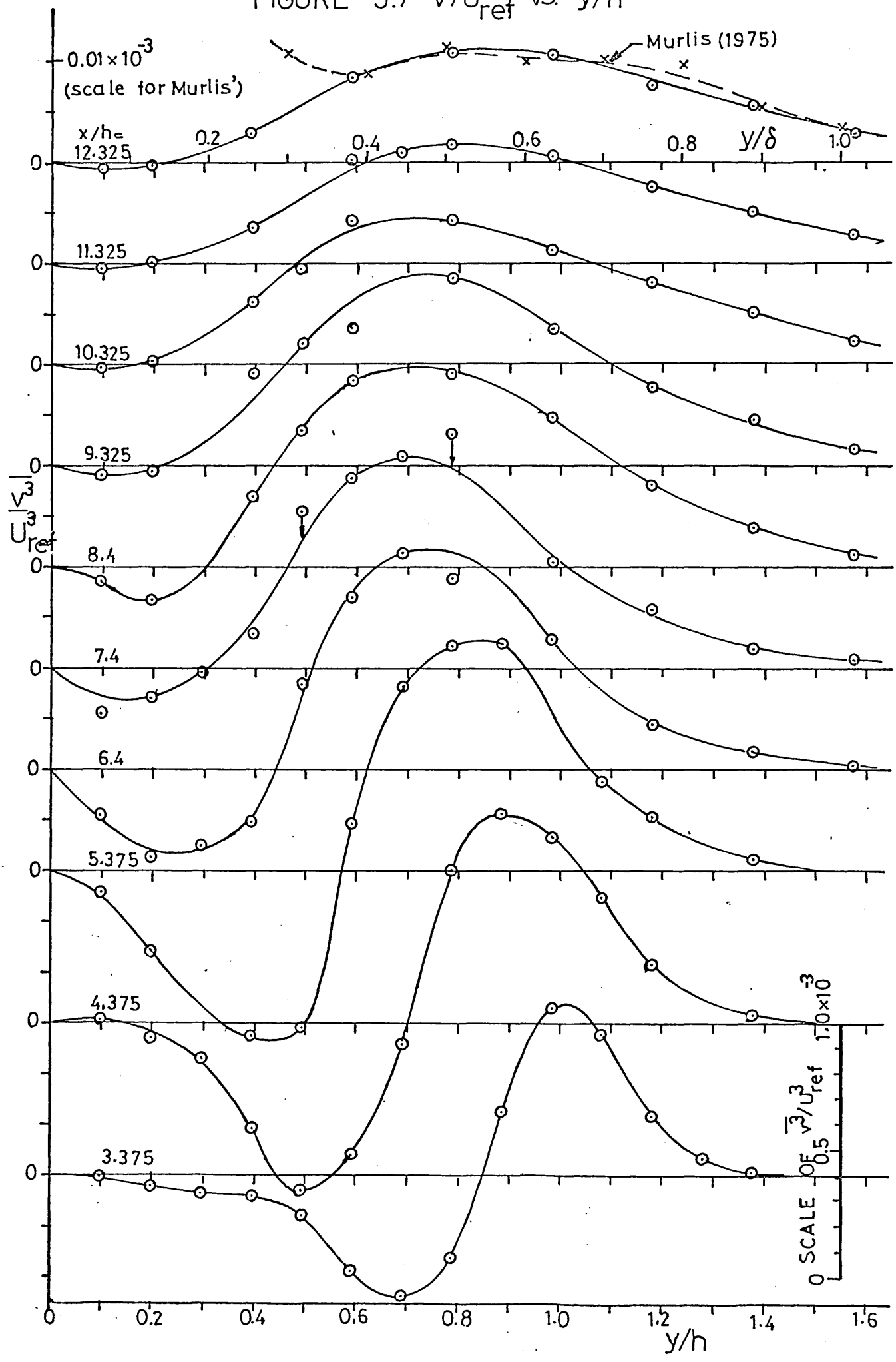


FIGURE 5.8(a) $\overline{u^2v}/U_{ref}^3$

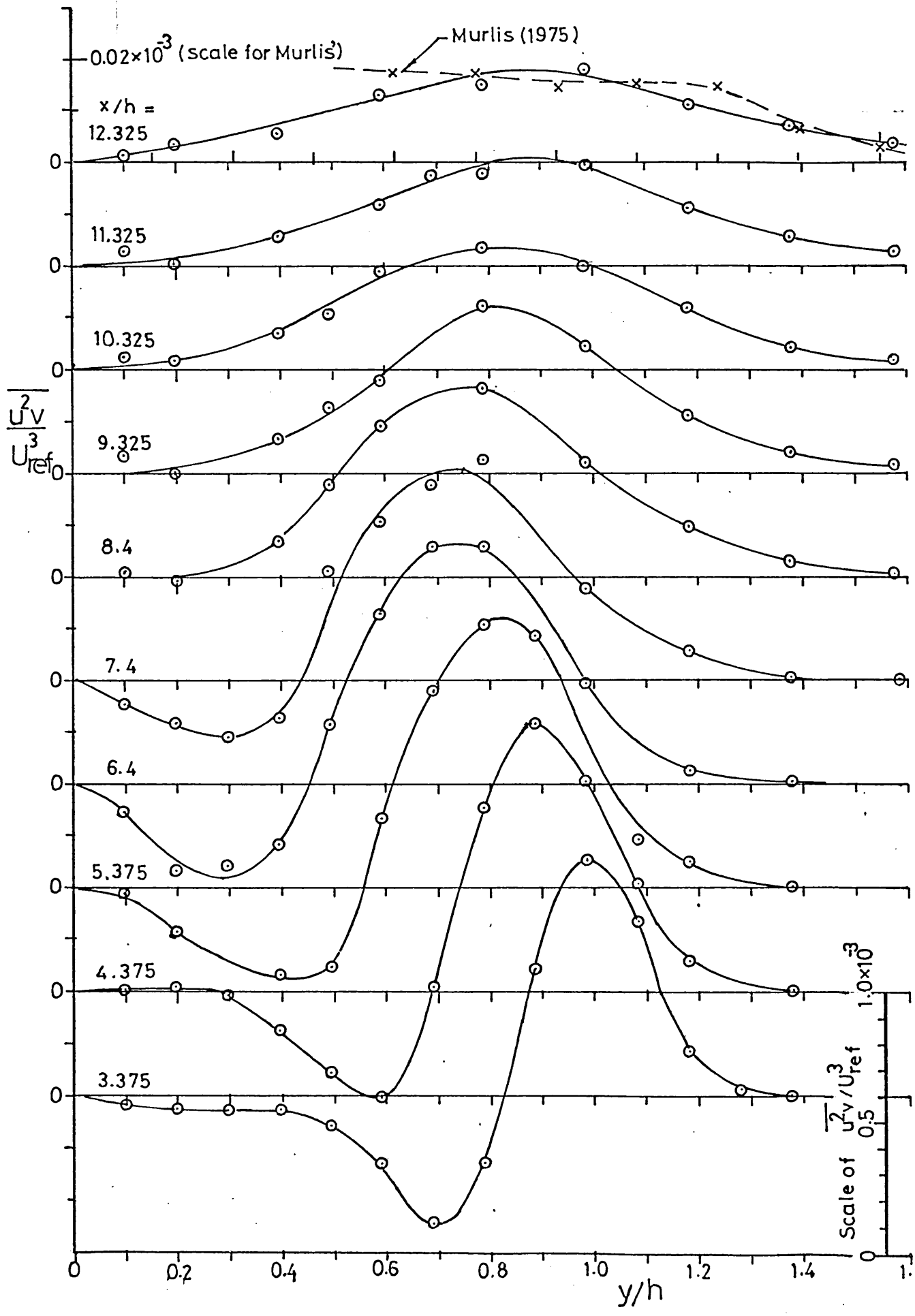


FIGURE 5.8(b) $\overline{u^2v}/U_{ref}^3$ vs. y/h

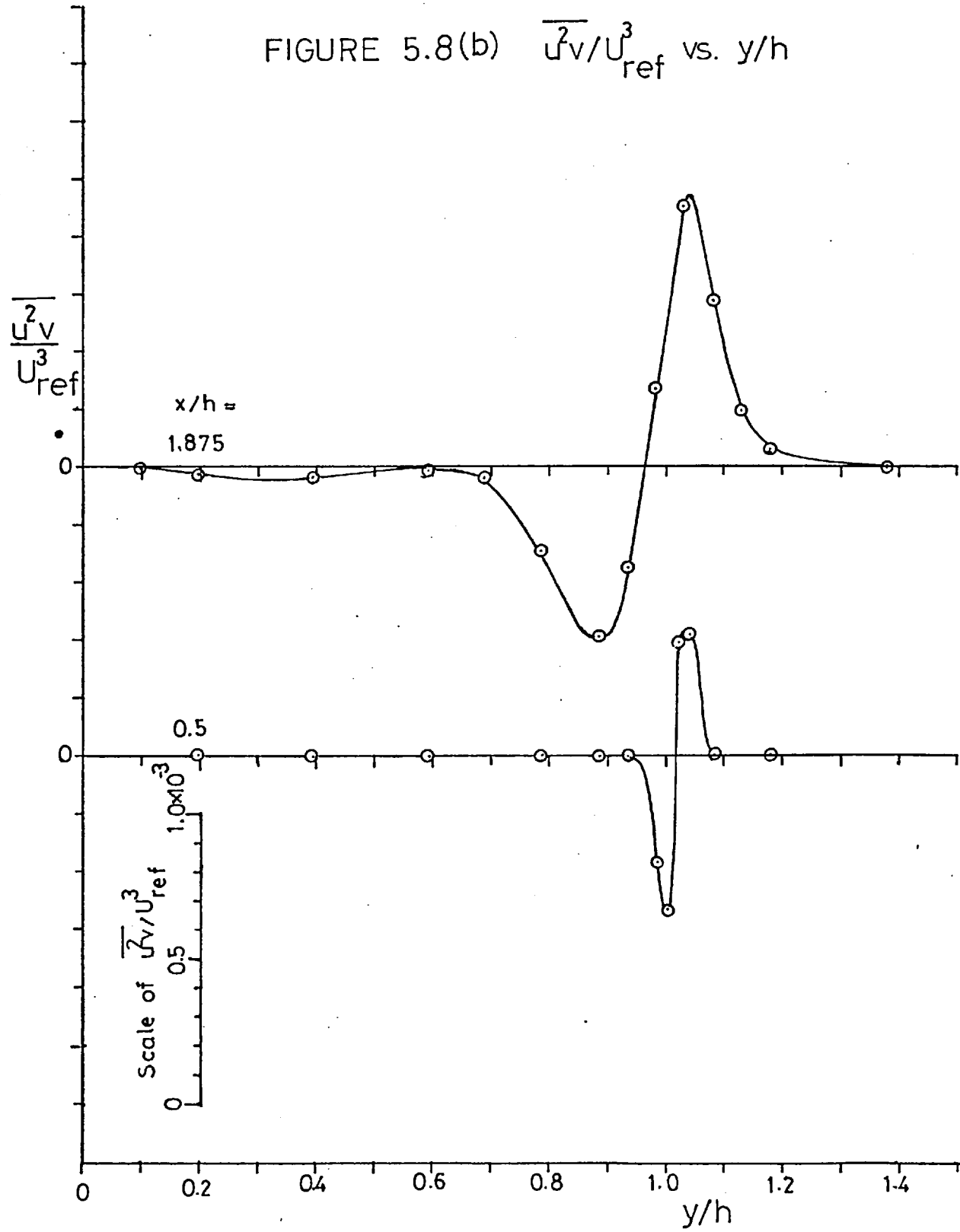


FIGURE 5.9(a) $\overline{uv^2}/U_{ref}^3$ vs. y/h

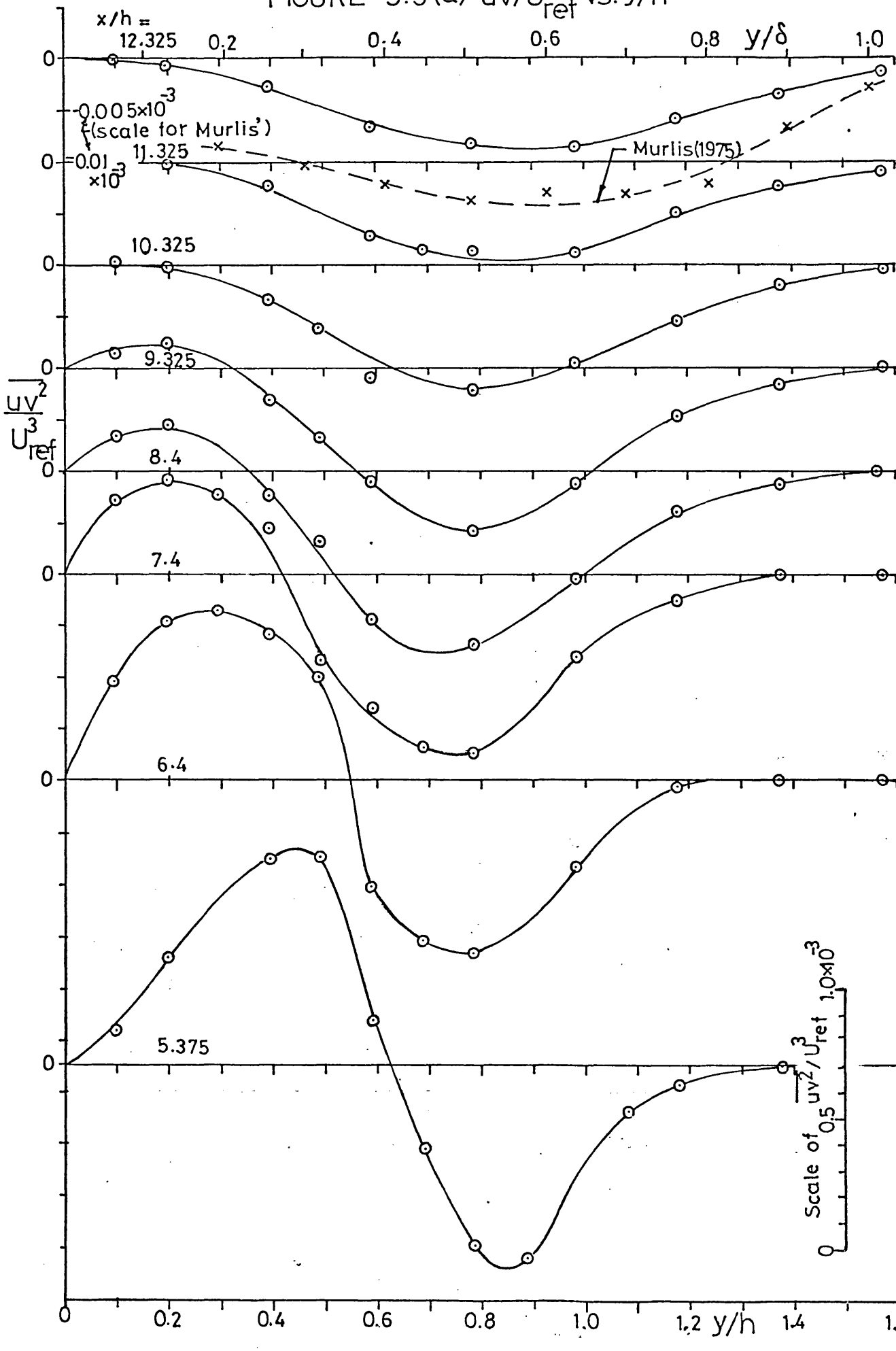


FIGURE 5.9(b) $\overline{uv^2}/U_{ref}^3$ vs. y/h

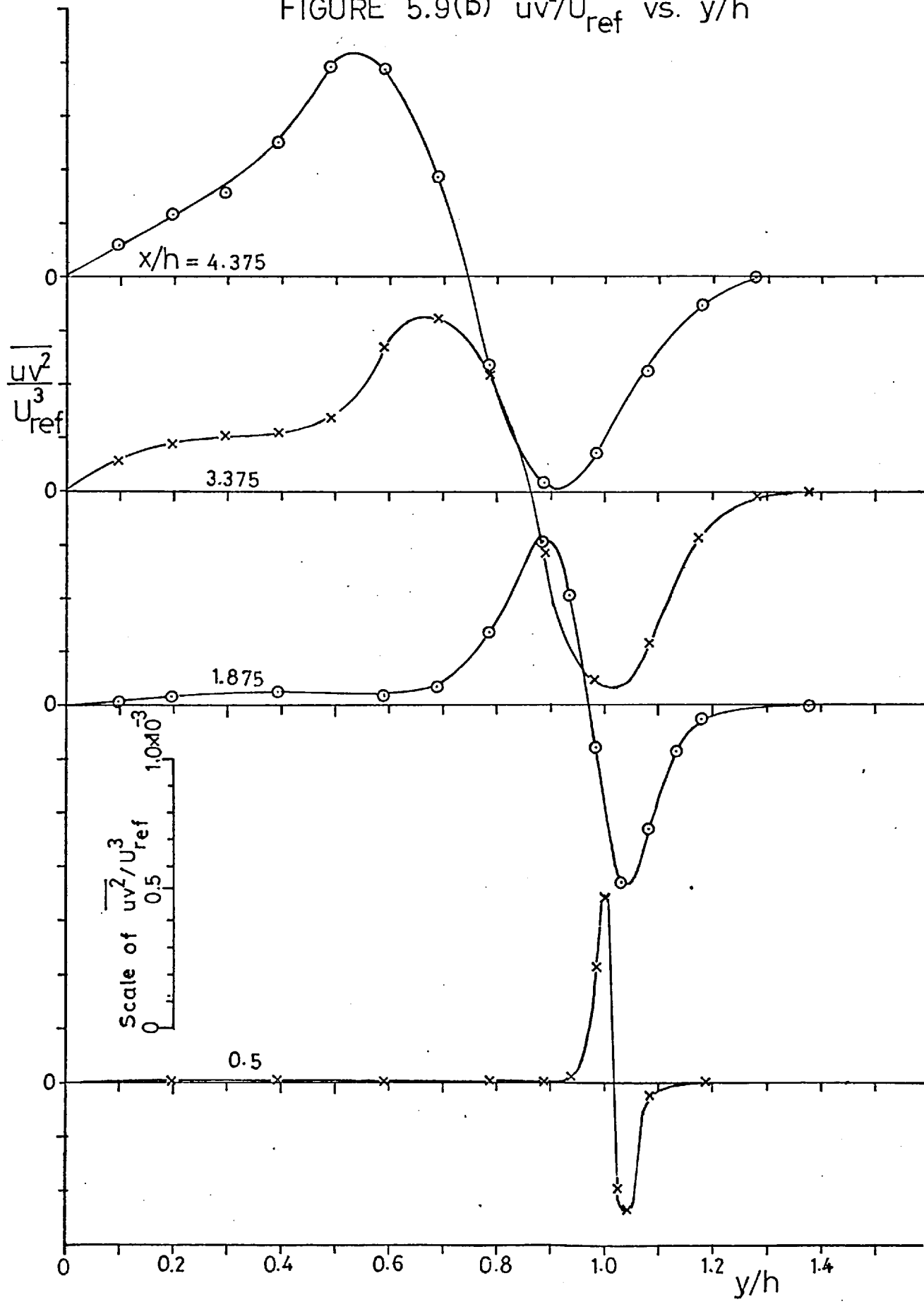


FIGURE 5.10(a) FLATNESS FACTORS

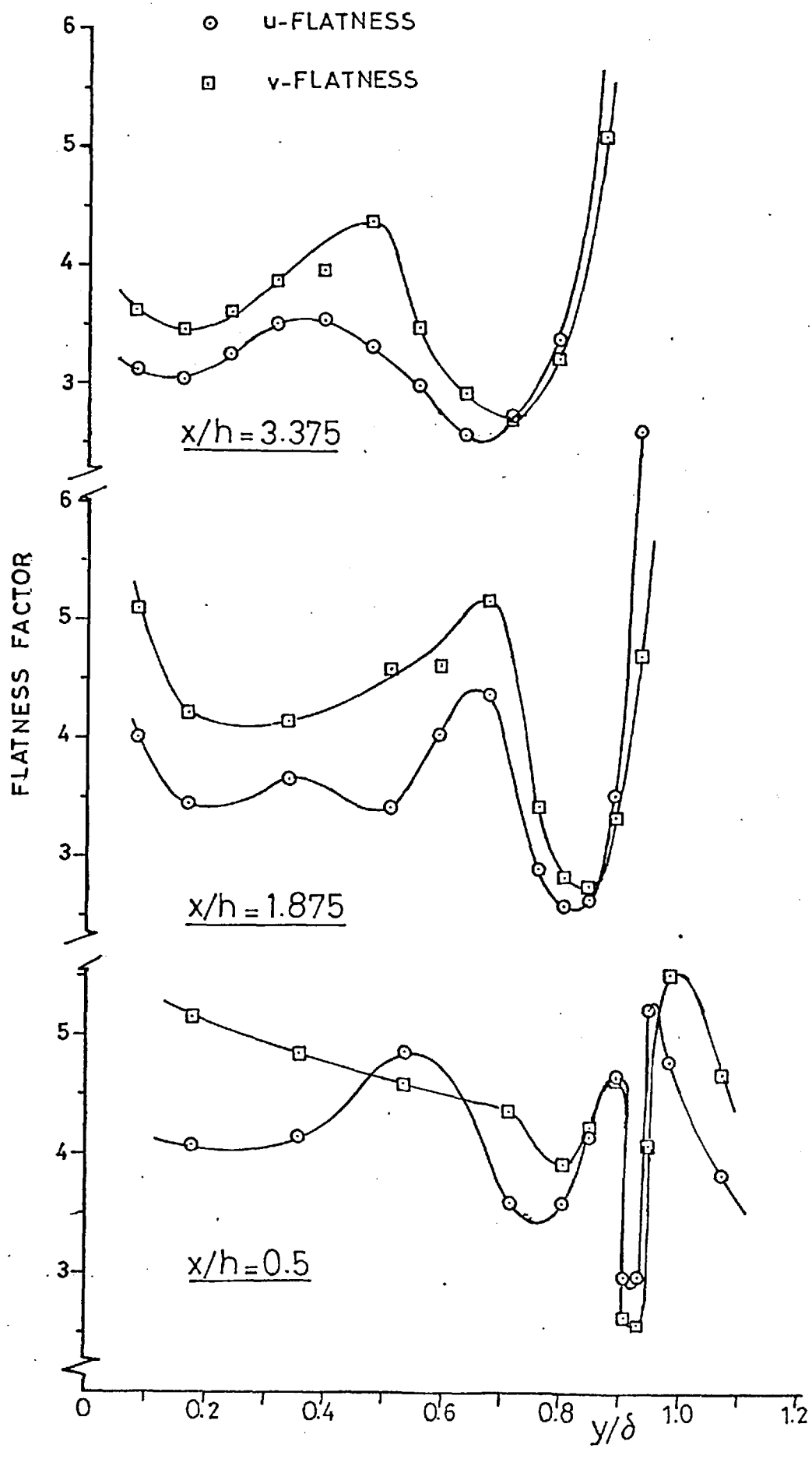


FIGURE 5.10(b) FLATNESS FACTORS

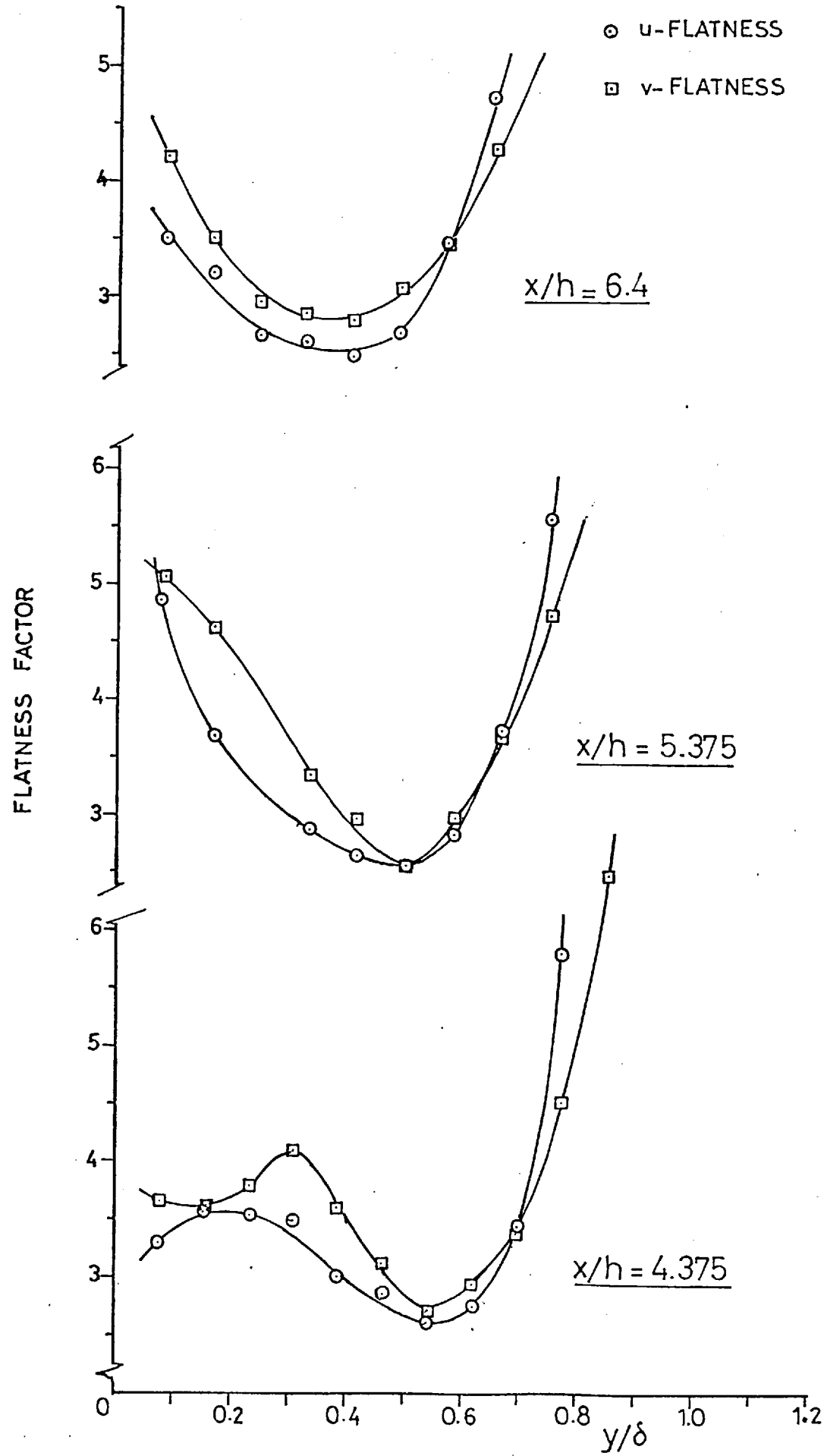


FIGURE 5.10(c) FLATNESS FACTORS

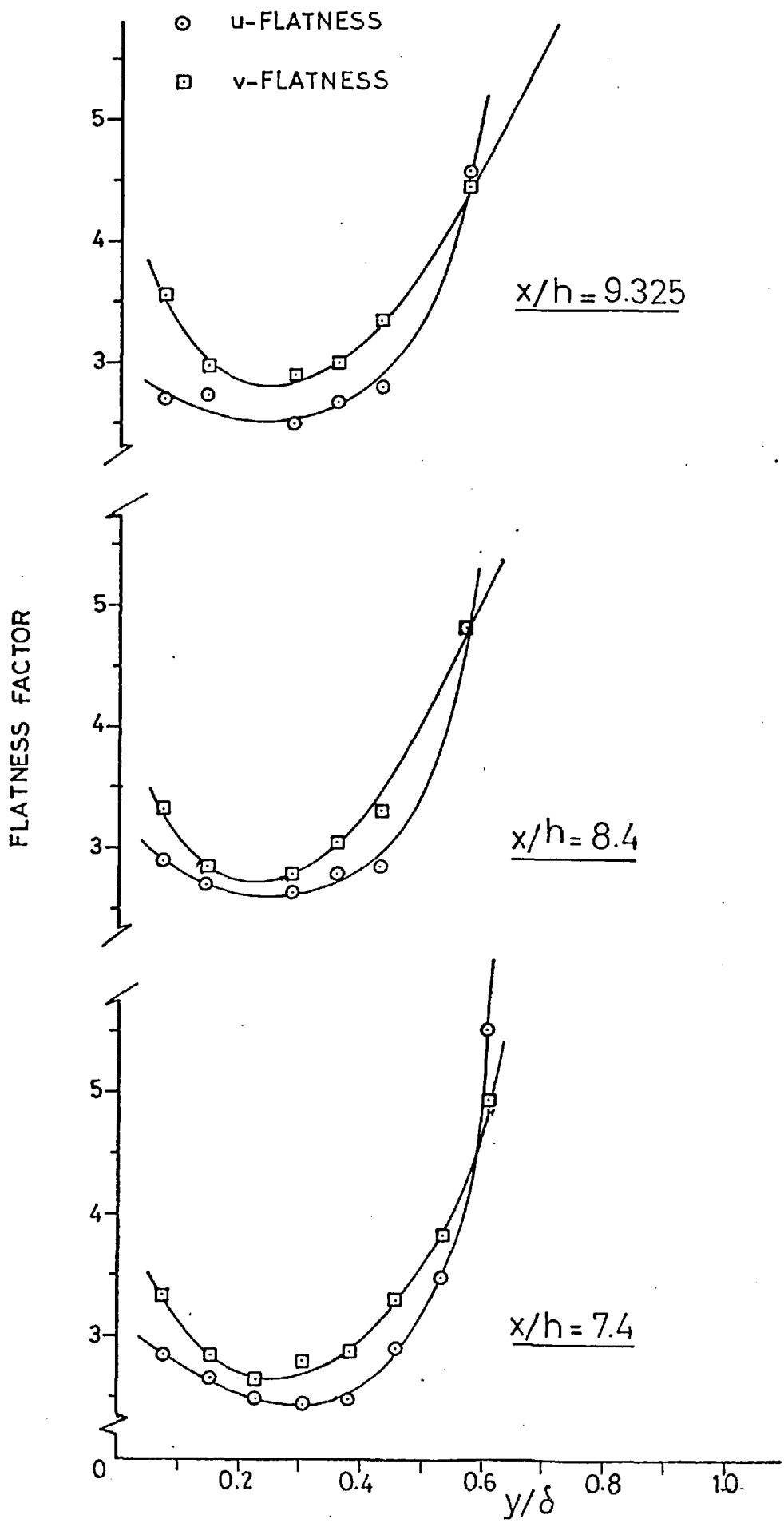
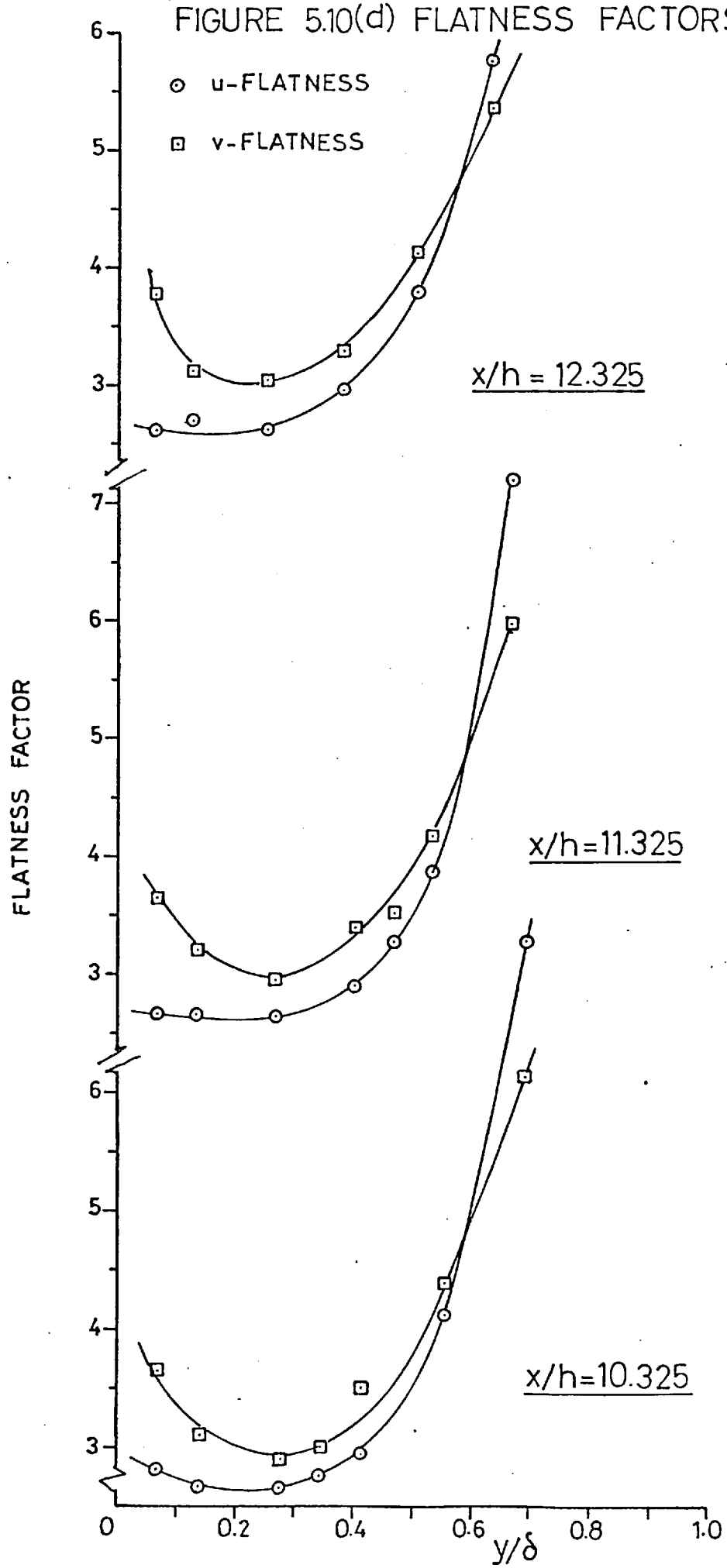


FIGURE 5.10(d) FLATNESS FACTORS



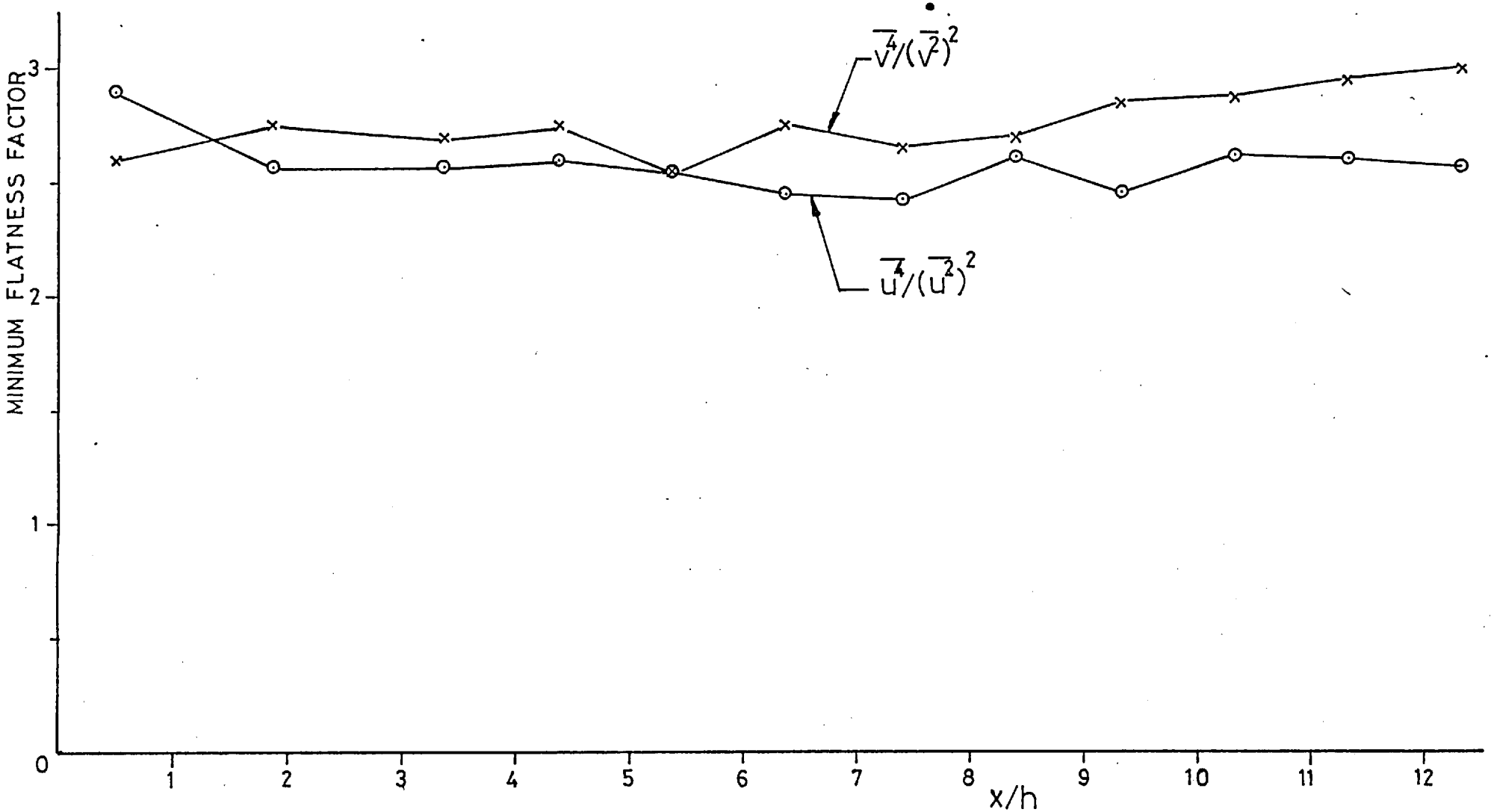


FIGURE 5.11 MINIMUM VALUES OF FLATNESS FACTOR

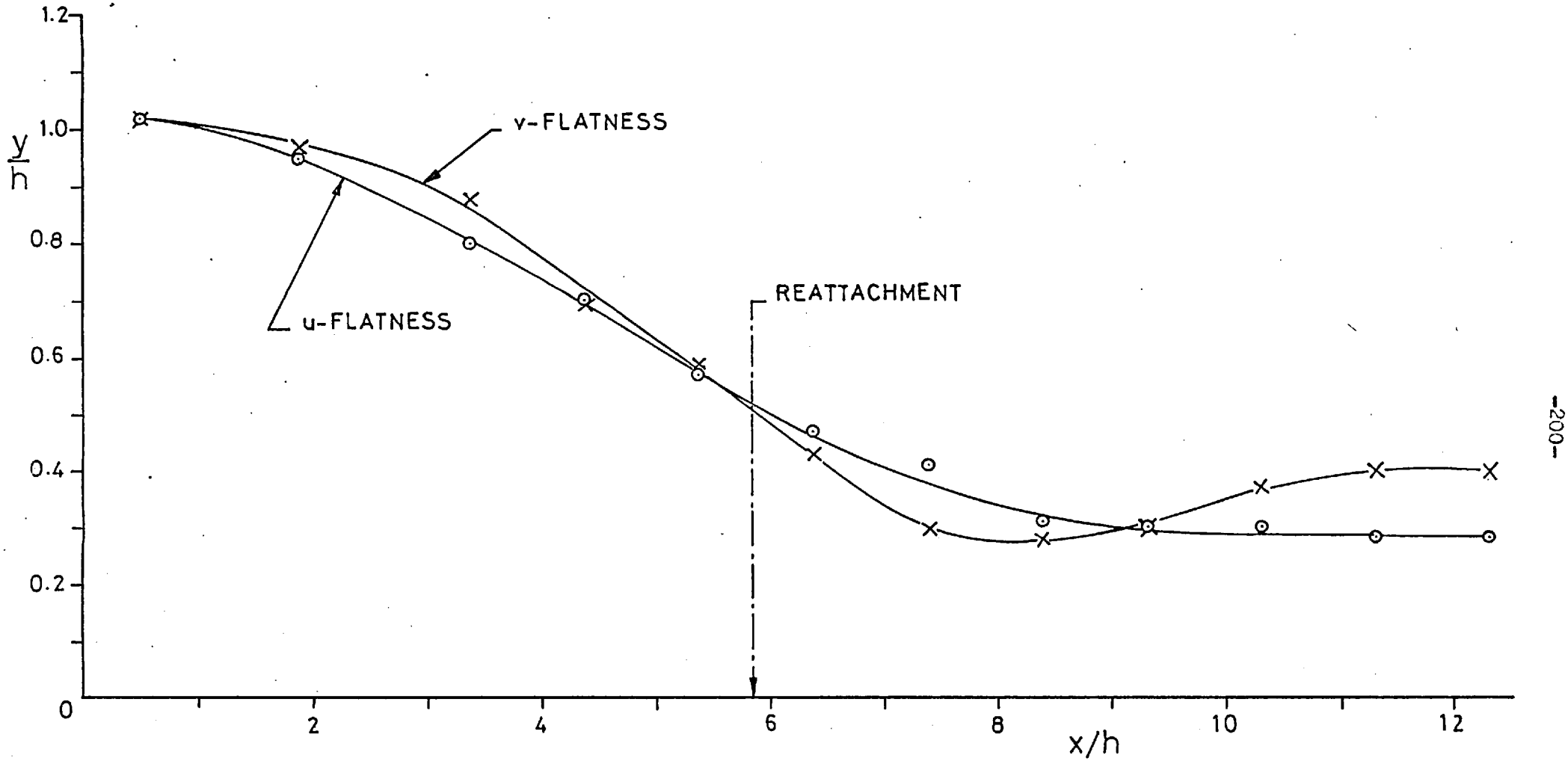


FIGURE 5.12 LOCI OF MINIMUM FLATNESSES

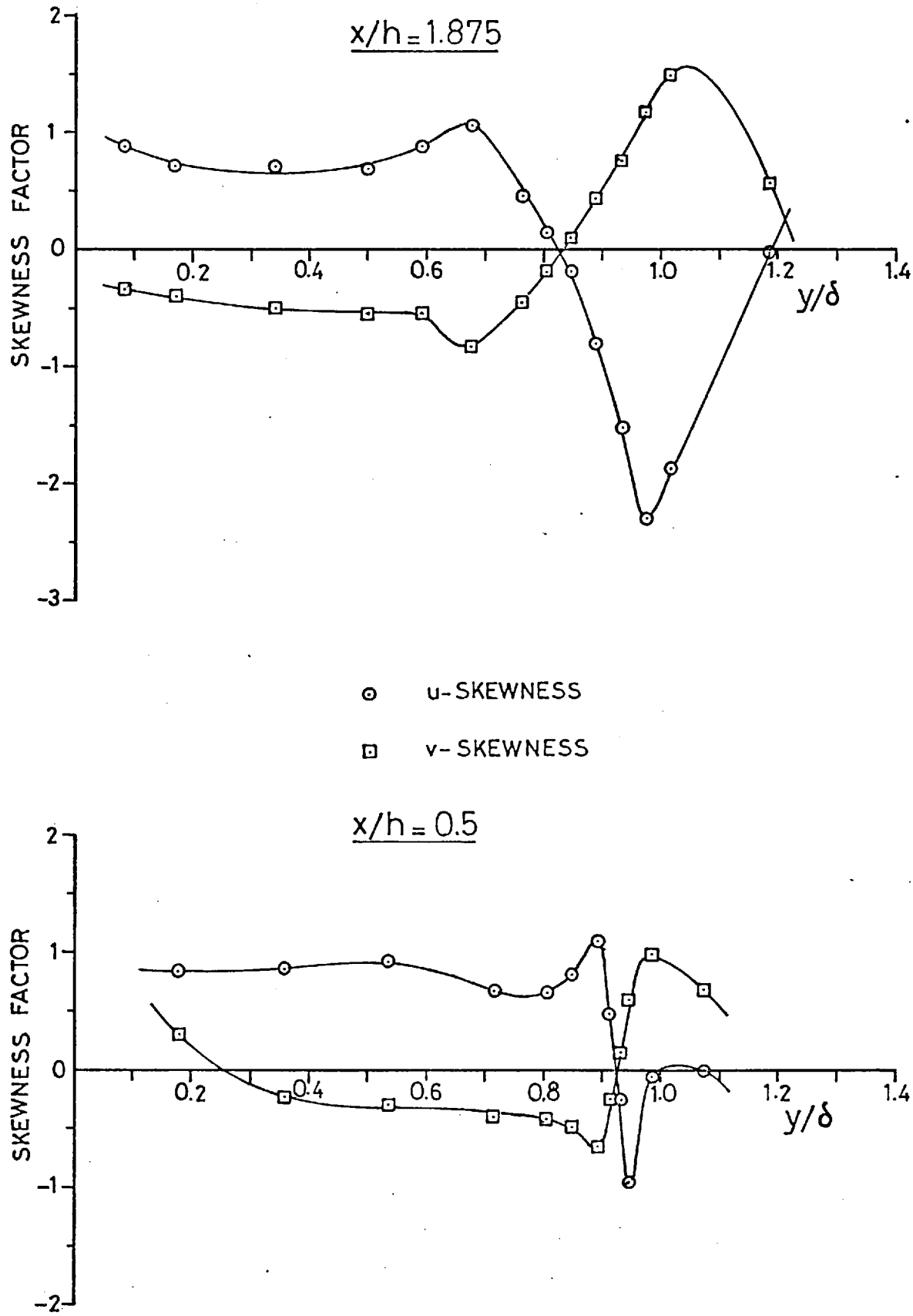


FIGURE 5.13(a) SKEWNESS FACTORS

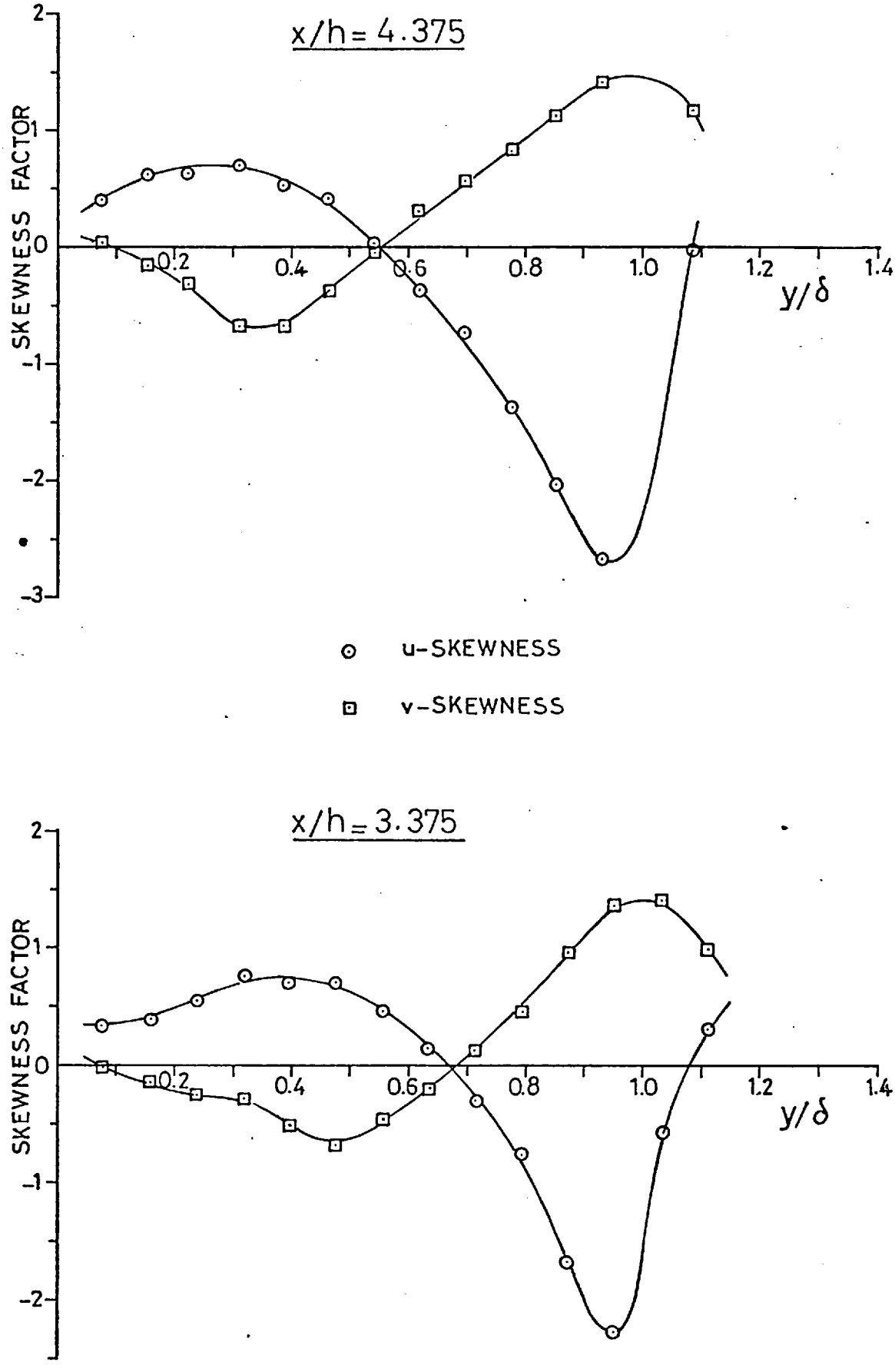
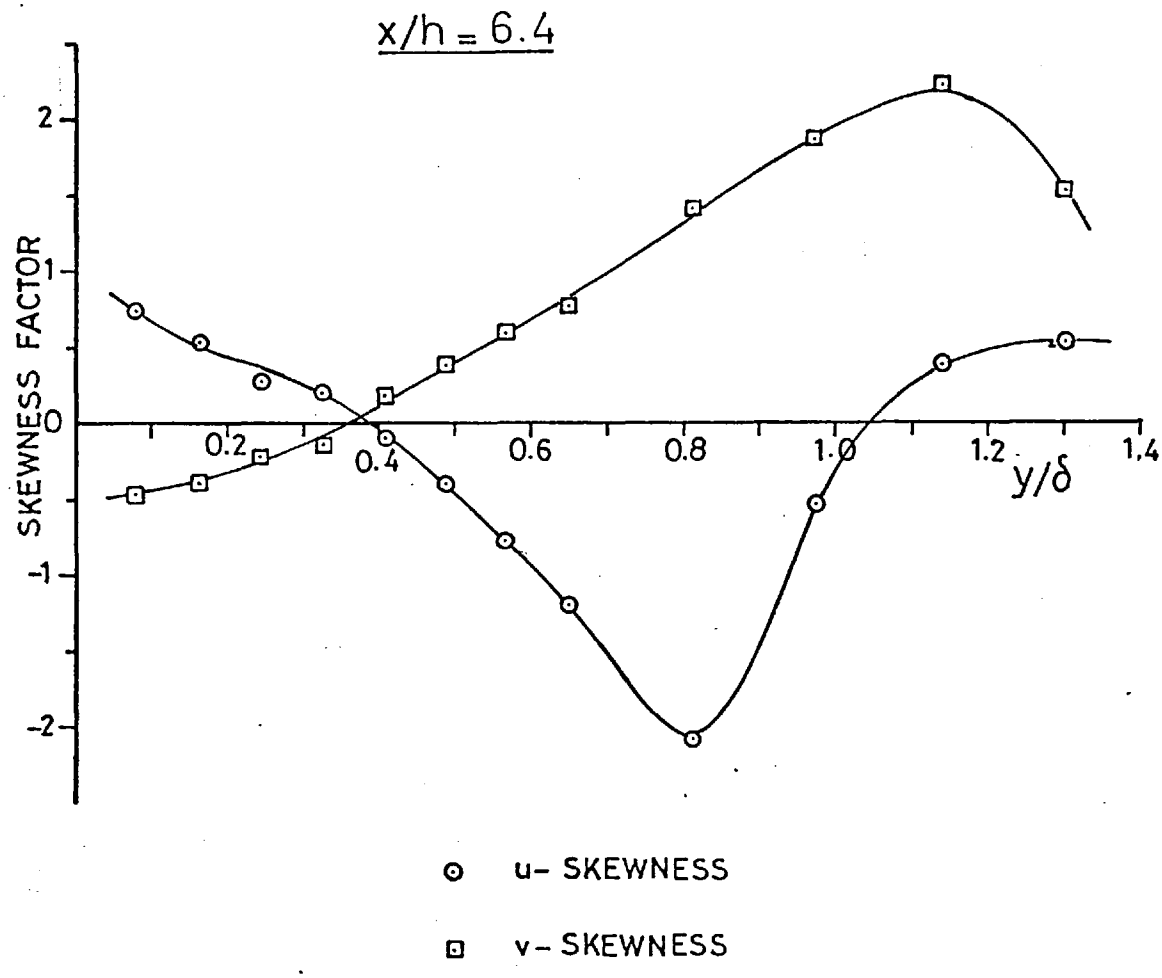


FIGURE 5.13(b) SKEWNESS FACTORS



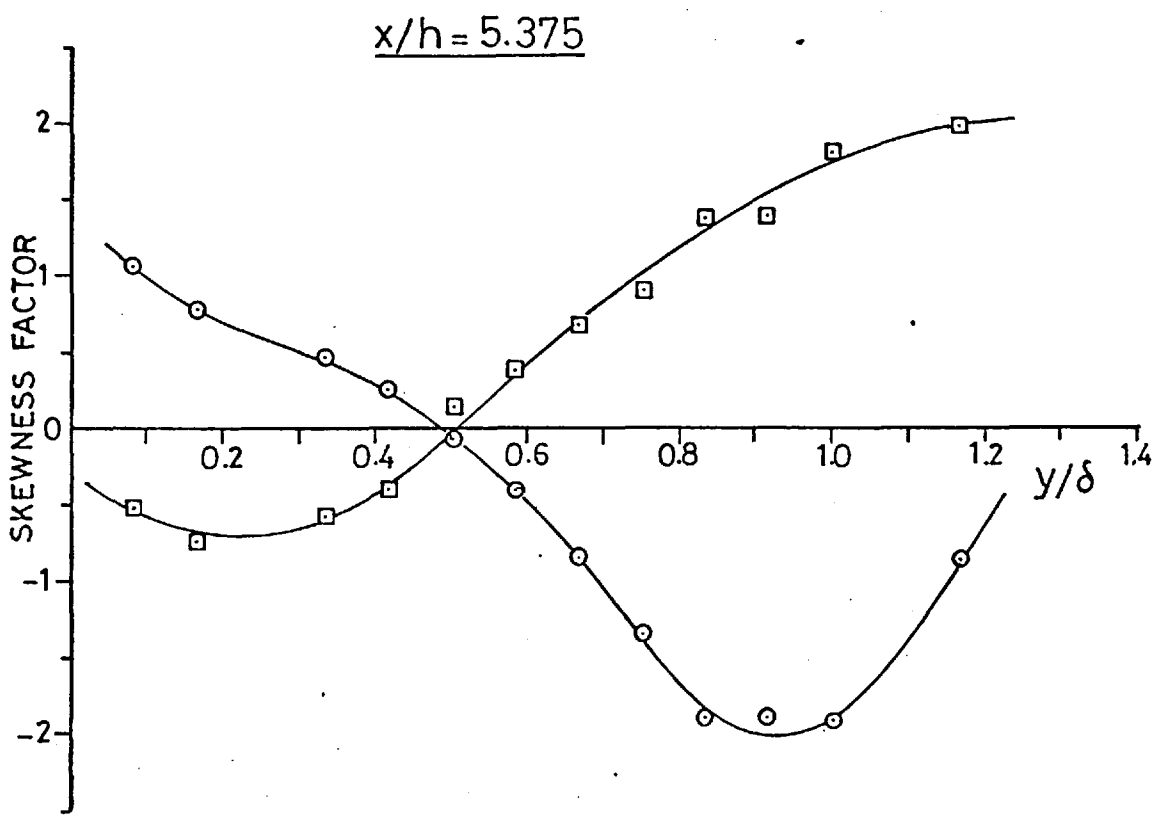


FIGURE 5.13(c) SKEWNESS FACTORS

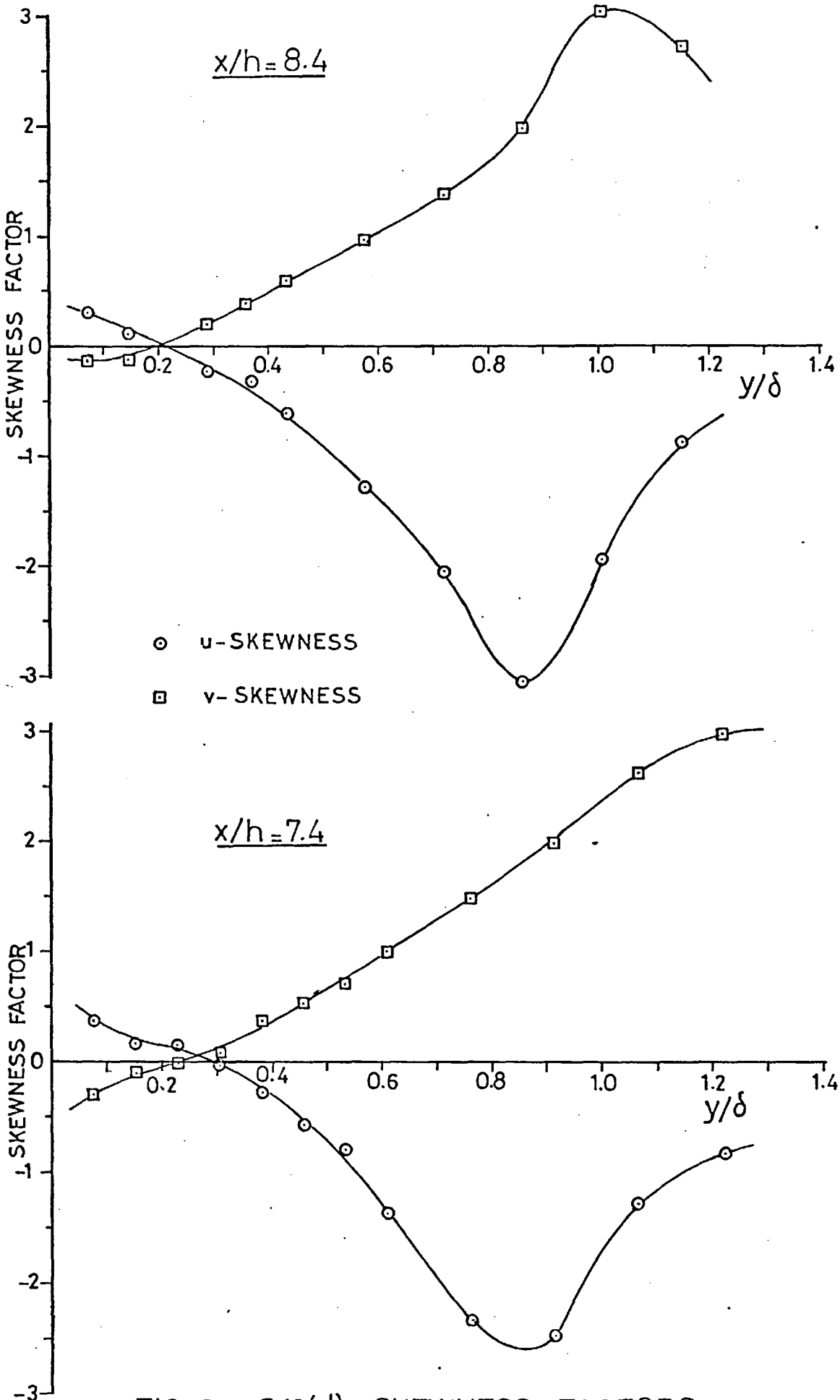


FIGURE 5.13(d) SKEWNESS FACTORS

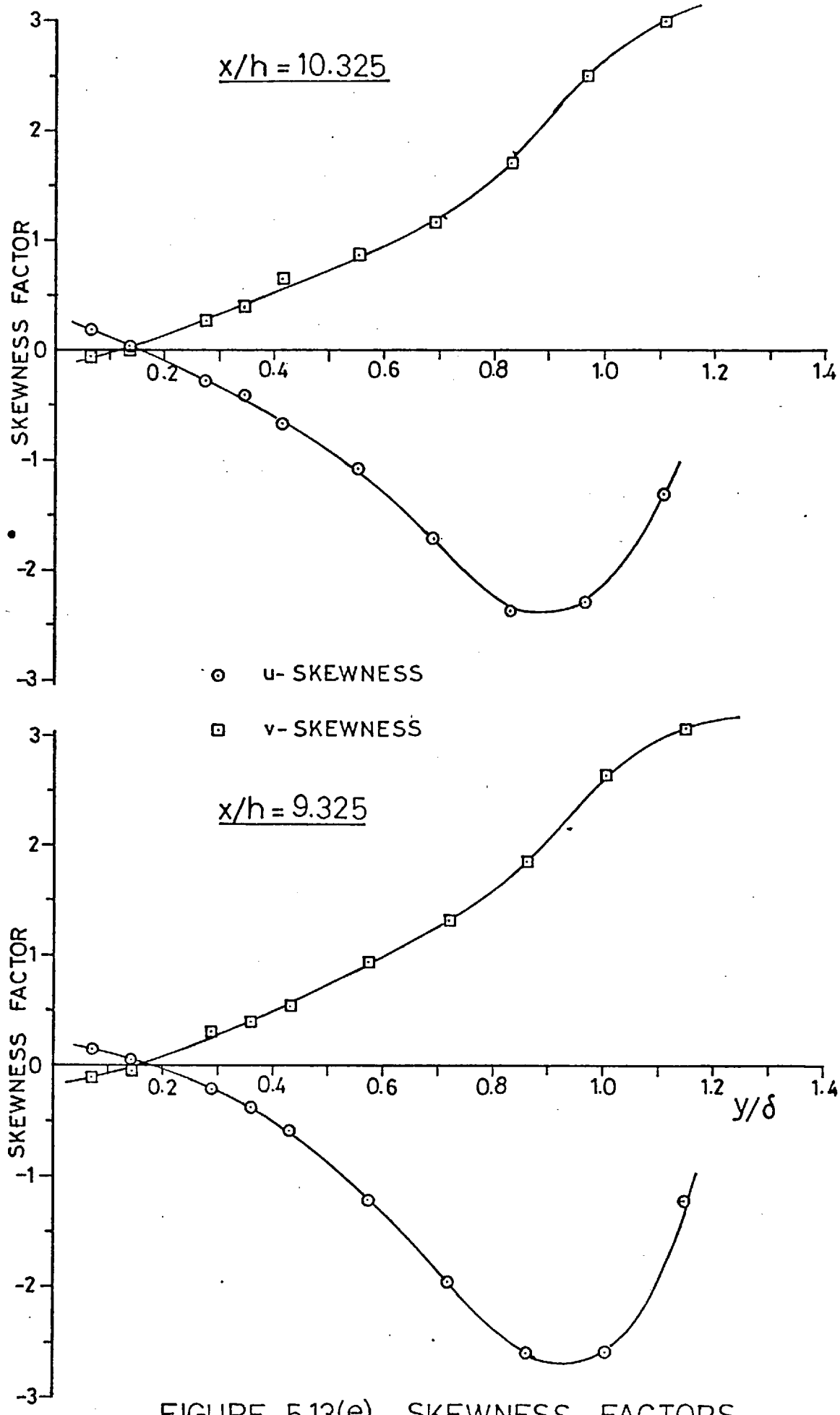


FIGURE 5.13(e) SKEWNESS FACTORS

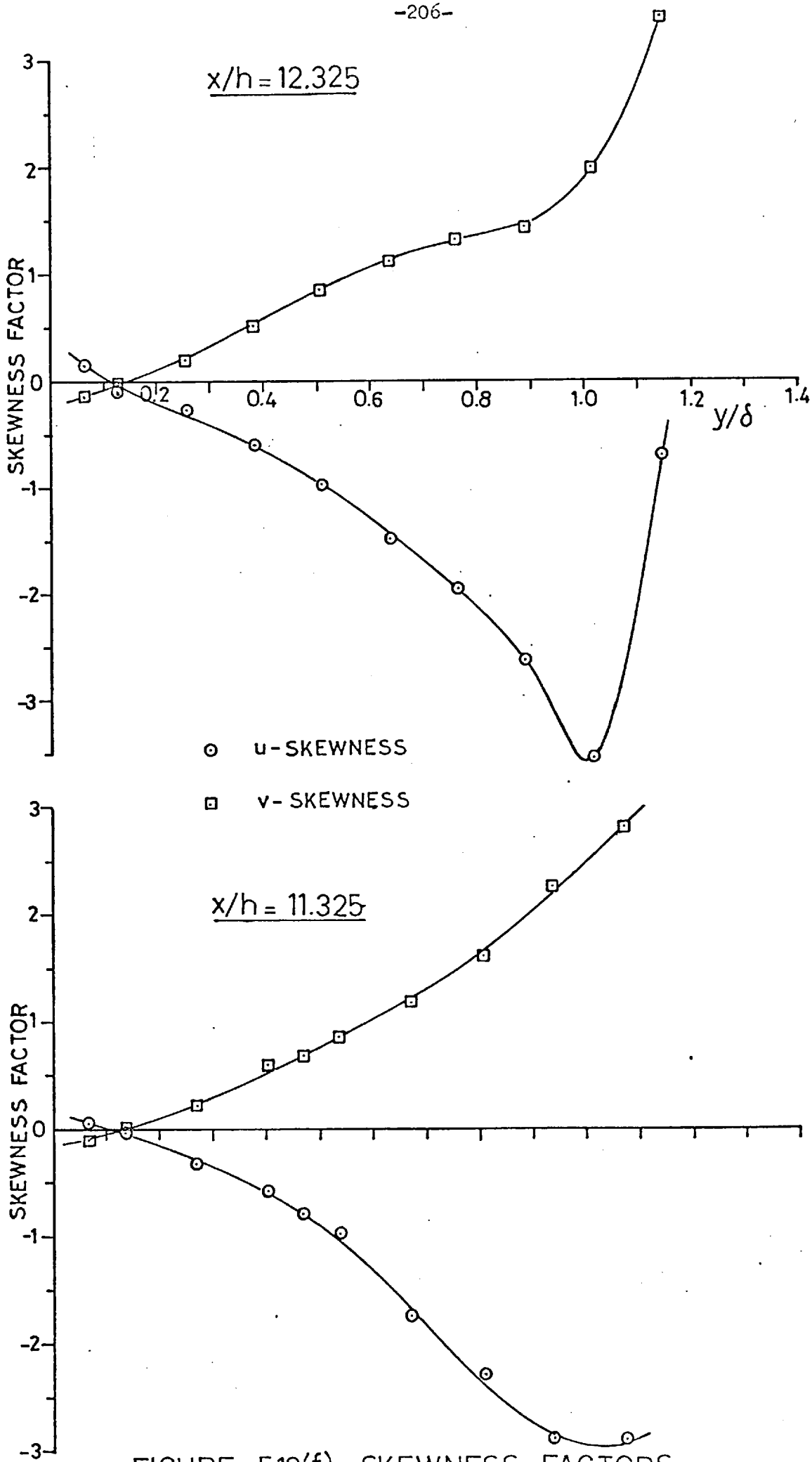


FIGURE 5.13(f) SKEWNESS FACTORS

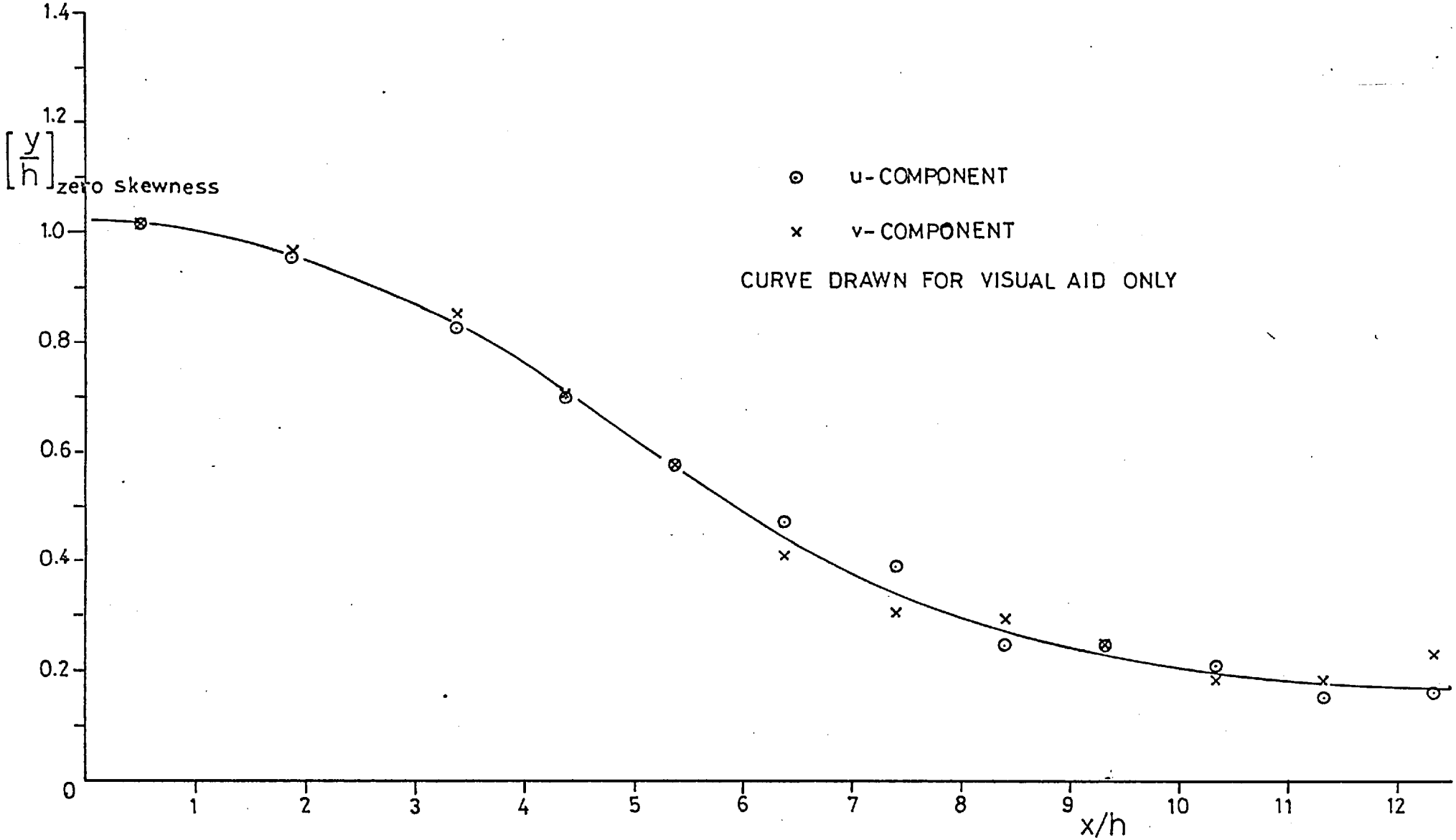
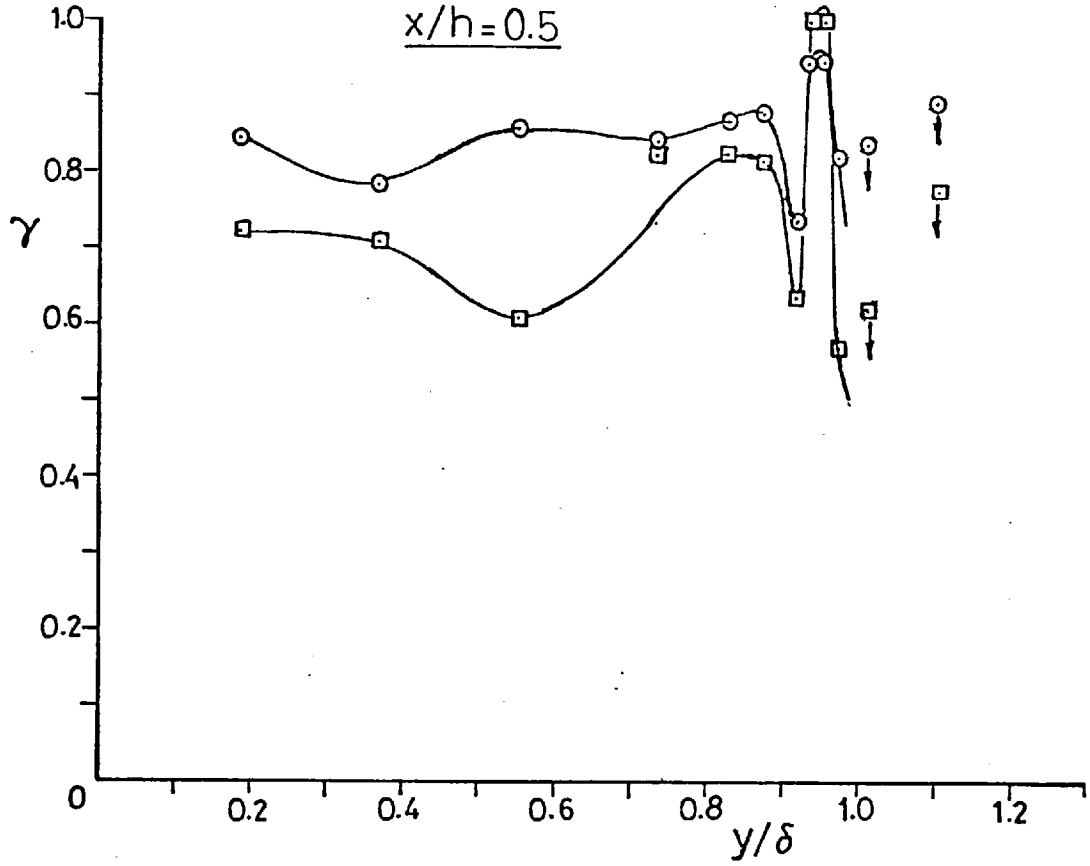


FIGURE 5.14 LOCATION OF ZERO SKEWNESS FACTOR

FIGURE 5.15(a) INTERMITTENCY FACTORS



⊙ Usual definition

⊡ Calculated from flatness factor

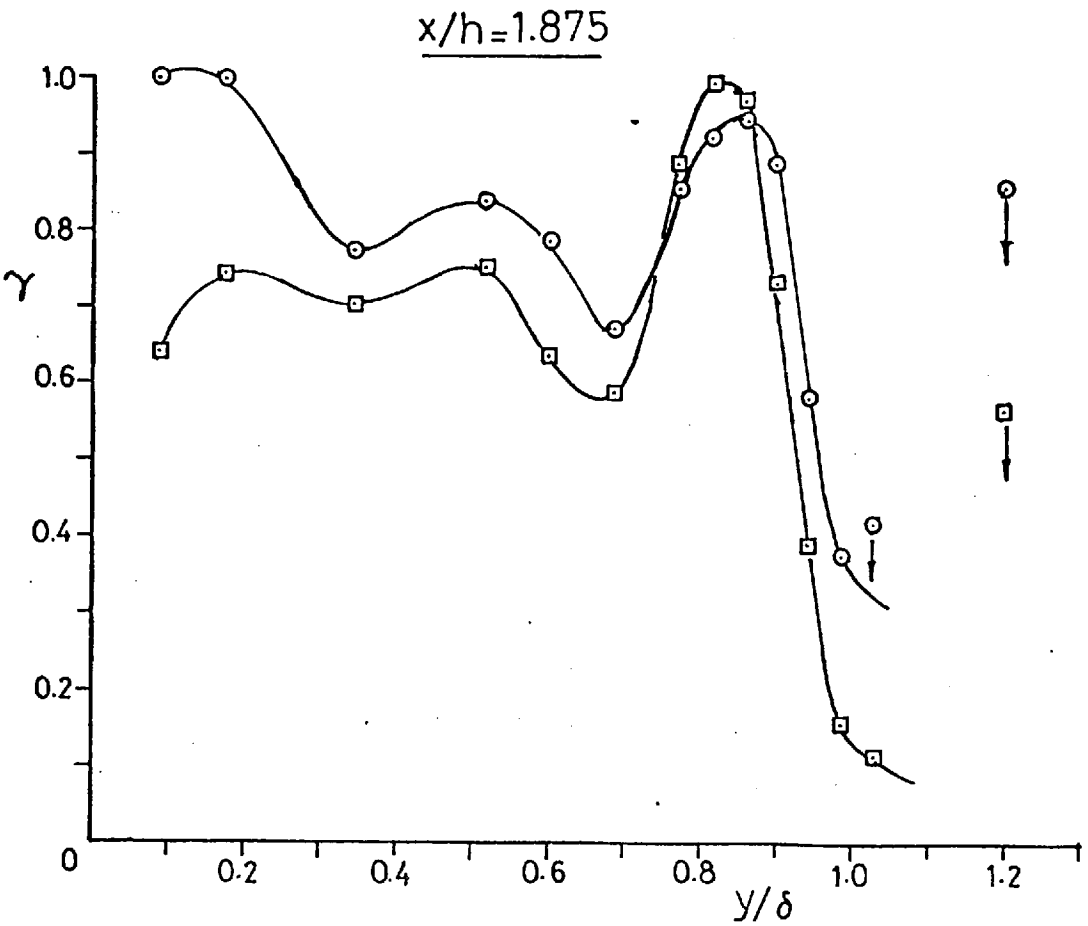
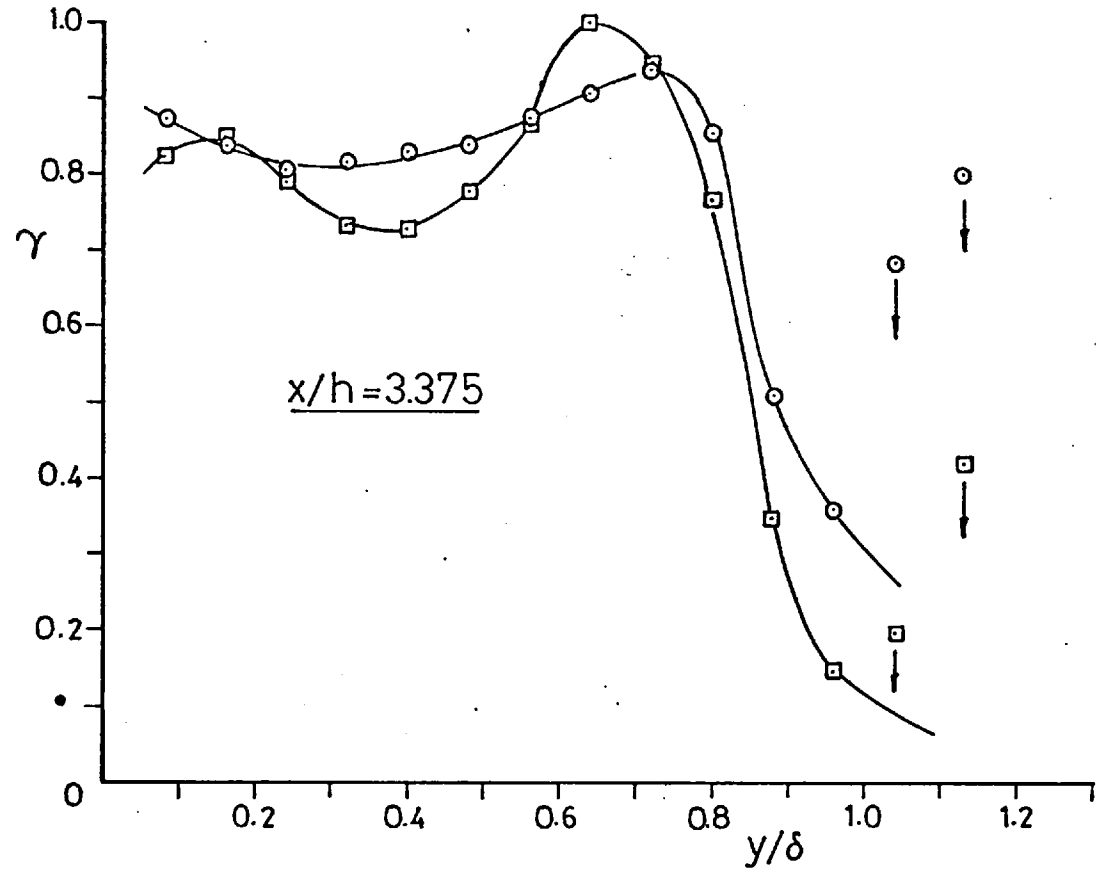


FIGURE 5.15(b) INTERMITTENCY FACTORS



⊙ Usual definition

⊡ Calculated from flatness factor

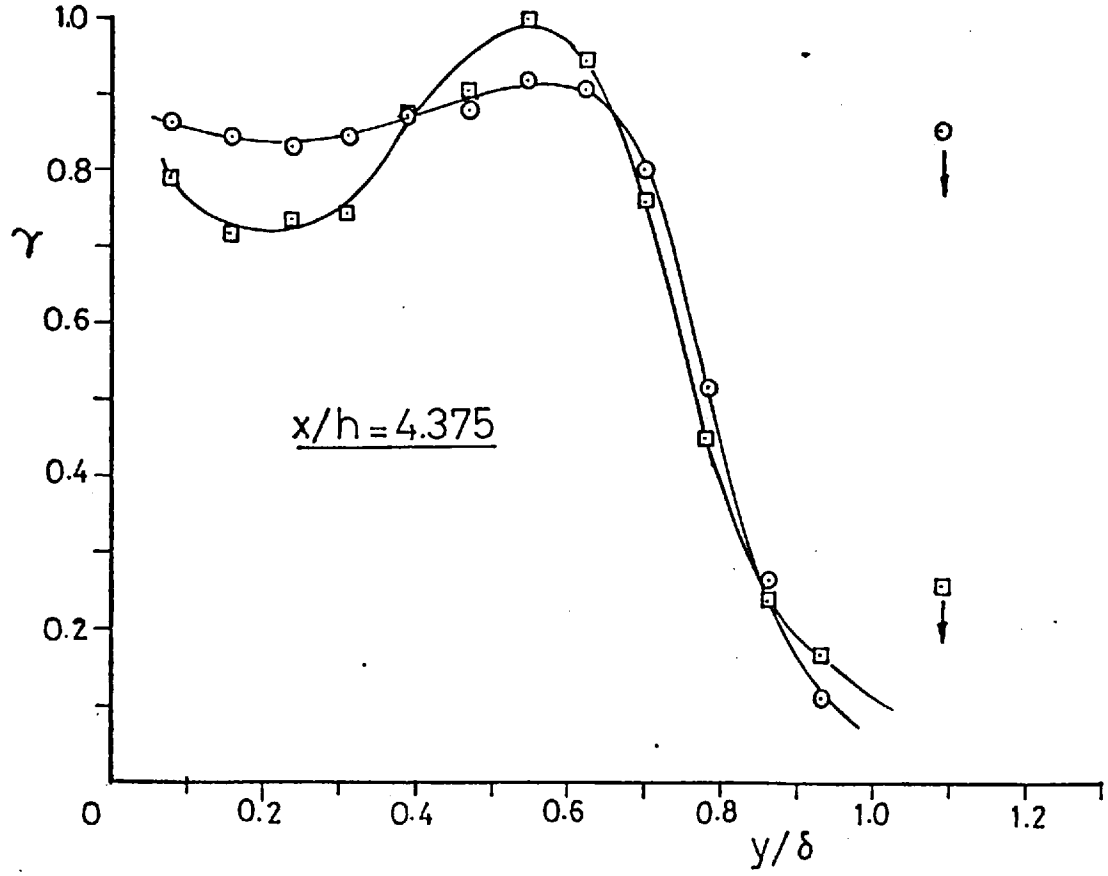
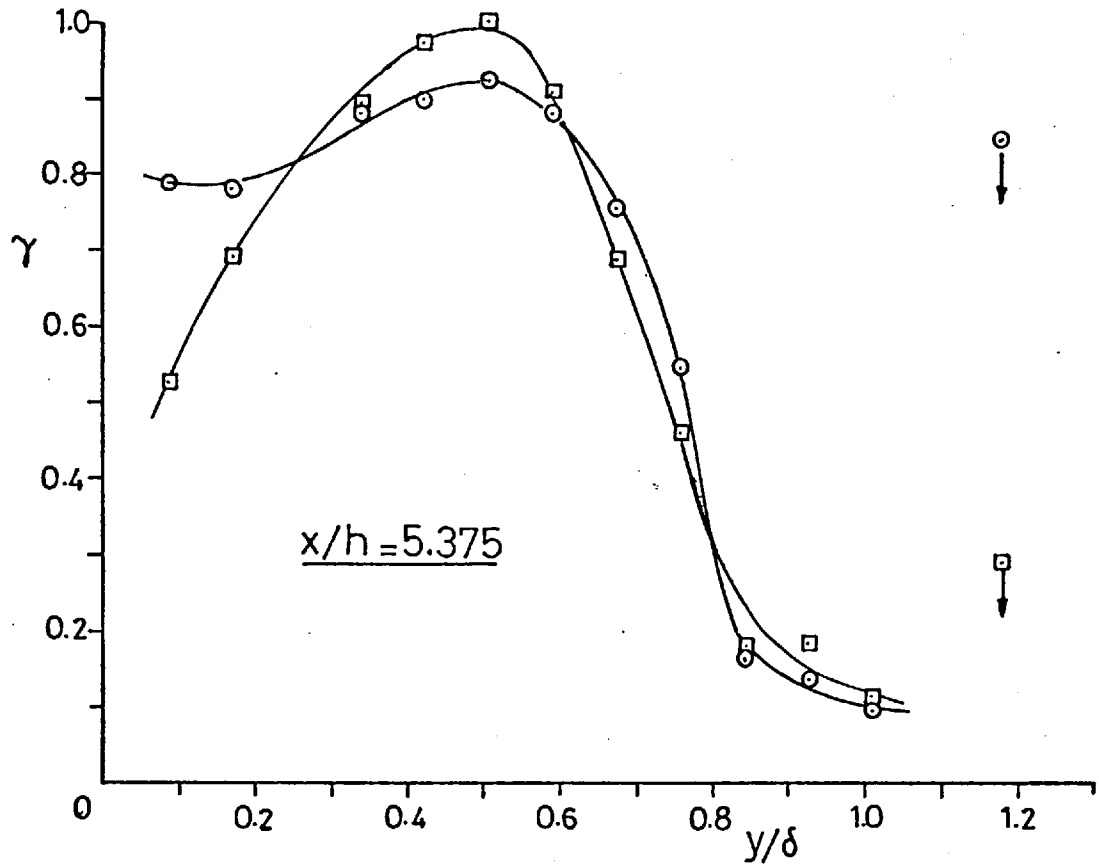


FIGURE 5.15(c) INTERMITTENCY FACTORS



⊙ Usual definition

⊡ Calculated from flatness factor

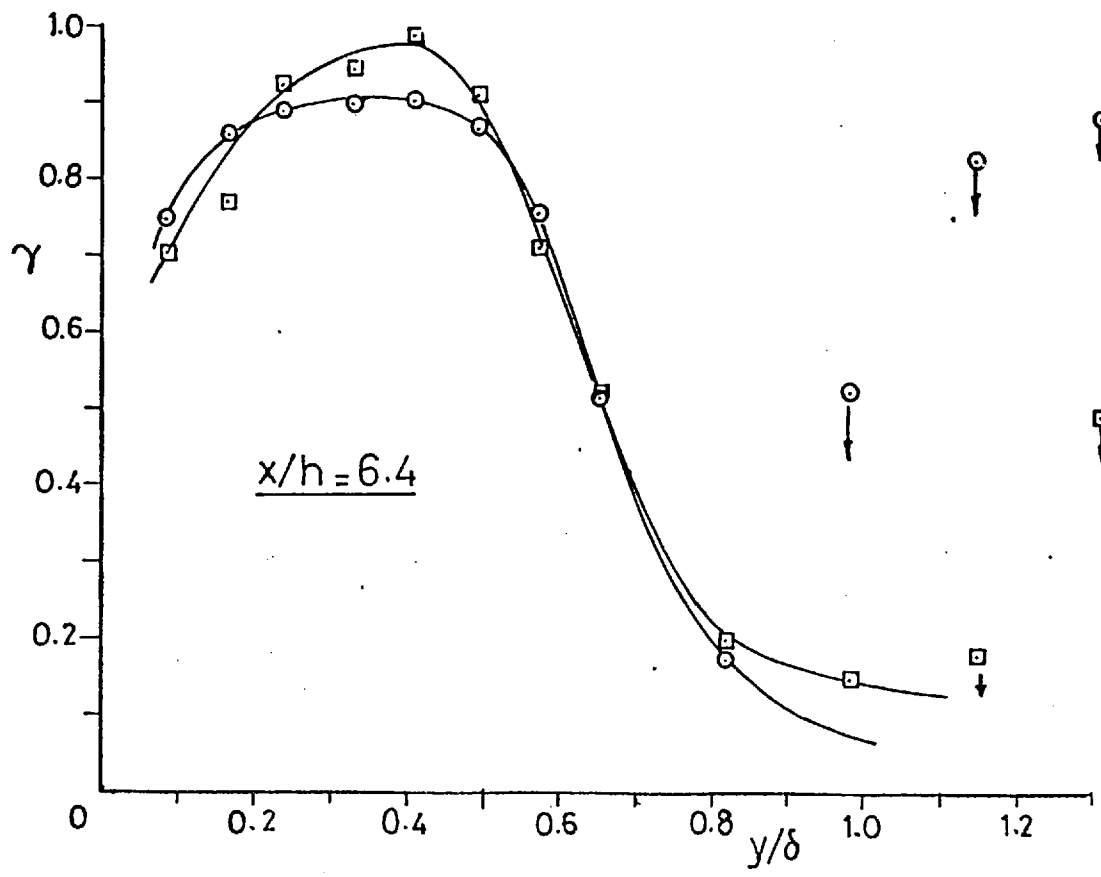
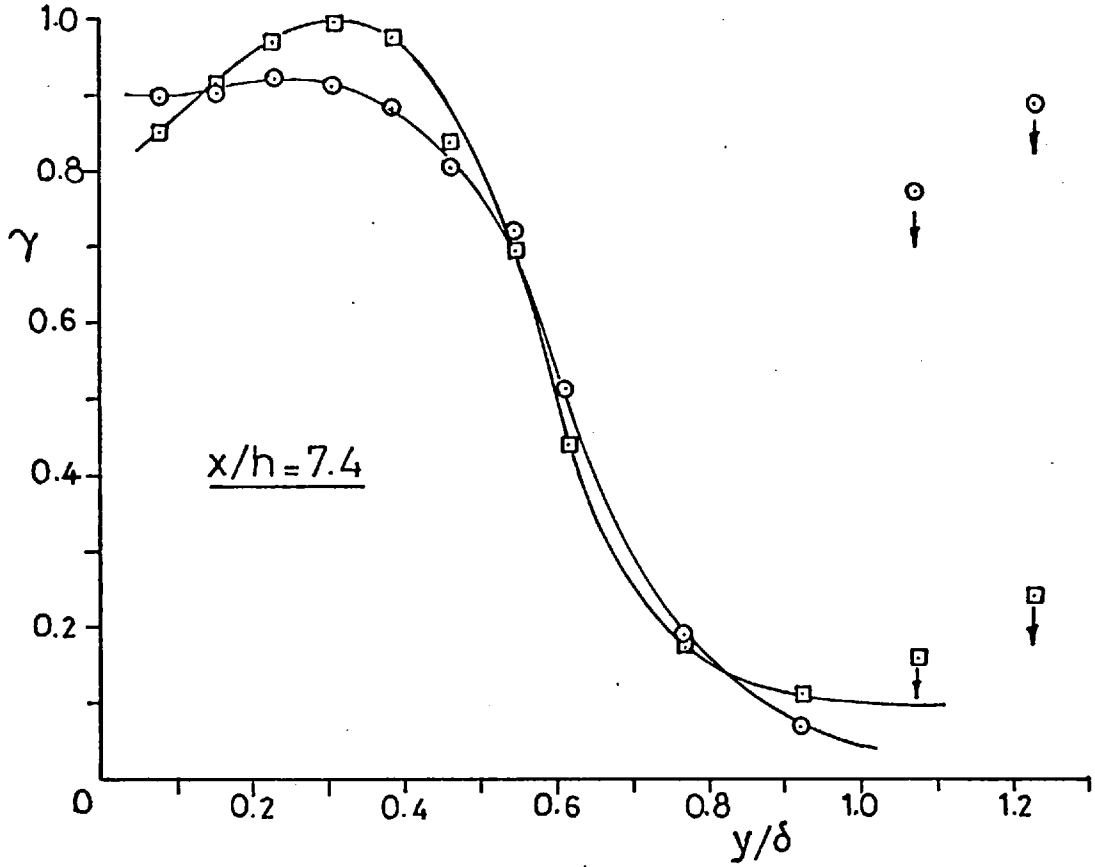


FIGURE 5.15(d) INTERMITTENCY FACTORS



⊙ Usual definition

⊡ Calculed from flatness factor

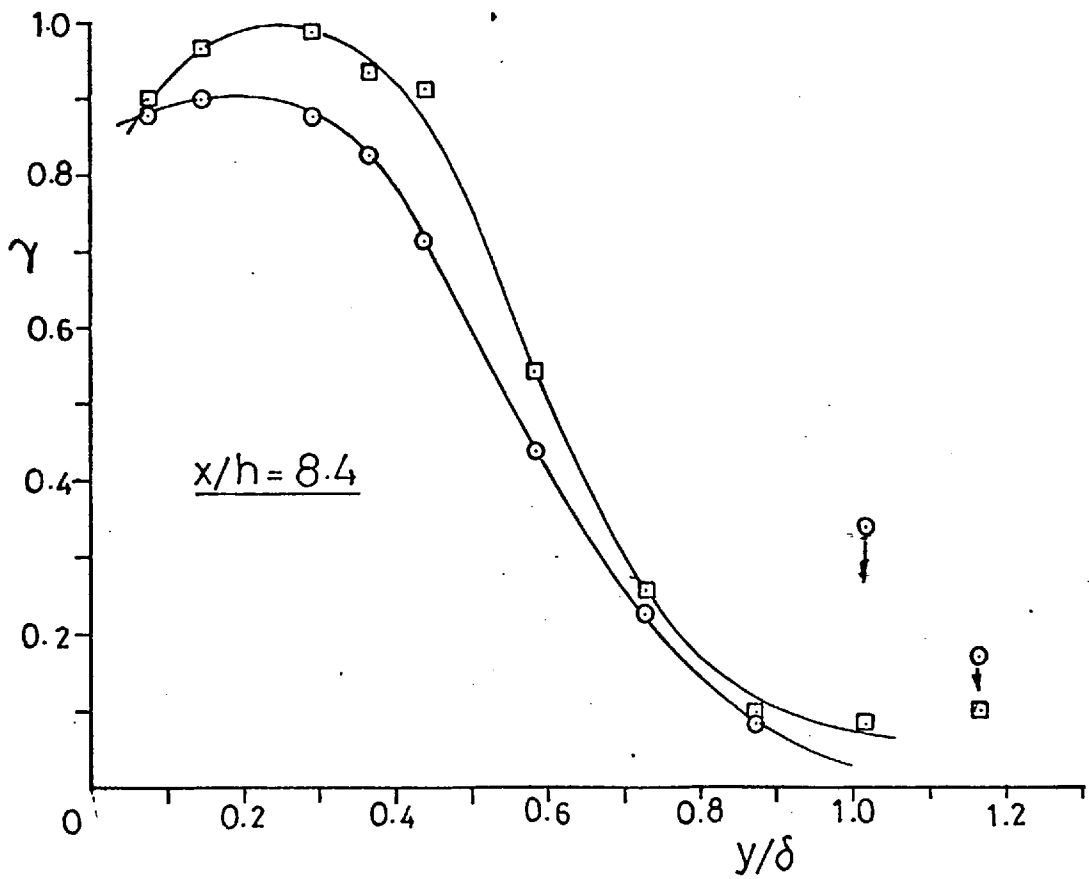
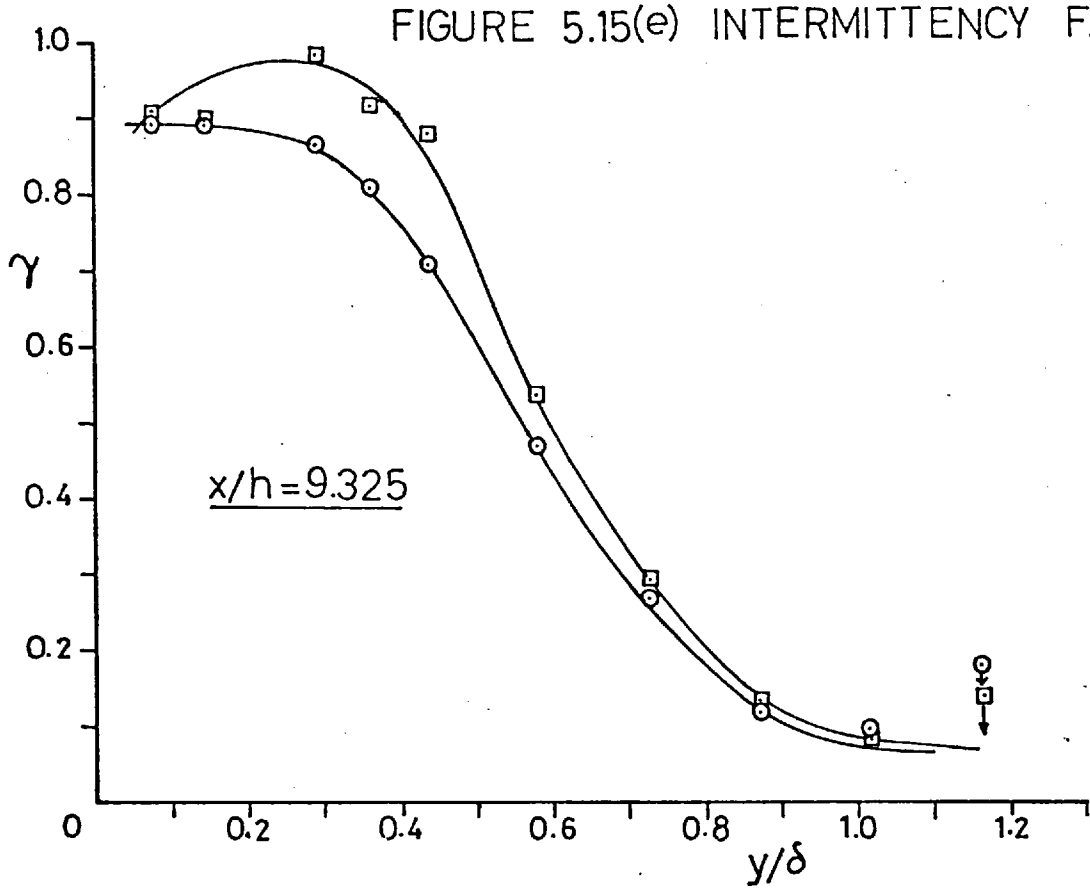


FIGURE 5.15(e) INTERMITTENCY FACTORS



⊙ Usual definition

⊡ Calculated from flatness factor

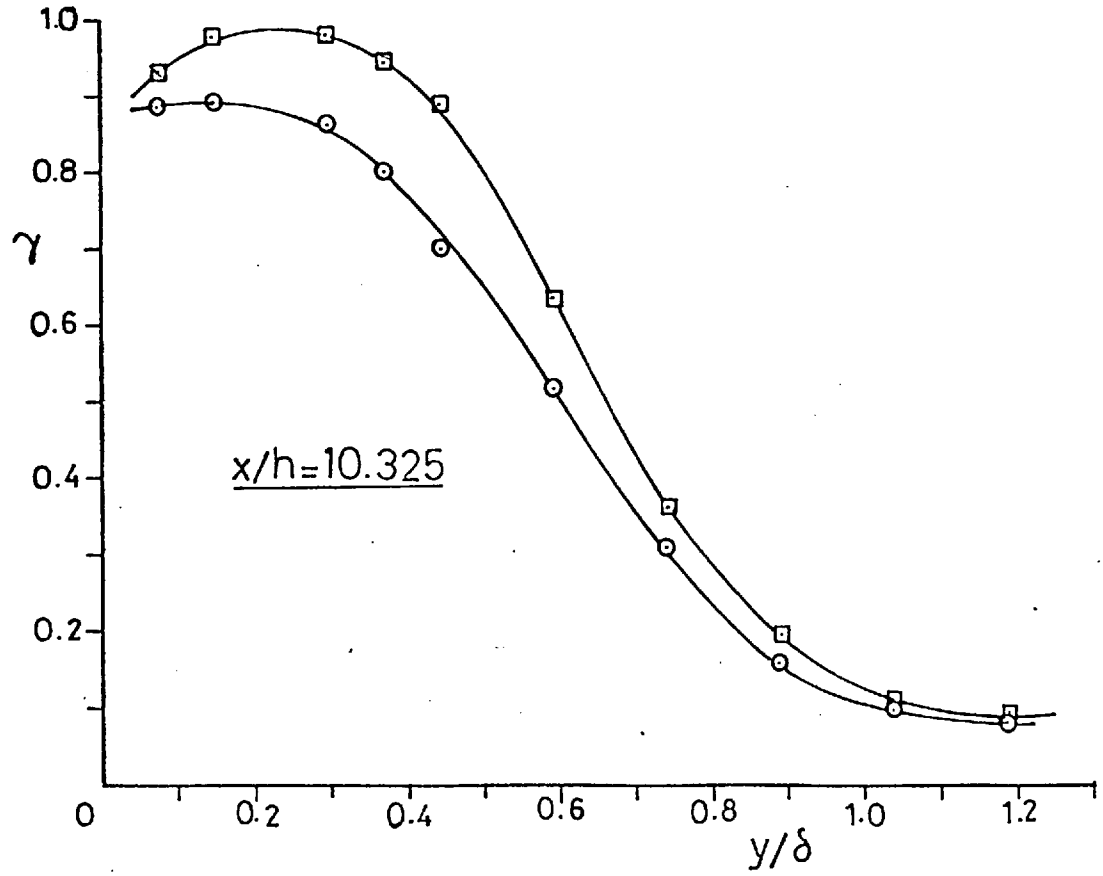
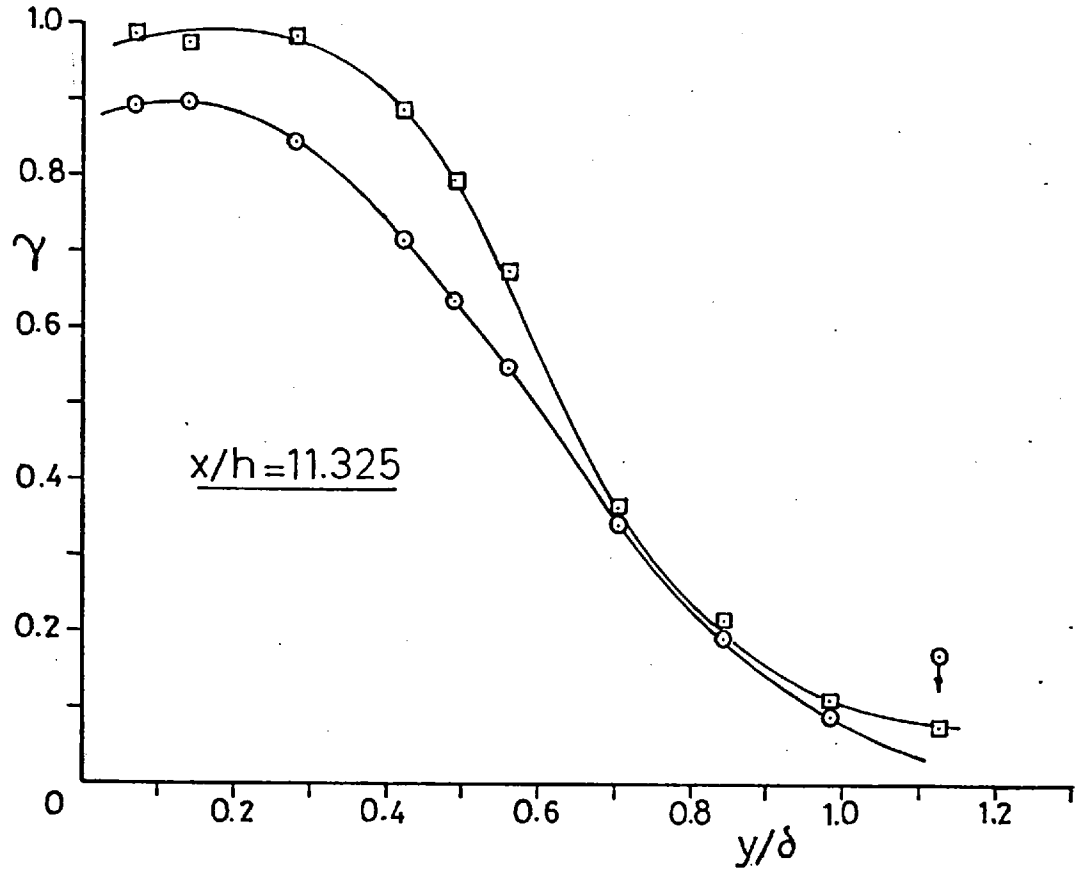
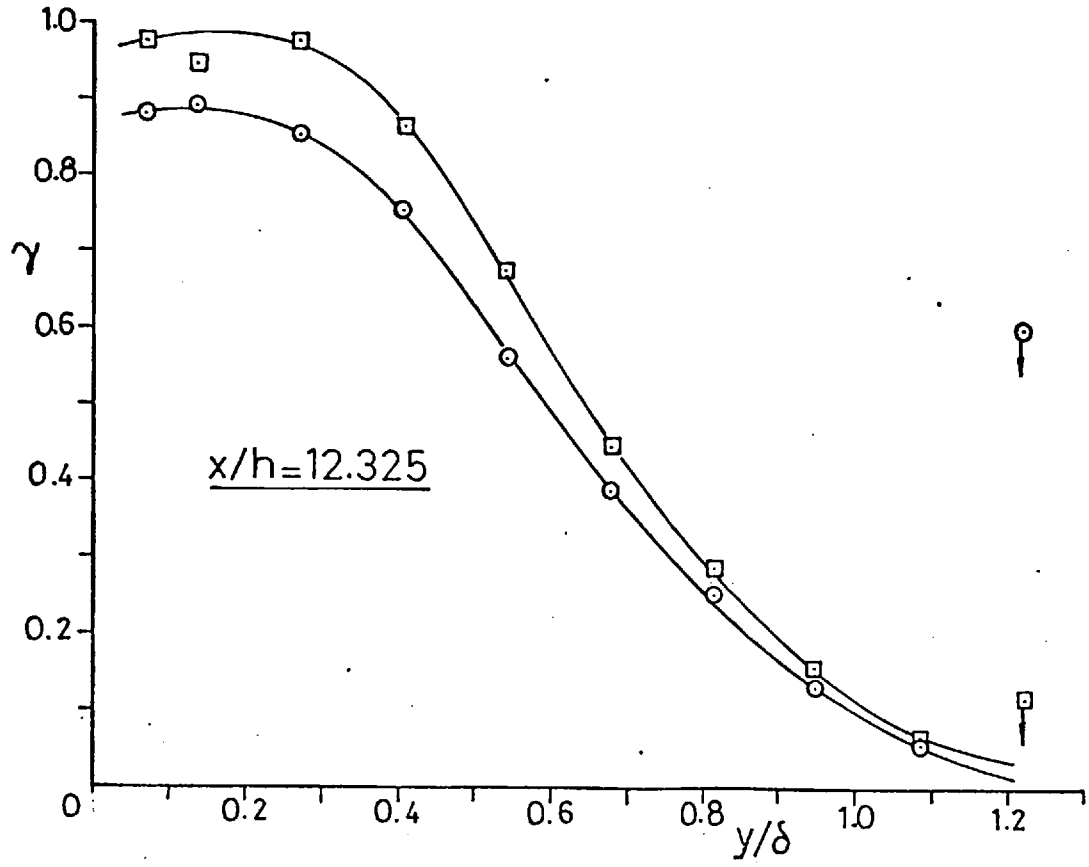


FIGURE 5.15(f) INTERMITTENCY FACTORS



⊙ Usual definition

⊡ Calculated from flatness factor



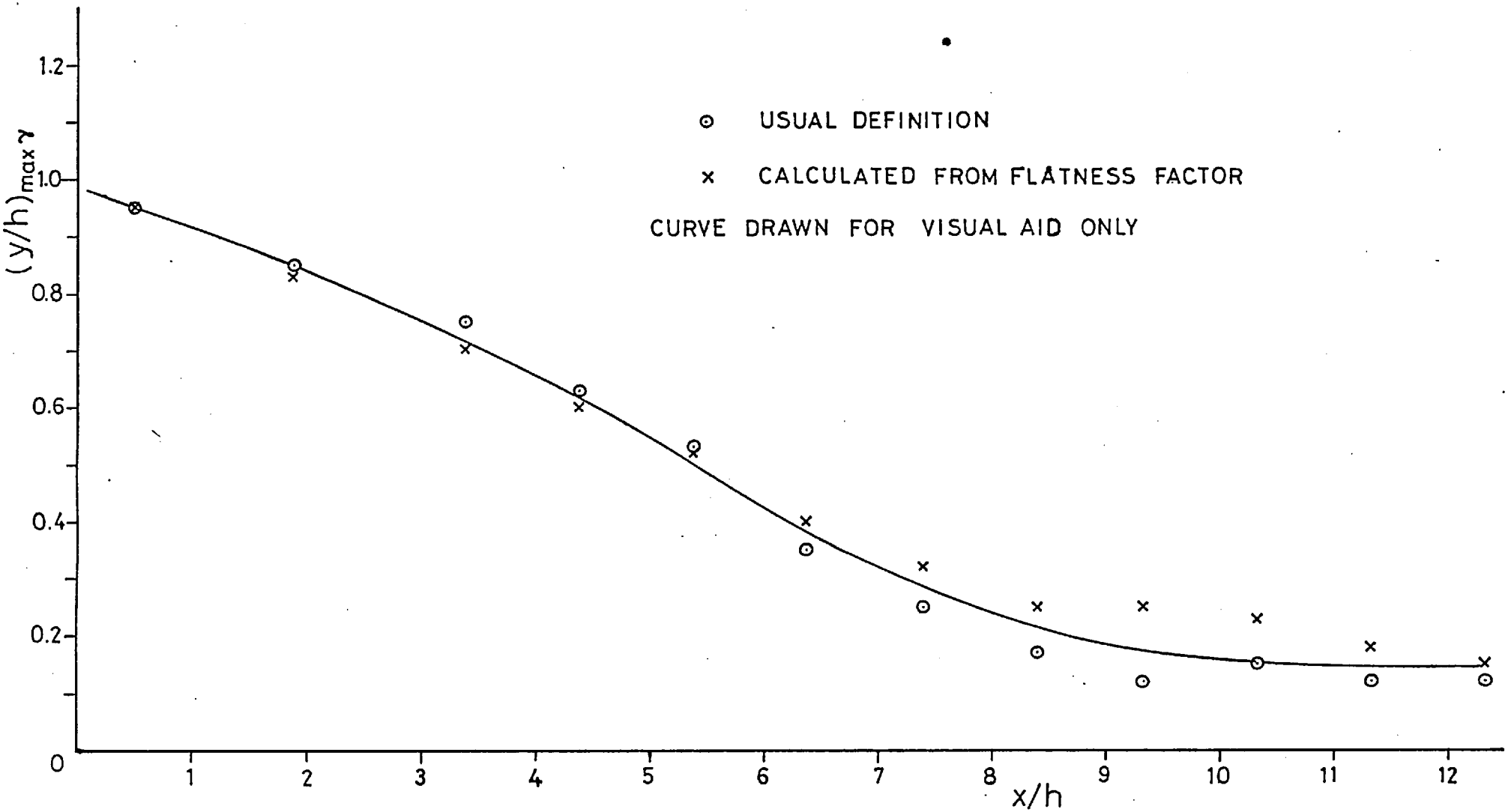


FIGURE 5.16 APPROX. LOCATION OF MAXIMUM INTERMITTENCY FACTOR

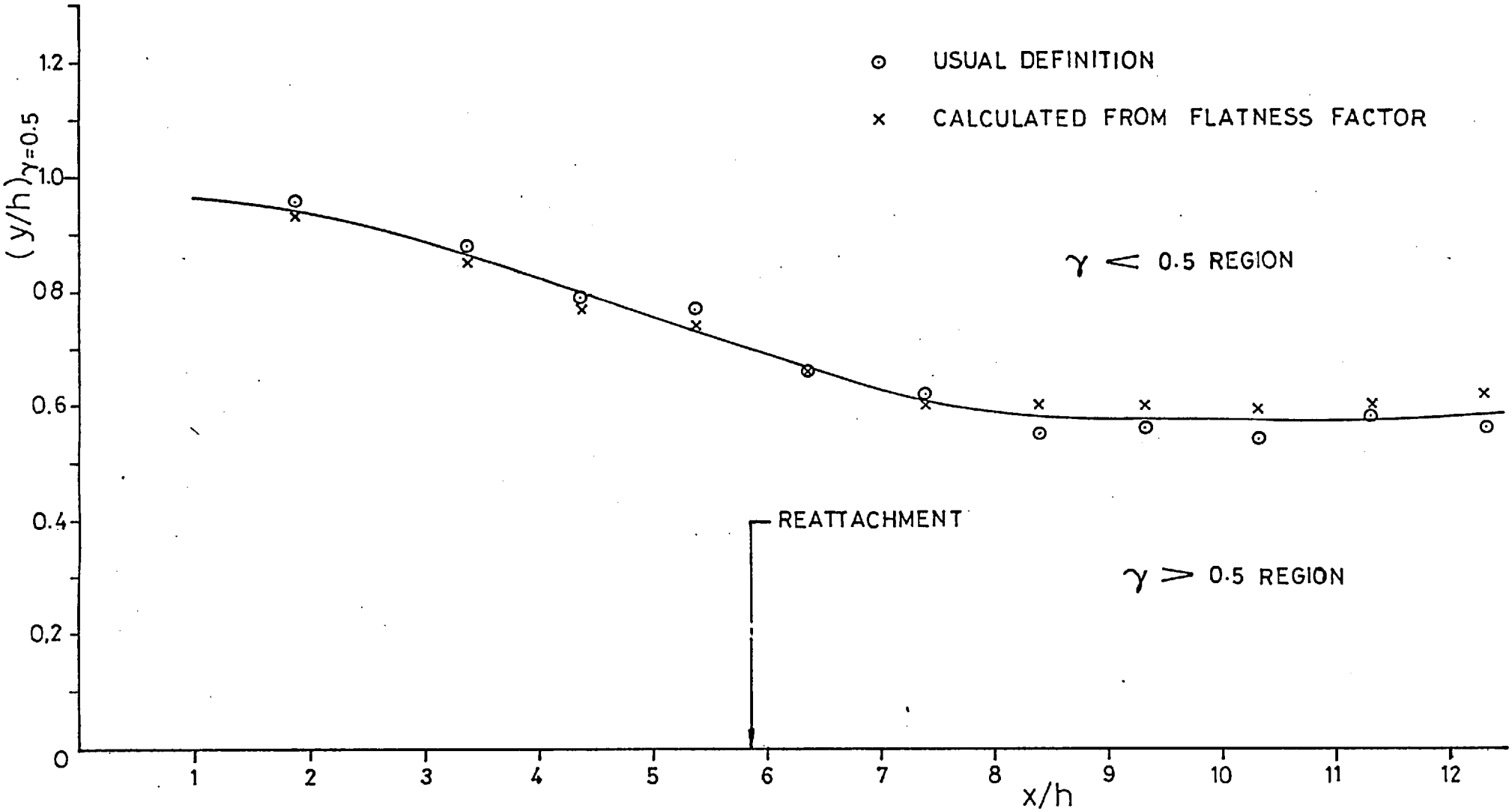


FIGURE 5.17 50% INTERMITTENCY INTERFACE

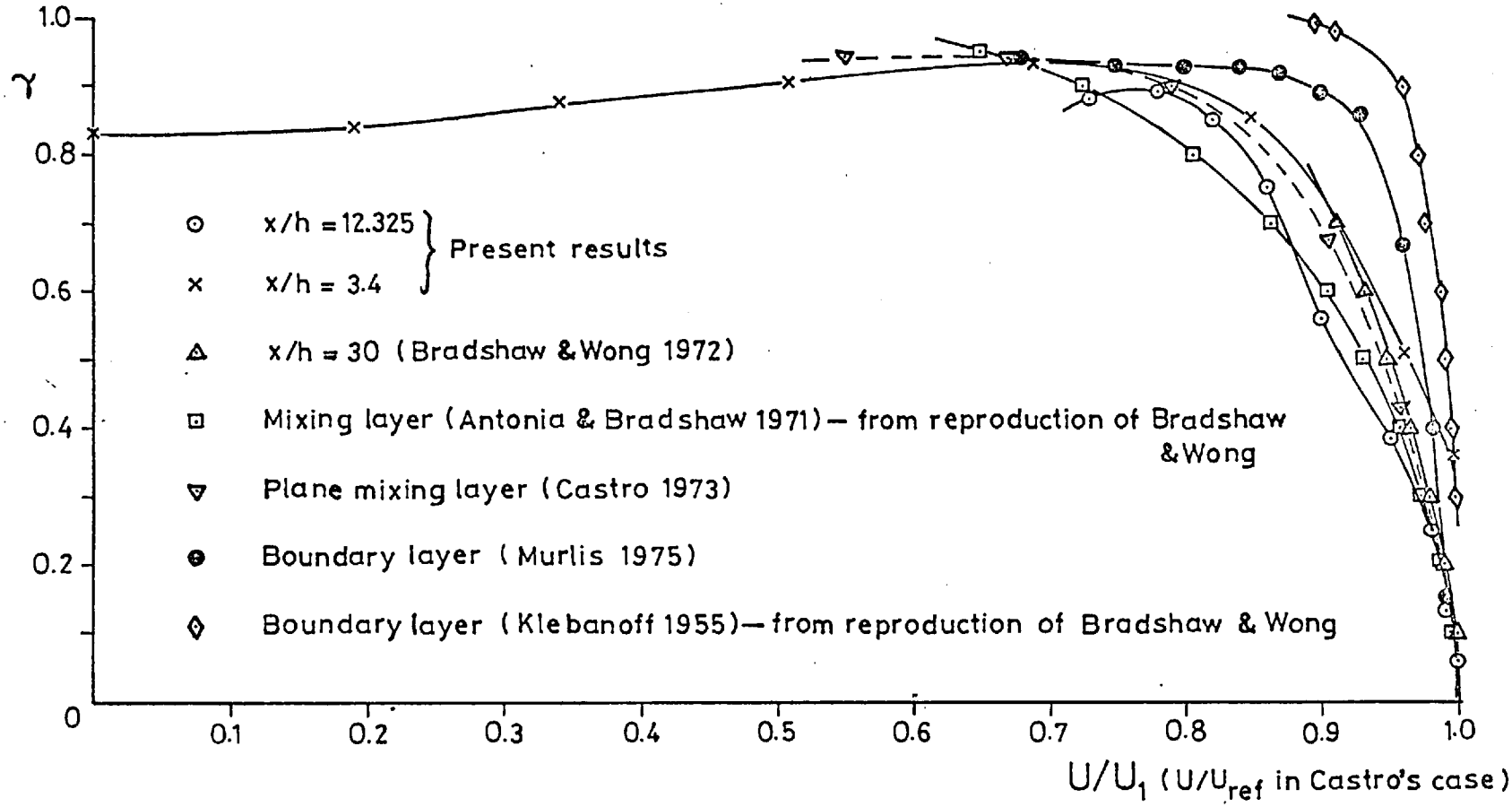


FIGURE 5.18 COMPARISON OF INTERMITTENCY FACTOR WITH RESULTS OF OTHER WORKERS

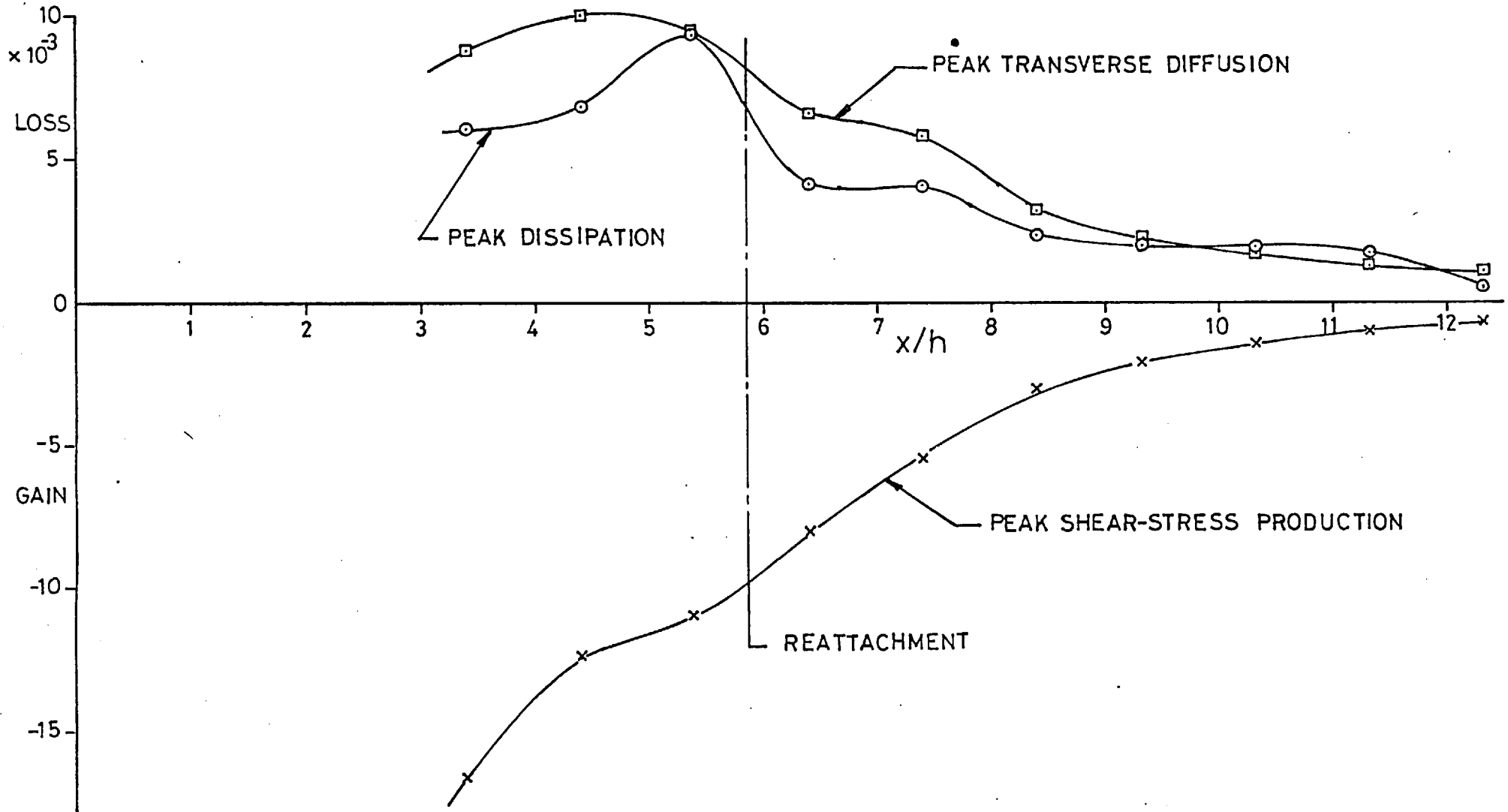


FIGURE 5.19 APPROX. STREAMWISE VARIATION OF PEAK VALUES OF ENERGY BALANCE TERMS

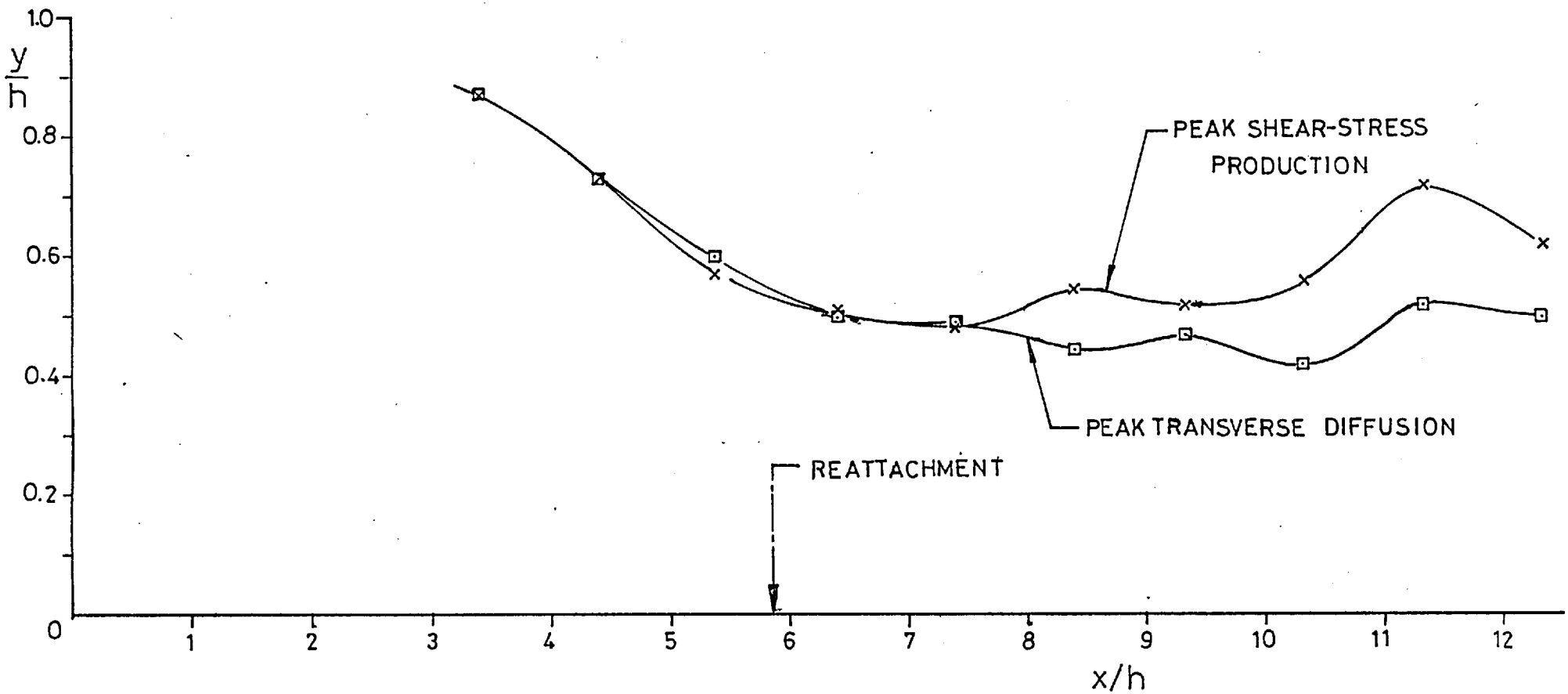


FIGURE 5.20 APPROXIMATE LOCATION OF PEAKS

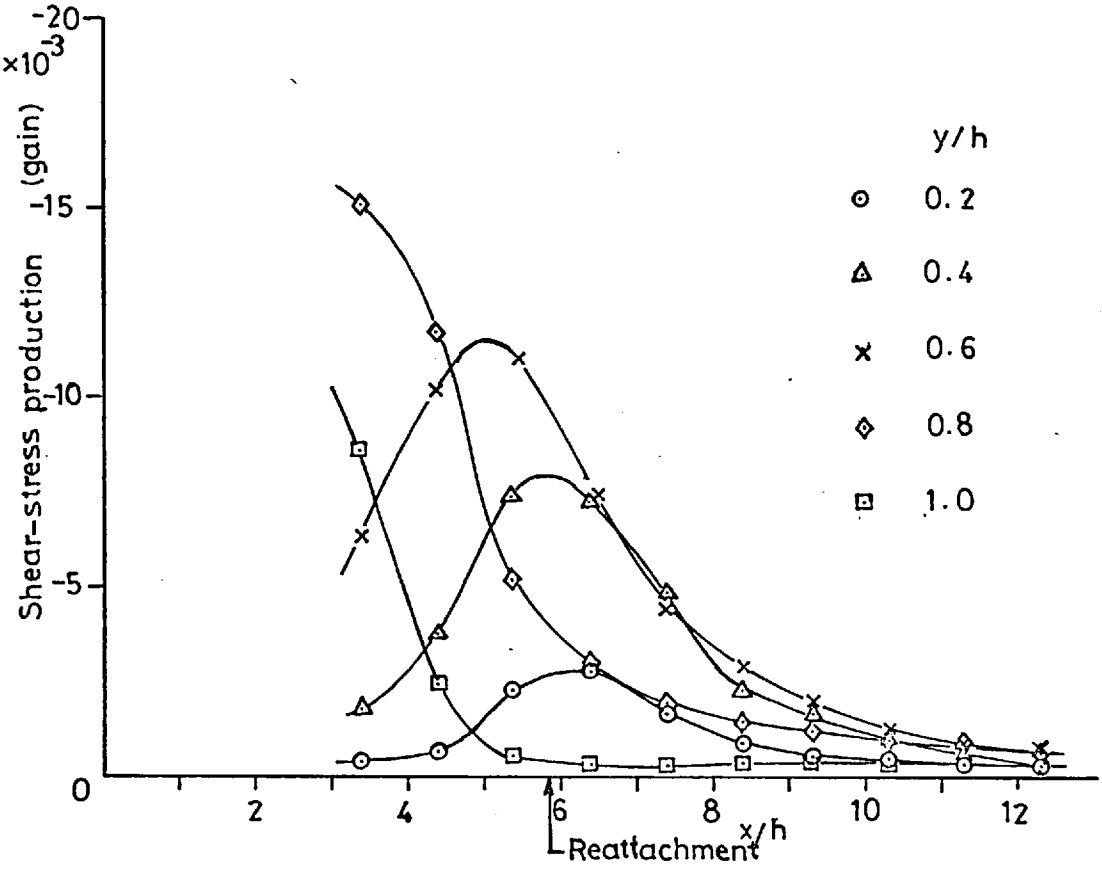


FIGURE 5.21 STREAMWISE VARIATION OF SHEAR-STRESS PRODUCTION

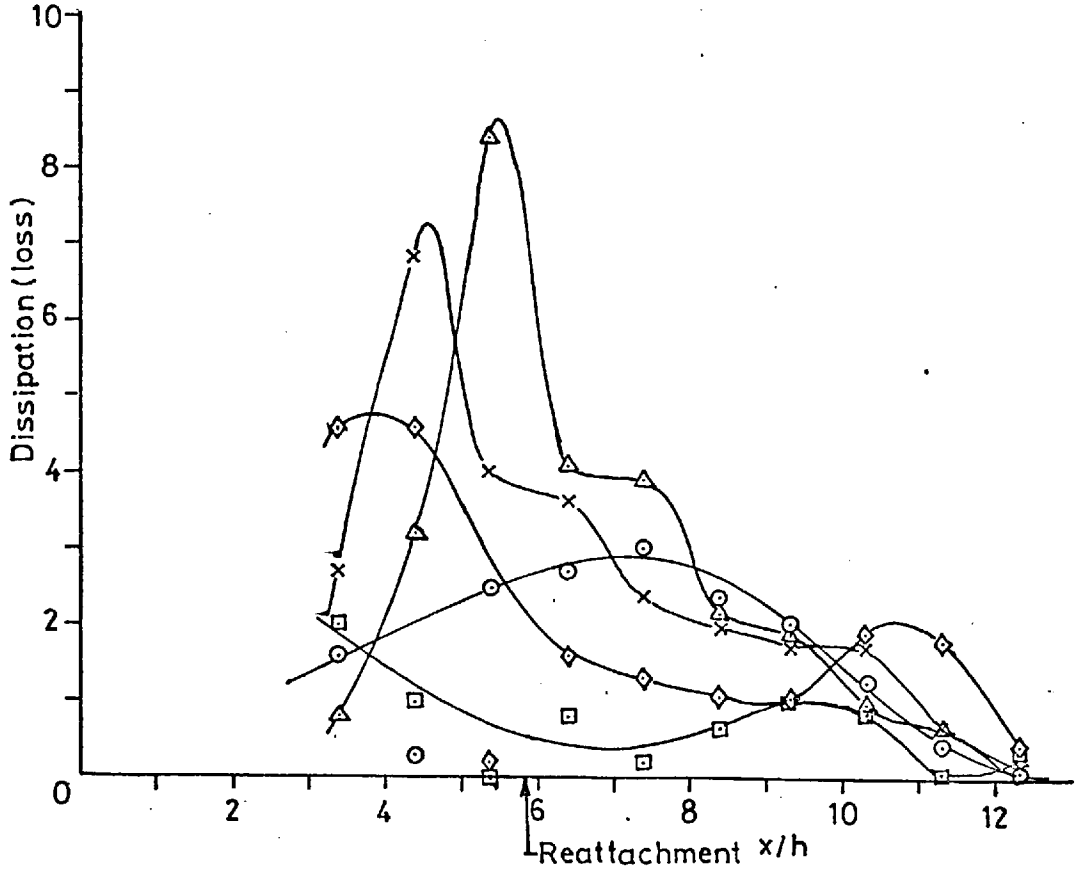


FIGURE 5.22 STREAMWISE VARIATION OF DISSIPATION

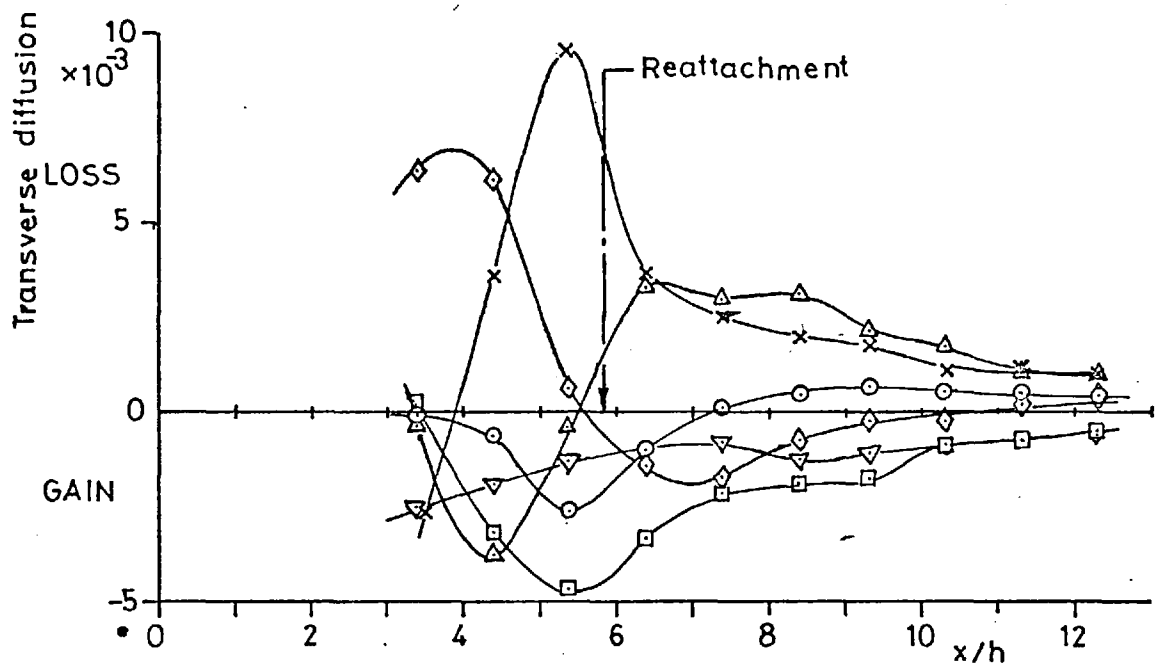


FIGURE 5.23 STREAMWISE VARIATION OF TRANSVERSE DIFFUSION

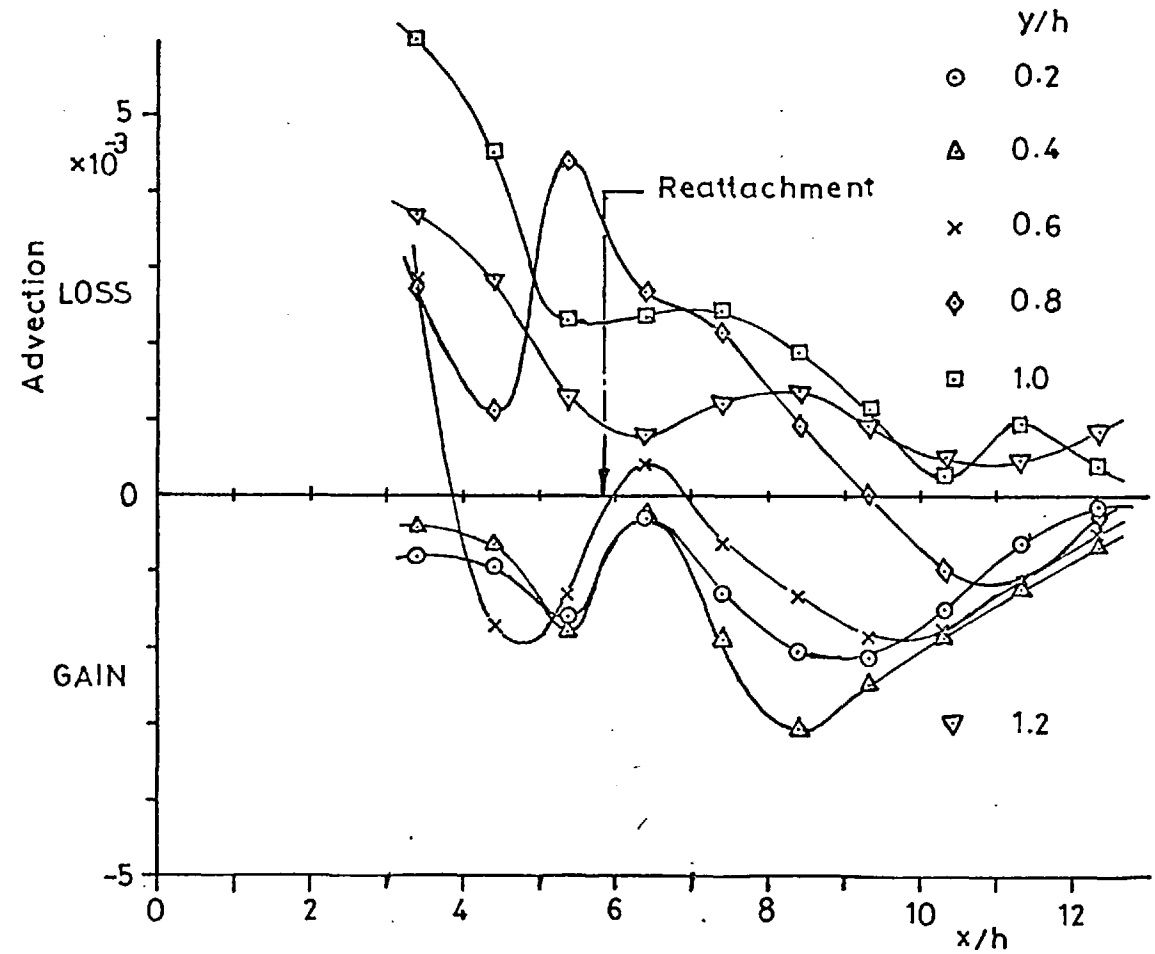


FIGURE 5.24 STREAMWISE VARIATION OF ADVECTION

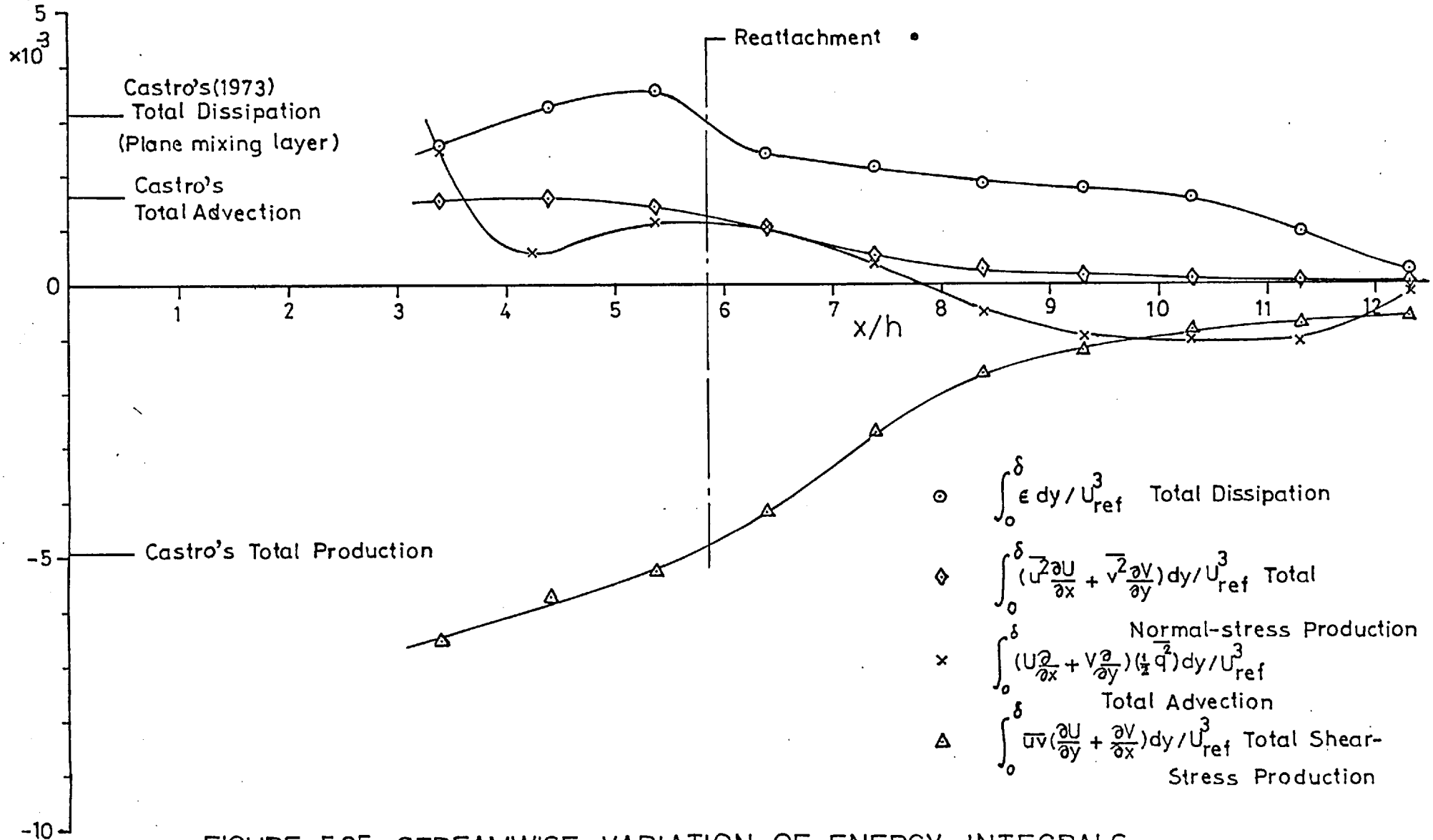


FIGURE 5.25 STREAMWISE VARIATION OF ENERGY INTEGRALS

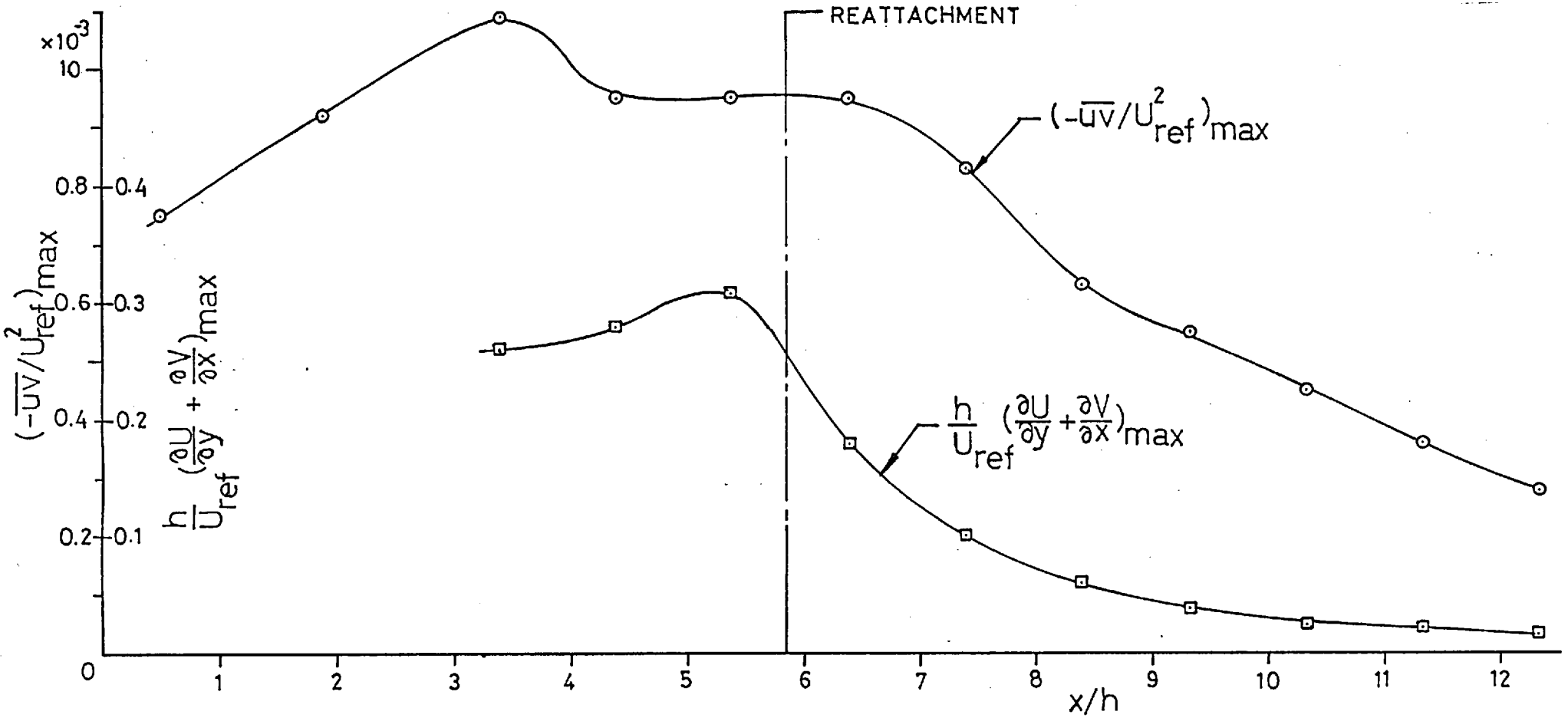


FIGURE 5.26 COMPARISON BETWEEN STREAMWISE VARIATION OF $(-\overline{uv})_{max}$ & $(\frac{\partial U}{\partial y}+\frac{\partial V}{\partial x})_{max}$

CHAPTER 6

GENERAL DISCUSSION AND CONCLUSIONS

In the previous chapters we have presented and discussed the results in detail, with certain immediate conclusions where possible. The object of this chapter is to give a more connected account of the main structural features of the reattachment region, to draw the best possible conclusions, and to pose some of the new problems encountered during the course of investigation to which future work may pay more attention.

The present results demonstrate further the complicated nature of the flow in the reattachment region which has been realized by most previous workers, e.g. Bradshaw & Wong (1972). The main difficulty is the lack of suitable and reliable means of measurement at present to cope with the investigation of the separated-flow region,which has a great direct effect on the reattachment region, and of the reattachment region itself. However with the existing methods of measurement it is believed that, within the experimental errors discussed in section 5.1, the present results represent more or less the true picture of the main reattachment characteristics, so that their effects on the slow non-monotonic return of the shear layer to the ordinary boundary layer state can be understood better than before.

With nominally two-dimensional flow over a backward-facing step under investigation, the results show that most basic properties - such as the reattachment distance, the surface-pressure distribution, the skin friction coefficient and the like - found in the present experiment agree fairly well with the previous results, indicating satisfactory experimental techniques in general. The static pressure

was found to vary considerably in the reattachment region. The semi-logarithmic profiles are of the same trend as those in Bradshaw & Wong's (1972) results, but show less dip close downstream of the reattachment. The inflexion which is seen even on a linear plot is a good indication of the distortion of the shear layer after reattachment, which is supported by further evidence to be discussed later.

6.1. THE SEPARATED-FLOW REGION

Although a great deal of work would be needed to document all the features of the separated-flow region (comprising the free shear layer and the recirculation zone below it), the present results can at least provide a qualitative description of its behaviour rather more clearly than previous experiments and will be discussed first. Bradshaw & Wong suggest that the flow of a thin boundary layer over a backward-facing step, like that in the present experiment, involves two 'overwhelming' perturbations (viz. boundary layer to mixing layer and mixing layer back to boundary layer) but the first perturbation can be ignored and the flow treated as if a fully developed mixing layer appeared at the separation point. This seems to be a reasonable postulate because the transition is complete at a distance less than 1/10 of the separation length in the present case. The state of the free shear layer approaching reattachment as well as the different species it has become after reattachment are both of interest. Bradshaw's (1966) criterion gives the distance it takes the plane mixing layer (laminar separation) to forget its initial condition of roughly $100\,\delta_o$ - thereafter the development depends on the boundary conditions only. Although this distance would be less than the reattachment distance in the present case, it is obvious that self-preservation is not permitted by the boundary conditions involving a large curvature approaching reattachment, the recirculation region, the region of rapid distortion and the bifurcation process at reattachment (see figure 4.1). Since all these parameters are related and interact strongly with the rate of entrainment - the most important factor in mixing process - it is

therefore not a great surprise that our mixing layer is somewhat different from an ordinary plane mixing layer such as that of Castro (1973). In an ordinary mixing layer (between a uniform stream and 'still' air) the entrainment on the lower-velocity side, which is connected closely with the phenomenon of intermittency (see e. g. Townsend 1966), is from the 'still' air whereas in our case it is the re-entrainment of the part of the energy-carrying large eddies, deflected upstream at reattachment, in the recirculation region. Thus, despite a good resemblance to a plane mixing layer of our free shear layer not very far from the step as noted in the previous chapter, the mixing layer in the present case seems to depart from, rather than to tend to, self-preservation as the reattachment region is approached. Therefore some effect of the mixing layer at reattachment is inevitable however thin the initial laminar boundary layer at separation.

To follow the point further, Bradshaw & Wong, relying partly on the existing experiments and partly on their observation of the reattached boundary layer, were able to suggest the causes of the differences between the separated shear layer and the plane mixing layer It is probably wo rth quoting their exact words:

> "... The differences between the separated shear layer and the plane mixing layer (between a uniform stream and still air) seem to be large even when the influence of the initial boundary layer is negligible.
>
> (i) Streamline curvature in the x, y plane tends to <u>reduce</u> the shear stress and turbulence intensity. (Wyngaard, Tennekes, Lumley & Margolis 1968).
>
> (ii) Backflow in the separated-flow region increases the effective velocity difference across the shear layer and hence tends to <u>increase</u> the shear stress and intensity.

(iii) Recirculation and re-entrainment of fluid deflected upstream at reattachment will tend to increase the shear stress and intensity; according to the measurements of Arie & Rouse and of Mueller & Robertson the shear stress in the reversed-flow region is certainly not negligible....."

Although most other workers found much higher values of shear stress, the maximum shear stress in the free shear layer of the present experiment is the same order as that in the plane mixing layer (Castro 1973), i.e. approximately $0.01\rho U^2$, (see figures 4.19(a) - (b) and 5.5). The measurements of Mueller & Robertson (1963), as reproduced by Bradshaw & Wong, show that the smaller the value of δ_0/h, the closer the value of shear stress gets to that of a plane mixing layer, indicating the effect of perturbation strength more than anything else, even though their boundary layer were turbulent at separation. The very high value of shear stress ($0.02\rho U^2$) of Arie & Rouse in their normal plate experiment is obviously due to the effect of geometry upstream of separation as discussed in section 5.2.1. The $(\overline{u^2}/U^2_{ref})_{max}$ and $(\overline{v^2}/U^2_{ref})_{max}$ of the free shear layer measured with the cross-wire probe in the present results are in the ranges of about 0.026 to 0.030 and 0.014 to 0.016 respectively, compared with the value 0.02 and 0.013 of Castro; the low values of both intensities are those at the station closest to the step. Based on the argument of Bradshaw & Wong, that our shear layer not far from the step (where streamline curvature, backflow and rate of re-entrainment are small) can approximate to a plane mixing layer, is therefore confirmed once more. Our results, if they can be trusted, suggest that the overall effects of the three causes listed by Bradshaw & Wong increase the intensities slightly but hardly change the shear stress. The results also confirm that the shear stress in the reversed-flow region is in fact significant (figures 4.19(a) to (e)).

The present results clearly show that the separated-flow region involves extremely large values of all energy-balance and shear-stress-balance terms, as expected, because in this region the turbulent shear stress and turbulent intensities as well as the mean velocity gradients are quite high. Energy is gained mostly by production which is balanced mainly by diffusion and dissipation. It is also seen that in the shear-stress transport equation (4.17) the pressure-strain and generation terms are the major terms. The only measured surface shear stress in the reversed-flow region we managed to obtain, using the Stanton tube, 3 step heights from the step, is about $-0.005\rho U^2_{ref}$ compared with the value of about $-0.001\rho U_e^2$ of Mueller & Robertson (1963), which was obtained from the mean-velocity profile near the wall by fitting it to the logarithmic 'law of the wall'. It is probably fair to comment that their results are rather doubtful because it depends on whether one can get close enough to the wall for the 'law of the wall' to apply. On the other hand the results from the Stanton tube, especially the type used in the present work, should be more reliable, as it was calibrated in the region where the 'law of the wall' is believed to apply approximately to the Preston tubes used as the means of calibration. However, the point we wish to make here is not the question of the magnitude of τ_w but its direction. Since all $-\overline{uv}/U^2_{ref}$ profiles in this region are positive or near zero at the lowest measured point, it is not clear how and where the shear stress changes sign, but it must take place within about 0.1h from the surface according to our results. This is probably the upstream-going 'wall-jet'; the fluid that is deflected upstream will retain its shear stress until it is cancelled by diffusion from the surface.

6.2. REATTACHMENT AND RELAXATION REGION

The turbulent intensity in the mixing layer at reattachment is much higher than in a constant-pressure 'equilibrium' boundary layer. Bradshaw & Wong found that the rate at which the outer-layer structure relaxes to the state of an ordinary boundary layer downstream of reattachment is very slow. However, rapid changes

take place in the reattachment region, where distortion and bifurcation occur. The point has been shown to be true in the previous chapter with regard to the energy-balance and shear-stress-balance terms. The surface shear stress rises rapidly, by boundary-layer standards, after reattachment up to about $x/h = 15$ (figure 4. 6), in good agreement with the results of Bradshaw & Wong; downstream of this the variation depends basically on the imposed streamwise pressure gradient but is usually very slow.

Most workers found that the maximum turbulent shear stress within the shear layer decreases rapidly soon after reattachment; the measurements of Tani et al (1961) show a rather sudden drop of maximum shear stress from reattachment to about $x/h = 10$, whereas the slightly less rapid decrease of the present maximum shear stress starts at about one step height downstream of reattachment and continues to the end of the working section ($x/h \simeq 12$, figure 5. 5). On the other hand, Gesso (1975) found an almost constant maximum shear stress from reattachment all the way to the end of his working section at about $x/h = 10$. Bradshaw & Wong describe this rapid decrease in shear stress as a curious feature, following an argument of fairly constant mean velocity gradient $\partial U/\partial y$ on a given streamline before and after the region of rapid distortion near reattachment, and suggest that large changes in turbulence structure occur when the shear layer bifurcates at reattachment. The rapid decrease of all parameters discussed above seem to extend as far downstream as about 10 step heights from the step, suggesting that the region of rapid distortion of the shear layer prolongs as far as about 4 step heights downstream of reattachment - thereafter the relaxation process begins. The present measurements at a couple of stations upstream of reattachment indicate that the maximum shear correlation coefficient is almost constant at about 0. 55, whereas the almost constant value a couple of stations downstream of reattachment is about 0. 45, in good agreement with the value 0. 4-0. 45 of Bradshaw

& Wong at x/h = 10. These values are somewhat smaller than in a plane mixing layer but not small enough to suggest any strong abnormal relation between the Reynolds stresses according to Bradshaw & Wong.

The question remains as to what fraction of the shear-layer mass flow is deflected upstream at reattachment, because this appears to be the key parameter to the behaviour of the relaxing layer downstream. In order to answer this question considerable work, with more accurate and more reliable measurement methods than in the present experiment, is needed, so that accurate streamlines in this region can be drawn. However, a very rough guess can be made by utilizing the few existing velocity profiles in the recirculation region of the present results. With the high degree of uncertainty of the Pitot results, discussed in section 5.1, in mind, we proceeded to compute the reversed volume flow at each station by graphical integration: it is plotted against x/h in figure 6.1. It should be noted that the volume flow here is based on the streamwise component of fluid velocity across a transverse cross-section; therefore the value of Q_R drops quickly to zero near reattachment point. Since only a small re-entrainment is likely very close to reattachment, the maximum Q_R at about x/h = 4 is probably the best possible guess of upstream-deflected fluid at reattachment we can get from the present results. The value of forward fluid volume flow within the shear layer was also determined at each measuring station in the recirculation region, as shown in figure 6.2. Calling the forward fluid volume at reattachment as a total volume of the shear layer, figures 6.1 and 6.2 show that the upstream-deflected fluid at reattachment is at least 1/6 of the total. In a plane mixing layer, mass flow on the low-velocity side of y = 0 is approximately 0.3 (e.g. results of Castro 1973), therefore only about half of this portion is deflected upstream. This is probably because the centre line of the shear layer leaving the dividing streamline (see discussion below) well ahead of

reattachment. Figure 6.2 clearly indicates an almost constant fluid mass of re-entrainment per unit downstream distance up to about 3 step heights from the step, then the re-entrained mass rate decreases asymptotically towards reattachment. Within about 3 step heights from the step the fluid mass in the shear layer increases roughly 1.4 its original value every step height downstream.

Figure 6.3. shows the location of various maxima, minima and zeros. It is seen that upstream of reattachment the data points collapse surprisingly well on a single curve, presumably representing centre line of the shear layer. Downstream of reattachment they somewhat scatter. Castro (1973) defines the 'centre line' of mixing layer as a line of maximum kinetic energy. In the present results $\overline{w^2}$ is approximated as $\frac{1}{2}(\overline{u^2} + \overline{v^2})$ therefore data points of $(\overline{u^2}/U^2_{ref})_{max}$ and $(\overline{v^2}/U^2_{ref})_{max}$ - which fall fairly close together - in figure 6.3 are used to represent the 'centre line' of our shear layer. The shear layer centre line seems to depart from the dividing streamline just behind $x/h \simeq 4$; it lies practically at the mid-point of the shear-layer thickness at reattachment.

At the end of the region of rapid distortion of the shear layer, about 4 step heights downstream of reattachment, all energy-balance terms are seen to still be much larger than the values in an ordinary boundary layer. The decay seems to be very slow but asymptotic towards the latter state, and it will take a very long distance downstream to complete the relaxation process. In this region the shape of shear stress profiles up to about $x/h = 12$ hardly changes at all.

The qualitative comparison of the intermittency with other results, made in the previous chapter (figure 5.18), shows that, even at $x/h \simeq 12$ in the present results and at $x/h = 30$ in Bradshaw & Wong's results, the intermittency falls closer to the plane mixing

layer trend of Castro (1973) and Antonia & Bradshaw (1971) rather than the boundary layer of Murlis (1975) and Klebanoff(1955). It has also been shown in the previous chapter that the boundary of $\gamma = 0.5$ is roughly half the shear-layer thickness from the surface downstream of reattachment instead of about 0.8δ in the conventional boundary layer. Furthermore, the typical profile shapes of most of the main energy-balance terms resemble that of the plane mixing layer, even many step heights downstream of reattachment. All these features seem to indicate that the influence of the mixing layer persists many step heights downstream of reattachment. It is probably fairer to conclude that at within some distance downstream of reattachment the present shear layer is a 'mixing layer-boundary layer' hybrid.

6.3. CONCLUSIONS

In summary, then, the flow over a simple backward-facing step manifests further complications in terms of the statistical description of turbulence and energy relations. Most mean flow parameters such as the reattachment distance, the surface-pressure distribution, the skin friction coefficient, found here agree reasonably well with previous results. Although we do not expect to get anything much from the separated-flow region it is interesting to note a few qualitative features and their effects on the reattachment behaviour, in particular the rate of re-entrainment in the recirculation region which is closely related to the fraction of the shear-layer mass deflected upstream at reattachment. It is seen that close to the step the free shear layer can approximate to a plane mixing layer, but as reattachment is approached it is departing from, rather than tending to, the self-preservation state. The fraction of the upstream-deflected mass of fluid at reattachment is believed to be not less than 1/6 of the total mass within the shear layer at reattachment, and within about 3 step heights from the step the rate of mass entrainment seems to be almost constant at roughly 1.4 of the local forward mass flow within the shear layer per step height. The reattachment region involves rapid decreases of most parameters, such as turbulent shear stress, turbulent intensity,

main energy-balance terms and shear-stress-balance terms. The 'law of the wall' can be used as first approximation very close downstream of reattachment. The region of rapid distortion of the shear layer is seen to extend to about 4 step heights downstream of reattachment, and in this region some quantities - such as maximum shear stress continue to decrease rapidly. The shear layer within many step heights downstream of reattachment seems to be a hybrid between the mixing layer and the conventional boundary layer, with a thick region of highly intermittent flow. The state of various parameters at our last measuring station suggests that it will take a great distance for the shear layer to relax asymptotically to an ordinary boundary layer state.

In order to document and explain all the features of the reattachment region, more accurate and reliable means of measurement are necessary; a laser anemometer is probably the answer The immediate need is for information concerning the fraction of the shear-layer mass flow which is deflected upstream at reattachment, as we can only produce a very rough estimation from the present results. Lastly, the investigation of the separated-flow region would throw some more light on the behaviour of the reattachment region, particularly the rate of re-entrainment of the mixing layer from the recirculation region. Laser anemometry seems to be the only suitable instrument for investigation of the separated-flow region at present.

Although the present investigation is a very small fraction of the work needed to understand this unusual flow well enough to predict its behaviour in general, it is hoped that the data that have been accumulated and the phenomena investigated and discussed have made some contribution to the basic information required in the development of suitable calculation methods for this type of complex flow.

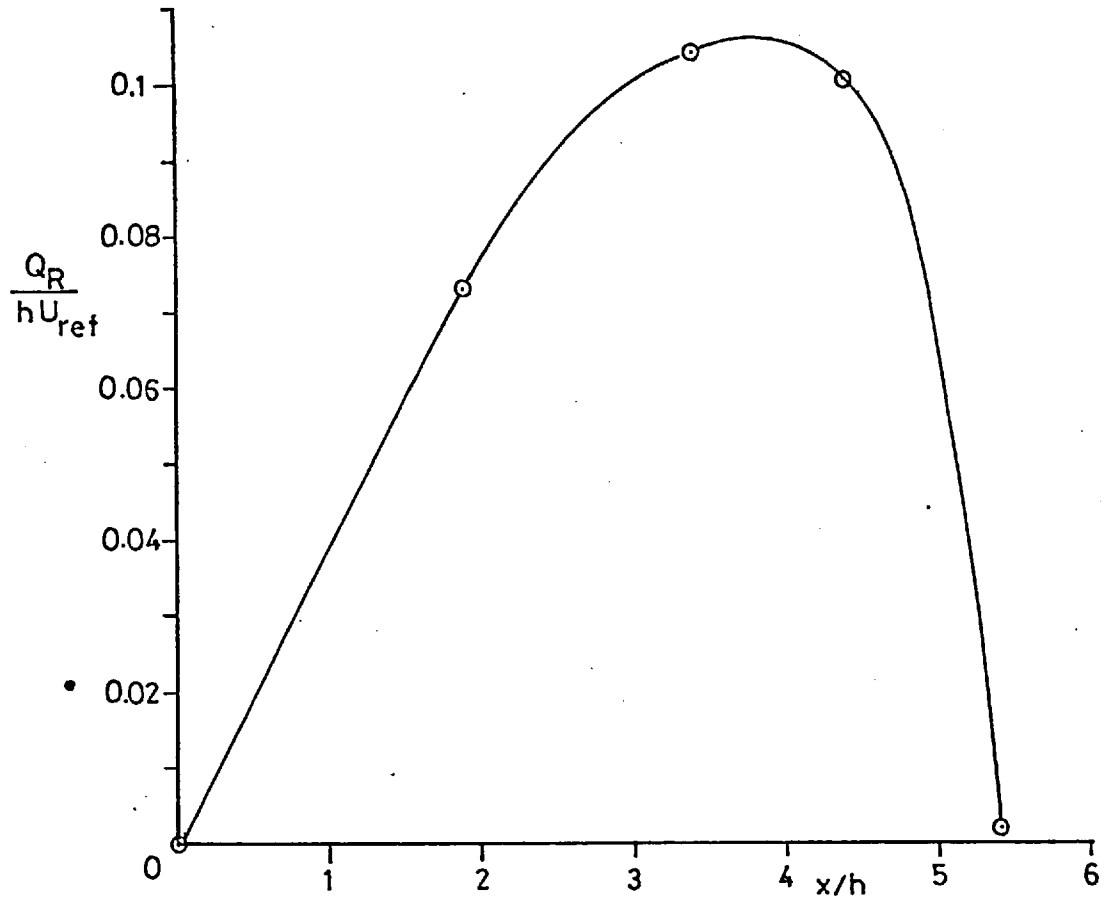


FIGURE 6.1 APPROX. VARIATION OF REVERSED VOLUME FLOW

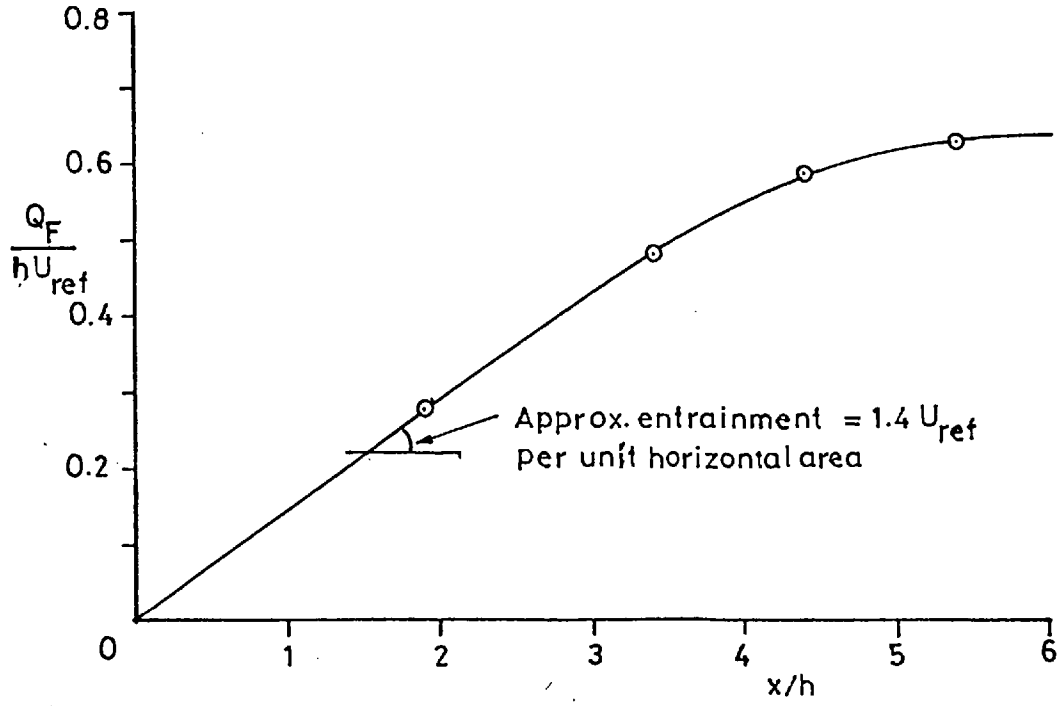


FIGURE 6.2 APPROX. VARIATION OF FORWARD VOLUME FLOW

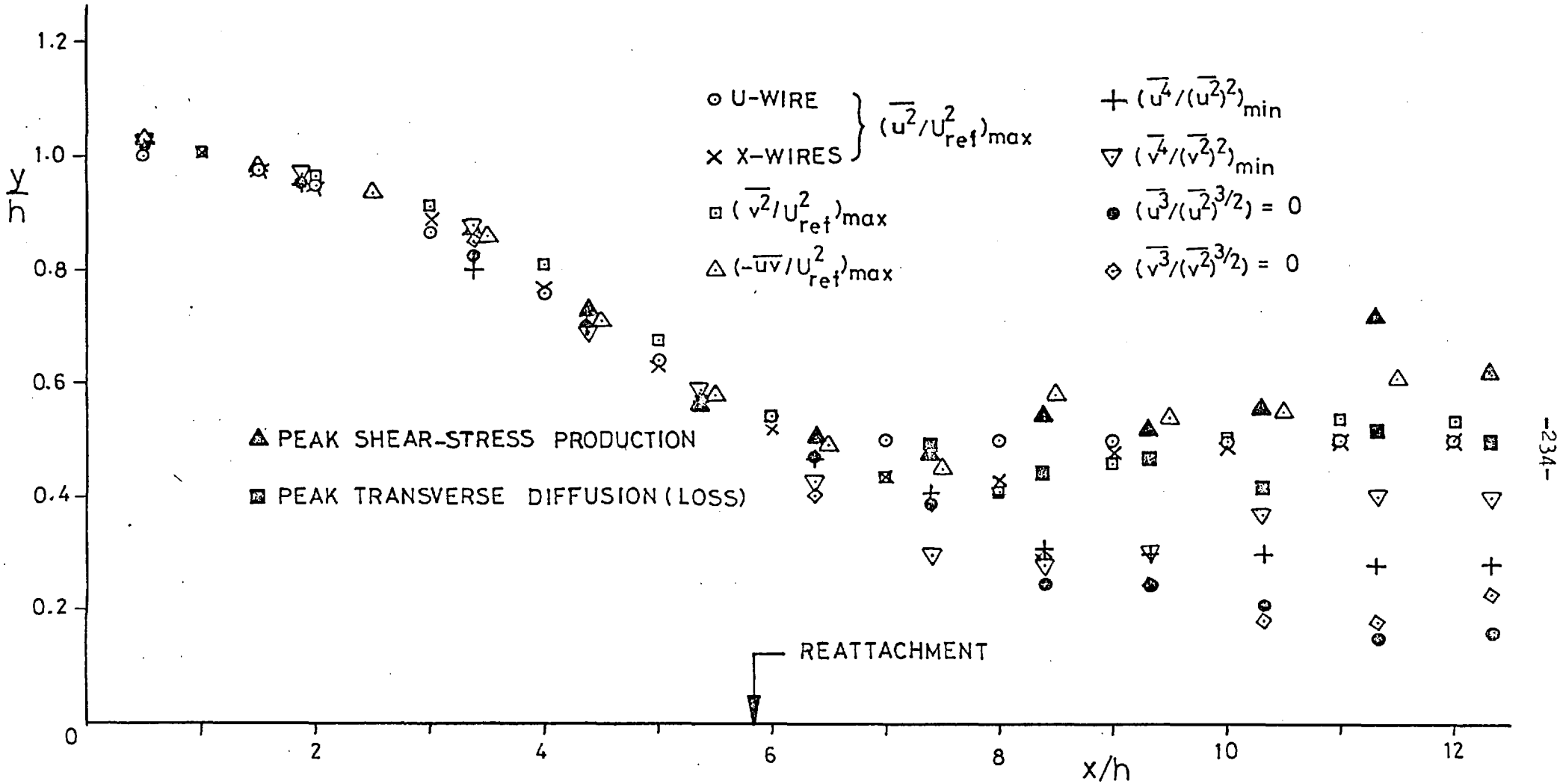


FIGURE 6.3 LOCATION OF MAXIMA, MINIMA AND ZEROS

REFERENCES

Abbott, D. E.
Kline, S. J. 1962 "Experimental investigation of subsonic turbulent flow over single and double backward facing steps", Trans. ASME, J. Basic Engng., 84, series D, 317-325.

Antonia, R. A.
Bradshaw, P. 1971 "Conditional sampling of turbulent shear flows", I. C. Aero Rept. 71-04.

Antonia, R. A.
Luxton, R. E. 1972 "The response of a turbulent boundary layer to a step change in surface roughness. Part 2. Rough-to-Smooth", J. Fluid Mech., 53, 737-757.

Arie M.
Rouse, H. 1956 "Experiments on two-dimensional flow over a normal wall", J. Fluid Mech., 1, 129-141.

Aung, W.
Goldstein, R. J. 1972 "Heat transfer in turbulent separated flow downstream of a rearward-facing step", Israel J. of Tech., 10, 35-41.

Badrinarayanan, M. A. 1961 "An experimental investigation of base flows at supersonic speeds", J. Roy. Aero. Soc., 65, 475-482.

Bearman, P. W. 1965 "Investigation of the flow behind a two-dimensional model with a blunt trailing edge and fitted with splitter plates", J. Fluid Mech., 21, part 2, 241-255

Bellhouse B. J.
Talbot, L. 1969 "The fluid mechanics of the aortic valve", J. Fluid Mech., 35, 721-735.

Bourque, C.
Newman, B. G. 1960 "Reattachment of a two-dimensional, incompressible jet to an adjacent plate", Aero. Quart., 11, 201-232.

Bourque, C. 1967 "Reattachment of a two-dimensional jet to an adjacent flat plate", Advanced in Fluidics, Paper presented at the Fluidics Symposium, Chicago, May 9-17, 1967, 192-204 (Ed. F. T. Brown), ASME.

REFERENCES (Cont'd)

Bradbury, L. J. S.	1975	Private communication.
Bradshaw, P. Ferriss, D. H. Johnson, R. F.	1964	"Turbulence in the noise-producing region of a circular jet", J. Fluid Mech., 19, 591-624.
Bradshaw, P. Ferriss, D. H.	1965	"The spectral energy balance in a turbulent mixing layer", NPL Aero. Rept. 1144, Aero. Res. Counc., C. P. 899.
Bradshaw, P.	1966	"The effect of initial conditions on the development of a free shear layer", J. Fluid Mech., 26, 225-236.
Bradshaw, P.	1967	"The turbulence structure of equilibrium boundary layers", J. Fluid Mech., 29, 625-645.
Bradshaw, P. Goodman, D. G.	1968	"The effect of turbulence on static-pressure tubes", Aero. Res. Counc., R & M No. 3527.
Bradshaw P.	1972	"Two more wind tunnels driven by aerofoil-type centrifugal blowers", I. C. Aero. Rept. 72-10.
Bradshaw, P. Wong, F. Y. F.	1972	"The reattachment and relaxation of a turbulent shear layer", J. Fluid Mech., 52, 113-135.
Brederode, V. A. S. L. de	1973	" 'VELPROF' - A boundary layer data analysis program", I. C. Aero. TN 73-107.
Brederode, V. A. S. L. de	1975	"Three-dimensional effects in nominally two-dimensional flows", Ph. D. Thesis, London Univ.
Brown, G. Roshko, A.	1974	"On density effects and large structure in a turbulent mixing layer", J. Fluid Mech., 64, 775-816.
Bruun, H. H.	1975	Private communication.

REFERENCES (Cont'd)

Bryer, D. W. Pankhurst, R. C.	1971	Pressure-probe methods for determining wind speed and flow direction, Her Majesty's Stationery Office, London.
Castro, I. P.	1973	"A highly-distorted turbulent free shear layer", Ph. D. Thesis, London Univ., and J. Fluid Mech. (to be published).
Castro, I. P.	1975	"Statistics of the instantaneous velocity vector and the consequent errors in anemometer measurements", to be published in J. Fluid Mech.
Chapman, D. R. Kuehn, D. M. Larson, H. K.	1957	"Investigation of separated flows in supersonic and subsonic streams with emphasis on the effect of transition", N. A. C. A. TN 3869 (Also N. A. C. A. Rept. 1356, 1958).
Charwat, A. F. Yakura, J. K.	1958	"An investigation of two-dimensional supersonic base pressures", J. Roy. Aero. Soc., 25, 122.
Cochrane, S. J. R.	1971	"Supersonic and subsonic blunt-base separation", Dept. of Mech. Engng., Queen's Univ. of Belfast, Rept. No. 590.
(Cockrell, D.J.-Ed.) Davies, T. W. Patrick, M. A.	1972	"A simplified method of improving the accuracy of hot-wire anemometry", Fluid dynamic measurements in the industrial and medical environments, Proc. Disa Conf. 1972, vol 1 (Ed. David J. Cocknell), Leicester Univ. Press.
Collis D. C. Williams, M. J.	1959	"Two-dimensional convection from heated wires at low Reynolds numbers", J. Fluid Mech., 6, 357-384.
Crabtree, L.F.	1957	"Effects of leading-edge separation on thin wing in two-dimensional incompressible flow", J. Aero. Sci., 24, 597-604.

REFERENCES (Cont'd)

Crocco, L. Lees, L.	1952	"A mixing theory for the interaction between dissipative flows and nearly isontropic streams", J. Aero. Sci., 19, 649-676.
Crow, S. C.	1968	"Viscoelastic properties of fine-grained incompressible turbulence", J. Fluid Mech., 33, 1 - 20.
Dean, R. B.	1974	"An investigation of shear layer interaction in ducts and diffusers", Ph. D. Thesis, London Univ.
Duncan, W. J. Thom, A. S. Young A. D.	1970	Mechanics of Fluids, 2nd Ed. (reprinted 1972, 1974) Edward Arnold.
Fiedler, H. Head, M. R.	1966	"Intermittency measurements in the turbulent boundary layer", J. Fluid Mech., 25, 719-735.
Fletcher, L. S. Briggs, D. G. Page, C. H.	1974	"Heat transfer in separated and reattached flows: an annotated review", Israel J. Tech., 12, 236.
Gesso, J. A. di	1975	"An experimental investigation of two-dimensional, separated, internal flows", Ph. D. Thesis, Exeter Univ.
Goldstein, S.	1936	"A note on the measurement of total head and static pressure in turbulent stream", Proc. Roy. Soc. (A), 155, 570.
Hastings, R. C.	1963	"Turbulent flow past two-dimensional bases in supersonic streams", R. A. E. TN Aero, 2931.
Hinze, J. O.	1959	Turbulence, an Introduction to its Mechanism and Theory, McGraw-Hill, New York.

REFERENCES (Cont'd)

Hsu, H. C.	1950	"Characteristics of mean flow and turbulence at an abrupt two-dimensional expansion", Ph. D. Thesis, Dept. of Mechanics & Hydraulics, God. Col. of the State Univ. of Iowa.
Kistler, A.L. Tan, F. C.	1967	"Some properties of turbulent separated flows", Phys. Fluids, 10, no. 9, 5165-5173.
Klebanoff, P. S.	1955	"Characteristics of turbulence in a boundary layer with zero pressure gradient", N. A. C. A. Rept. 1247.
Kline, S. J.	1959	"On the nature of stall", J. Basic Engng., ASME, 81, series D, 305-320.
Kovasznay, L. G. S. Kibens, V. Blackwelder, R. F.	1970	"Large scale motion in the intermittent region of a turbulent boundary layer", J. Fluid Mech., 41, 283.
MacMillan, F. A.	1956	"Experiments on Pitot, tubes in shear flow", Aero. Res. Counc., R & M, No. 3028.
Mathews, L. Whitelaw, J. H.	1973	"Plane-jet flow over a backward-facing step", Proc. Instn. Engrs., 187, 447-454.
Maull, D. J. East, L. F.	1963	"Three-dimensional flow in cavities", J. Fluid Mech., 16, 620-632.
McEwan, A. D.	1965	"Some studies of viscous fluid motions with free boundaries and separated turbulent flow behind a step", Ph. D. Thesis, Cambridge Univ.
McKee, D. I. Edwards, J. A.	1970	"A simplified two-dimensional jet reattachment model", ASME paper 70-WA/Flcs - 5.
Moore, T. W. F.	1960	"Some experiments on the reattachment of a laminar boundary layer separating from a rearward facing step on a flat plate aerofoil", J. Roy. Aero. Soc., 64, 668-672.

REFERENCES (Cont'd)

Mueller T. J. Robertson, J. M.	1963	"A study of the mean motion and turbulence downstream of a roughness element", Modern Development in Theor. Appl. Mech., 1, 326.
Mueller, T. J. Korst, HH. Chow, W. L.	1964	On the separation, reattachment, and redevelopment of incompressible turbulent shear flow", J. Basic Engng., 86D, 221.
Murlis, J.	1975	"The structure of a turbulent boundary layer at low Reynolds number", Ph. D. Thesis, London Univ.
Nash, J. F.	1962	"A review of research on two-dimensional base flow", Aero. Res. Counc., R & M No. 3323.
Nash, J. F. Quincey, V. G. Callinan, J.	1966	"Experiments on two-dimensional base flow at subsonic and transonic speeds", Aero. Res. Counc., R & M No. 3427.
Owen, P. R.	1971(a)	"The prospect ahead", Phil. Trans. Roy. Soc. Lond. A, 269, 545-554.
Owen, P. R.	1971(b)	"The aerodynamics of buildings", Fluid Dynamics Trans., 6, Warsaw.
Perry, A. E. Morrison, G.L.	1971	"Static and dynamic calibrations of constant temperature hot-wire systems", J. Fluid Mech., 47, 765-777.
Perry, A. E. Fairlie, B. D.	1975	"A study of turbulent boundary-layer separation and reattachment", J. Fluid Mech., 69, 657-672.
Petryk, S. Brundrett, E.	1967	"Recovery of a turbulent boundary layer disturbed by a single roughness element", Dept of Mech. Engng., Waterloo Univ., Res. Rept. No. 4.
Plate, E. J. Lin, C. W.	1964	"The velocity field downstream from a two-dimensional hill", Colorado State Univ. Rept. CER-65-EJP-14 AD-614067.

REFERENCES (Cont'd)

Rockwell, D. O. Fiske, P. M.	1970	"Jet reattachment to walls of various shapes", ASME paper 70-Flcs - 2.
Roshko, A.	1955	"On the wake and drag of bluff bodies", J. Aero. Sci, 22, 124.
Roshko, A. Thomke, G.J.	1964	"Flow separation and reattachment behind a downstream facing step". Douglas Rept. S. M. 43056-1.
Roshko, A. Lau, J. C.	1965	"Some observations on transition and reattachment of a free shear layer in incompressible flow", Proc. of the 1965 Heat Transfer and Fluid Mech. Inst. (Ed. A. F. Charwat), Stanford Univ. Press.
Rotta, J. C.	1962	"Turbulent boundary layer in incompressible flow", Progress in Aero. Sci., 2, 1-219, Pergamon, Oxford.
Sawyer, R. A.	1963	"Two-dimensional reattaching jet flows including the effects of curvature on entrainment", J. Fluid Mech., 17, 481-498
Scherberg, M. G. Smith H. E.	1967	"An experimental study of supersonic flow over a rearward facing step", AIAA J., 5, 51-56
Seban, R. A.	1964	"Heat transfer to the turbulent separated flow of air downstream of a step in the surface of a plate", Trans. ASME, J. Heat Transfer, 86, 259, 264.
Simpson, R. L.	1975	"Characteristics of a separating incompressible turbulent boundary layer", AGARD paper from Conference Pre-Print No. 168 on Flow Separation (to appear as ASARD Conf. Proc. 168).
Sivasegaram, S.	1971	"The evaluation of local skin friction in compressible flow", J. Roy. Aero. Soc., 75, 793-795.

REFERENCES (Cont'd)

Statham, J.	1970	"Supersonic turbulent step induced separation", Ph.D. Thesis, Mech. Engng. Dept., Queen's Univ. of Belfast.
Tani I. Iuchi, M. Komoda, H.	1961	"Experimental investigation of flow separation associated with a step or groove", Aero. Res. Inst., Tokyo Univ., Rept. No. 364.
Tillmann,W.	1945	"Investigation of some particularistics of turbulent boundary layer on plates", British Min. of Aircraft Prod. Völkenrode Translation MAP-VG 34-45T.
Toomre, A.	1960	"The effect of turbulence on static pressure measurements", Aero. Res. Counc. 22010
Townsend, A.A.	1956	The structure of turbulent shear flow, Cambridge Univ. Press.
Townsend, A.A.	1966	"The mechanism of entrainment in free turbulent flows", J. Fluid Mech., 26, 689, 715.
Weir, A.D. Bradshaw, P.	1974	"Apparatus and Programs for digital analysis of fluctuating quantities in turbulent flow", I.C. Aero. Rept. 74-09.
Winant, C.D. Browand, F.K.	1974	"Vortex paring: the mechanism of turbulent mixing-layer growth at moderate Reynolds number," J. Fluid Mech., 63, 2.
Wong, F.Y.F.	1970	"Shear flow over a rearward facing step", M.Sc. Thesis, London Univ.
Wygnanski, I. Fiedler, H.E.	1969	"The two-dimensional mixing region", J. Fluid Mech, 11.
Wyngaard, J.C. Tennekes, H. Lumley, J.L. Margolis, D.P.	1968	"Structure of turbulence in a curved mixing layer", Phys. Fluids, 11, 1251.

APPENDIX I

This appendix is a copy of I.C. Aero Report 75-03 (1975).

The authors were jointly responsible for the work described in this paper.

IMPERIAL COLLEGE OF SCIENCE AND TECHNOLOGY

DEPARTMENT OF AERONAUTICS

Prince Consort Road, London SW7 2BY.

I.C. Aero Report 75-03 May 1975

AN ASSESSMENT OF THE EVIDENCE FOR ORDERLY STRUCTURE IN TURBULENT MIXING LAYERS

by

C. Chandrsuda and P. Bradshaw

SUMMARY

Comparison of Brown and Roshko's shadowgraphs with new smoke-injection pictures suggests that real differences may exist between the transition process in Brown and Roshko's two-stream mixing layer and in single-stream mixing layers entraining weakly-turbulent ambient fluid. Such differences will probably persist for a large distance downstream but a quasi-two-dimensional large-eddy structure is most unlikely to survive indefinitely. The essential difference in the transition process is that "vortex pairing" is often helical when one stream is weakly turbulent, leading to rapid development of fully-three-dimensional turbulence, while in the absence of helical pairing intense quasi-two-dimensional structures may form.

1. INTRODUCTION

Several recent papers (e.g. Brown & Roshko 1971, 1974, Winant & Browand 1974) have presented evidence that the nominally turbulent mixing layer between two uniform parallel streams, or between one uniform stream and still air, has a much more orderly structure than other turbulent shear layers. The large scale motion appears to be effectively two-dimensional. All the experiments were done in the laboratory, sometimes at quite small scales, and the results may therefore be affected by viscosity or by the initial boundary layer. The essential problem may be posed as a main question and a supplementary: "Does the structure of the energy-containing turbulence in a plane mixing layer attain a unique asymptotic (self-preserving) state at a sufficiently large distance from the origin? If so, which if any of the existing flows attained that state?" The present paper is an attempt to answer these questions, using data published by the present authors and others together with the results of a recent flow-visualization experiment at Imperial College. We conclude that an asymptotic state with a well-defined large eddy structure exists, but that it is not spectacularly more orderly than that of other shear layers.

It is suggested that the orderly structure inferred by Brown and Roshko from shadowgraph pictures is attributable partly to the rather low Reynolds number of their experiment and partly to the spanwise-averaging properties of the shadowgraph technique in a low-aspect-ratio test rig. However it is at least possible that the Brown and Roshko structure always arises in the later stages of transition if free-stream irregularities have not already induced three-dimensionality, and that it relaxes only very slowly into conventional turbulence with small spanwise coherence.

2. OUTLINE OF PREVIOUS WORK

The early stages of transition to turbulence in a plane or axisymmetric mixing layer are now well understood and uncontroversial (e.g. Miksad 1972, 1973). If the boundary layer on the inner lip of the nozzle is not in an advanced state of transition, the eigenvalues of the preferred two-dimensional (or axisymmetric) travelling-wave disturbance will be determined by the shape of the boundary layer velocity profile near the

surface, because this determines the profile near the inflexion point of the free shear layer just downstream of the lip. The Reynolds number above which small disturbances grow is uncertain but is very low: in the work of Winant and Browand (1974) the momentum-thickness Reynolds number of the initial boundary layer, $U_e\theta_o/\nu$, was about 8 and disturbances appeared to grow almost immediately after separation at the lip. The velocity fluctuations can remain roughly sinusoidal until they reach amplitudes significantly larger than those found after transition (e.g. Bradshaw 1966) but marked fluid injected into the boundary layer at the nozzle lip collects in discrete rolls with spanwise axes connected by thin sheets (figure 1). A residual misconception is that these rolls are necessarily concentrations of vorticity: filament lines can roll up even when all fluctuations are small and sinusoidal, as can be seen by considering the Kelvin "cat's eye" pattern of streamlines viewed by an observer moving with the phase velocity. However when the disturbance amplitude is large, even if sinusoidal, the maximum instantaneous (mean plus fluctuating) vorticity will be much larger at the rolls than between them, and in practice the rolls do seem to approximate to concentrated vortices connected by thin sheets of boundary-layer fluid.

The work of Sato (1956), followed by that of Wille and his collaborators (e.g. Wille 1963) showed that vortex rolls can join up in pairs (figure 2) and that the paired rolls can repeat the process, so that the distance between rolls increases with increasing distance from the nozzle lip. The work of Wille's school was done in circular jets and - at low Reynolds numbers - the effects of axisymmetry become apparent before any self-preserving state could be reached. Bradshaw (1966) measured the (large) Reynolds stresses in the vortex-pairing region in a circular jet at a high enough Reynolds number for self-preservation of mean velocity and Reynolds stresses to be reached before axisymmetry becomes important. He also discussed the reason for the accurate circumferential (or spanwise) uniformity of the disturbances: it appears that the pressure-fluctuation field set up by a given disturbance provides the next disturbance at the lip. Crow and Champagne (1971), following Wille's group, showed that the structure of the transition region became even more orderly when the mean flow was pulsed artificially: the preferred frequency of the vortex-ring disturbance in a circular jet was found to be about $0.3\ U_e/D$ over a large range of Reynolds number U_eD/ν. The exact relation

between columnar oscillations in a circular jet (scaling on diameter) and transitional oscillations in a plane shear layer (scaling on nozzle boundary layer thickness) is not clear: undoubtedly both are manifestations of an essentially inviscid instability but the earlier stages of transition, at least, seem to be the same in plane and axisymmetric flows. In what follows we shall concentrate on disturbances scaling on the thickness of the growing shear layer, and regard disturbances scaling on the width of the apparatus as "spurious".

Davies et al. (1963) and Bradshaw et al. (1964) made detailed fluctuation measurements in circular jets which had nominally reached the fully turbulent asymptotic state (the paper by Bradshaw (1966) being an apparently satisfactory demonstration of this for the jet used by Bradshaw et al.). Bradshaw et al. deduced the preferred shape of the large eddies from correlation measurements at $x/D = 2$ (in the range claimed to be asymptotic) and found no evidence of strong circumferential correlation of the eddies as would have been expected if the vortex-ring structure had persisted. The longitudinal correlations and frequency spectra of Bradshaw et al. (satisfactorily repeated by Weber 1974) showed a strongly preferred wavelength, especially for the v and w components, which was thought to be due to the presence of three-dimensional "mixing jet" eruptions, like those found in the boundary layer and wake but of considerably greater strength. The preferred wavelength was closely proportional to distance from the nozzle, x, in the range $1 < x/D < 4$, indicating self-preservation and freedom from columnar disturbances scaling on D.

The above mentioned work was all done in circular jets in still air, except for the two-dimensional work of Sato (1956, 1959) which compares well. Wygnanski & Fiedler (1970) presented fairly detailed turbulence measurements in a plane mixing layer but, for reasons still to be explained, the spreading rate of the layer was much larger than in most other sets of mean-flow measurements (e.g. Liepmann & Laufer 1947) and the results are therefore suspect. Several recent experiments will be mentioned below. Brown and Roshko (1974) presented measurements in the mixing layer between two streams with a velocity ratio of 7:1. The mean velocity profiles were quite accurately self-preserving (even at distances from the nozzle lip smaller than expected from previous work)

but shadowgraph pictures like Fig. 3(a) showed a strongly preferred wavelength in the transitional and turbulent regions. Later analysis showed that the wavelength varied in steps as the large eddies merged, but was on average proportional to distance from the nozzle, again as required for self-preservation. The outline of the irrotational-turbulent interface on the high-velocity side of the layer, as seen in shadowgraph pictures, was unnaturally regular, being trochoidal in shape. Most recently Winant and Browand have made measurements in the mixing layer between two streams with a velocity ratio of about 3:1, at a very low initial Reynolds number. Repeated vortex-roll pairings occurred, and the rate of growth of the mixing-layer thickness became constant (i.e. independent of Reynolds number) so that self-preservation was closely approached in what would normally be called the transition region. Theoretical confirmation that continued pairing leads to a self-preserving, spreading mixing layer with a conventional-looking mean velocity profile is given by Damms & Kuchemann (1974).

The present position is , therefore, that we are not sure whether (i) the plane mixing layer indefinitely retains a quasi-two-dimensional structure like that shown in Fig. 3(a) (reproduced from Brown & Roshko (1974)), or whether (ii) the two-dimensionalities or axisymmetries reported in various laboratory experiments are residues of transition (shown by Bradshaw (1966) to persist for a surprisingly long time) or "spurious" oscillations scaling on the whole flow width and possibly interacting with the transitional disturbances as in Crow and Champagne's (1971) experiment. We proceed to discuss the later, and more controversial, stages of transition, and then the approach to the asymptotic self-preserving state if it exists.

In this paper "orderly structure" means a velocity-fluctuation field which is significantly more ordered than in flows which are normally called turbulent. This requires that coherence lengths within the turbulence shall be an order of magnitude greater than typical wavelengths and that spectrum peaks shall be at least an order of magnitude higher than surrounding levels: a working definition is that "orderly structure" is easily seen in flow visualization photographs. Some authors have used the term to describe quite conventional large-eddy structures: we reject this usage as thoroughly confusing.

3. THE ONSET OF THREE-DIMENSIONALITY

As has been pointed out by Browand (1966) it is remarkable that transitional oscillations in a free shear layer can grow to such a large amplitude before becoming three-dimensional, while in boundary layer transition three-dimensionality sets in at a very early stage. It may be that typical laboratory boundary layers are more liable to contain spanwise irregularities than typical free shear layers (though the arguments for this are not straightforward): however it seems that if the most highly-amplified disturbance in a free shear layer is initially two-dimensional it remains so, being stable against small three-dimensional disturbances caused by spanwise irregularities in the free stream. This stability must be attributable to the presence of a mean shear - an isolated vortex line is mildly unstable because perturbations grow through self-induction - and it is therefore likely that vortex rolls in a plane shear layer will inevitably develop three-dimensionality when the vorticity in the roll is no longer small compared to the mean vorticity (i.e. the negative of the rate of shear strain).

Previous experimenters have reported several different inceptions of three-dimensionality. Hama, Long and Hegarty (1957), studying the flow over a backward-facing step of height about 8 times the boundary-layer momentum thickness θ at an initial Reynolds number $U_e\theta/\nu$ of about 200, found that the axis of the vortex roll became spanwise-periodic in the plan view, with breakdown to turbulence occurring at the foremost and rearmost parts of the axis. Wille (1963) presented smoke photographs at an unspecified but fairly low Reynolds number (probably of the order of 200): in general, breakdown to turbulence seemed to occur before any large-scale spanwise periodicity occurs, but after one stage of vortex pairing. Browand (1966) deduced, from hot-wire measurements at an initial Reynolds number $U_e\theta/\nu$ of 200, occurrence of one stage of vortex pairing (apparently irregular, since the sub-harmonic of the hot-wire signal was "strongly intermittent") followed by a secondary instability, at about ten times the fundamental frequency, which was certainly three-dimensional. Freymuth (1966), who states that the transition process is essentially independent of Reynolds number in his test range $61 < U_e\theta/\nu < 334$ and is also independent of nozzle diameter or height, found one vortex pairing followed by three-dimensionality (apparently breakdown to turbulence rather than large-scale deformation of

the vortex roll). Bradshaw (1966) found longitudinal streaks, indicating spanwise periodicity, before breakdown to turbulence but after one vortex pairing. Miksad (1972) working with a plane mixing layer between two streams, with a velocity ratio of 5.7:1 and a Reynolds number of 160 based on the higher velocity and the sum of the two momentum thicknesses at the lip, found evidence of sub-harmonics at a low fundamental amplitude. The final breakdown to turbulence, following one vortex pairing, was found to involve a three-dimensional longitudinal-vortex structure. Clark and Markland (1973), using hydrogen-bubble visualization in a plane mixing layer with $60 < U_e\theta/\nu < 80$ found pronounced spanwise waviness of the vortex-roll axis, which increased to the point where the inclined portions could be regarded as longitudinal vortices: they do not seem to have observed pairing. Winant and Browand (1974), with $U_e\theta/\nu \simeq 8$, found repeated vortex pairings and no breakdown to turbulence up to the point where the local momentum-thickness Reynolds number reached 150. The present authors, with $U_e\theta/\nu \simeq 60$ in a single-stream plane mixing layer in the rig used by Castro & Bradshaw (1975), find one or two pairings before breakdown to turbulence; often the vortex rolls pair in a double helix (figure 4) rather than remaining parallel, in which case breakdown follows rapidly. Helical pairing seems to involve an eruption towards the low-velocity side of the layer (uncharacteristically strong in the downstream part of figure 4)*.

To summarize, Hama et al. (1957), Bradshaw (1966), Miksad (1972, 1973) and Clark & Markland (1973) find significant large-scale three-dimensionality of the vortex rolls before breakdown to turbulence occurs; Wille, and apparently Browand, Freymuth and Brown & Roshko, observed breakdown from an essentially two-dimensional structure following pairing; the present authors observed breakdown after two-dimensional or helical pairing. There is no discernible correlation between the early appearance of three-dimensionality and poor flow quality (especially the presence of spanwise irregularities), although such a correlation would not be surprising, and no obvious influence of Reynolds number except that more than one pairing may occur before breakdown if $U_e\theta/\nu < 60$, very roughly.

---

*The sheet of smoke injected into the flow at the nozzle lip is divided into parallel filaments by the spacing pieces in the injector slot.

4. THE APPROACH TO SELF-PRESERVATION

After breakdown to turbulence begins, the whole of a vortex roll rapidly becomes turbulent, and most of the flow-visualization pictures suggest that the shortest wavelengths are a small fraction of the roll diameter, as expected in turbulence that is fully developed spectrally by the three-dimensional vortex stretching. The interpretation of smoke, dye or refraction photographs is always difficult because the pattern represents an integration over the history of the rate-of-strain field rather than an indication of the current deformation rate, but smoke-flow observation by the present authors (figures 4, 5) strongly suggests that rolls spread and join up so that the shear layer is turbulent throughout, with an intermittency factor close to unity near the shear-layer axis. Helical pairing may not be necessary for this to occur but it is certainly sufficient. Brown and Roshko's orderly structure preserves relatively independent, spanwise-coherent rolls. It seems inevitable that any spanwise coherence present before breakdown should be gradually lost: the typical wavelength of turbulent eddies is no larger than the shear-layer thickness, so that information cannot be transmitted over large spanwise distances (even pressure fluctuations decay). Undoubtedly the loss of coherence will be very slow: in the present experiments, distinct spanwise correlations of smoke distribution are seen up to distances from the nozzle lip of as much as 1000 initial momentum thicknesses. Flow visualization is likely to exaggerate the spanwise coherence: as mentioned above, the pattern records history, while shadowgraph pictures such as those of Brown and Roshko have the additional disadvantage of recording spanwise averages. However, even if one makes a reasonable allowance for difficulties of interpretation the spanwise coherence and simplicity of structure shown in Fig. 3 (a), a typical photo from Brown & Roshko (1974), is very remarkable. In particular the interface on the high-velocity side of the shear layer is far more regular than those of Figures 1, 3 (b), 4 in the present paper, which show a typically ragged interface. The present flow may well have been more subject to random disturbances and spanwise irregularities than Brown and Roshko's, since the rig was being run at only one or two feet per second in a large laboratory, but no gross fluctuations were observable in the exit flow and indeed the flow photographs presented here conform to the conventional view of turbulence as opposed to the highly-ordered structure of Brown and Roshko. The more obvious arguments why Brown and Roshko's flow should be untypically well-ordered, such as resonance, were specifically

demolished by them. In the absence of further data we must accept that their experiment was free of spurious influences, but it must also be accepted that the conventional turbulence structure reflected in quantitative fluctuation measurements at high Reynolds numbers is real, and different from the well-ordered structure inferred by Brown and Roshko from their shadowgraphs.

The simplest explanation, based on the foregoing discussion of persistent transition effects, is that the structure found by Brown and Roshko appears only at fairly low Reynolds number (strictly, at distances from the exit insufficiently large for the effects of the exit boundary layer to have been obliterated). This is supported by the even more ordered structure found by Winant and Browand at an even lower Reynolds number based on exit boundary layer thickness. However, the present flow-visualization study was done at a Reynolds number intermediate between Winant and Browand's and Brown and Roshko's, and shows a significantly less ordered structure than either. Another objection is that Brown and Roshko's flow appears to be self-preserving, with a spreading rate that agrees well with the results of Miles and Shih (1968) and of Spencer and Jones (1971) which extended to Reynolds numbers of 1.5 and 2.5 million respectively, based on distance from exit. However even Winant and Browand's spreading rate is not too far from the high-Reynolds-number values, and it appears that spreading rate is not a very sensitive measure of turbulence structure - or conversely that two or more significantly different structures can produce nearly the same spreading rate.

The opinion of the present authors - a hypothesis rather than a conclusion - is that a combination of a low aspect ratio and a flow-visualization technique that integrates spanwise caused Brown and Roshko's photographs to give an exaggerated impression of the orderliness of the turbulence structure within a mixing layer and of the regularity of the turbulent-irrotational interface on the high-velocity side.

As a partial test of this, Dr. A.D. Weir made some shadowgraph visualizations of the present flow. Beyond a distance $\sim 15000\ (\nu/U)$ downstream of the nozzle, the patterns resembled the conventional turbulence of our own smoke pictures rather than the orderly structure of Brown & Roshko's shadowgraphs, though very occasional large strong structures were observed. In the transition stages, however, the vortex rolls had stronger structure in the shadowgraphs (Fig. 3(b)) than in the smoke pictures (Fig. 1), even at a distance as small as half the flow width. The effect would be much more

pronounced in Brown & Roshko's apparatus with x/(flow width) > 2.

We are, however, not convinced that the differences between Brown & Roshko's results and our own are entirely attributable to differences in observational techniques or even to genuine effects of small aspect ratio on the flow. If the decision between rapid breakdown to conventional turbulence and persistence of vortex rolls depends on whether or not helical pairing occurs, it is at least possible that the structure at the end of transition to turbulence is strongly dependent on free-stream conditions, particularly on the low-velocity side of the layer. In that case, a structure with strong spanwise coherence is more likely to occur in a two-stream mixing layer like Brown & Roshko's than in a mixing layer in "still" air, as used in the present work and in most previous turbulence measurements, because the "still" air is in fact drawn from the recirculating flow in the laboratory. It is at present a matter of opinion whether the spanwise coherence can ever be maintained indefinitely. Once the structure has become established, with rms velocity fluctuations of 10 to 20 percent of the free-stream speed, it is not likely to be influenced by one or two percent of turbulence in the free stream. However if the "orderly" flow has even a small fraction of the dissipative or dispersive ability of conventional turbulence it carries the instrument of its own disruption. It is therefore highly probable that the spanwise coherence will eventually disappear, leaving a self-preserving structure which, though it undoubtedly carries a pronounced large-eddy structure leading to strong spectral peaks, is nevertheless what we normally call "turbulence".

5. CONCLUSIONS

The answer to the main question posed in the Introduction can be given with some confidence: the mixing layer does tend to a unique asymptotic state which is what we normally call "turbulence". The answer to the supplementary question is that flows with a Reynolds number based on downstream distance of less than 10^6, or at a downstream distance less than 1000 times the momentum thickness of initial boundary layer, should be regarded with suspicion. Some confusion is caused because the rolling-up of a semi-infinite vortex sheet (the idealization of Winant and Browand's flow) can be self-preserving, the average distance between vortex rolls being maintained proportional to distance from the origin by "vortex pairing". Moreover the spreading rate and

gross statistical properties of the vortex-pairing transitional flow are not different from those of the fully-turbulent flow. We feel that Brown and Roshko's use of the spanwise-integrating shadowgraph technique in a mixing layer of relatively low aspect ratio exaggerated the orderly structure, while smoothing out the irrotational/turbulent interface, in what was already a flow at too low a Reynolds number to achieve exact self-preservation. The discovery of helical pairing in the present experiments suggests, however, that the rate of breakdown of two-dimensional spanwise vortices to fully three-dimensional turbulence depends on the level of free-stream disturbances. It is also probable that if the Brown & Roshko type of orderly structure is once formed it can last for a large number of characteristic wavelengths - that is, up to high Reynolds numbers based on streamwise distance - but not indefinitely. The question can be settled only by measurements in a two-stream mixing layer at a much higher Reynolds number than was used by Brown & Roshko.

6. ACKNOWLEDGEMENTS

We are grateful to Dr. A.D. Weir and Mr. J.P. O'Leary for assistance with the experiments and with the photography respectively, and to Prof. A. Roshko for helpful discussions. The first author wishes to acknowledge the financial support of the Royal Thai Air Force. The work was partly supported by MoD (PE) research agreement AT/2037/0141.

7. REFERENCES

1. Bradshaw, P., Ferriss, D.H. & Johnson, R.F. Turbulence in the noise-producing region of a circular jet, J. Fluid Mech., 19, 591 (1964).
2. Bradshaw, P. The effect of initial conditions on the development of a free shear layer, J. Fluid Mech., 26, 225 (1966).
3. Browand, F.K. An experimental investigation of the instability of an incompressible separated shear layer, J. Fluid Mech., 26, 281 (1966).
4. Brown, G. & Roshko, A. The effect of density difference on the turbulent mixing layer, Turbulent Shear Flows, AGARD-CP-93, 23-1 (1971).
5. Brown, G. & Roshko, A. On density effects and large structure in a turbulent mixing layer, J. Fluid Mech., 64, 775 (1974).

6. Castro, I.P. & Bradshaw, P. The turbulence structure of a highly-curved mixing layer, Submitted to J. Fluid Mech., (1975).

7. Clark, J.A. & Markland, E. Flow visualization in free shear layers, Proc. ASCE, J. Hydr. Div., 99, HY11, 1897 (1973).

8. Crow, S.C. & Champagne, F.H. Orderly structure in jet turbulence, J. Fluid Mech., 48, 547 (1971).

9. Damms, S.M. & Küchemann, D. On a vortex-sheet model for the mixing between two parallel streams, Proc. Roy. Soc. A., 339, 451 (1974).

10. Davies, P.O.A.L., Fisher, M.J. & Barratt, M.J. The characteristics of the turbulence in the mixing region of a round jet, J. Fluid Mech., 15, 337 (1963).

11. Freymuth, P. On transition in a separated laminar boundary layer, J. Fluid Mech., 25, 683 (1966).

12. Hama, F.R., Long, J.D. & Hegarty, J.C. On transition from laminar to turbulent flow, J. Appl. Phys., 28, No. 4, 388 (1957).

13. Liepmann, H.W. & Laufer, J. Investigation of free turbulent mixing, NACA T.N. 1257, (1947).

14. Miksad, R.W. Experiments on the non-linear stages of free-shear-layer transition, J. Fluid Mech., 56, 695 (1972).

15. Miksad, R.W. Experiments on non-linear interactions in the transition of a free shear layer, J. Fluid Mech., 59, 1 (1973).

16. Miles, J.B. & Shih, J. Similarity parameter for two-stream turbulent jet-mixing region, AIAA Journal, 6, TN, 1429 (1968).

17. Sato, H. Experimental investigation on the transition of laminar separated layer, J. Phys. Soc. Japan, 11, No. 6, 702 (1956).

18. Sato, H. Further investigation on the transition of two-dimensional separated layer at subsonic speeds, J. Phys. Soc. Japan, 14, No. 12, 1797 (1959).

19. Spencer, B.W. & Jones, B.G. Statistical investigation of pressure and velocity fields in the turbulent two-stream mixing layer, AIAA Paper No. 71-613, (1971).

20. Weber, D.P. Turbulent velocity field structure in a round jet and its relation to fluctuating pressure fields, Ph.D. Thesis, Univ. of Illinois at Urbana Champaign, (1974).

21. Wille, R. Beiträge zur Phänomenologie der Freistrahlen, Zeitschrift für Flugwissenschaften, 11, Heft 6, 222 (1963).

22. Winant, C.D. & Browand, F.K. Vortex pairing: the mechanism of turbulent mixing-layer growth at moderate Reynolds number, J. Fluid Mech., 63, 2 (1974).

23. Wygnanski, I. & Fiedler, H.E. The two-dimensional mixing region, J. Fluid Mech., 11, Part 2, 327 (1970).

Captions

Figure 1 — Discrete rolls connected by spanwise thin sheets. (Smoke in air, flow from left to right, fast side below, "still" air above, $U \simeq 0.61\ ms^{-1}$, $\theta \simeq 0.15$ cm, $U\theta/\nu \simeq 60$. Third vortex is at $x \simeq 25$ cm $\simeq 5000\ (\nu/U)$).

Figure 2 — Vortex pairing in the same flow, observed from above. Test-rig width = 75 cm, picture width 50 cm.

Figure 3 — Shadowgraphs of mixing layers. (a) (from Brown & Roshko 1974). N_2 below, H_e above: $U\theta/\nu \simeq 50$ in N_2, $U(N_2)/U(H_e) = 2.6$. (b) Present results, same region as right of Fig. 1, but with CO_2 injected instead of smoke.

Figure 4 — Top view of double helix pairing.

Figure 5 — Overall top view of smoke-filled mixing layer.



FIG. 1

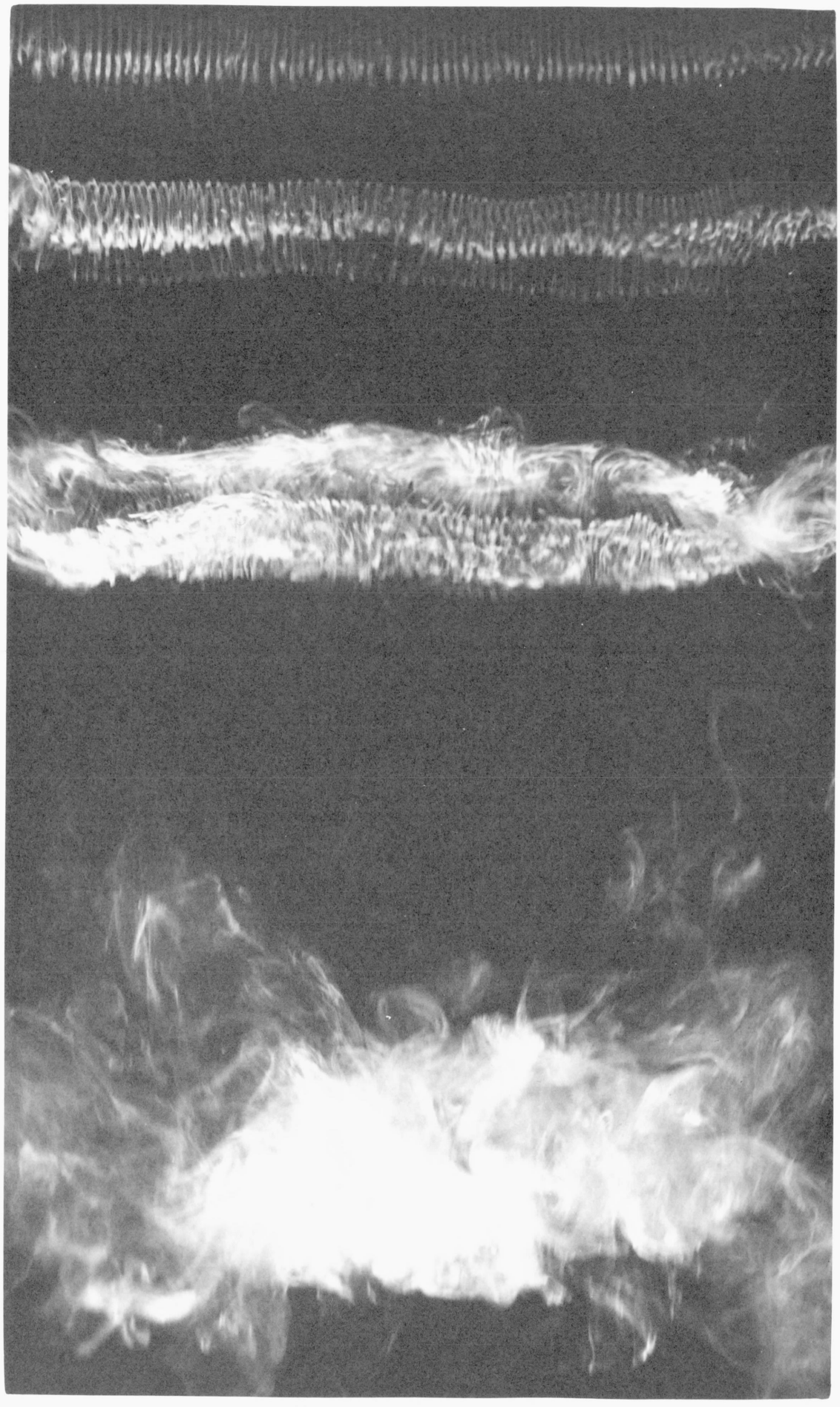
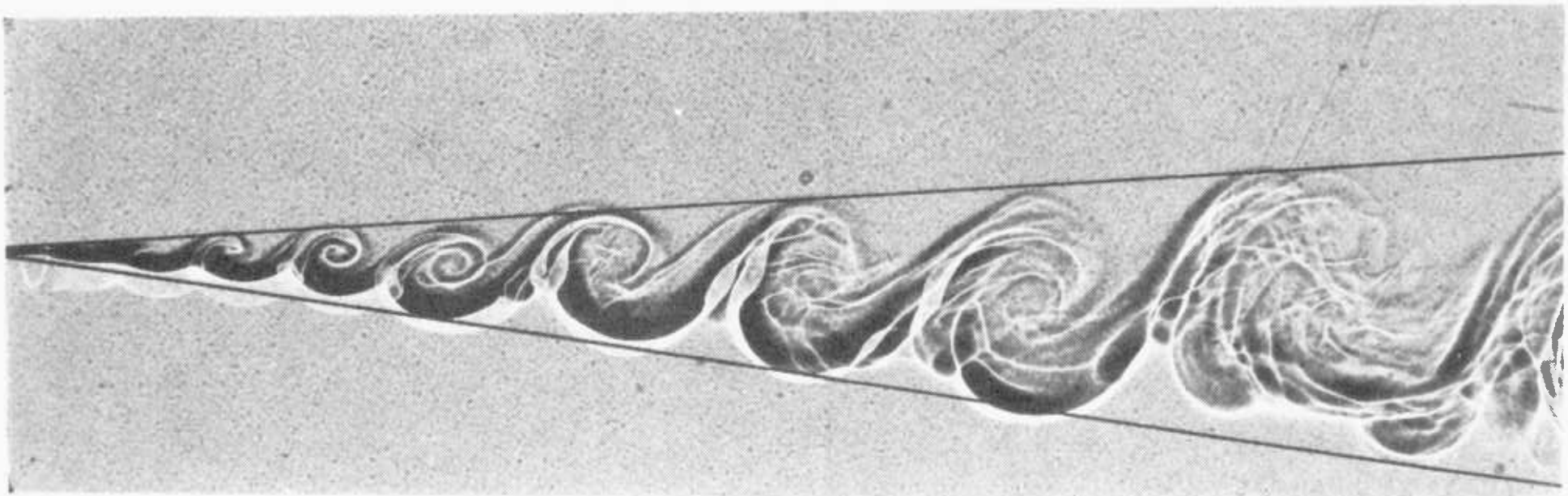


FIG. 2



(a)

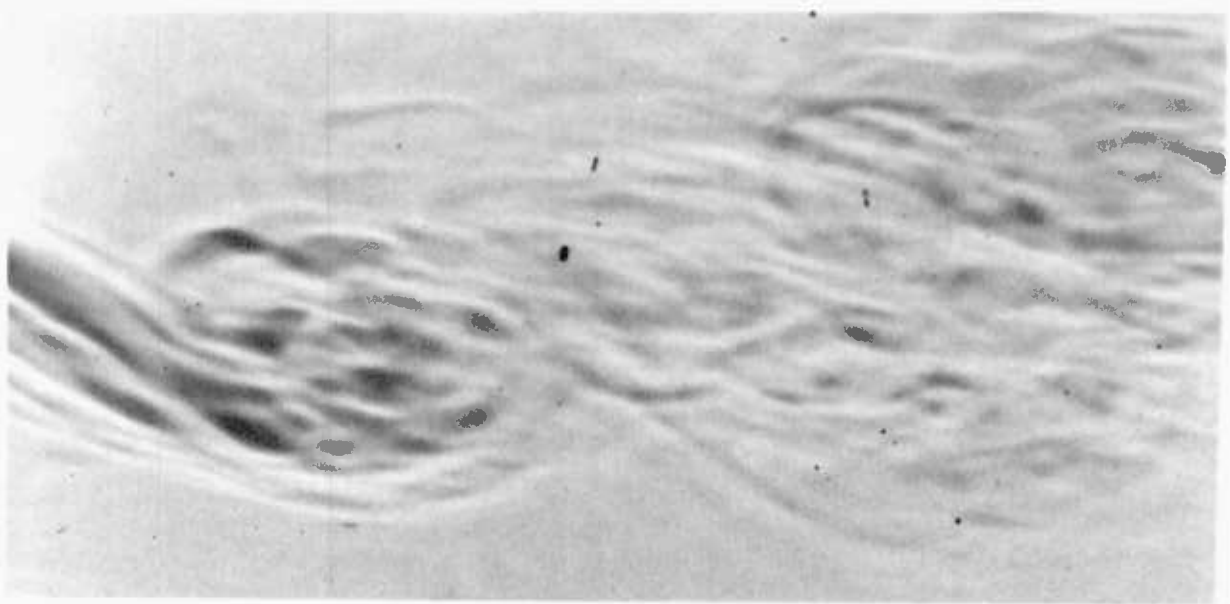


FIG. 3 (b)

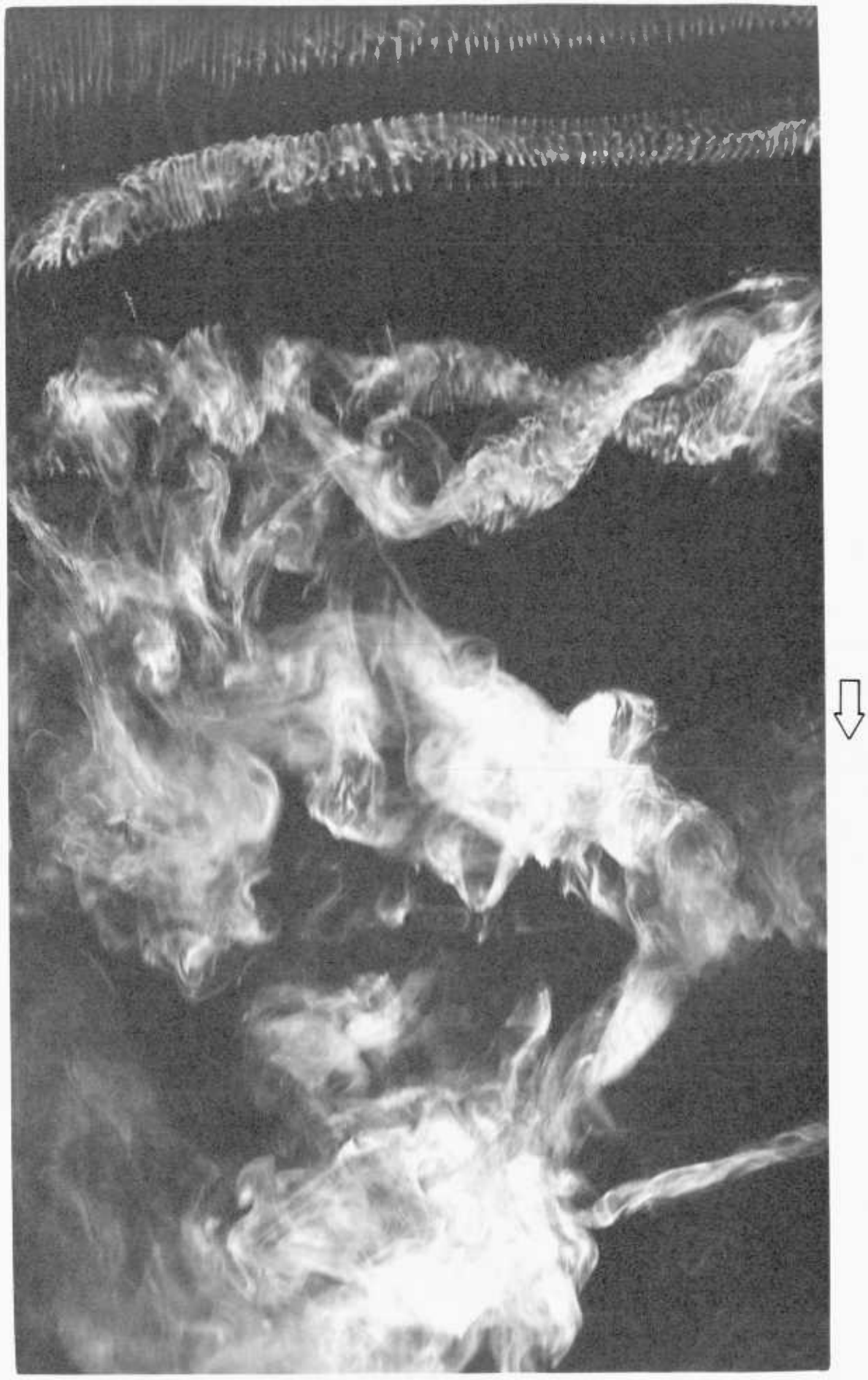


FIG. 4



FIG. 5

APPENDIX II

AN IMPROVED METHOD OF HOT-WIRE CALIBRATION CURVE FITTING.

It is well known that a hot-wire response equation in the form $E^2 = A + BU^n$, at a particular constant index n, will not be linear over a large range of mean velocity (e.g. Bruun 1971). However, workers who concern themselves with either nominally constant mean speed or a narrow speed range can happily use such an equation with n chosen to suit a particular wire. There is still no general agreement on the choice between static and dynamic calibration methods. Although dynamic calibration seems to be more reliable, the need for special apparatus (i.e. a rig for vibrating the probe) makes the method somewhat unattractive to most workers, and an improved method of better approximation of static calibration data is being sought as an alternative. Bruun (1971) shows the variation of the exponent n with U and introduces his so-called "universal calibration function" for hot-wire static calibration, which contains one or two parameters chosen to suit a given wire.

In the course of the present work it has been found that all calibration curves, plotted in the form $E^2 = A + BU^{0.45}$, curve down slightly when the mean velocity is greater than about 25 m/s. Because the present data are all for speeds below 45 m/s, the data of Bruun (1971), which go up as high as 150 m/s, have been used as a test case of the calibration curve-fitting method.

The plot of E^2 vs.$U^{0.45}$ in figure II.1. shows that the approximate linear part exists from $U^{0.45} = 0$ to $U^{0.45} \simeq 4$, i.e. up to the speed of about 22 m/s, and the values of A and B are 1.2 and 0.93 respectively. The difference in E^2 between the straight line and the curve (figure II.1), ΔE^2, is plotted against $U^{0.45}$ in figure II.2. The ΔE^2 vs.$U^{0.45}$ curve clearly suggests a parabolic relation with origin at $(\Delta E^2, U^{0.45}) = (0, 4)$. Consequently, the values of ΔE^2 are plotted against $(U^{0.45} - 4)^2$ in figure II.3. where data points fall approximately onto a straight line through the origin with the slope about 0.026. Hence for $U^{0.45} \geq 4$ $(U \geq 22$ m/s), the equation becomes

$$E^2 = A + BU^{0.45} - \Delta E^2$$

$$= 1.2 + 0.93\ U^{0.45} - 0.026\ (U^{0.45} - 4)^2,$$

for this particular case; i.e.

$$E^2 = 0.784 + 1.138\ U^{0.45} - 0.026\ U^{0.9}.$$

The final equation above is similar to that suggested by Davies & Patrick (1972 - see reference in text) who use n = 0.5 and apply the equation to the full range of U. Figure II.4. shows the comparison between Bruun's data and the above equation.

Therefore, for a large range of mean velocity the equations $E^2 = A + B\ U^n$, for the lower-velocity end, and $E^2 = A + BU^n + CU^{2n}$, for the higher-velocity end, appear to be a better approximation than a single straight-line fit over the whole range. The constants A, B and C in the latter equation can be determined as follows:-

(i) Plot E^2 vs.U^n, so that A and B in $E^2 = A + B\ U^n$ can be found.

(ii) Draw a straight line through a linear portion, extending to cover the range of curve in (i). Choose D, the point where the calibration curve departs from the straight line and read off corresponding ΔE^2 for a set of U^n values.

(iii) Plot ΔE^2 against $(U^n - D)^2$ and draw an approximate straight line through data points, so as to find the slope $\propto$.

(iv) Substitute all values (A, B , D and $\propto$) in

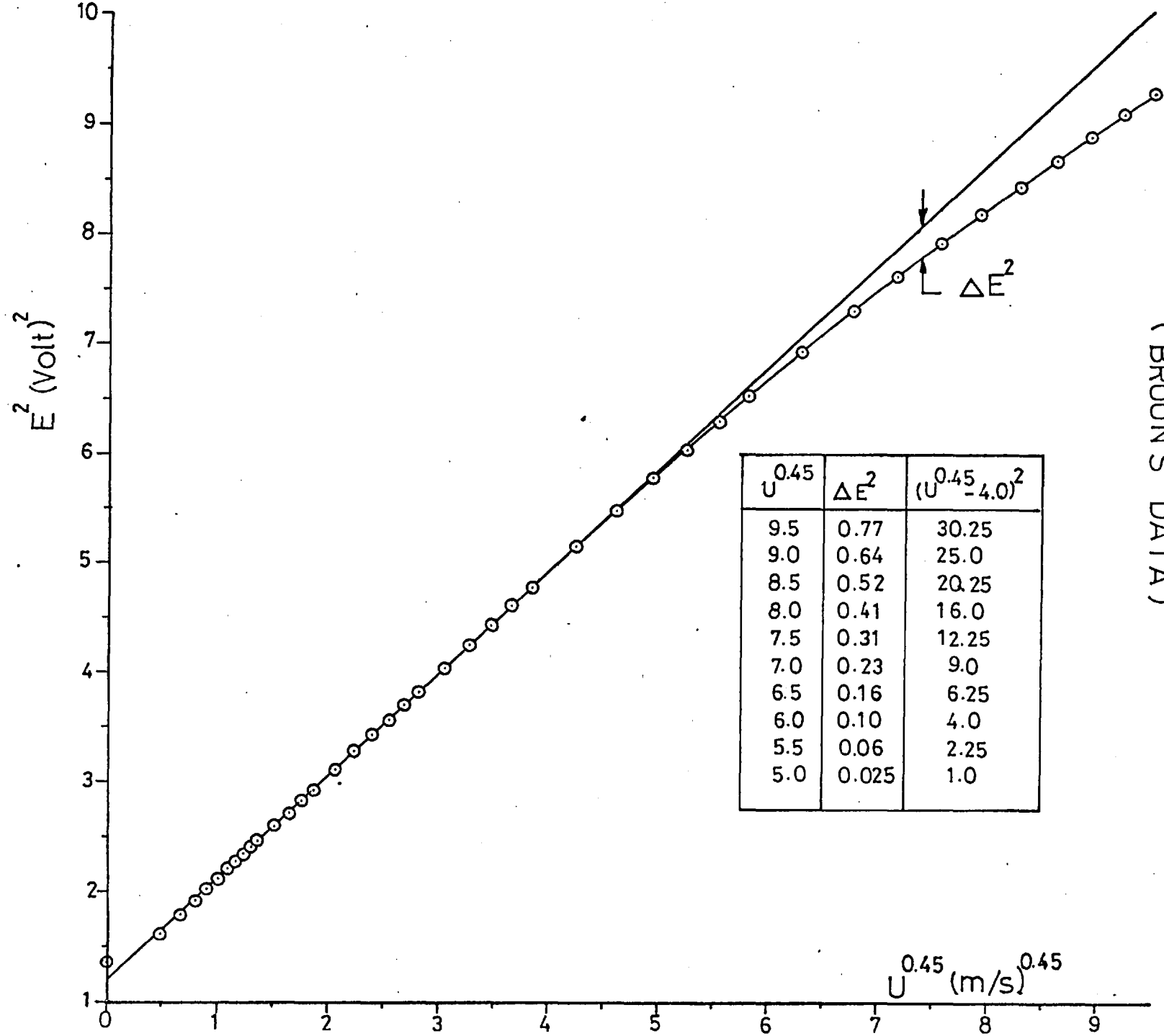
$$E^2 = A + B\ U^n - \propto (U^n - D)^2$$

so as to obtain $E^2 = A + BU^n + CU^{2n}$.

This method was tried on the present data and satisfactory results were obtained, as shown in figure II.5. The change in calibration fit above the point 'D' is not a significant inconvenience either in computer calculations or analysis by hand.

REFERENCE

Bruun, H.H. 1971 "Interpretation of a hot-wire signal using a universal calibration law". J. of Physics E, Sci. Instruments, 4, 225-229.



$U^{0.45}$	ΔE^2	$(U^{0.45}-4.0)^2$
9.5	0.77	30.25
9.0	0.64	25.0
8.5	0.52	20.25
8.0	0.41	16.0
7.5	0.31	12.25
7.0	0.23	9.0
6.5	0.16	6.25
6.0	0.10	4.0
5.5	0.06	2.25
5.0	0.025	1.0

FIGURE II.1 E^2 vs. $U^{0.45}$
(BRUUN'S DATA)

FIGURE II.2 E^2 vs. $U^{0.45}$

(BRUUN'S DATA)

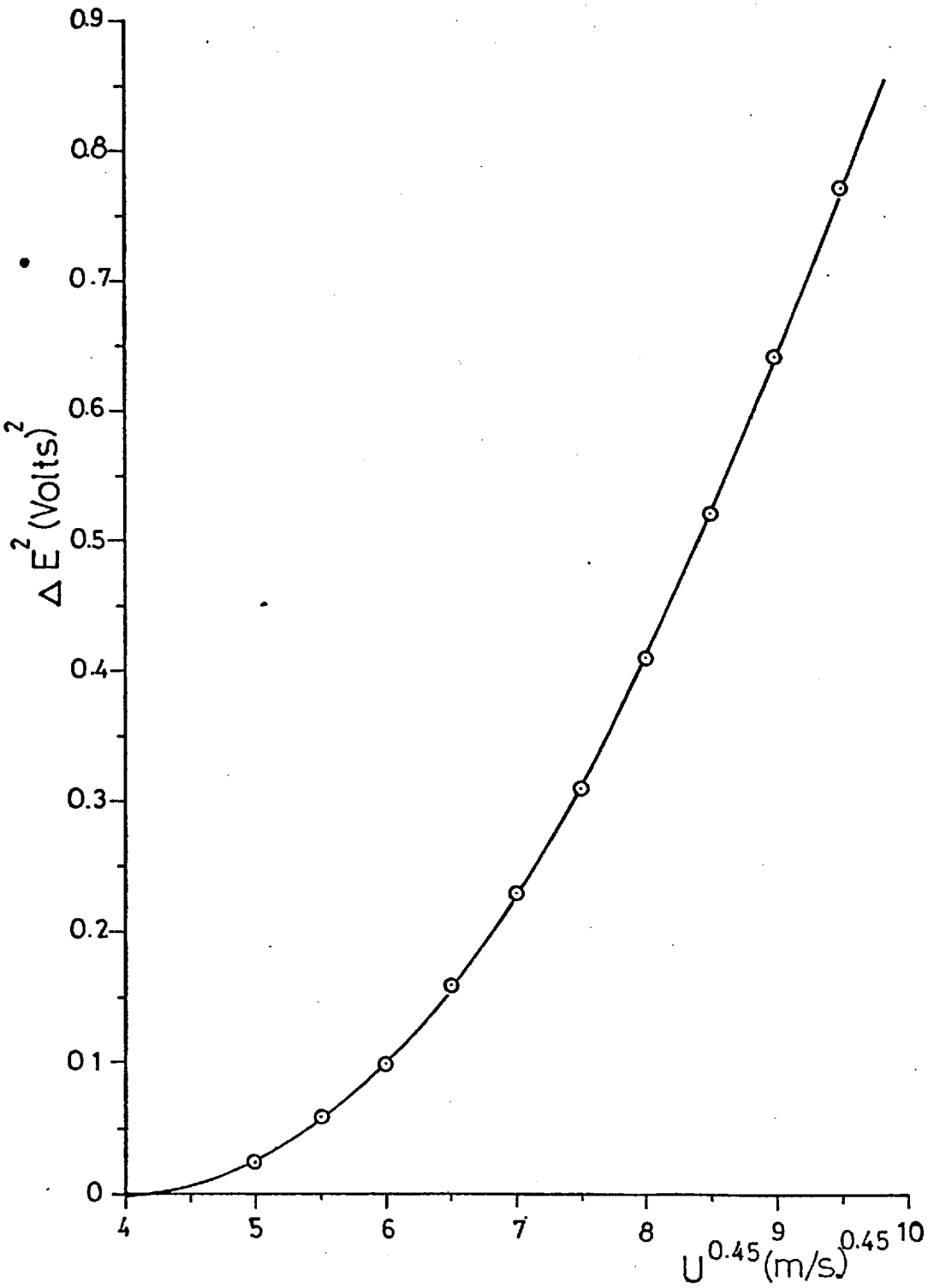


FIGURE II.3 ΔE^2 vs. $(U^{0.45} - 4.0)^2$

(BRUUN'S DATA)

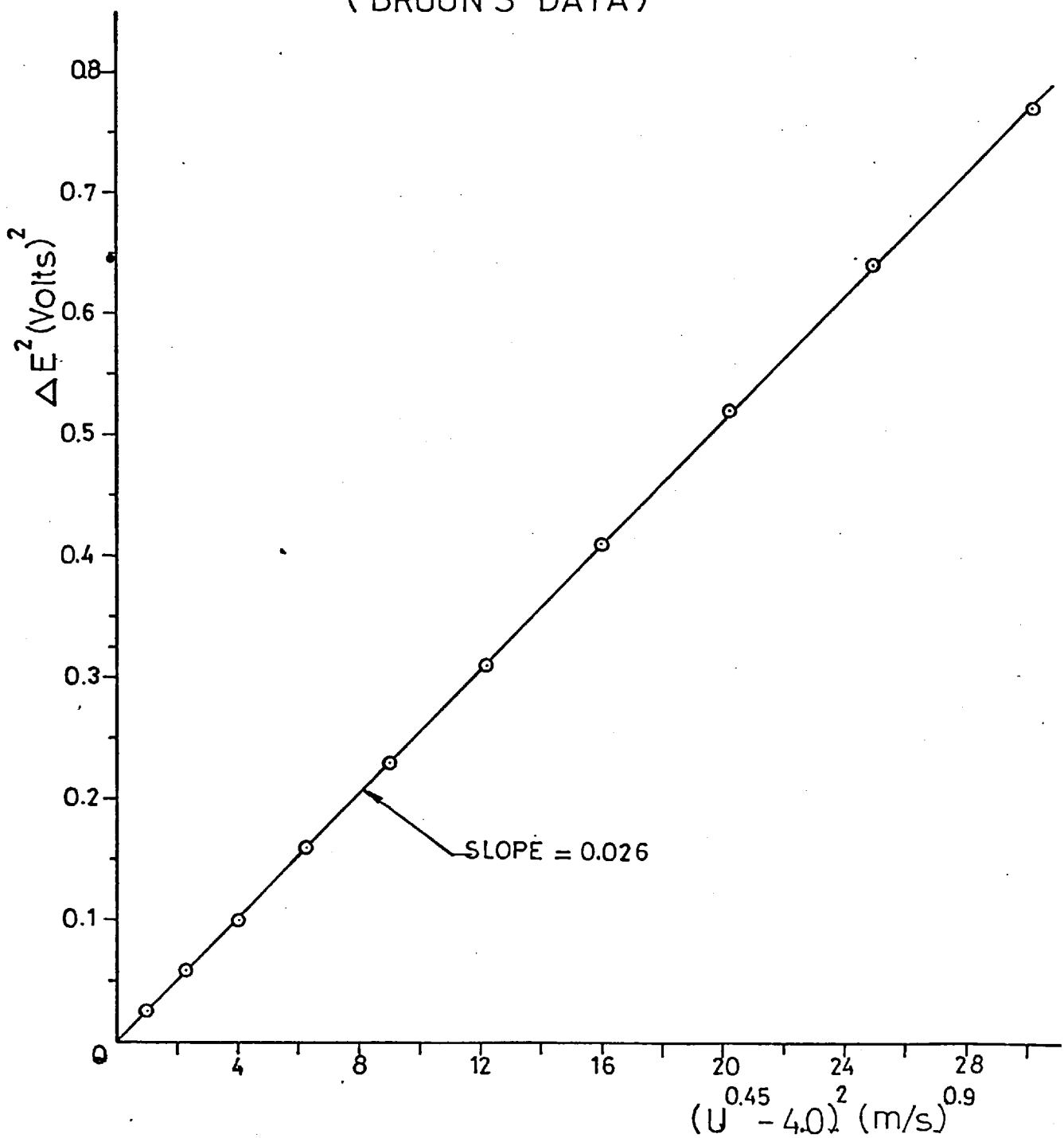


FIGURE II.4 COMPARISON BETWEEN PRESENT CALIBRATION CURVE AND BRUUN'S DATA

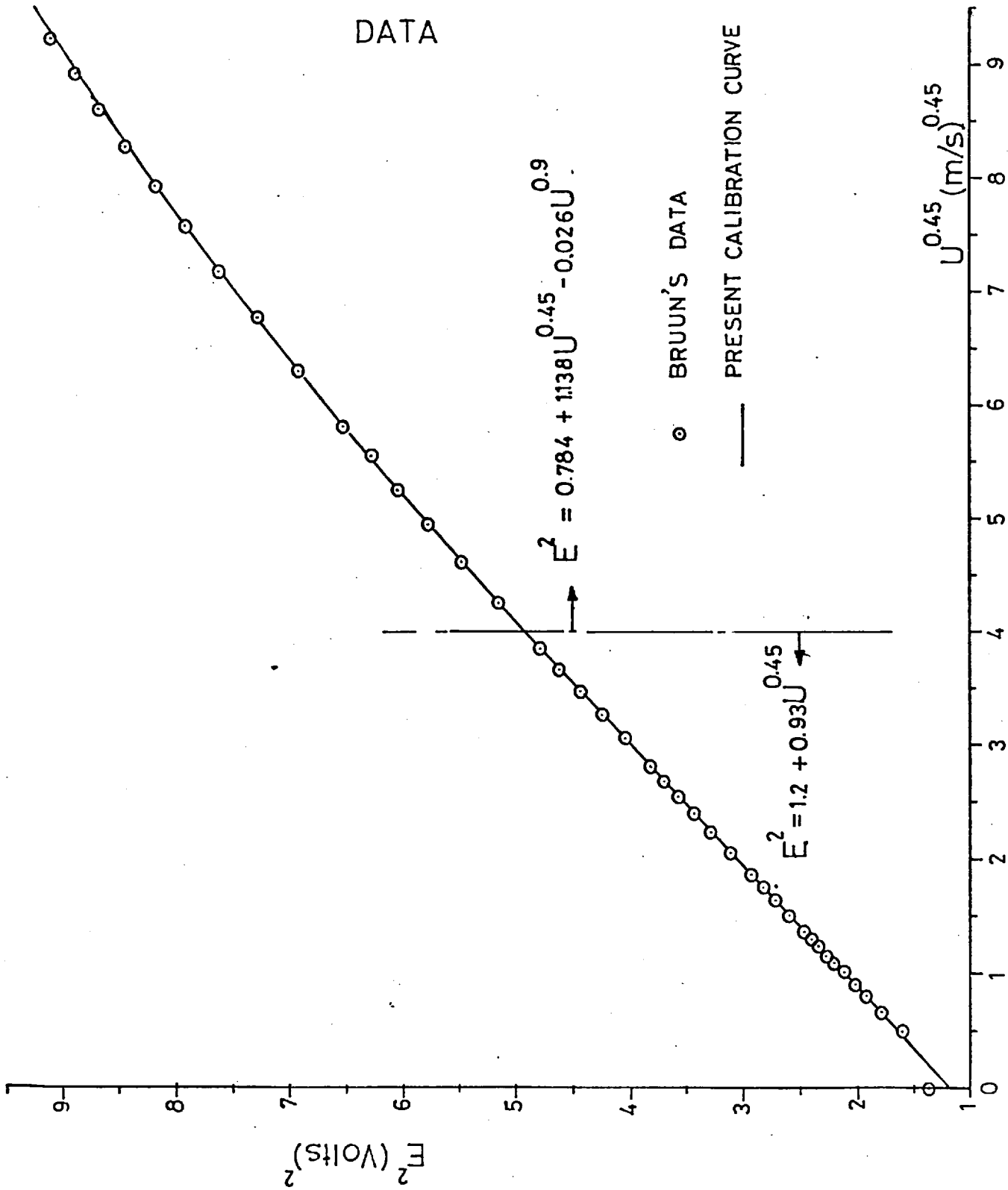
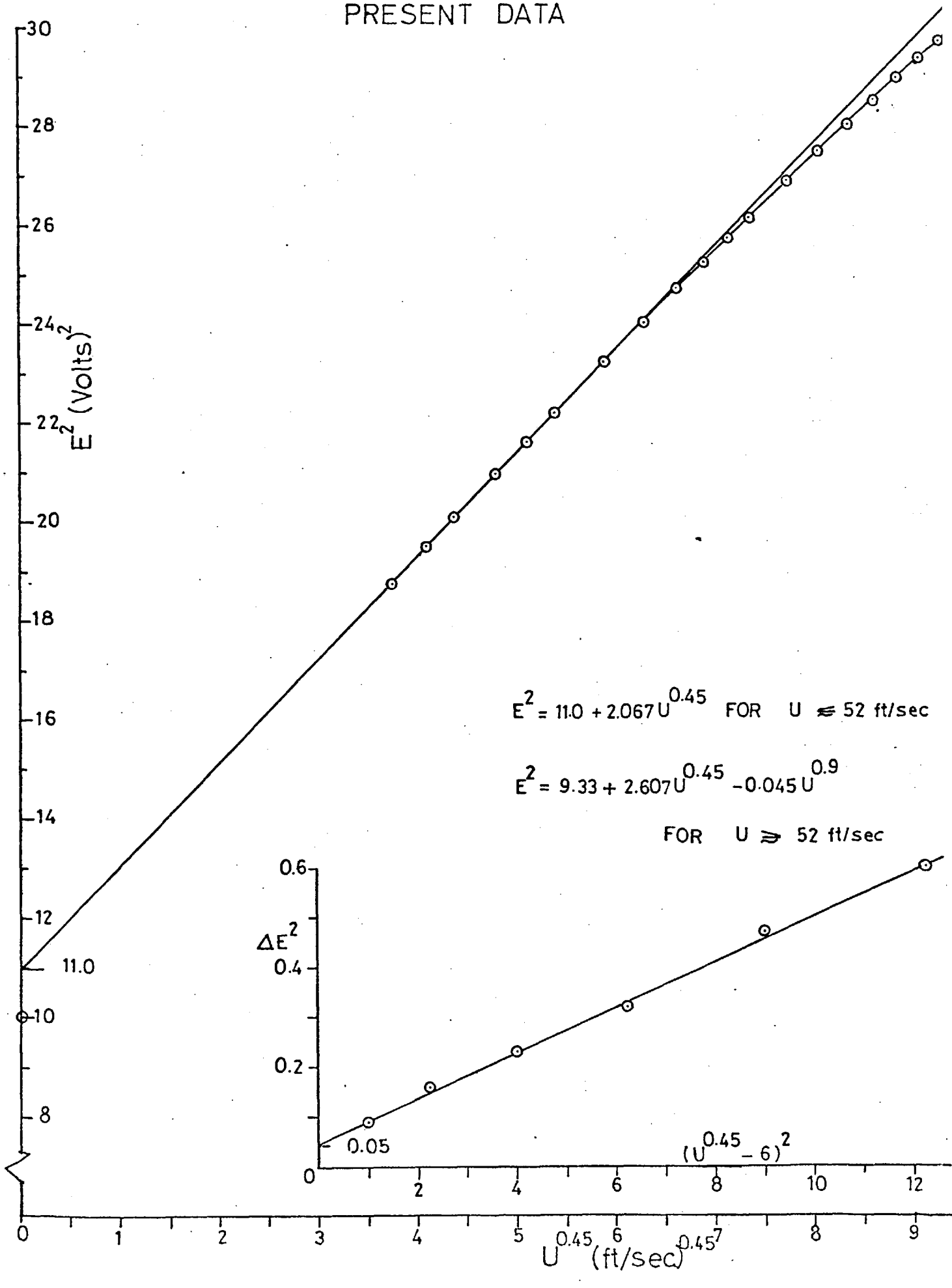


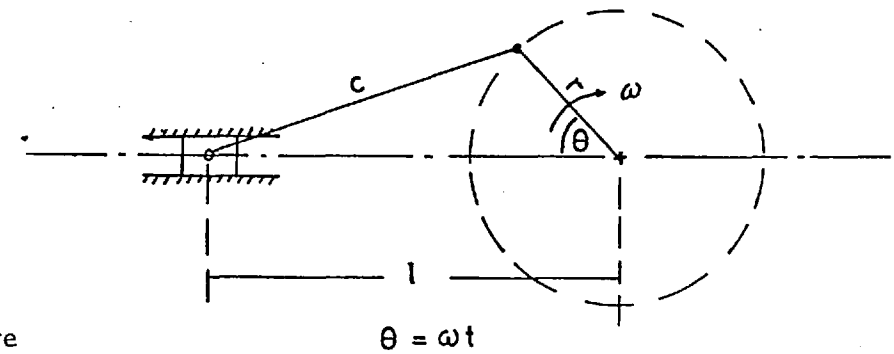
FIGURE II.5 TYPICAL CALIBRATION CURVE OF PRESENT DATA



APPENDIX III

A NOTE ON RMS VELOCITY OF DYNAMIC CALIBRATION

The longitudinal oscillation of the dynamic calibrator described in section 2.7.1. of the text is provided by a crank mechanism, as shown in the sketch below:



We have $\theta = \omega t$

$$\therefore \quad \frac{d\theta}{dt} = \omega$$

From geometry,

$$l = r\cos\theta + \sqrt{c^2 - r^2\sin^2\theta} \qquad \ldots\ (i)$$

$$u = \frac{dl}{dt} = \frac{dl}{d\theta}\cdot\frac{d\theta}{dt} = \omega\frac{dl}{d\theta} = \omega\left[-r\sin\theta + \tfrac{1}{2}(c^2 - r^2\sin^2\theta)^{-\frac{1}{2}}(-2r^2\sin\theta\cos\theta)\right]$$

$$\therefore\ u = -\omega r\sin\theta\left[1 + \frac{\cos\theta}{\sqrt{(c/r)^2 - \sin^2\theta}}\right], \qquad \ldots\ (ii)$$

which is an odd function of .

Since the rms value of a periodic function, $f(t)$, , over one period may be expressed in its Fourier expansion as

$$f(t)\Big|_{rms} = \sqrt{\frac{a_0^2}{4} + \tfrac{1}{2}\sum_{n=1}^{\infty}(a_n^2 - b_n^2)}, \qquad \ldots.(iii)$$

for an odd function as in (ii) we have

$$u_{rms} = \sqrt{\tfrac{1}{2}\sum_{n=1}^{\infty} b_n^2} \qquad \ldots\ (iv)$$

The coefficients b_n may be found by direct expansion of the right-hand side of (ii). For the smaller rotating arm of the present calibrator the ratio c/r is 5.08 and we obtain $u_{rms} \simeq 0.711\,\omega r$ compared with $0.707\,\omega r$ for a true sine-wave.

Hence the departure from the true sine-wave in this case is negligibly small as noted in the text. In any case, the use of a band-pass filter to remove low-frequency electronic noise and tunnel turbulence also removes the harmonics.